ROYAL INSTITUTE
OF TECHNOLOGY

Fundamental Control Performance Limitations for Interarea Oscillation Damping and Frequency Stability

JOAKIM BJÖRK

Doctoral Thesis
Stockholm, Sweden 2021

KTH Royal Institute of Technology
School of Electrical Engineering and Computer Science
Division of Decision and Control Systems
SE-100 44 Stockholm
SWEDEN

TRITA-EECS-AVL-2021:27
ISBN 978-91-7873-841-0

Akademisk avhandling som med tillstånd av Kungliga Tekniska högskolan framläges till offentlig granskning för avläggande av teknologie doktorsexamen i elektro- och systemteknik tisdagen den 1 juni 2021 klockan 15.00 i sal F3, Kungliga Tekniska högskolan, Lindstedtsvägen 26, Stockholm.

Tryck: Universitetsservice US-AB

Abstract

With the transition towards renewable energy and the deregulation of the electricity markets, the power system is changing. Growing electricity demand and more intermittent power production increase the need for transfer capacity. Lower inertia levels due to a higher share of renewables increase the need for fast frequency reserves (FFR). In this thesis, we study fundamental control limitations for improving the damping of interarea oscillations and frequency stability.

The first part of the thesis considers the damping of oscillatory interarea modes. These system-wide modes involve power oscillating between groups of generators and are sometimes hard to control due to their scale and complexity. We consider limitations of decentralized control schemes based on local measurements, as well as centralized control schemes with limitations associated to actuator dynamics and network topology. It is shown that the stability of asynchronous grids can be improved by modulating the active power of a single interconnecting high-voltage direct current (HVDC) link. One challenge with modulating HVDC active power is that the interaction between interarea modes of the two grids may have a negative impact on system stability. By studying the controllability Gramian, we show that it is possible to improve the damping in both grids as long as the frequencies of their interarea modes are not too close. It is demonstrated how the controllability, and therefore the achievable damping, deteriorates as the frequency difference becomes small. With a modal frequency difference of 5 %, the damping can be improved by around 2 percentage points whereas a modal frequency difference of 20 % allows for around 8 percentage points damping improvement. The results are validated by simulating two HVDC-interconnected 32-bus power system models. We also consider the coordinated control of two and more HVDC links. For some network configurations, it is shown that the interaction between troublesome interarea modes can be avoided.

The second part considers the coordination of frequency containment reserves (FCR) in low-inertia power systems. A case study is performed in a 5-machine model of the Nordic synchronous grid. We consider a low-inertia test case where FCR are provided by hydro power. The non-minimum phase characteristic of the waterways limits the achievable bandwidth of the FCR control. It is shown that a consequence of this is that hydro-FCR fails at keeping the frequency nadir above the 49.0 Hz safety limit following the loss of a HVDC link that imports 1400 MW. To improve the dynamic frequency stability, FFR from wind power is considered. For this, a new wind turbine model is developed. The turbine is controlled at variable-speed, enabling FFR by temporarily borrowing energy from the rotating turbine. The nonlinear wind turbine dynamics are linearized to facilitate a control design that coordinate FFR from the wind with slow FCR from hydropower. Complementary wind resources with a total rating of 2000 MW, operating at 70–90 % rated wind speeds, is shown to be more than enough to fulfill the frequency stability requirements. The nadir is kept above 49.0 Hz without the need to install battery storage or to waste wind energy by curtailing the wind turbines.

Sammanfattning

Övergången till förnybar energi och avregleringen av elmarknaden leder till förändringar i elnätet. En växande efterfrågan på el och en mer väderberoende och osäker produktion ökar behovet av överföringskapacitet. En minskning av rotationsenergin till följd av en högre andel förnyelsebar elproduktion medför även ett ökat behov av snabba frekvensreserver, *fast frequency reserves* (FFR). I denna avhandling så studeras fundamentala begränsningar för att med återkoppling dämpa interareapendlingar och förbättra frekvensstabiliteten.

Den första delen av avhandlingen undersöker fundamentala prestandabegränsningar för dämpningen av interareapendlingar. Dessa systemövergripande pendlingar involverar grupper av generatorer som svänger i förhållande till varandra. Interareapendlingar är ibland svåra att styra på grund av deras skala och komplexitet. Vi studerar begränsningar vid återkoppling från lokala mätsignaler, samt för centraliserade regulatorstrukturer med begränsningar kopplade till ställdonsdynamik och elsystemets topologi. Det visas hur stabiliteten hos två olika synkrona nät sammankopplade med högspänd likström, *high-voltage direct current* (HVDC), kan förbättras genom att modulera den aktiva effekten hos en enda HVDC-länk. En utmaning med aktiv effektmodulering är att växelverkan mellan interareapendlingar hos de två näten kan ha en negativ inverkan på systemets stabilitet. Genom att studera styrbarhetsgramianen visar vi att det alltid är möjligt att förbättra dämpningen i båda näten så länge som frekvenserna hos deras interareapendlingar inte ligger för nära varandra. Det visas hur styrbarheten, och därmed de möjliga dämpningsförbättringarna, försämras då frekvensskillnaden blir liten. Då frekvensskillnad är 5 % så kan dämpningen förbättras med cirka 2 procentenheter medan en frekvensskillnad på 20 % möjliggör cirka 8 procentenheters förbättring av dämpningen i båda näten. Resultaten valideras i en detaljerad simuleringsstudie av två elnät (vardera med 32 noder) sammankopplade med en HVDC-länk. Utöver detta undersöks även koordinerad styrning av två och fler länkar. För vissa elnätstopologier visas det att växelverkan mellan besvärliga interareapendlingar kan undvikas.

I avhandlingens andra del undersöks koordinering av frekvenshållningsreserver, *frequency containment reserves* (FCR), i kraftsystem med låg rotationsenergi. En fallstudie genomförs i en modell av det nordiska kraftsystemet bestående av 5 maskiner. Vi undersöker ett scenario med låg rotationsenergi där FCR tillhandahålls från vattenkraft. Vattenvägarnas icke-minfasegenskaper medför en bandbreddsbegränsning. En konsekvens av detta är att FCR baserad på enbart vattenkraft misslyckas med att hålla frekvensen över det tillåtna gränsvärdet 49,0 Hz efter bortfallet av en HVDC-länk som importerar 1400 MW. För att förbättra frekvenssvaret undersöks möjligheten att tillhandahålla FFR från vindkraft. För detta ändamål så utvecklas en ny vindkraftverksmodell. Turbinen styrs med variabelt varvtal och tillåter FFR genom att tillfälligt låna energi från turbinen. Vindkraftverket linjäriseras för att möjliggöra en koordinering med långsam FCR från den befintliga vattenkraften. Kompletterande vindresurser med totalt 2000 MW märkeffekt (vid 70–90 % av nominell vindhastighet) visar sig vara mer än tillräckligt för att uppnå frekvenskraven. Frekvensen hålls över 49,0 Hz utan att behöva installera batterilager eller begränsa vindkraftens produktion och spilla energi från vinden.

Acknowledgments

First and foremost, I would like to express my deep gratitude to my supervisor Karl Henrik Johansson. Your enthusiasm and curiosity is a true inspiration. Thank you for providing me the opportunity to study at KTH and for all the freedom to choose my research path that I was given. Although the path has been intimidating and despairing at times, your guidance and relentless optimism has helped me persevere. I would also like to thank my co-supervisor Lennart Harnefors for guidance, feedback, and the inspiration given to this interesting research topic.

I want to express my gratitude to Florian Dörfler for your inspiring ideas and valuable feedback. I would also like to thank Robert Eriksson for the collaboration and helpful guidance in my work. Thanks to my co-authors Danilo Obradović and Daniel Vázquez Pombo for fruitful discussions. Heartfelt thanks also to Bertil Berggren, Elling Jacobsen, Emma Tegling, and Richard Pates for your feedback. I look forward to further discussions in the future.

Special thanks to Henrik Sandberg for being the advance reviewer for both my licentiate and doctoral theses as well as for chairing the public defense. I would like to thank Joe H. Chow, for kindly accepting to serve as my opponent, and to Göran Andersson, Marija Ilić, and Robin Preece for agreeing to be on the committee for the defense of this thesis. I am also very grateful to Matthieu Barreau and Xinlei Yi for proofreading and providing feedback on parts of this thesis. Thanks also to Elling Jacobsen and Xiongfei Wang for agreeing to act as substitutes committee members.

I wish to express my sincere gratitude to all my colleagues (current and former) at the Division of Decision and Control Systems—far too many to name everyone here—thank you for creating such a friendly and active working atmosphere.

The research leading to this thesis has received funding from the Swedish Research Council, the Swedish Foundation for Strategic Research, Knut and Alice Wallenberg Foundation, and the KTH PhD Program in the Digitalization of Electric Power Engineering. I am grateful for their support.

I would like to express my appreciation to my parents Ann-Christine and Johan, and to my brother Pontus for their love and unconditional support. Thanks also to all my friends that have brought me much joy throughout my life and career. Without you, I would never have gotten to where I am today. Last, but not least, I would like to thank my loving and supportive fiancée Stina. You brighten up my every day.

Joakim Björk
Stockholm, May 2021

Contents

Acronyms

AVR	Automatic voltage regulator
CE	Continental Europe
COI	Center of inertia
DPF	Dynamic participation factor
FACTS	Flexible ac transmission systems
FCR	Frequency containment reserves
FCR-D	FCR for disturbance situations
FCR-N	FCR for normal operation
FFR	Fast frequency reserves
FRR	Frequency restoration reserves
HVAC	High-voltage alternating current
HVDC	High-voltage direct current
IGBT	Insulated-gate bipolar transistor
LCC	Line commutated converter
LHP	Left half-plane
LQG	Linear quadratic Gaussian
LTI	Linear time-invariant
MIMO	Multiple-input multiple-output
MMC	Modular multilevel converter
MP	Minimum phase
MPP	Maximum power point
MTDC	Multi-terminal HVDC
N5	Nordic 5-machine
N32	Nordic 32-bus
NMP	Non-minimum phase
NREL	National Renewable Energy Laboratory
PDCI	Pacific HVDC Intertie
PMU	Phasor measurement unit
POD	Power oscillation damping
PSS	Power system stabilizer
PWM	Pulse-width modulator
RG	Regional group
RGA	Relative gain array

RHP	Right half-plane
CRHP	Closed RHP
ORHP	Open RHP
RoCoF	Rate of change of frequency
SIME	Single-machine equivalent
SISO	Single-input single-output
SMIB	Single-machine infinite bus
STATCOM	Static synchronous compensator
SVC	Static var compensator
SVD	Singular value decomposition
VPP	Virtual power plant
DVPP	Dynamic VPP
VSC	Voltage source converter
WAMS	Wide-area measurement systems
WT	Wind turbine

Chapter 1

Introduction

With the transition towards renewable energy, and the deregulation of the electricity markets, generation patterns and grid topology are changing. A more weather dependent intermittent power production, growing electricity demand, and a more interconnected electricity market increase the need for transfer capacity. At the same time, the frequency stability of grids are becoming more sensitive to load imbalances due to the growing share of converter-interfaced generation. The utilization of controllable power electronics devices, such as high-voltage direct current (HVDC) transmission lines, is considered a key to ensuring stable and secure operation of today's power system. The present thesis aims to study uses and limitations of controllable power electronics devices for improving dynamic stability of power systems. Of particular interest are the fundamental control limitations arising when dynamic interactions with the power source is in conflict with the control objective.

The first part of the thesis considers the use of HVDC control for stabilizing interarea oscillations. An analysis of the fundamental control limitations imposed by the interactions of two synchronous grids over a single controlled HVDC line is performed. Following this we study how coordinated control of two or more links can be used to circumvent these limitations. In addition we also consider control performance limitations associated with the measurement type. We identify conditions for when damping control based on local measurements may conflict with transient rotor angle stability.

The second part consider frequency stability. Here we extend the scope past HVDC transmission to also include other controllable energy sources such as wind turbines, battery storage, and hydropower plants. A decentralized control scheme is developed to achieve a global frequency containment objective in a low-inertia power system. The control scheme assumes that higher-order network dynamics, such as interarea modes, are stable. To ensure this, a scalable stability criterion is developed that provide a priori stability guarantees for connecting new devices to the power system, using only local information.

This introductory chapter is organized as follows. Section 1.1 gives a motivation

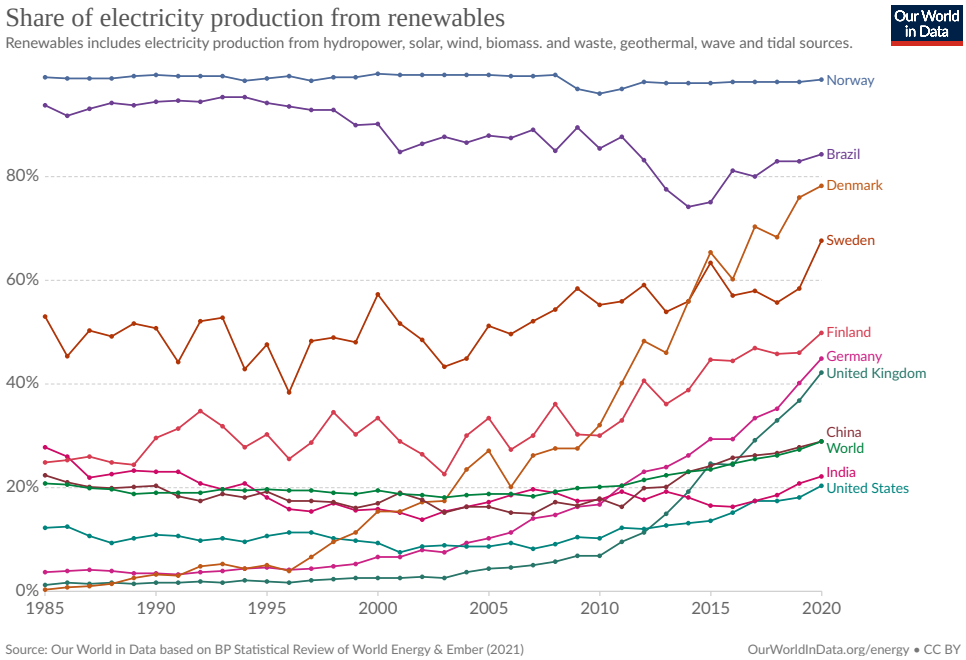

Figure 1.1: Graphic illustrating the share of renewables [1] (with data from [2, 3]).

to why further research in power system stability is necessary. In Section 1.2 practical examples of HVDC damping control are studied. The examples show how dynamic interactions between the interconnected systems limit the usefulness of HVDC control. Section 1.3 considers frequency control in a low-inertia power system. An example show how fast acting control from converter-interfaced renewable energy can be used to fulfill dynamic requirements, not achievable by conventional synchronous generation. In Section 1.4, we formulate the problem this thesis addresses. Lastly, Section 1.5 lists the remaining structure of the thesis, its contents and contributions.

1.1 Motivation

Electric power systems are facing significant changes, motivated by a changing climate and increased environmental awareness. Between 1985 and 2020 the world share of electricity production from renewables grew from 21 % to 29 % as illustrated in Figure 1.1. In 1990, around 71 % of the world's population has access to electricity; this has increased to 87 % in 2016 [1]. Much of this growth has been met by an increase in coal and gas as shown in Figure 1.2. But the total share of renewable energy is increasing. A continued growth in renewable energy will lead to power system with lower synchronous generation and a more intermittent energy supply.

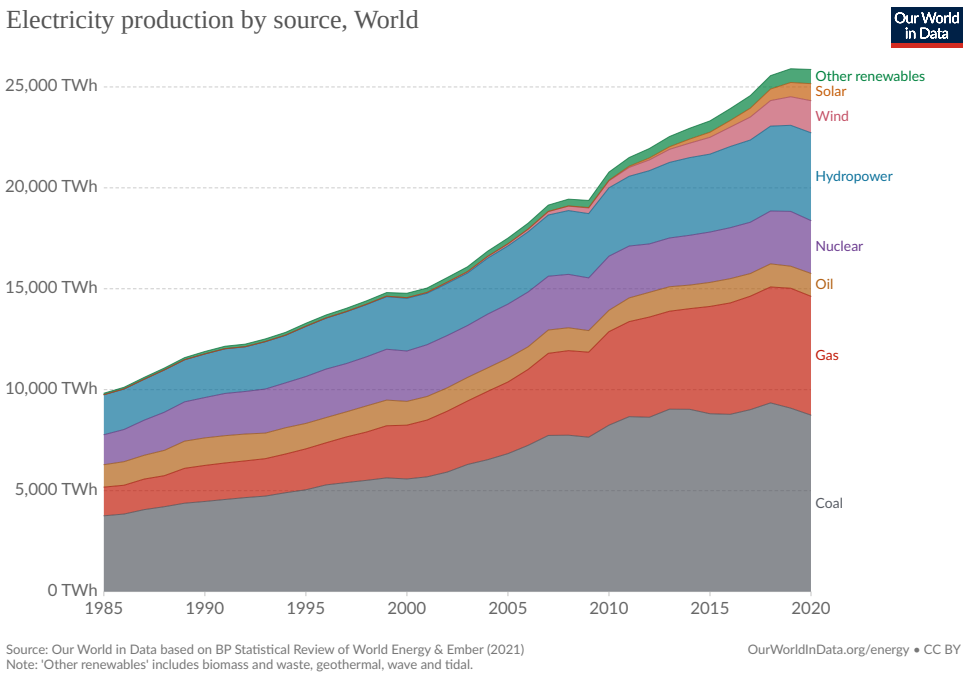

Figure 1.2: Graphic illustrating the global electricity mix [1] (with data from [2, 3]).

This imposes new technological challenges. In this thesis we study control methods for improving power system stability margins. The goal is to improve reliability and allow for a more cost efficient use of the power system infrastructure. To sustain a growth backed by renewable energy, technological developments are needed to make renewables a cost effective alternative to fossil fuels.

The increased share of renewable energy also leads to a transition from centralized large-scale electricity producers, towards a more decentralized system with small-scale producers. Another alteration to the power system seen during the last couple of decades is the deregulation of the electricity market [4, 5]. The classical vertically integrated system is split up into generation, transmission system operators, distribution system operators, and retailers. System operators used to have full control over the system, but this is no longer the case. At the same time we see an increase in long distance transmission. An increase enabled by a growing interconnection between countries, e.g., using HVDC. Investments, motivated by climate change, and deregulation of the power system have led to an increase in installed generation and transactions. However, due to uncertainties and long lead times, investments in the transmission system have not followed the same pace. As a result, congestion and stability problems are a growing problem in today's power systems. This thesis deals with the latter of these issues.

(a) The Nordic power system

(b) Nuclear power

(c) Hydro power

(d) Wind power

(e) HVDC

Figure 1.3: The Nordic power system (a) is an extensive power system with generation relying mainly on hydro (c) and nuclear (b). The system is experiencing great changes due to a decommissioning of nuclear power plants and an increase in converter-interfaced wind power (d). At the same time HVDC transmission (e), purple lines in (a), are increasingly installed in the power system integrating the Nordic electricity market with the Continental European, the Baltic, and the UK grid. Thermal plants (including nuclear power plants) are indicated by triangles in (a). Hydro plants, mostly located in Norway and northern Sweden and Finland, are indicated by squares. (a) Map courtesy of Svenska kraftnät. (b) Image courtesy of Vattenfall, photo: Elin Bergqvist. (c) Image courtesy of Vattenfall, photo: Hans Blomberg. (d,e) Images courtesy of ABB.

System operators need to ensure that the variable load demand is constantly matched with generation from dispatchable energy sources such as coal, gas, nuclear (Figure 1.3b), and hydro (Figure 1.3c), together with intermittent energy sources such as solar and wind (Figure 1.3d). For power systems with long transmission corridors, such as the Nordic power system (Figure 1.3a), transmission capacity is sometimes limited by dynamical stability [6, 7]. In this work, we study a dynamic phenomenon known as interarea oscillations. The dynamics of these involve electromechanical interactions between large generator groups in different regions (or areas) of the system oscillating against each other in poorly damped modes. Sufficient stabilizing control often requires coordinated tuning of multiple components. The strength and controllability of HVDC (Figure 1.3e) make it suitable for stabilization of these system-wide oscillatory modes.

With an increasingly intermittent power production and a deregulated electricity market, we see an increase in long distance transmission and international trade. Because of this, operation in highly stressed conditions is becoming more common. Instability in the form of interarea oscillations have therefore become an even greater concern than in the past [8]. At the same time, the number of controllable devices in the grid is growing rapidly. The control of power electronic based devices such as HVDC links and flexible ac transmission systems (FACTS) is recognized as a key factor in maintaining a secure and dependable power system. The interaction between multiple controllable devices and dynamical components is far from trivial. To deal with this complexity, researchers have studied optimization-based control methods [9–14]. Resorting to numerical optimization-based methods may be necessary for practical applications. However, it can reduce valuable physical insight into the system. To aid the increasingly complex control problem, this thesis focuses on understanding the limitations imposed by the network structure and the interaction between physical devices and controllers.

The potential of HVDC control for damping of interarea modes have been studied for decades. A prime example of this is the damping of the 0.3 Hz north–south interarea mode in the western North American power system in the 1970s. During heavy loading, the transmission system frequently experienced growing power fluctuations as seen in Figure 1.4. This phenomenon constrained the amount of surplus hydro power that could be transmitted to the southwest. Active power modulation of the Pacific HVDC Intertie (PDCI) was implemented to counteract these power oscillations, thereby increasing the transfer capacity of the parallel ac transmission system [15, 16]. However, the PDCI damping control scheme never left prototype status. This is because the feedback signal, based on local ac power flow, had a transfer-function zero which limited the controller gain and caused oscillations at higher frequencies to worsen [17]. Poor damping of the north–south interarea mode has continued to be an issue in the western North American power system where it was one of the major factors in the Blackout of August 10, 1996 [18, 19].

To maintain a high power quality with stable and secure supply, it is important that new devices aid in services previously provided by synchronous machines. The strength and controllability of HVDC makes it a suitable technology to aid

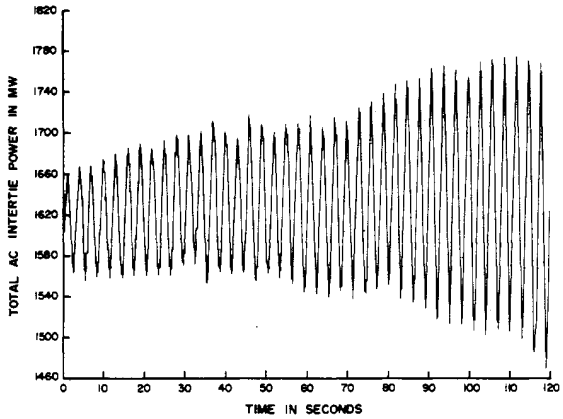

Figure 1.4: Negatively damped power oscillations in the western North American power system recorded August 2, 1974 [15]. © 1976 IEEE

in controlling the system-wide interarea modes. However, most existing HVDC installations today are not utilized for this purpose. The purpose of this thesis is to improve the theoretical understanding of the problem and increase confidence in new control solutions. Thus increasing the chances for auxiliary HVDC control schemes, such as damping control, to be adopted by the system operators.

When controlling point-to-point HVDC links that interconnects asynchronous power systems, both of the connected systems will be affected. As seen in Figure 1.5, troublesome interarea modes may exist in the power system at either end of the HVDC link. The focus of this work is on the control limitations imposed by the interaction of poorly damped modes when controlling HVDC interconnections between two asynchronous ac grids.

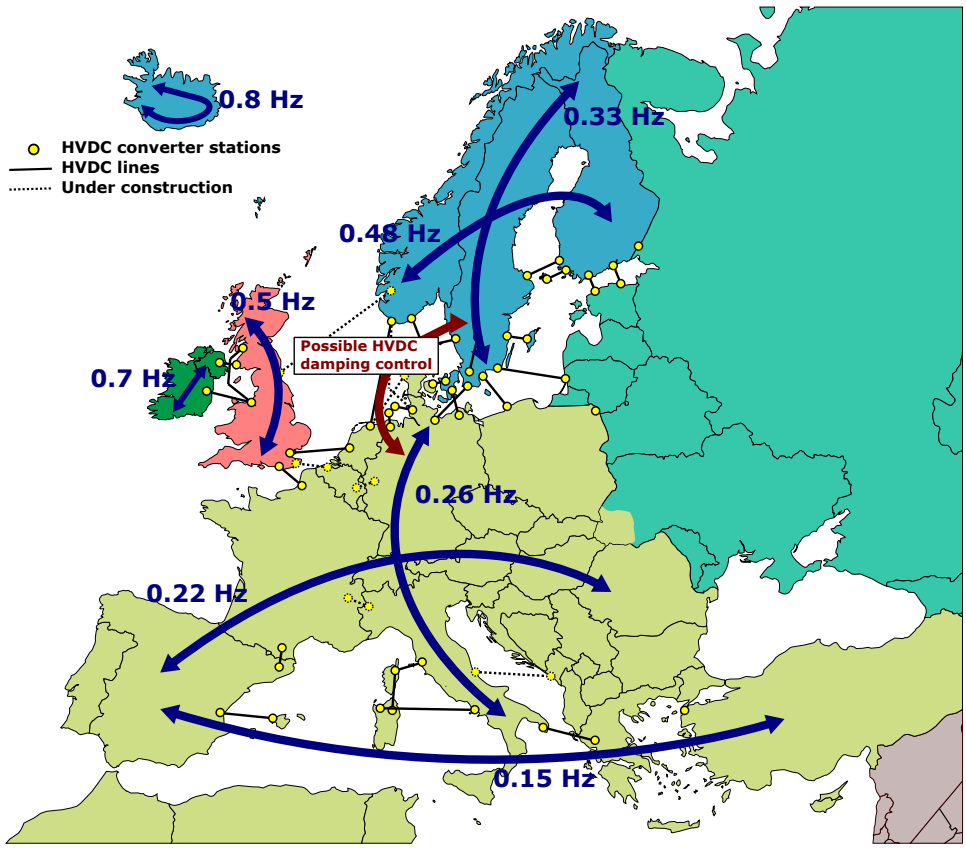

Figure 1.5: Interarea modes in Europe. Credit Florian Dörfler.

1.2 HVDC Power Oscillation Damping

HVDC is used to strengthen transmission corridors in power systems. Since the HVDC installations often bridge long distances, they have a strong influence on dominant power system modes. Through active power injection, damping of interarea modes, or so called power oscillation damping (POD), can be improved by reducing local rotor speed deviations between the HVDC terminals. In the following, results from the operating experience of the PDCI damping control [16] are presented as practical examples of how HVDC modulation can improve POD. Following this, simulations on a simplified model are done to further illustrate the concept. The setup is conceptually the same as the practical example where the PDCI is embedded in the western North American power system in parallel with the ac transmission (Figure 1.6). The examples shows that dc active power modulation is effective at improving POD in a parallel setting. When using HVDC active power modulation

between asynchronous systems however, damping control may excite poorly damped modes in the assisting system.

Control of active power injections to provide damping of interarea modes is an important research topic today [10–14, 20–23] due to the increasing amount of power electronics, battery storages, and renewable production. However, most research does not consider the interaction that may occur with the power source, which in this case would be the other ac grid. In the last example it is shown how the interaction between interarea modes of two HVDC interconnected ac systems may limit POD performance.

Example 1.1 (Modulation of the PDCI) The western North American power system spans the continent from the western Pacific coast to the foot of the Rocky Mountains in the east, from Canada in the north and partly into Mexico in the south as seen in Figure 1.6. The system has a history of poorly damped interarea modes (Figure 1.4) limiting the amount of surplus hydro power that could be transmitted to the southwest. To increase the transfer capacity, the Bonneville Power Administrator began studies which led to the development of a control system to modulate the PDCI running parallel to the ac transmission system in north–south direction as seen in Figure 1.6. In Figures 1.7a and 1.7b large disturbances effect on the parallel Pacific AC Intertie is shown. In Figure 1.7a a 600 MW generating unit is relayed off line. Without the dc modulation in service, the disturbance results in a poorly damped interarea mode visible as oscillating ac power flow. In Figure 1.7b the response to a 1100 MW load rejection is shown. With dc modulation activated the improved POD is clearly visible. The POD improvement, allowed for an ac line rating increase from 2100 MW to 2500 MW [15, 16].

Although showing promising results, the PDCI control never became production grade. One of the major reasons for this was that the local ac power flow measurement used for feedback, showed a non-minimum phase (NMP) zero that caused the modulation to introduce a 0.7 Hz oscillation under certain operating conditions [17]. With the installation of wide-area measurement systems (WAMS), the project has seen new developments. Preliminary studies in [17] found local frequency measurement at the northern dc terminal (bus 24 in Figure 1.6) to be a suitable signal for POD, showing good observability and robust performance over a range of operating conditions. However, it was observed that damping based on local frequency measurements may deteriorate transient performance and cause first swing instability for some scenarios, as shown in Figure 1.8a. A centralized controller, communicating frequency measurements from the southern dc terminal (bus 49 in Figure 1.6), was found to be a more robust alternative, as seen in Figure 1.8b. The recent implementation of a proof-of-concept WAMS controller found that a 4–5 % damping improvement of the north–south interarea mode could be achieved, without degradation of other modes [24].

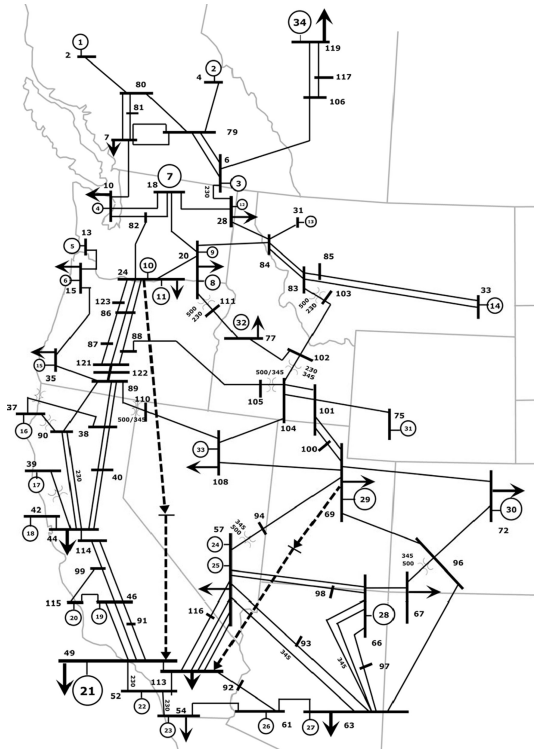

Figure 1.6: One-line diagram of the western North America power system [17]. © 2013 IEEE

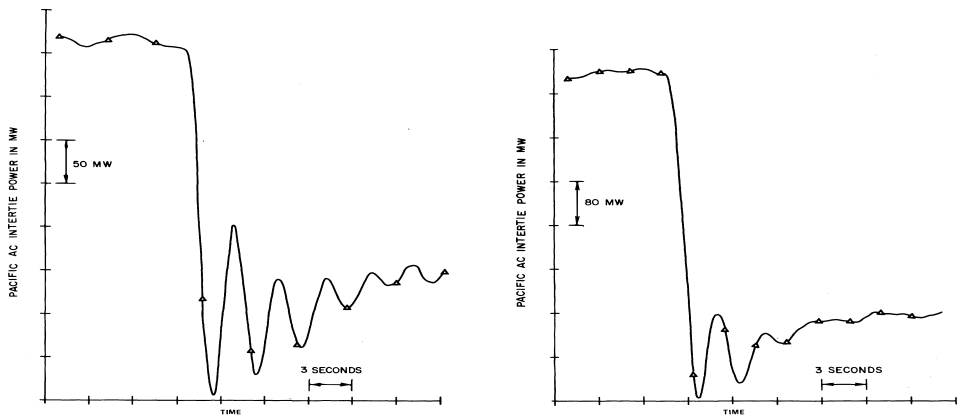

(a) System response to relaying 600 MW generating unit without dc modulation.

(b) System response to a 1100 MW load rejection test with dc modulation.

Figure 1.7: Power oscillations in the Pacific AC Intertie following a system disturbance. Initial ac intertie loading is approximately 2500 MW in both scenarios [16]. © 1978 IEEE

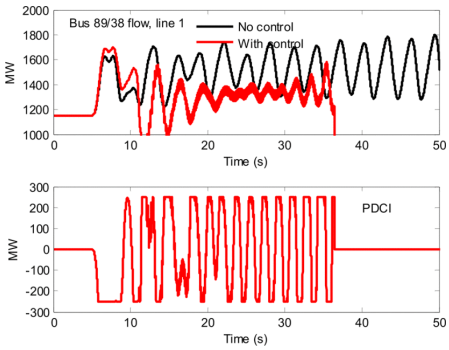

(a) System response using feedback from local frequency measurement at bus 24.

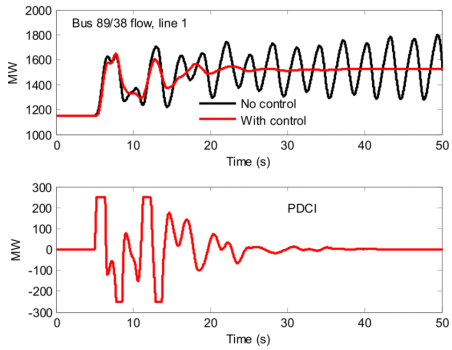

(b) System response using relative frequency measurement between buses 24 and 49.

Figure 1.8: Simulation of power flow following the disconnection of generator 26 using PDCI control, with proportional feedback gain 1000/0.1 Hz, and $P_{\max} = 250$ MW [17]. © 2013 IEEE

Example 1.2 (Four-Machine Two-Area Test System) This example simulates HVDC damping control in a parallel configuration similar to the previous example. An HVDC interconnection is installed in a four-machine two-area power system as shown in Figure 1.9. The test system was developed in [25] for the study of electromechanical modes. The implemented model, fitted with some modifications, is available in the Simulink library [26]. All four generators are equipped with a steam turbine governor and automatic voltage regulator (AVR). To illustrate damping improvement, power system stabilizers (PSS) have been deactivated making the interarea oscillation between Area 1 and 2 unstable. The HVDC link is a 400 MVA, 200 kV point-to-point voltage source converter (VSC) HVDC. The VSC-HVDC is represented using an averaged model and a Π-circuit transmission line with typical converter and line data according to [27].

The system is initiated with a 400 MW ac and 300 MW dc power flow from Area 1 to Area 2 as seen in Figure 1.9. The interarea oscillation is triggered by tripping one of the ac transmission lines interconnecting the two areas. Without HVDC damping control the system is unstable and the two areas eventually separate as shown in Figure 1.10.

To stabilize the system we use feedback control of the VSC-HVDC link. Controllability analysis shows, as seen in previous studies [11, 28, 29], that active power-modulation is effective at improving POD in the proposed system. For illustrative purposes we here assume an ideal scenario were rotor speed measurements from all four machines are available to represent the interarea mode. Since the two machines in each area are of equal size [25], the interarea mode can be represented

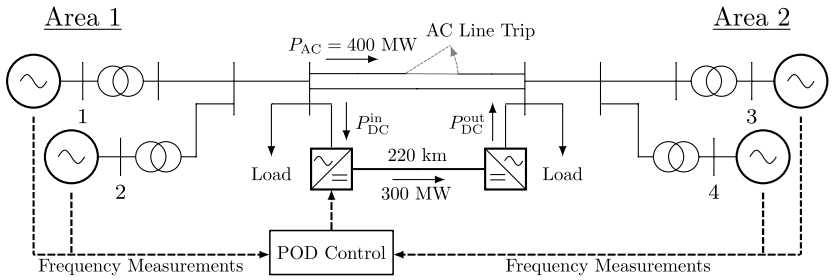

Figure 1.9: A simple four-machine two-area test system with a VSC-HVDC link in parallel with the ac interconnection.

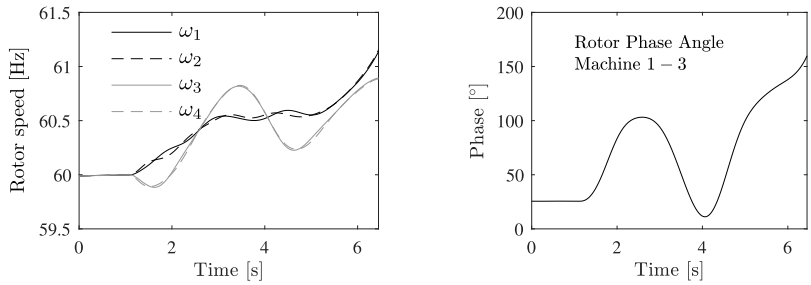

Figure 1.10: Rotor speeds and phase angle difference between machine 1 and 3 of the four-machine two-area test system following ac transmission line trip as seen in Figure 1.9. Without HVDC POD control the system is unstable.

by

$$\Delta\omega = \frac{\omega_1 + \omega_2}{2} - \frac{\omega_3 + \omega_4}{2}.$$

HVDC active power is modulated using proportional control

$$P_{\mathrm{DC}}^{\mathrm{in}} = K_{\mathrm{DC}}\Delta\omega. \tag{1.1}$$

With feedback gain $K_{\mathrm{DC}} = 200\,\mathrm{MW/Hz}$ we see in Figure 1.11 that POD is improved. By increasing the feedback gain K_{DC} to $600\,\mathrm{MW/Hz}$ we see (in Figure 1.12) that damping of the interarea mode is improved at the cost of higher active power usage.

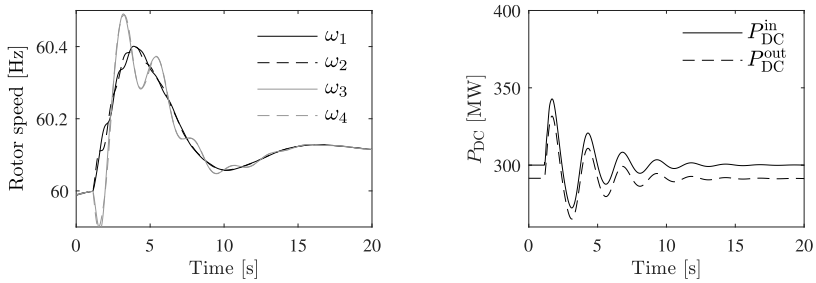

Figure 1.11: Rotor speeds and dc active power of the four-machine two-area test system following ac transmission line trip as seen in Figure 1.9. DC active power is controlled using (1.1) with a proportional gain, $K_{\mathrm{DC}} = 200\,\mathrm{MW/Hz}$.

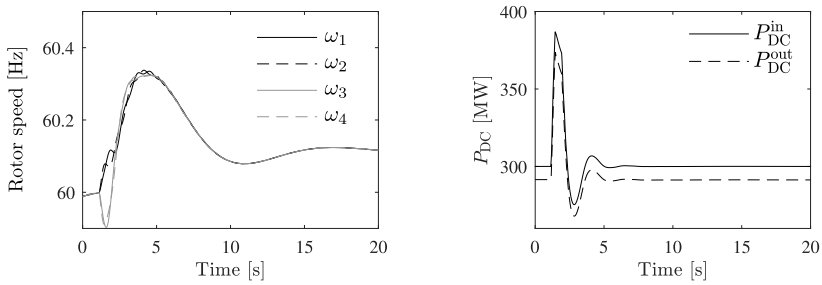

Figure 1.12: Rotor speeds and dc active power of the four-machine two-area test system following ac transmission line trip as seen in Figure 1.9. DC active power is controlled using (1.1) with a proportional gain, $K_{\mathrm{DC}} = 600\,\mathrm{MW/Hz}$. Compared to Figure 1.11 we see that a faster disturbance attenuation is achieved at the cost of a higher dc active power.

Example 1.3 (HVDC-Interconnected Asynchronous AC Networks) The system in Example 1.2 is modified. Two two-area test systems are interconnected using a VSC-HVDC as seen in Figure 1.13. The two systems are structurally identical, and as in Example 1.2, they are inherently unstable. An interarea oscillation is triggered by a load disturbance in the top ac network. The disturbance is attenuated with the help of the bottom network, through HVDC POD control. The system will be uncontrollable if the eigenvalues corresponding to the considered interarea modes coincide [30]. To avoid this, the machine inertia of the bottom network have been scaled to increase the frequency of the interarea mode by 20 %, compared to the top network. In Figure 1.14a it is seen that both ac networks are stabilized by the HVDC active power modulation. With increasing feedback gain however, the controllability of the interarea modes are reduced until the controller can no longer stabilize the system as seen in Figure 1.14b. As shown in Chapter 4, the proximity of the interarea modes put an upper bound on the achievable damping.

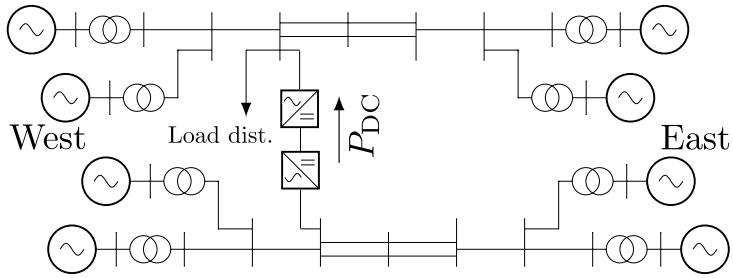

Figure 1.13: Two four-machine test systems interconnected with a VSC-HVDC link.

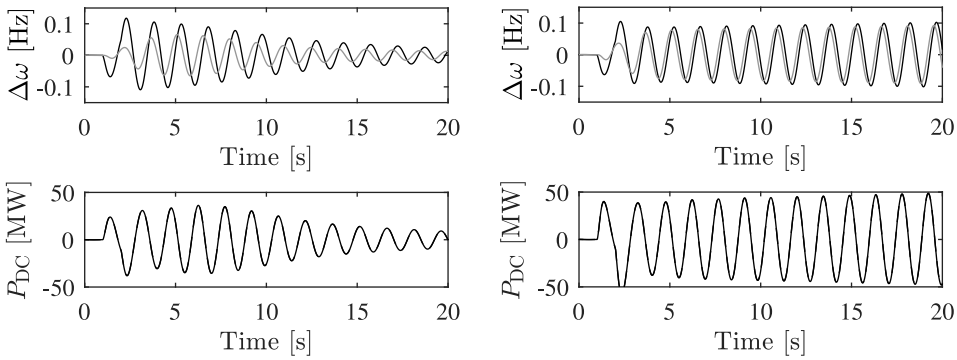

(a) 400 MW/Hz (b) 800 MW/Hz

Figure 1.14: Frequency difference between western and eastern areas in the two HVDC-interconnected ac networks following a 200 MW load disturbance at time 1–2 s. With a higher feedback gain in (b) we see that the control fails to stabilize the system.

1.3 Frequency Stability in Low-Inertia Power Systems

Power systems exhibiting low rotational inertia present faster frequency dynamics, making frequency control and system operation more challenging. Small-scale power systems, which have historically supplied small geographical regions or cities, have therefore been interconnected into large synchronous ac grids. With long distance transmission, modern power systems interconnect, not only cities and regions, but also countries and continents. This has made it easier to maintain the frequency quality since more synchronous machines are able to contribute to the rotational inertia of the grid. Asynchronous HVDC interconnections however, offer no direct physical improvement to the frequency stability. The reason is that HVDC active power flow does not depend directly on bus voltage phase angles, but on the converter control. This adds flexibility, since HVDC links can often react faster

than conventional transmission, but it also brings an increased complexity. Similarly, converter-interfaced generation such as wind or solar does not contribute either, to the inertia of the grid. As renewable production begins to replace conventional production, frequency stability is a growing challenge for the modern grid [31, 32]. Increasingly unpredictable generation patterns are also putting more stress on today's already strained transmission infrastructure [33]. A number of relatively recent blackouts are related to large frequency disturbances. The incidence of this phenomena is expected to increase in the future as the energy transition continues; in fact they have doubled from the early 2000s [34]. Examples from the literature attributes the root causes of recent blackouts to overloading of transmission lines following an unsuccessful clearing of a short circuit fault [35], damage on transmission lines due to extreme weather [36], and power plant tripping due to malfunctioning of protections [37]. In all of them, the lack of frequency response from converter-interfaced renewable production made the system operators incapable of avoiding blackouts. With growing shares of renewables, system operators are therefore increasingly demanding renewable generation to participate in frequency containment reserves (FCR) [38].

1.3.1 Frequency Containment in the Nordic Synchronous Grid

The Nordic synchronous grid includes the transmission grids of Sweden, Norway, Finland, and eastern Denmark. The grid has a high amount of hydro production with reservoirs that provide a relatively cheap flexibility both on a day-ahead and hourly operation. This has enabled the Nordic grid to maintain a good frequency quality, despite its relatively small size. However, as renewable generation begins to replace conventional generation the amount of kinetic energy in the system is decreasing. This has an impact on the ability of the system to handle frequency changes following load and production imbalances.

The Nordic system currently applies two types of FCR. FCR for normal operation (FCR-N) keeps the frequency within the normal 50.0 ± 0.1 Hz frequency range. FCR for disturbance situations (FCR-D) is used to mitigate the impact of incidental disturbances. Following larger disturbances the maximum instantaneous frequency deviation (the nadir) should be limited to 49.0 Hz [39]. At steady-state, FCR-D is designed to keep the frequency between 49.9 and 49.5 Hz. FCR in the Nordic grid is almost exclusively provided by hydropower. The same units typically deliver both FCR-N and FCR-D. Although providing a cheap flexible reserve, hydropower has dynamic constraints that limits its use in operating conditions with low kinetic energy. Due to the bandwidth limitations imposed by the NMP dynamics of the waterways, the response speed of hydro units may not be increased, without reducing the closed-loop stability margins [40]. Because of this, the Nordic system operators have developed a new market for fast frequency reserves (FFR), to supplement FCR-D [41]. The following example is taken from Chapters 7 and 8 of this thesis. The example show how FFR from converter-interfaced wind power can be used as a complement to hydro-FCR, fulfilling the system operators FCR-D requirements.

Example 1.4 (Coordinating Hydro and Wind) Consider a severe load disturbance in a 5-machine model of the Nordic synchronous grid,[1] shown in Figure 1.15. We consider a low-inertia scenario where the total kinetic energy is only 110 GWs. Assume the dimensioning fault to be the instant disconnection of the NordLink HVDC cable [42] importing 1400 MW from Germany into Norway as shown in Figure 8.2. Following the incident, FCR-D manages to restore the center of inertia (COI) frequency ω_{COI} to 49.5 Hz, as seen in Figure 1.16a. We consider two scenarios: one where FCR is provided by ideal controllable power sources (black curves), and a second more realistic scenario (red curves) where FCR is provided by hydro units at buses 1, 2, and 3. As seen in Figure 1.16b, the hydro-FCR shows the characteristic NMP initial drop, as governors react to the falling frequency. This reduces the transient FCR response. Thus, hydro-FCR fails to keep the nadir above 49.0 Hz.

The requirements can be fulfilled by supplementing hydro-FCR with other power sources, that are able to deliver power with faster response time. One such energy source is wind power. Since wind turbines (WTs) are connected to the grid through back-to-back converters, they can increase their power output to the grid almost instantly (assuming that the converter is operated within allowed current limits). Combining hydro-FCR with FFR from wind in Figure 1.17a, we see that the dynamic FCR-D requirements are now fulfilled.

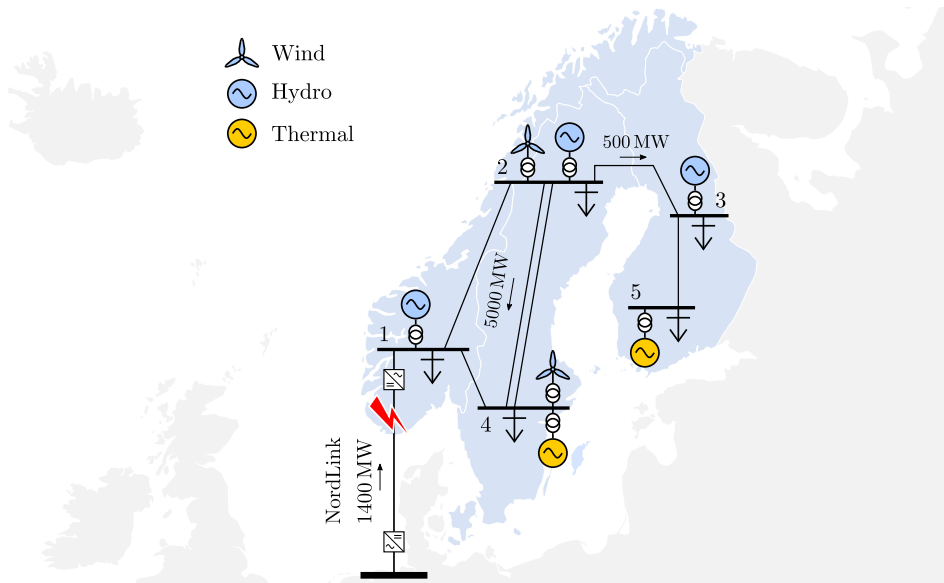

Figure 1.15: One-line diagram of the Nordic 5-machine (N5) test system.

[1]The N5 test system is described in Chapters 7 and 8. The full model, and test cases, are available at the GitHub repository `https://github.com/joakimbjork/Nordic5`.

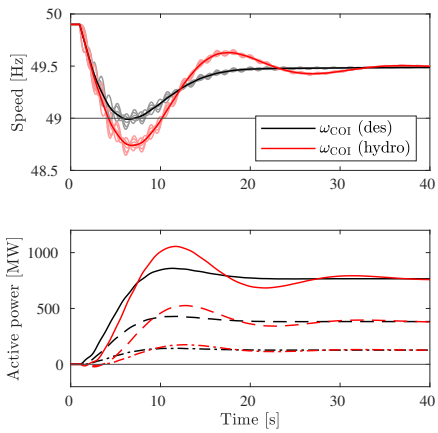

(a) FCR response.

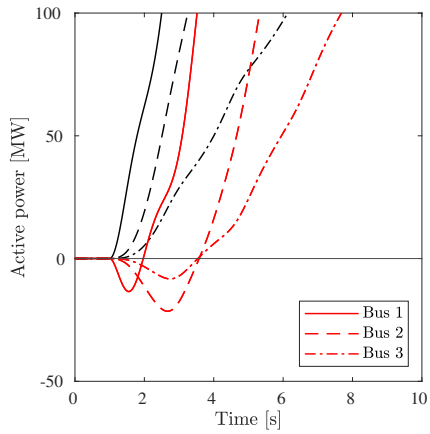

(b) Zoom in on initial FCR response.

Figure 1.16: Response to a 1400 MW fault. The black curves shows the power injections and corresponding frequency response where FCR is provided by ideal controllable power sources. The red curves show the system response with FCR from hydropower.

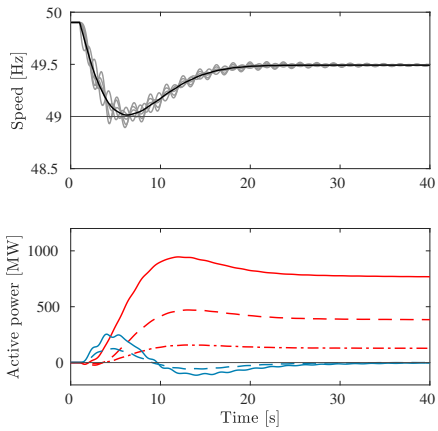

(a) FCR and FFR response.

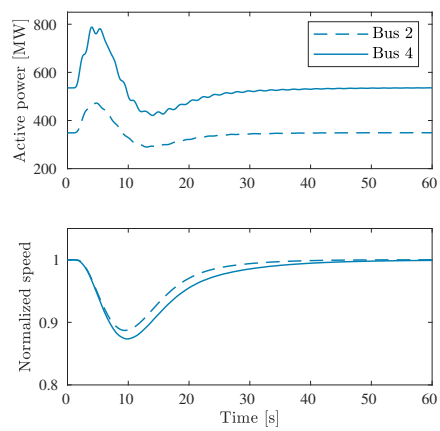

(b) WT power output and speed.

Figure 1.17: Response to a 1400 MW fault with coordinated FCR and FFR.

In this scenario, we assume that FFR is supplied by uncurtailed wind power, providing steady power at the maximum power point (MPP). Since the WTs cannot increase their steady-output, the extra power excursion can only be obtained by borrowing kinetic energy from the rotating turbines. When returning to the MPP, the WTs will have to draw extra power from the grid, as seen in Figure 1.17. This behavior is characterized by slow NMP zeros in the WT's corresponding transfer function. In Chapters 7 and 8, we study the control design and models needed to deliver the coordinated FCR and FFR response shown in Figure 1.17.

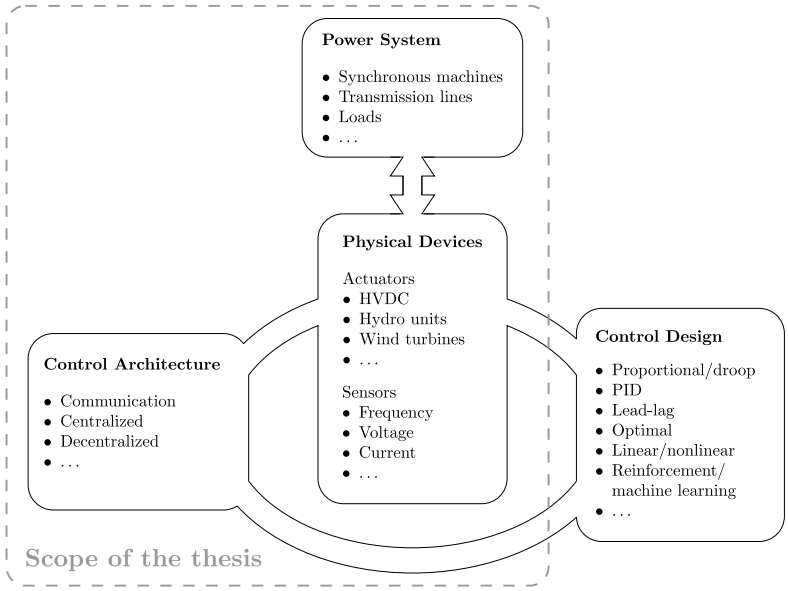

Figure 1.18: The thesis focuses on fundamental control performance limitations imposed by the power system, control architecture, and actuators and sensors.

1.4 Problem Formulation

In this thesis we consider fundamental control performance limitations for improving the damping of interarea modes and frequency stability. Of particular interest is the use of converter-based generation and transmission. Power electronics components offer controllability of active power injections, unparalleled by conventional technologies that are often limited by the dynamic constraints of mechanical valves, servo systems, etc. [41]. Active power modulation, however, leads to interactions with other dynamical subsystems of the power system. In this thesis, we study the limitations arising from these interactions. As illustrated in Figure 1.18, the limitations relate to the dynamics of the system to be controlled; the available actuators and sensors; and the control architecture. The control design itself does not impose particular limitations, but is more of a mean to compute a specific control law. The thesis does not focus on developing new such methods, but the results are mainly independent of the control design.

1.4.1 Models for Interarea Oscillations

Interarea modes are a complex dynamic phenomenon involving groups of machines in one end of the system swinging against machines in other parts of the system. Swinging of the machine results in ac power oscillating in the interconnecting tie-

lines. Interarea oscillations are therefore also known as power oscillations. Frequency stability is concerned with the average network mode. It refers to the ability of a power system to maintain steady COI frequency following a severe disturbance in load and generation [8].

To simplify the analysis, a model abstraction is performed. We let the COI mode and the dominant interarea mode be represented by a two-machine network model. Consider the Nordic 32-bus Cigré test system [43] shown in Figure 1.19a. The mode of interest is chosen as the poorly damped interarea mode between the north and south area. The dynamics of this mode are represented using a two-machine model where each machine represents a lumped sum of the machines in each respective area. In Figure 1.19b a similar simplification is shown on the four-machine two-area test system. Aggregating multiple machines in one area into a single machine is a common simplifying approach used in analysis [44]. The benefit of the simplified representation is that the interarea mode is easier to analyze. However, interesting dynamics might be lost in the simplification. For instance the two-machine model contains no information about the local modes occurring between the machines within the two areas in Figure 1.19b.

The dynamics of a power system can be described by a set of differential algebraic equations

$$\begin{aligned} \dot{x} &= f(x, \gamma, u) \\ 0 &= g(x, \gamma, u) \end{aligned}$$

where vectors x and γ contain system state and algebraic variables, respectively. The vector u contains control inputs. For the purpose of analyzing the stability of electromechanical modes, a linearized small-signal model suffices. The small-signal model considers small deviations $[\Delta x, \Delta\gamma, \Delta u]$ around an operating point $[x, \gamma, u] = [x^*, \gamma^*, u^*]$. Deviations are assumed sufficiently small so that (if $\frac{\partial g}{\partial \gamma}$ is invertible) the linearized model

$$\Delta\dot{x} = \left(\frac{\partial f}{\partial x} - \frac{\partial f}{\partial \gamma}\left(\frac{\partial g}{\partial \gamma}\right)^{-1}\frac{\partial g}{\partial x}\right)\Delta x + \left(\frac{\partial f}{\partial u} - \frac{\partial f}{\partial \gamma}\left(\frac{\partial g}{\partial \gamma}\right)^{-1}\frac{\partial g}{\partial u}\right)\Delta u \qquad (1.2)$$

accurately describes system dynamics [25]. Since the linear model always consider deviations from a linearization point, we drop the "Δ" notation. The linearized model (1.2) gives a linear time-invariant state-space representation

$$\begin{aligned} \dot{x} &= Ax + Bu \\ y &= Cx + Du \end{aligned}$$

where A and B are system state and input matrices given by the partial derivatives in (1.2), and y is some output with output matrix C and direct feed-through matrix D.

1.4.2 Interarea Oscillation Damping

The overarching question addressed in Part I of this thesis is: what are the fundamental control limitations for improving the stability of interarea modes using

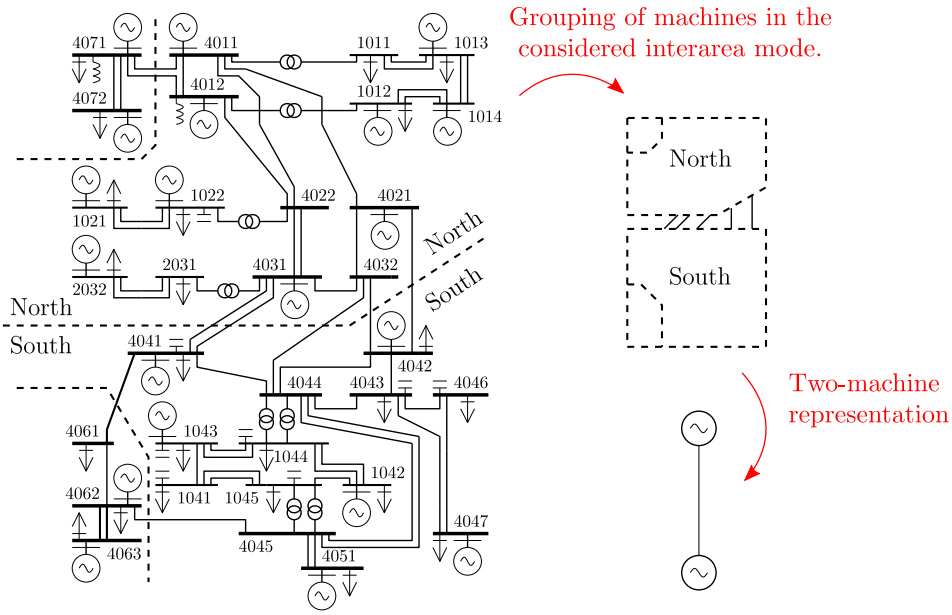

(a) Nordic 32-bus test system.

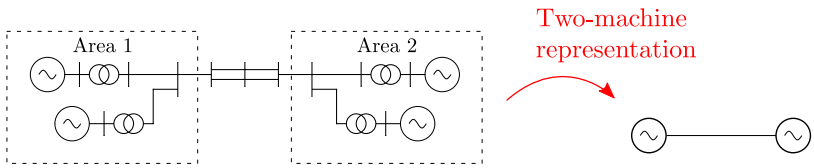

(b) Four-machine two-area system.

Figure 1.19: Model abstraction of dominating interarea mode in two power system models. The simplified two-machine representation lose information about tie-line flows and local modes within the two areas and between other machine groupings.

HVDC active power modulation?

A common method to assess the suitability of POD control is using the notation of controllability and observability, e.g., using the residue method [25, 45, 46]. Although proven to be useful in practice, there is no straight-forward way to relate the notion of observability and controllability to the fundamental limitations of the closed-loop performance. In this thesis we instead address limitations associated with zero dynamics and the dynamics of the controlled power source.

The first question we ask is how and when high-speed excitation control from AVR affects the potential of ancillary POD control. In particular we are interested in input-output signal combinations when the AVR influence gives rise to NMP zeros, since NMP zeros affect the achievable performance and robustness of the

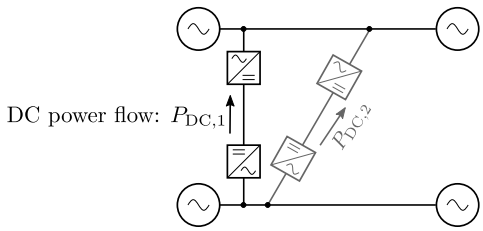

Figure 1.20: Two asynchronous power systems interconnected by two HVDC links.

closed-loop system. This question is answered in Chapter 3.

Another question we ask is what the fundamental control limitations are when modulating the active power of HVDC transmission interconnecting asynchronous power systems. Controlled active power injections can be used to improve POD. The electrical position of the HVDC terminals affects the controllability and therefore the efficiency of POD control from the considered network bus. In the simplified model representation shown in Figure 1.20, line impedance, and thus electrical position, is visualized as length of the transmission line. However, when modulating the HVDC link between two networks, active power is injected from one network to the other causing the interarea modes of the two networks to interact. This may impose further control limitations. The objective is to describe the underlying system properties that limit achievable performance in terms of POD. Using HVDC links interconnecting two asynchronous power systems as shown in Figure 1.20, with a feedback controller

$$u = Ky,$$

the goal is to stabilize the interarea modes by increasing the POD in both the HVDC-interconnected ac networks. The controller K can be either static or dynamic. The question answered in Chapter 4 is how the modal interactions between two ac networks affect the achievable damping performance when controlling a single interconnecting HVDC link. In Chapter 5 we consider the control of two or more HVDC links. Here, we identify HVDC configurations that may improve the achievable POD performance. How can we design controllers to avoid modal interaction between the interconnected ac networks and when can this be done without making the system sensitive to actuator, sensor, or communication failure?

The final question we ask is how the measurements available for POD affect the transient stability following large load disturbances. Is it possible to design a POD controller, using local frequency measurements, that improves small-signal stability while avoiding a negative impact on large-signal stability? This question is answered in Chapter 6.

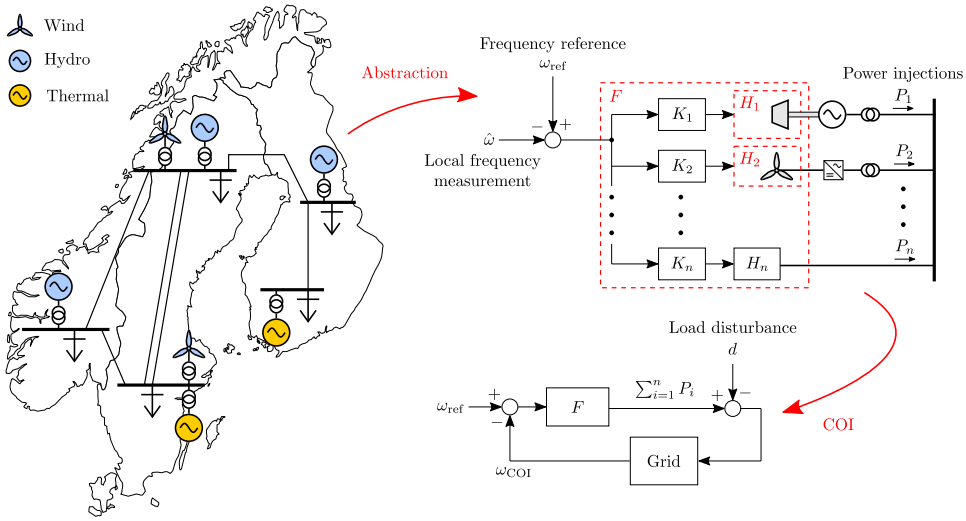

Figure 1.21: COI model abstraction of the N5 test system. The simplified representation lose information about tie-line flows and interarea modes.

1.4.3 Frequency Stability

The overarching question in Part II is how to coordinate frequency reserves in large-scale power systems. Frequency reserves are provided by a heterogeneous collection of devices with different capacities and dynamic constraints. To facilitate the analysis we abstract the power system model to a single-machine equivalent as illustrated in Figure 1.21. The reduced model describes the COI frequency (ω_{COI}) dynamics and assumes that higher-order dynamics (such as interarea modes) are stable. We do not address limitations associated with local measurements, instead the focus is on limitations associated with the dynamics of the controlled power sources H_i, $i \in \{1, \dots, n\}$. Controllers K_i are to be designed so that the heterogeneous ensemble collectively fulfills the system operator's FCR requirement.

To facilitate the control design, models of the actuators H_i are needed. When it comes to conventional thermal or hydro plants, these models are readily available from the literature [25]. When it comes to batteries, curtailed wind power plants, or HVDC links (operated below the converters maximum current capacity), the dynamics are typically neglected since the converter dynamics are too fast to be relevant for FCR. For WTs, curtailed operation means that the turbines are operated at a sub-optimal steady-power output, in order to participate in FCR. In Chapter 8, we develop a controller that allows WTs to participate in FCR, without the need for curtailment. The goal is robustness, and for the WT to behave in a predictable manner for various wind speed conditions.

In Chapter 7 we show how to coordinate controllers K_i so that the global FCR requirement is fulfilled. We answer the question to when the design target can be

fulfilled, while accounting for the dynamic constraints of all participating devices. In Chapter 8 we answer how to model a variable-speed WT so that its FCR response can be coordinated with other units, while ensuring stable operation of the turbine.

The COI frequency abstraction (Figure 1.21) does not allow us to directly address the stability of interarea modes. The question answered in Chapter 9 is how stability can be guaranteed using only locally available information and without modeling the network, while allowing for a heterogeneous ensemble $H_i \neq H_j$, $i \neq j$, where actuators may have time delays and NMP dynamics.

1.5 Outline and Contributions

The outline of the remainder of this thesis and its main contributions are summarized below.

Chapter 2: Background

In this chapter we give a short overview of power system stability and control. A brief introduction to HVDC technology and a literature study of HVDC control for power oscillation damping are given.

Part I: Interarea Oscillation Damping

Chapter 3: Zero Dynamics Coupled to High-Speed Excitation Control

In Chapter 3, we present a second-order network model, modeling voltage phase angles and amplitudes in a connected network. The model is used to study fundamental control limitations for improving rotor angle stability. Chapter 3 differs from the remainder of the thesis in that we include voltage dynamics in the analysis. This is done in order to explicitly study the consequences that interactions between voltage and phase angle dynamics have on achievable control performance. In a single-machine infinite bus (SMIB) model, it is shown that the presence of NMP zeros are closely linked to the destabilizing effect of AVRs. It is found that NMP zeros may persist in the system even if the closed-loop system is stabilized through feedback control. A simulations study show that NMP zeros introduced by AVR limit the achievable performance and stabilization using feedback control.

Chapter 3 is based on

- J. Björk and K. H. Johansson, "Control limitations due to zero dynamics in a single-machine infinite bus network," in *IFAC World Congress*, Berlin, Germany, Jul. 2020

Chapter 4: Single-Line HVDC Control Limitations

Here, we study the fundamental performance limitations in utilizing HVDC for POD when interconnecting two asynchronous power systems with a single HVDC line. Using a simplified model, an analytical study is performed. The goal is to investigate the limitations for POD using active power modulation of a single HVDC link with no energy storage. It is shown how the proximity of interarea modes puts a fundamental limit on the achievable performance. The findings are evaluated on a two HVDC-interconnected two-machine network as well as on an interconnection of two Nordic 32-bus Cigré test systems [43].

Chapter 4 is based on

- J. Björk, K. H. Johansson, and L. Harnefors, "Fundamental performance limitations in utilizing HVDC to damp interarea modes," *IEEE Transactions on Power Systems*, vol. 34, no. 2, pp. 1095–1104, Mar. 2019

Chapter 5: Coordinated HVDC Control

In this chapter, we build on the problem formulation of Chapter 4 by adding additional HVDC links. By coordinated control of multiple HVDC links, the limitations studied in Chapter 4 can be circumvented. In addition it is shown that decoupled control of the concerned modes is achievable using a proportional controller. The best coordinated control design is investigated by looking on input usage and stability following dc link failure.

Chapter 5 is based on

- J. Björk, K. H. Johansson, L. Harnefors, and R. Eriksson, "Analysis of coordinated HVDC control for power oscillation damping," in *IEEE eGrid*, Charleston, SC, Nov. 2018

Chapter 6: Transient Stability when Measuring Local Frequency

Chapter 6 considers fundamental sensor feedback limitations for improving rotor angle stability using local frequency or phase angle measurements. Using a simplified two-machine model, it is shown that improved damping of interarea oscillations must come at the cost of reduced transient stability margins, following larger load or generation disturbances. This holds regardless of the control design method. The results are validated on a modified Kundur four-machine two-area test system [25] where the active power is modulated on an embedded HVDC link.

Chapter 6 is based on

- J. Björk, D. Obradović, K. H. Johansson, and L. Harnefors, "Influence of sensor feedback limitations on power oscillation damping and transient stability," *IEEE Transactions on Power Systems*, under review

Part II: Frequency Stability

Chapter 7: Coordination of Dynamic Frequency Reserves

Chapter 7 considers the coordination of conventional (slow) FCR with faster FFR. The design results in a dynamic virtual power plant (DVPP) whose aggregated output fulfills the system operator requirements at all time scales, while accounting for the capacity and bandwidth limitation of participating devices. The results are validated in a 5-machine representation of the Nordic synchronous grid. By coordinating wind and hydro resources, it is shown that the system requirements can be fulfilled in a realistic low-inertia scenario, even with moderate wind resources, without the need for curtailment or battery installations.

Chapter 7 is based on

- J. Björk, K. H. Johansson, and F. Dörfler, "Dynamic virtual power plant design for fast frequency reserves: Coordinating hydro and wind," *IEEE Transactions on Power Systems*, under review

Chapter 8: Uncurtailed Wind Power for Fast Frequency Reserves

In this chapter, we design a wind power model useful for FFR. It is shown that the dynamical shortcomings of a WT, in providing steady power or slow FCR support, is suitably described by a linear first-order transfer function with a slow NMP zero. The model is tested in a 5-machine representation of the Nordic synchronous grid using the DVPP control developed in Chapter 7.

Chapter 8 is based on

- J. Björk, D. V. Pombo, and K. H. Johansson, "Variable-speed wind turbine control designed for coordinated fast frequency reserves," *IEEE Transactions on Power Systems*, under review

Chapter 9: A Scalable Nyquist Stability Criterion

Here, we consider stability of electromechanical power system dynamics, separated into two categories: stability of the average frequency mode, and small-signal rotor angle stability. Using the generalized Nyquist criterion, a condition that gives a priori stability guarantees for the connection of new devices are presented. The method allows for various degree of conservatism depending on the available information. In particular, a criterion that guarantees stability using only local information is derived. The method can be applied to a network with heterogeneous devices.

Part III: Conclusions

Chapter 10: Conclusions and Future Work

Finally, in this chapter we conclude the thesis, summarizing and discussing the result. We also outline some future and ongoing work, indicating some possible directions in which this work can be extended.

Other Publications

A number of the results presented in this thesis have previously appeared in

- J. Björk, "Performance quantification of interarea oscillation damping using HVDC," Licentiate Thesis, KTH Royal Institute of Technology, Stockholm, Sweden, 2019

The Author's Contributions

In the publications listed above, the author of this thesis had the most significant role in developing the results, and has completed all or the majority of the writing. Remaining authors have contributed to problem formulations and taken advisory or supervisory roles.

Chapter 2

Background

A power system can be divided into three parts: generation, transmission, and distribution as shown in Figure 2.1. Its objective is to generate electricity from naturally available forms and to transmit it to customers connected to the distribution grid. The advantage of electrical energy is that it can be transported and controlled with high efficiency and reliability. However, unlike other types of energy, electricity cannot be conveniently stored. A major challenge of the power system is therefore to meet the continuously changing load demands. Today this is becoming increasingly challenging as conventional synchronous generation such as coal, gas, and nuclear, is being replaced by inverter based generation from intermittent sources such as wind and solar.

Energy should be supplied at minimum cost and optimal efficiency. Losses in the transmission system are minimized by controlling tie-line flows. This can be done by allocating generation, connecting and disconnecting transmission lines, controlling HVDC power transmission etc. Tie-line flows can also be controlled by adjusting

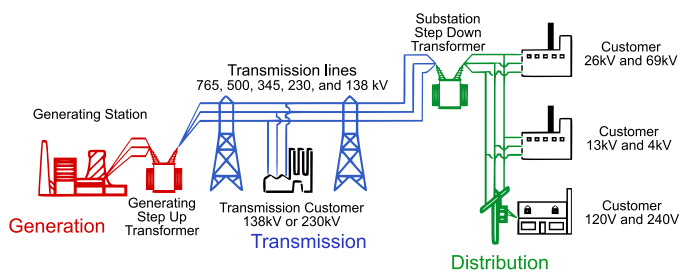

Figure 2.1: A typical power system. Image courtesy of United States Department of Energy[1].

[1]United States Department of Energy (DOE), version by User: J J Messerly [CC BY 3.0 (`https://creativecommons.org/licenses/by/3.0`) or Public domain], via Wikimedia Commons. Changes made to label positions and the text of customer labels.

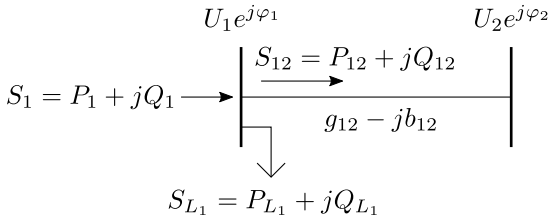

Figure 2.2: A two-bus power system

system voltages using tap-changing transformers, generator excitation, or power electronic devices controlling reactive power such as HVDC and FACTS.

Controls should also contribute to maintaining an adequate power quality with respect to: constancy of frequency, constancy of voltage, and level of reliability. The aforementioned control methods all have a big impact on the dynamic performance of the power system [25]. The focus of this thesis is on reliability in terms of dynamic stability of the power system.

The remainder of this chapter is organized as follows. Section 2.1 gives a brief introduction to power system dynamic modeling. In Sections 2.2 and 2.3 an introduction to classifications of power system stability and interarea oscillations is given. In Section 2.4, we briefly discuss how converter-based power sources: HVDC connections between asynchronous grids, and wind power, can be used to provide frequency support. In Section 2.5 an introduction to HVDC technologies is given. In Section 2.6 the function, control and modeling of HVDC are briefly explained. Finally, Section 2.7 presents a literature survey of work on HVDC damping control methods.

2.1 Power System Modeling

Power systems can be modeled on various levels of detail depending on the purpose of the study. For the analyses in this thesis, we will consider fairly simple models. All the findings are however validated in detailed power system simulations in Simulink Simscape Electrical. Simulations are run in phasor mode, which is a useful method for studying electromechanical oscillations of power systems consisting of large generators and motors [51].

2.1.1 Balanced Three-Phase Power Flow

Consider a simple power system model consisting of two buses interconnected by a transmission line, as shown in Figure 2.2. The balanced three-phase voltage at each bus is given by the phasors $U_1e^{j\varphi_1}$ and $U_2e^{j\varphi_2}$, respectively, and the line admittance[2] is given by $g_{12} - jb_{12}$. The power transmitted from bus 1 to bus 2 is

[2]The impedance of the line is $R_{12} + jX_{12} = (g_{12} - jb_{12})^{-1}$.

given by $S_{12} = P_{12} + jQ_{12}$, where active power

$$P_{12} = g_{12}U_1\big(U_1 - U_2\cos(\varphi_1 - \varphi_2)\big) + b_{12}U_1U_2\sin(\varphi_1 - \varphi_2)$$

and reactive power

$$Q_{12} = b_{12}U_1\big(U_1 - U_2\cos(\varphi_1 - \varphi_2)\big) - g_{12}U_1U_2\sin(\varphi_1 - \varphi_2).$$

The power balance equation gives $S_1 = S_{12} + S_{L_1}$, where $S_{L_1} = P_{L_1} + jQ_{L_1}$ is the load at bus 1, and S_1 is the power injected at bus 1.

2.1.2 Static Load Modeling

In power system stability studies, loads are typically classified into two broad categories: static models and dynamic models. The static load model expresses the characteristics of the aggregated loads connected to a network bus as an algebraic function of the voltage magnitude, U, and frequency, $\omega = \frac{d}{dt}\varphi$.

The voltage dependency can be expressed by the exponential model

$$P_L = P_L^*\left(\frac{U}{U^*}\right)^{m_p}, \quad Q_L = Q_L^*\left(\frac{U}{U^*}\right)^{m_q}$$

where P_L^* and Q_L^* are the active and reactive components when the bus voltage magnitude $U = U^*$. The characteristics of the load are given by the parameters m_p and m_q. With exponents equal to 0, 1, or 2, the model represent constant power, constant current, or constant impedance characteristics, respectively [25].

Frequency dependency is typically represented by multiplying the exponential model by a factor. For instance, a frequency dependent active power load is given by

$$P_L = P_L^*\left(\frac{U}{U^*}\right)^{m_p}\big(1 + D(\omega - \omega^*)\big). \tag{2.1}$$

2.1.3 Synchronous Machines Modeling

The dynamics of the power system are dominated by the dynamics of the synchronous machine. Synchronous machines can be modeled at various levels. In this thesis, we make use of the one-axis machine model (Chapter 3) and classical machine model (Chapters 4 to 9). These are fairly simple representations of machine dynamics, which are useful for analytical purposes. To validate the analytical results obtained with these simple models, more detailed simulations are performed at the end of each chapter.

One-Axis Machine Model

Assume that the two-bus power system in Figure 2.2 represents the connection of a synchronous machine to an algebraic network bus as shown in Figure 2.3. In the

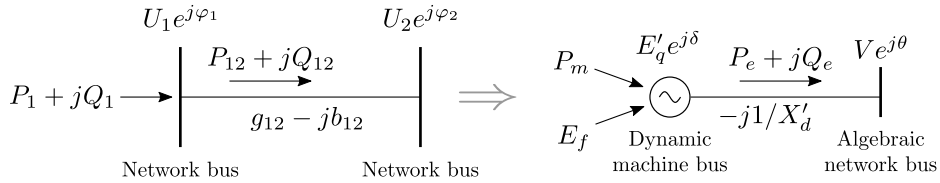

Figure 2.3: Two buses representing a synchronous machine connected to an algebraic network bus, e.g., the machine terminal.

one-axis model (also known as the flux-decay model) the voltage at the machine bus is approximated by the q-axis transient voltage, $E'_q e^{j\delta}$. To emphasize that bus 2 is an algebraic bus, let the voltage at bus 2 be written as $Ve^{j\theta}$. Using the notation from [52], the machine dynamics are given by

$$\begin{aligned} \dot{\delta} &= \omega \\ M\dot{\omega} &= -\frac{1}{X'_d} E'_q V \sin(\delta - \theta) + D\omega + P_m \\ T'_{do}\dot{E}'_q &= -\frac{X_d}{X'_d} E'_q + \frac{X_d - X'_d}{X'_d} V \cos(\delta - \theta) + E_f. \end{aligned} \tag{2.2}$$

Parameters M represent the machine inertia, T'_{do} the d-axis transient open-circuit time constant, and X'_d and X_d the d-axis transient reactance and synchronous reactance respectively (including transformers and line reactances). The small non-negative damping constant D can represent higher-order dynamics from machine damper winding or frequency dependent loads (2.1) close to the machine bus. External inputs are the mechanical power P_m, from the turbine, and the field voltage E_f, controlled by the exciter.

Classical Machine Model

Truncating the voltage dynamics in (2.2) gives us the classical machine model,

$$\begin{aligned} \dot{\delta} &= \omega \\ M\dot{\omega} &= -\frac{1}{X'_d} E'_q V \sin(\delta - \theta) + D\omega + P_m. \end{aligned}$$

The simplicity of this model makes it useful for analysis of multi-machine power systems. However, it is important to remember that voltage dynamics have been neglected before drawing any conclusions from analysis based on this model.

2.2 Power System Stability

The modern power system is mankind's largest and most complex machine. It is the backbone of the modern economy and our daily lives. Many crucial parts of our

society rely on a high quality, constant and dependable supply of electricity. Thus, stability of the power system, like the stability of any dynamic system, is crucial. The stability of a power system can be defined as follows.

"Power system stability is the ability of an electric power system, for a given initial operating condition, to regain a state of operating equilibrium after being subjected to a physical disturbance, with most system variables bounded so that practically the entire system remains intact" [8].

This definition is wider than that of a single stable operating point. However, in this work we will mostly consider stability in the sense of stable operating points. The definition of system security is closely related to stability but may be distinguished from stability in terms of the resulting consequences.

"Security of a power system refers to the degree of risk in its ability to survive imminent disturbances (contingencies) without interruption of customer service. It relates to robustness of the system to imminent disturbances and, hence, depends on the system operating condition as well as the contingent probability of disturbances" [53].

Power system security is usually guaranteed in the sense on $N-1$ stability. The $N-1$ criterion states that the power system must be operated at all times such that after an unplanned loss of an important generator or transmission line it will remain in a secure state.

The ability of ac networks to reliably transfer power is referred to as transfer capacity (or capability). The net transfer capacity may be limited by various factors:

- *Thermal limits* are given by the maximum current a conductor can tolerate before risking overheating. Higher than rated currents may be allowed for some period of time.
- *Voltage limits* are given by the acceptable voltage levels at each point in the system. Voltage drop due to reactive power flows in an inductive power system sets a limit to the amount of power that can be transfered while still maintaining acceptable voltages.
- *Stability limits* are determined by system stability following small and large disturbances of different types. The system must be operated so that it is able to survive disturbances through the transient and following time period ranging from millisecond to minutes. In complex, heavily loaded transmission systems, stability limitations often set the transfer capacity limit.

Dynamic power system stability is usually separated into the three categories shown in Figure 2.4, namely, frequency stability, voltage stability, and rotor angle stability [8]. The following is an introduction to these definitions.

2.2.1 Voltage Stability

Voltage stability refers to the power system's ability to maintain acceptable voltages at all buses following a system disturbance. The driving force for instability is

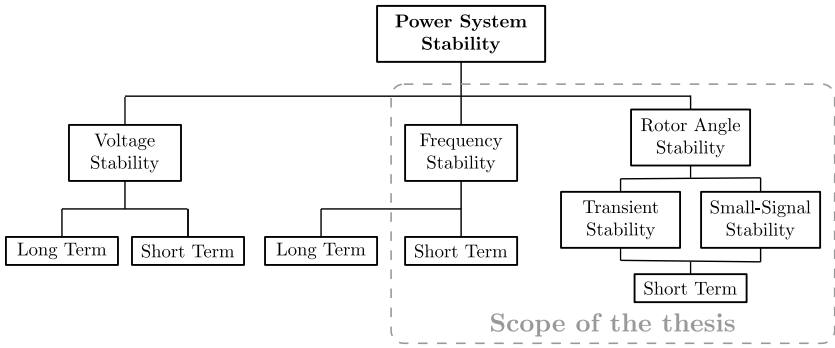

Figure 2.4: Classification of dynamic power system stability.

usually loads attempting to restore their power using control mechanisms such as tap-changers. Failure to meet load demands leads to a progressive drop in voltage. Voltage instability is usually a local phenomena, although its consequences can be wide spread.

On way to improve the voltage stability is through load reduction or reactive power support. Reactive power support from the transmission system is limited by the voltage drop that occurs when active and reactive power flow in the inductive transmission lines. Since voltage stability is a local phenomenon, an efficient solution is to provide local reactive power support. Reactive power injection using flexible ac transmission system (FACTS) devices such as, static var compensators (SVCs) or a static synchronous compensator (STATCOM) has been proven to be efficient at improving voltage stability of power systems [54].

2.2.2 Frequency Stability

System frequency is maintained by balancing mechanical and electrical torques resulting from generation and load. A simple representation of overall frequency dynamics is given by the aggregate swing equation

$$M\dot{\omega}_{\mathrm{COI}} = P_m(\omega_{\mathrm{COI}}) - P_{\mathrm{load}}(\omega_{\mathrm{COI}}) \tag{2.3}$$

where ω_{COI} is the center of inertia (COI) frequency and M is the combined inertia of all the synchronous machines. Following a load disturbance, change in P_{load}, the system frequency will start to deviate from its initial state. Frequency stability is concerned with the ability to maintain and restore the frequency by balancing load demands with that of mechanical input power P_m. In this section, frequency control measures will be discussed in terms of frequency containment reserves (FCR) and frequency restoration reserves (FRR).

FCR, also referred to as primary reserves, have the purpose to stabilize the system frequency following a load disturbance, and to maintain the frequency within

allowed boundaries [55]. As seen in (2.3), an increase in system load will lead to a deceleration of system frequency. To counteract this, generated power needs to be increased to stabilize the frequency.

FRR, also referred to as secondary reserves, act to replace the activated FCR and possibly to restore system frequency to its nominal value. This can be done either by manually control, or by adding a integrating feedback. There are also other slower mechanics with the purpose of restoring FRR and to redistribute production to increase system safety and minimize losses [55].

The concept of FCR and FRR is illustrated in the following example.

Example 2.1 (Frequency Stability) As mentioned in Section 1.3.1, the Nordic system currently applies two types of FCR: FCR for normal operation (FCR-N), for operation in the normal 50 ± 0.1 Hz frequency range; and FCR for disturbance situations (FCR-D), activated when the frequency falls below 49.9 Hz. FCR-D reserves have a faster response time and are designed to limit the maximum instantaneous frequency deviation (the nadir) to 49 Hz, and to stabilize the system at 49.5 Hz . Within 15 min, the FRR should restore the frequency to normal [39].

Consider again the Nordic 5-machine (N5) test system in Example 1.4, where FCR are provided solemnly by hydro units in Norway, northern Sweden and Finland, at buses 1, 2, and 3, respectively. Assume that the system is operated at 49.9 Hz so that FCR-D is activated directly following a down-frequency event. Here, we consider a high-inertia scenario with a total kinetic energy, $W_{\text{kin}} = 240$ GWs. As seen in Figure 2.5, hydro-FCR manage to keep the nadir above 49.0 Hz (compared to the low-inertia scenario shown in Figure 1.16) following a loss of the 1400 MW NordLink HVDC cable.

The FCR-D control input is

$$u_i = K_i(s)(49.9 - \hat{\omega}_i), \tag{2.4}$$

where $\hat{\omega}_i$ is the machine speed at bus $i \in \{1, 2, 3\}$, and $K_i(s)$ is the FCR controller at bus i (designed later in Chapter 7). As an illustrative example, FRR are activated 2 min after the fault, using the control law

$$u_i = K_i(s)\left(1 + \frac{1}{40s}\right)(49.9 - \hat{\omega}_i). \tag{2.5}$$

As shown in Figure 2.5, the PI-controller brings the frequency back to 49.9 Hz.

Initial frequency stability concerns are the rate of change of frequency (RoCoF) and the maximum frequency deviation (the nadir) shown in Figure 2.5. RoCoF is proportional to the occurring load/generation disturbance and inversely proportional to the system inertia. The nadir is proportional to the size of the disturbance and the inverse system inertia as well as the available FCR and the speed of which these can be activated. Exceeding allowed RoCoF or nadir limits may lead to tripping of system components and a cascading failure [56].

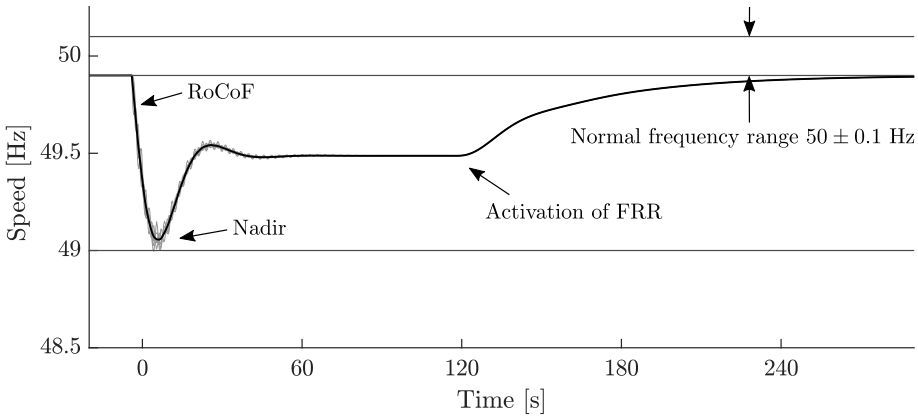

Figure 2.5: System response to a 1400 MW load step. Reserves are provided by hydropower at buses 1, 2, and 3, as shown in Example 1.4. With $W_{\text{kin}} = 240$ GWs, the FCR control (2.4) manages to keep the nadir above 49.0 Hz, and to restore the steady-frequency to 49.5 Hz. The FRR controller (2.5), is activated 2 min after the disturbance event. This restores the frequency to the normal operating range.

Historically, power systems where small scale with operators supplying small geographical regions or cities, frequency stability was a big problem since variability of load and production caused a severe impact on system power balance. The solution to this problem was the introduction of large-scale power systems with long distance transmission interconnecting not only cities and regions but also countries. As power systems grow larger, the impact of single variations becomes smaller. The dynamics of the system become slower, making it easier to maintain a steady frequency. As the power system grow in complexity however, new issues are introduced.

2.2.3 Rotor Angle Stability

Rotor angle stability refers to the power system's ability to maintain synchronism following disturbances. Instability may occur in the form immediate separation or increasing angular swings between synchronous generators. This may result from the disconnection of one or a group of generators from the rest of the system.

Transient Stability

Transient stability is concerned with the power systems ability to maintain synchronism following large disturbances such as the outage of a transmission line or a generating unit. Transient stability is influenced by the non-linear power-angle relationship resulting in aperiodic instability. Following a fault, the speed of generators start to deviate due changing operating condition, resulting in a deviation of rotor angle. A lack of synchronizing torque may cause a system separation resulting in

what is called *first-swing instability*. Installing fast-acting exciters with automatic voltage regulation (AVR) can greatly improve the synchronizing torque of the generator as seen in Example 2.2. The need for AVR becomes greater as transmission distances and transmitted power increases. In large power systems however, this phenomena may be more complex and instability may not always occur with the first swing. Transient stability depends on both the initial operating point as well as the location of the failure [57].

As seen in Example 2.2 the AVR tends to reduce the damping torque of the system, risking the system to become oscillatory unstable. Thus, AVR often has to be accompanied by stabilizing controllers such as power system stabilizers (PSS), stabilizing FACTS control, or HVDC control as seen in Examples 1.2 and 1.3.

Small-Signal Stability

Small-signal (or small-disturbance) stability considers the power system's response to small changes around an operating point. The disturbances are considered to be sufficiently small so that a linearized model is suitable for analysis.

Instability can occur in two forms [8]:

- aperiodic increase in rotor angle due to lack of sufficient synchronizing torque;
- rotor oscillation of increasing amplitude due to lack of damping torque.

In today's power systems, small-signal stability is mainly an issue of damping of oscillations.

Oscillations are due to natural modes in the power system and cannot be completely eliminated. One of the primary source of negative damping torque is the AVR control of synchronous generators as illustrated in the following example.

Example 2.2 (Rotor Angle Stability) We implement Example 13.2 from [25] in Simulink Simscape Electrical [51]. A single machine, representing the aggregation of four synchronous machines, feeds 0.9 per unit (p.u.) active power into an infinite bus as shown in Figure 2.6. At time $t = 1\,\text{s}$ a three phase ground fault occurs at one of the transmission lines. The fault is cleared by disconnecting the affected line at both ends. Two scenarios with a fault clearing time of 0.07 s and 0.10 s respectively are run to illustrate the destabilizing effect of AVR control and the need for PSS.

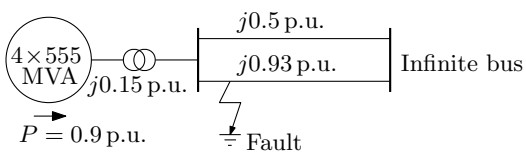

Figure 2.6: A single-machine network with p.u. reactances on a 2220 MVA base.

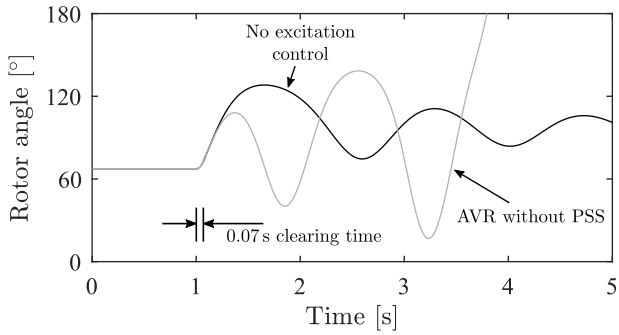

Figure 2.7: Simulation result showing rotor angle response with fault cleared in 0.07 s.

- *Constant field voltage:* With no excitation control, the generator survives with 0.07 s fault clearing time and remains stable under the new configuration as seen in Figure 2.7. However, for a 0.10 s fault clearing time, the generator is first-swing unstable due to a lack of synchronizing torque as seen in Figure 2.8.
- *AVR without PSS:* A fast-acting exciter and AVR are used to increase the synchronizing torque making the generator first-swing stable for a 0.10 s fault clearing time as seen in Figure 2.8. However, the degradation of damping torque causes the generator to lose synchronism during the second swing. In addition, the introduction of AVR makes the previously stable system unstable due to a lack of damping torque as seen in Figure 2.7. Because of this, the system can no longer survive even with 0.07 s fault clearing time. To increase the allowed fault clearing time without sacrificing stability, damping torque can be increased by adding a PSS to the generators excitation control.
- *AVR with PSS:* The addition of a PSS contributes to the damping torque ensuring transient as well as small-signal stability of the system as seen in Figure 2.8.

Electromechanical dynamics are those associated with the oscillation of synchronous machine such as the one seen in previous example. These come in two types [58]:

- *Local modes* between one our a group of generators in a geographical region, swinging against the rest of the system. The time frame of such oscillations is typically around 1–3 Hz.
- *Interarea modes*, associated with groups of generators in one area of the system swinging against machines in other areas of the power system. Interarea oscillations are caused by weak transmission line and large line loadings.

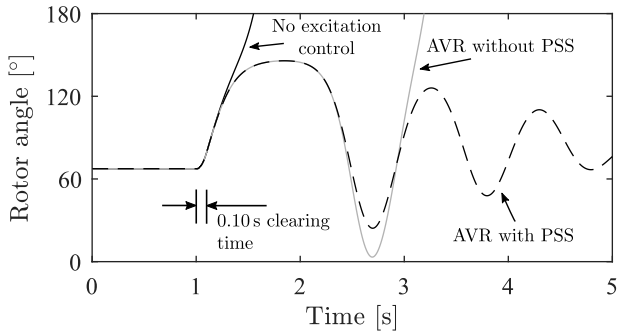

Figure 2.8: Simulation result showing rotor angle response with fault cleared in 0.10 s.

Other modes relevant for the analysis of synchronous machine involve [58]:

- *Control modes* associated with control equipment. Poorly tuned exciters, HVDC converters, or STATCOM devices are the usual causes of instability of these modes which typically are close to 3 Hz.

- *Torsional modes*, associated with the turbine-generator shaft rotations system. These are faster modes, typically in the range of 10–50 Hz. Instability is generally caused by interaction with control equipment.

2.3 Stability of Interarea Modes

Interarea modes involve complex interactions between multiple machines. As more power is being transferred over long distances, stability of these mode may deteriorate. For long networks, such as the Nordic transmission system, or the Western Interconnection of North America, this often poses a limiting factor for ac transmission capacity [17, 59]. In the 10 August 1996 power blackout in the western North America, growing power oscillation due to insufficient damping was found to be a decisive factor [18]. As interconnection increases with an increase in international trade due to deregulated electricity markets, these problems are likely to become worse in the future. At the same time, the shift towards renewable energy sources such as wind and solar imposes further changes to the grid. The intermittent nature of these sources increases the demand for international interconnection to help balancing load and production and maintaining system frequency [60].

In addition to excitation control of synchronous machines, interarea modes are also heavily affected by load dynamics. With an increasing amount of power electronics in loads and production facilities, constant power load characteristics are becoming increasingly dominant in the system. This further reduces the inherent damping in the system.

Conventional control methods such as PSS based on local measurements may prove insufficient to damp interarea modes due to actuator limitations and limited observability of the considered modes. The methods to improve performance include coordinated PSS control using either local or wide-area measurements from phasor measurement units (PMUs). Control of power electronic devices such as FACTS and HVDC has also been proved a useful complement for improving the damping of interarea modes [7, 59]. In what follows are two incidents reports where poor damping of interarea modes were reported in the synchronous grid of Continental Europe (CE). In both occasions the investigations concluded that new methods are needed for ensuring stability in the changing power system.

On the 1$^{\text{th}}$ of December 2016 an unexpected tripping of a line interconnecting the French power system to the Spanish system occurred. The event triggered an east–center–west interarea oscillation in the CE system. In the event the Iberian Peninsula and the Turkish system oscillated in anti-phase with the central part of the CE system. The oscillations were damped in three minutes after mitigation actions were taken by the Spanish transmission system operator. Analysis of the incidents showed that reactive power modulation of the HVDC line between France and Spain contributed in damping of the oscillation. Investigations into optimizing active and reactive HVDC modulation for damping of interarea oscillations were investigated following the event [61].

On the 3$^{\text{rd}}$ December 2017 a north–south interarea oscillation was registered in the CE system. The oscillation began at 1.09 a.m. and reached its maximum at around 1.15 a.m. when actions were taken. The causes of the incident were identified as

- low consumption (low load contribution to damping)
- high-voltage phase angle differences in the Italian power system
- unavailability of some generators caused non-standard power flows
- huge imports to the southern part of the CE system

leading to a gradual decrease of general damping. A conclusion drawn from the event was that changes and integrations of new technologies in the European power grid call for additional innovative damping countermeasures. New devices and methods must be developed to minimize serious consequences of interarea oscillations [62].

In this thesis we investigate the usage of active power modulation in HVDC lines for damping of interarea modes. The critical operation requirement on the grid and the complexity of interarea oscillations motivate the need for an increased system understanding. In this thesis we therefore strive to understand the fundamental nature and limitations of oscillation damping control using simplified dynamic models.

2.4 Converter-Based Frequency Support

Power systems exhibiting low rotational inertia present faster frequency dynamics, making frequency control and system operation more challenging. Unlike conventional synchronous generation, converter-interfaced generation such as wind or solar does not contribute to the inertia of the grid. As renewable production begins to replace conventional production, frequency stability is a growing challenge for the modern grid [32]. With growing shares of renewables, system operators are therefore increasingly demanding renewable generation to provide FCR [38, 63].

2.4.1 Frequency Support Using HVDC

Contrary to traditional ac transmission, HVDC enables the interconnection of asynchronous grids. Active power modulation, if made fast enough, allows for the networks to share FCR, reducing the nadir and the steady-state frequency deviation following disturbances in load or production [30, 64–69]. This facilitates a higher penetration of renewable energy, where inertia and FCR are important concerns.

HVDC transmission allows resources to be shared between asynchronous power systems such as the CE system and the Nordic system as seen in Figure 2.9. HVDC-interconnections are becoming increasingly important to balance the increased share of intermittent renewable production [60, 72]. An increased interconnection of the energy market is crucial in the transition towards a renewable and sustainable power sector. Since this expansion may lead to an increased system complexity, and an even higher demand on transmission capacity, the stability of interarea modes is likely to become a greater concern in the future.

Utilization of hydro power in the Nordic system, as flexible production reserves, is an interesting business opportunity but will also play an important role in reducing the fossil dependency in the CE grid. However, due to its geographic extensiveness, the Nordic system is already limited by stability of interarea modes [6, 59]. Sharing FCR through HVDC interconnections may put further stress on system transmission [60, 71]. This may increase the need for both damping and synchronizing torque, which could be provided by the interconnecting HVDC links.

2.4.2 Frequency Support From Wind Power

For wind power, the concept of synthetic inertia has gained a lot of attention. Synthetic inertia allows to temporally increase the output power of a wind turbine (WT) in exchange for reducing the rotor speed. The speed of which active power can be modulated makes it possible to reduce the initial RoCoF and nadir following load disturbances.

If the turbine is operated at its maximum power point (MPP), the act of frequency support will have to be followed by a recovery period in which the output power is less than the starting point, until the rotor speeds up again [73–78]. To supply FCR for a sustained period of time, curtailed operation is required. With

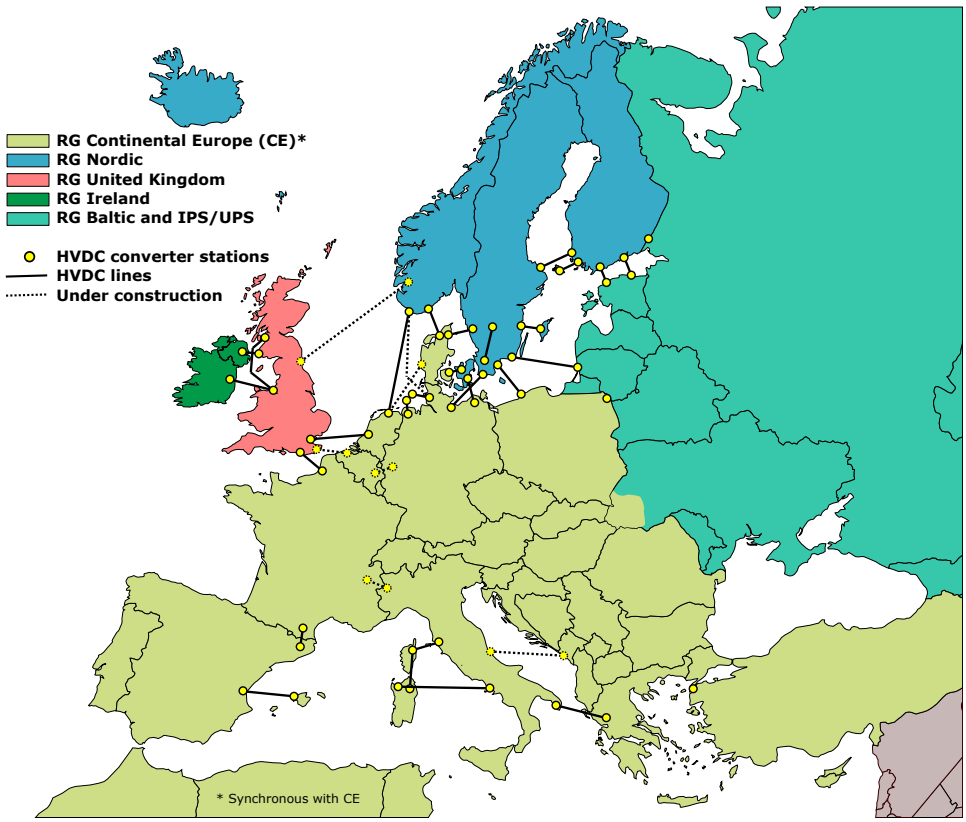

Figure 2.9: Map of the synchronous ac interconnections in Europe with an overview of HVDC interconnections in operation and under construction [70]. The high amount of hydro production with reservoirs in the Nordic region provides a relatively cheap flexibility both on a day-ahead and hourly operation. With increasing interconnection to the CE, the UK, and the Baltic regions, the competition for this low cost flexibility provided by hydro will increase. This may lead to changes in power flows and a more stressed system [71].

respect to electromechanical oscillations and frequency control, a curtailed WT can be viewed as an ideal controllable power source (if operated within the converter capacity rating). The downside of curtailed operation is the economic cost due to the sub-optimal utilization of the wind resources. In Chapters 7 and 8 we present a method for coordinating FFR from uncurtailed wind power with slow FCR from hydropower plants. The method allows for meeting the requirements on RoCoF, nadir, and steady-state frequency deviation, while avoiding the economic cost of curtailment.

Figure 2.10: The first commercial HVDC link manufactured by ASEA (now ABB) connected the Island of Gotland to the mainland of Sweden in 1954.

2.5 HVDC Technologies

HVDC is one of the most promising technologies for strengthening the future grid due to its high efficiency and controllability. In this section we give a brief overview of different HVDC converter technologies.

2.5.1 Line Commutated Converters

The first commercial application of HVDC was to connect the island of Gotland to the mainland of Sweden in 1954 (Figure 2.10). The installation provided 20 MW through a 96 km underwater cable using mercury-arc valves developed by Uno Lamm and his team at ASEA (now ABB). Since the 1970s thyristor valve converters have replaced the less durable and cost efficient mercury-arc technology. The first commercial thyristor based HVDC installation was the Eel River scheme, installed in 1972 between the Canadian provinces of New Brunswick and Québec [25, 79]. Thyristors are capable of conducting the current in one direction only and will do so when switched on by the gate signal and will continue to do so as long as the anode is positive with respect to the cathode. This technology is called line commutated converter (LCC) HVDC. As this control method relies on the grid voltage to stop conducting, switching has to occur at grid frequency.

LCC-HVDC could in theory be operated as either current source or voltage source. In practice however, current source converters prevail as the commutation process is less sensitive to ac voltage disturbances [80]. The converters absorb reactive power, as the current is always lagging behind the voltage. The reactive power requirement is in the order of 60 % of power rating and depends on power flow level. Due to this, LCC-HVDC installations, in weak systems, need to be accompanied by reactive power compensation such as STATCOM or SVC [25, 79–82]. The shortcomings of

LCC-HVDC, such as reactive power consumption and ac grid requirements, spurred the development of force commutated converters.

2.5.2 Force Commutated Converters

Since the 1990s insulated-gate bipolar transistors (IGBTs) have been implemented in voltage source converter (VSC) HVDC applications. This new semiconductor technology allows for commutation (switching) operations regardless of ac line voltage and allows for control of reactive power and installation in weak ac systems [81]. Early adoptions of the VSC technology use an pulse-width modulation (PWM) at high frequency to approximate the ac waveform. However due to switching losses this method is unfavorable to the traditional thyristor based LCC converters for high power installation. The modular multilevel converter (MMC) has improved the efficiency of VSC-HVDC since switching can be done at grid frequency. This greatly reduces power losses making VSC competitive with the traditional LCC technology.

Some of the advantages of force commutated voltage source converters over line commutated current source converters are that [79]:

- the commutation does not fail when ac voltage is decreased or distorted;
- PWM reduces low-order harmonics, greatly reducing requirements of harmonic filters;
- it allows for independent control of active and reactive power;
- no local reactive power supply is required;
- it allows for connection to weak ac grids such as off-shore wind power plants.

2.5.3 Multi-Terminal HVDC

Most HVDC installations today are point-to-point installations. However, a lot of research focus today is on multi-terminal HVDC (MTDC) systems interconnecting three (or more) converters. The most promising technology for this is MMC-HVDC as it offers lower switching losses, better fault performance, and higher controllability [9, 65, 76, 82–87]. There are currently two MTDC projects in operation using the MMC technology: the Nan'ao Multi-terminal VSC-HVDC project [88], and the Zhoushan dc power grid project [89].

2.5.4 Advantages of HVDC

HVDC transmission has some advantages over ac transmission [25, 79, 90].

- Transmission losses for HVDC are lower than ac making it an attractive solution for bulk energy transmission. However, the terminal cost and losses are higher for HVDC. Typically, the break-even distance for overhead lines is around 500–800 km as shown in Figure 2.11.

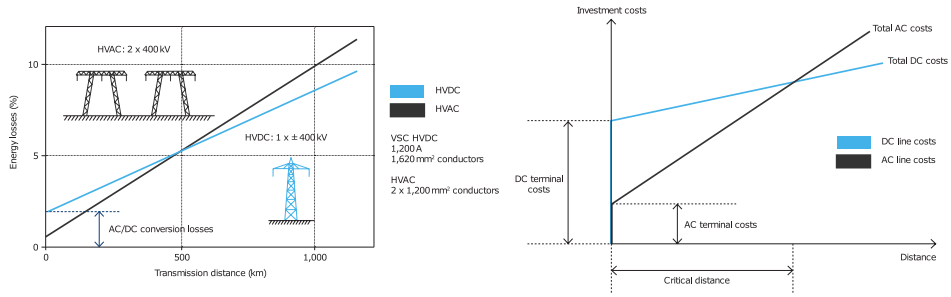

(a) Losses of HVDC compared to HVAC. (b) Cost of HVDC compared to HVAC.

Figure 2.11: Losses and cost for HVDC converter stations and transmission compared to similarly rated high-voltage alternating current (HVAC) overhead lines [90]. Images courtesy of ABB.

- AC transmission via long underground or submarine cable is impractical due to the high capacitance. These restrictions do not apply to dc. The typical break-even distance is reduced to around 50 km for submarine cables.
- DC constitutes an asynchronous connection allowing for the interconnection of asynchronous power systems, possibly with different frequencies, as seen in Figure 2.9.
- The asynchronous connection allow for an increased transmission capacity without increasing the short-circuit power at the connection points. This means that it will not be necessary to change ac circuit breakers.
- The active power flow in the HVDC links can easily be controlled at high speed. With appropriate control the HVDC link can be used to improve ac-system stability.

HVDC is typically installed where ac is infeasible such as between asynchronous grids or for long submarine cables. However, together with other properties such as controllability there are many important factors to consider in the overall cost analysis for HVDC installations.

The property that is of most interest in this work is the controllability of HVDC active power flows. The possibility to almost instantaneously control power injections between different ends of the power system may prove a vital role of ensuring stable and secure operations in the future grid.

2.6 HVDC Dynamics and Control

The converters of HVDC act as a bridge between ac and dc sides. By the switching of valves, dc is turned in to ac and vice versa. In this section we show the principle

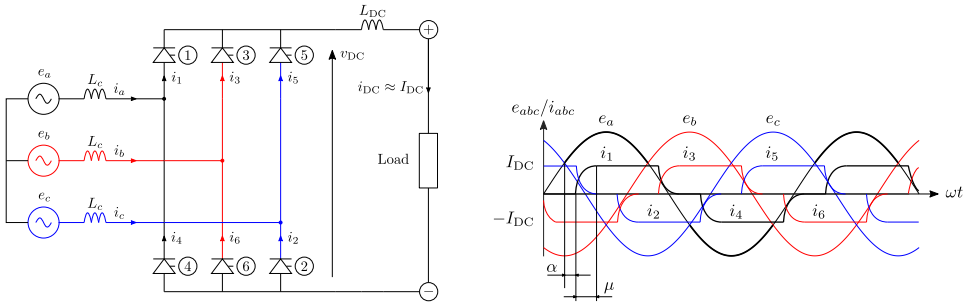

(a) 6-pulse thyristor bridge.

(b) AC line-to-neutral voltage and current at converter terminal under rectifier operation.

Figure 2.12: A simplified single-line diagram of a three-phase LCC 6-pulse bridge.

of how this is done for LCC- and VSC-HVDC.

2.6.1 LCC-HVDC

The workings of a LCC can be understood by studying the 6-pulse thyristor bridge shown in Figure 2.12a. A nearly constant dc current[3], $i_{DC} = I_{DC}$, is ensured by a large dc inductance L_{DC}. Thus the converter is operated as a current source. The thyristor is switched between phases to crate an ac waveform. The resulting square wave seen in Figure 2.12b is rich in harmonics that need to be filtered out. Typically two 6-pulse bridges are stacked to create a 12-pulse bridge, producing an output with less harmonics.

Thyristors are capable of conducting the current in one direction only and will do so when switched on by the gate signal and will continue to do so as long as the anode is positive with respect to the cathode. By controlling the firing angle, α, turn-on is controlled. The dc output voltage is given by

$$v_{DC} = \frac{3\sqrt{2}E}{\pi} \cos\alpha - R_c I_{DC}, \tag{2.6}$$

where E is the line-to-line root-mean-squared ac voltage [91]. Due to commutation inductance, L_c, the ac current cannot change instantly. This results in a commutation delay, μ, where the current commutates between phases. The resistance R_c in (2.6) models the resulting voltage drop due to commutation losses.

From (2.6) we see that if $\alpha < 90°$ the converter works as a rectifier. With higher firing angle the dc voltage goes negative and the converter becomes an inverter. The firing angle in rectifying operation can be reduced to around 5°. This is to ensure sufficiently high positive voltage over the valves and to account for small asymmetries in ac line voltages. Inverter operation is a bit more complicated. A

[3]Lower case letters are used to emphasize that we are considering time varying parameters.

commutation margin $\gamma = \pi - \alpha - \mu$ of 15° (18°) is typically needed for 50 Hz (60 Hz) systems. This is because the thyristor valves require a certain time interval with negative voltage to recover their blocking capability. If the thyristor fails to turn off, commutation failure occurs where the dc side becomes short circuited [79, 80, 91].

As the current is always lagging behind the voltage, the LCC consumes reactive power proportional to active power at both rectifier and inverter terminals.

2.6.2 VSC-HVDC

The VSC synthesizes an ac voltage from a dc voltage source maintained by a large dc capacitance. Thus the converter is inherently a voltage source. Since the IGBTs used in VSC can be turned off regardless of ac line voltage, any desirable ac voltage can be imposed at the converter terminal. Provided that operation is within the voltage/current capability of the converter and a power source/sink is able to maintain the dc voltage v_{DC} at desired level V_{DC}.

The basic operation of a VSC can be understood by studying the single-phase two-level converter shown in Figure 2.13a. The ac terminal is switched between positive and negative dc voltage. Pulse-width modulation is implemented by comparing a triangular wave to a sinusoidal carrier wave of desired shape. By switching between voltage levels a sinusoidal is emulated as seen in Figure 2.13a. Only filtering of higher switching harmonics is required. This significantly reduces ac filter sizes compared to LCC-HVDC. By adding a connection at neutral dc voltage (Figure 2.13b), a three-level converter gives a better ac approximation. [91]

Switching frequency is typically 1–2 kHz. For high power applications, switching losses limit the achievable switching frequency and the usefulness of VSC. Thyristors are also a more mature technology than IGBTs allowing for higher voltage ratings. Therefore LCC is still the dominating technology when it comes to high power applications. With the development of MMCs the efficiency of VSC is approaching LCC however.

The MMC synthesize a high-quality sinusoidal voltage waveform by incrementally switching between a high number of series-connected voltage sources as shown in Figure 2.13c[4]. The switching frequency can be reduced to 100–150 Hz. Thus, switching losses are reduced. Typically converter station losses are 1.5–2 % for two- and three-level VSC, 0.8–1 % for MMC, and 0.6–0.8 % for LCC [82].

2.6.3 Modeling HVDC Dynamics

Traditional LCC-HVDC still dominates applications for bulk power transmission as the mature thyristor technology offers lowest losses. However, with the development of MMC, VSC is approaching the efficiency of LCC and is thus seeing an increased market share. The independent control of active and reactive power and ability to connect to weak ac systems make VSC-HVDC an important technology in a power

[4] In practice PWM occurs between adjacent voltage levels similar to the three-level VSC.

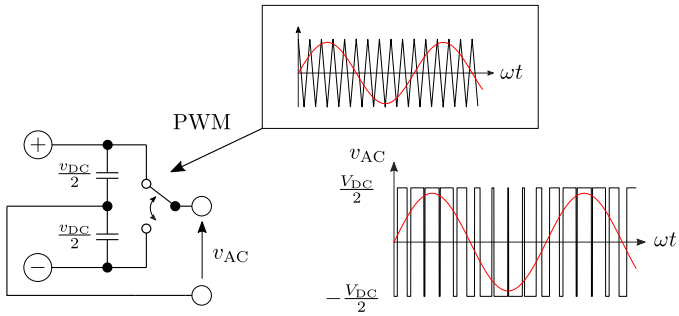

(a) Single-phase two-level converter.

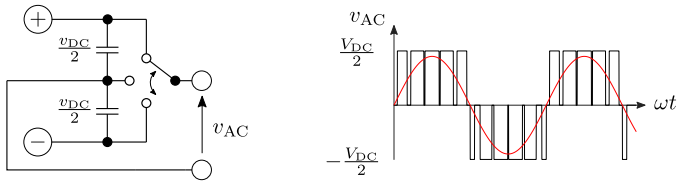

(b) Single-phase three-level converter.

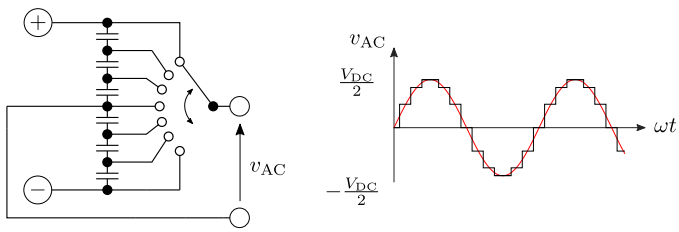

(c) Single-phase MMC.

Figure 2.13: Operating principle of VSC-HVDC.

system where synchronous generation is being phased out [9, 91]. Because of this, this work mainly focuses on VSC-HVDC but the results can also be extended to LCC, provided that sufficient reactive power compensation is available, e.g., from complementary STATCOM or SVC installations.

As previously mentioned, one of the benefits of power electronic based components such as HVDC is the speed of which these can be controlled. Bandwidths in tens of Hz can easily be obtained for the HVDC current control. Even for devices rated hundreds of MW [92]. When analyzing the electromechanical dynamics involved in interarea oscillations (0.1–1 Hz) most HVDC dynamics can be neglected. For the analysis of interarea modes, HVDC links are therefore often modeled as constant power loads [30, 93]. This simplification is justified in the following example.

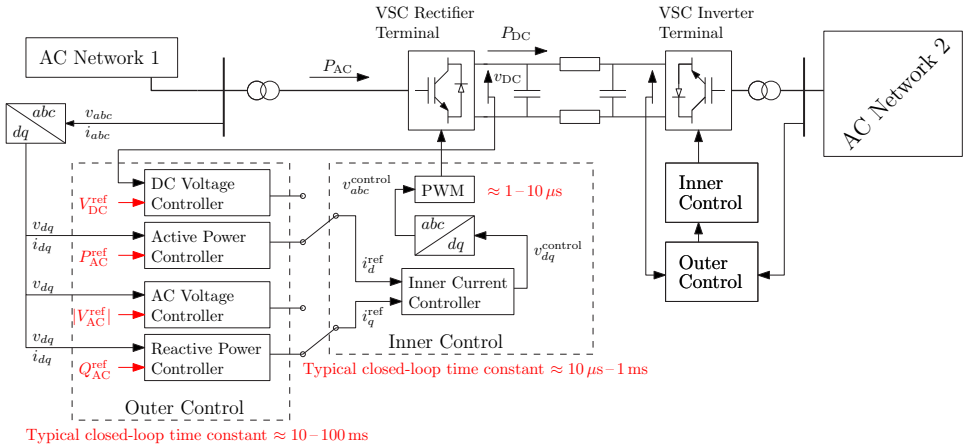

Figure 2.14: Topology of VSC-HVDC with control system in a dq reference frame.

Simulating a VSC-HVDC Link

Figure 2.14 shows a typical control scheme of a VSC-HVDC link. Controls are implemented in a dq framework where the d current controls either the dc voltage or the activate power and the q current controls either the ac voltage or the reactive power. For stable operation, one of the terminals needs to control the dc voltage. In the following example it is shown how the dc link can be controlled using a *leader-follower* architecture where the rectifier control active power while the inverter control dc voltage.

Example 2.3 (Leader-Follower Control) Consider a VSC-HVDC link interconnecting two ac terminals as seen in Figure 2.15. In this example we use an average value model[5] of the converters. This means that switching dynamics are not modeled. This is typically the level of detailed needed to study ac and dc dynamics for the high-level control system design [91]. Modeling the dc transmission as a Π-circuit, the dynamics of interest for the dc system are

- voltage dynamics at the dc terminals

$$C\frac{dv_{DC}^{rec}}{dt} = i_{rec} - i_{DC},$$
$$C\frac{dv_{DC}^{inv}}{dt} = i_{DC} - i_{inv},$$

  where C includes capacitance of converter sub-modules, dc cable, and dc capacitors;

[5]Simulations are implemented in Simulink. VSCs are based on a STATCOM phasor type model available in the Simulink library [51].

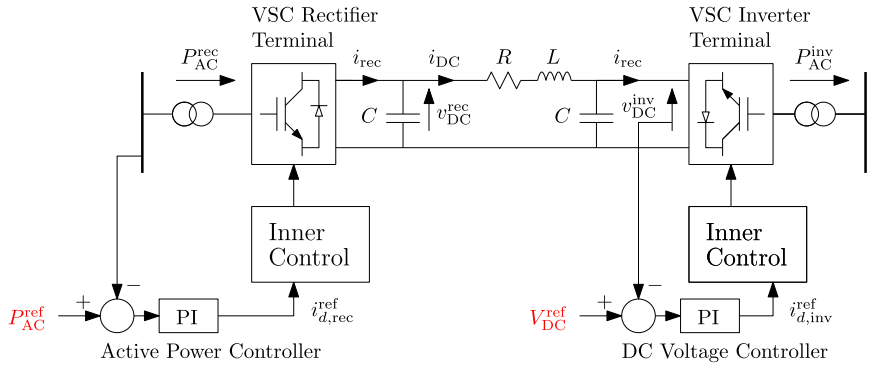

Figure 2.15: Leader-follower control of a VSC-HVDC link.

- dc current dynamics

$$L\frac{di_{DC}}{dt} = v_{DC}^{rec} - v_{DC}^{inv} - Ri_{DC},$$

where L and R are the inductance and resistance of the dc cable, respectively.

Neglecting converter losses, active power at the dc and ac terminals are given by

$$P_{AC}^{rec} = i_{rec}v_{DC}^{rec},$$
$$P_{AC}^{inv} = i_{inv}v_{DC}^{inv}.$$

Power flow and dc voltage can be controlled using a leader-follower architecture as shown in Figure 2.15.

Here, active power is controlled using a PI-controller at the rectifier with sufficient bandwidth to follow a reference step with 0.2 s rise time and a 0.5 Hz sinusoid as shown in Figure 2.16. Similarly the dc voltage is controlled at the inverter terminal as seen in Figure 2.17. The dc voltage is controlled so that the inverter active power tracks the power injected at the rectifier terminal. For the time frame of interest, the only considerable difference between the two power flows is the small resistive losses in the converters and the cable. For the analysis of interarea modes, which falls in the 0.1-1 Hz range, modeling the converters as constant power loads can therefore be considered a reasonable approximation.

The rating of the dc cable and the tuning of the PI-controllers are shown in Tables 2.1 and 2.2, respectively.

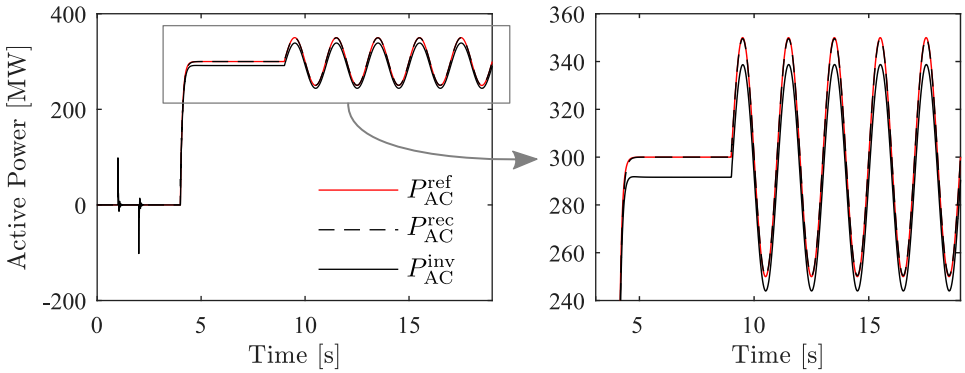

Figure 2.16: Active power reference tracked by using a PI-controller at the rectifier terminal. Initial disturbances are due to a change in dc voltage reference according to Figure 2.17.

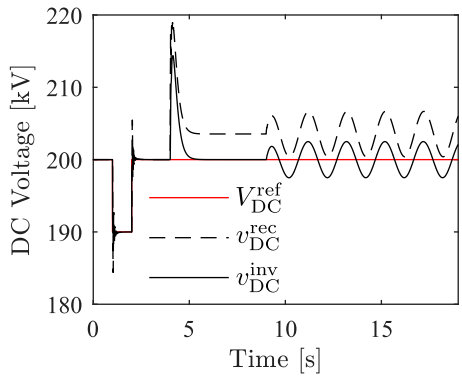

Figure 2.17: DC voltage reference tracked by using a PI-controller at the inverter terminal. Initially, small voltage reference steps are done. This is followed by active power changes according to Figure 2.16.

The dc controller needs to maintain the voltage within acceptable levels. Thus sufficient closed-loop bandwidth is needed. For connection to weak ac systems, this can be a problem as non-minimum phase (NMP) behavior of the ac transmission system limits the achievable bandwidth. With larger dc capacitors, however, the voltage control can be relaxed. Taking advantage of dc energy storage, the rectifier and inverter power flows could also be decoupled to some extent. For instance, auxiliary control such as a virtual synchronous generator control [94] could be added at the inverter terminal to provide power oscillation damping (POD) to the ac network connected on the inverter side. In this thesis however, we do not consider dc energy storage. Instead the focus is on the interaction between the HVDC-interconnected ac networks.

Table 2.1: Converter and line data obtained from [27]. DC capacitance includes lines, converter sub-modules and dc capacitors.

Voltage rating	200 kV
Power rating	400 MVA
Length	220 km
R	0.011 Ω/km
L	2.615 mH/km
C	175 µF

Table 2.2: PI-controller settings. Both controllers prevent windup by limiting integral action at ±1 p.u.

Active Power Controller	
Proportional gain	10 p.u.
Integral gain	100 p.u./s
DC Voltage Controller	
Proportional gain	5 p.u.
Integral gain	25 p.u./s

2.7 Power Oscillation Damping Using HVDC

Since HVDC transmissions often bridge long distances, they have a strong influence on dominant power system modes. Controlling the active power, local rotor speed deviations at the HVDC terminals can be reduced, thereby improving POD. In the 1970s active power modulation of the Pacific HVDC Intertie (PDCI) was implemented to improve POD in the western North American power system, thereby increasing the transfer capacity of the parallel Pacific AC Intertie [15, 16]. In LCC-HVDC, active and reactive control are heavily coupled. With coordinated control of rectifier firing angle and inverter extinction angle however, some degree of decoupling can be achieved. In [95], Grund *et al.* develop such a method by modulating rectifier dc current and the inverter dc voltage. The implemented controller is a linear quadratic Gaussian (LQG) regulator designed to minimize the system measurement requirements. The incorporation of reactive power control is shown to give an increased POD performance. With VSC technology, possible POD benefits are even higher as active power (typically at the rectifier terminal) and reactive power at both dc terminals can be controlled independently within the capability curve of the VSC system [96].

The addition of reactive power control may not always improve POD performance as it depends on ac network topology and placement of the dc terminals. In [93], Smed and Andersson show that the effect of active and reactive modulation is complementary. Active modulation is effective at dc terminals adjacent to generators participating in the interarea mode, while reactive modulation has highest controllability in the mass-weighted electrical midpoint between the two areas. An example of this is seen in [11] where Pipelzadeh *et al.* design a coordinated control scheme for VSC-HVDC POD control. The control design was implemented in the four-machine two-area test system [25] shown in Example 1.2. It is found that although reactive power control at both terminals is implemented, the control design favors active power control. It is found that controllability from reactive power control improved as the ac power flow increased which agrees with the findings of [93].

2.7.1 Wide-Area Measurement Systems

The availability of wide-area information from PMUs offers new possibilities for damping of interarea oscillations in large systems. Recent development in wide-area measurement systems (WAMS) allows for greater observability and coordination of multiple control units [97]. Kamwa *et al.* [98] recall the 30-year history of wide-area measurements at Hydro-Québec. It is found that damping control based on specific local measurements may cause transient instability for some contingencies, whereas WAMS yield transient stability improvements as well as damping over a wide range of operating conditions. Trudnowski *et al.* [17] evaluate PDCI damping control in the western North American power system. The conclusion is that the relative feedback between the two dc terminals of the PDCI gives better robustness properties than local frequency or ac power flow measurements. Practical tests of the PDCI wide-area damping controller showed a 4–5 % damping improvement of the north–south interarea mode, without degradation of other modes [24]. In [28], Preece *et al.* evaluate the robustness and performance of WAMS based POD control using a probabilistic methodology. The centralized and decentralized control of two VSC-HVDC links are designed using a modal LQG method targeting weakly damped modes. The method allows for individual modes to be targeted and synthesizes a controller based on the available measurement [28, 99]. In [100], Hadjikypris *et al.* use the same modal LQG design to coordinately control two FACTS devices and a VSC-HVDC link for POD. Juanjuan *et al.* [101] design a WAMS-based POD control for multiple HVDC lines in the China Southern Power Grid, known as the largest ac/dc paralleling transmission system in the world. The transfer capacity of the system is often limited by weakly damped interarea modes. The control of HVDC showed advantages over conventional methods where achievable POD is limited by the adjustable capacity of generators under PSS control and FACTS supplementary damping control. In [14], Azad *et al.* design a decentralized supplementary control of multiple LCC-HVDC links in a meshed ac network. The controller is designed using sparsity-promoting optimal control to prevent interactions among the HVDC links and to enhance damping of interarea modes. The sparsity-promoting optimal control simultaneously identifies the optimal control structure and optimizes the closed-loop performance [13, 102].

Although providing unprecedented advantages for system monitoring and control, WAMS have some obvious drawbacks, such as, increased system complexity as well as potential reliability [103] and security issues [104, 105]. Researches and developers from utilities, national labs, and universities are currently focusing on addressing the threats and vulnerabilities connected to cybersecurity. In [106], Adhikari *et al.* develop a WAMS cyber-physical test bed to model realistic power system contingencies and cyber-attacks. In [107], Jevtić and Ilić address power system reliability issues in presence of malicious cyber-attacks on measurement signals. A moving-target defense algorithm based on dynamic clustering is developed to detect stealthy cyber-attacks.

In light of potential reliability and security issues, the use of WAMS should be

well motivated. In Chapter 6 we study the fundamental control limitations imposed by choosing local frequency measurements, as compared to WAMS. Improving the understanding of the control problem helps to understand if control problems, such as the issue with transient stability, motivate the need for WAMS or if re-tuning of local POD controllers may suffice.

2.7.2 Multi-Terminal HVDC

More controllable devices in the system improves the ability to control poorly damped modes. In [108], Fuchs and Morari present a linear matrix inequality based method for optimal placement of multiple point-to-point HVDC lines within a meshed ac network, for improving POD. Coordinated control of MTDC offers potentially more controllability and flexibility than point-to-point HVDC. In [30], Harnefors *et al.* investigate POD from active power modulation of three- and four-terminal HVDC networks embedded in a single ac network and when interconnecting two asynchronous grids. The study shows that the pairing of two terminals in general provides the best result. Using an analytical approach, recommendations for terminal pairings are developed. With few active systems in operation today, MTDC is receiving a lot of research focus [9]. In [83], Eriksson develops a decentralized control method to improve POD through an MTDC system connected to an ac grid. Active power is controlled at the dc terminal with strongest controllability of the oscillatory mode. Voltage droop controllers, at the remaining dc terminals, are then tuned to maximize POD without the need of communication between the terminals. In [76] a cascaded control strategy is developed to provide virtual inertia to an ac network by utilizing energy stored in dc capacitors and the inertia of the wind turbines. It is shown that utilizing power stored in dc capacitors before exerting power from wind turbine inertia could help increase wind power production by allowing for a better power point tracking. The HVDC capacitor value, however, was shown to have little effect on overall inertia support compared to the kinetic energy stored in the wind turbines. In [84] the interaction between an ac network and an MTDC system integrated with wind power is analyzed. Normally, electromechanical dynamics are much slower than the converter control of the MTDC. But under certain conditions, the dc voltage control is shown to cause strong dynamic interactions between the MTDC and ac systems, degrading POD performance. In [85], Shah *et al.* analyzes the impact of MTDC grid reconfiguration on the host ac system. It is found that dc reconfiguration has little impact on ac small-signal stability. The analysis show, however, that dc reconfigurations can have a high impact on large-disturbance stability and frequency stability due to loss of infeed.

2.7.3 HVDC Interconnecting Asynchronous Power Systems

Most existing literature focuses on the dc and inverter dynamics, or paralleling ac/dc transmission systems. To complement existing research, this work instead focuses on the electromechanical interactions between HVDC-interconnected asynchronous

grids. One concern that arises when utilizing HVDC active power control for POD is that interarea modes of the assisting network may be excited [30]. Since poorly damped interarea modes usually fall in the same frequency ranges [25], control methods should avoid unnecessary excitation of weekly damped modes. In a case study of a future North Sea grid, Ndreko *et al.* [22] describe how HVDC active power modulation can be utilized to improve a poorly damped 0.5 Hz oscillatory mode in the UK grid. This, however, results in a disturbance propagating through the North Sea HVDC network, exciting a poorly damped 0.5 Hz interarea mode in the Nordic grid at the other end. The interaction between the interconnected ac systems can be mitigated by utilizing the wind power resources in the North Sea grid [22] or in the dc capacitors [94, 109]. The latter method may however increase the cost of the dc installation since larger capacitors may be needed. In addition such control methods require careful tuning since the dc dynamics may interact with the ac system and degrade the POD performance [84]. In [110], Van Hertem *et al.* show that coordinated control of two links that interconnect two asynchronous ac system can be used to improve POD in one of the networks. The poorly damped system is modeled as a two-machine system with a dc terminal close to each machine. Controlling the terminals in anti-phase, the setup resembles a long HVDC link interconnecting the two areas. Oscillation damping is improved by injecting power between the two areas, using the external asynchronous ac network to which the HVDC links are connected as a power sink. In Chapter 5 we extend this analysis to include more general configurations. In particular we consider the case where dynamics of the external HVDC-interconnected system cannot be neglected. The considered design criteria are stability of interarea modes, input usage, and stability in the event of dc link failure.

Due to the complexity and high order of the power systems, almost all works addressing POD rely on numerical studies. Although necessary for practical application, resorting to a numerical representation sacrifices physical intuition. In this thesis we build on the analytical approach of [21, 30, 93] to achieve more insight into the problem at hand. In [93], Smed and Andersson lay the foundational work for the theory used in this thesis. It is shown that active and reactive power control complement each other in the ability to provide POD. The focus of this work is on how electromechanical interactions limit achievable POD from HVDC that interconnect asynchronous grids. Thus, we will mainly consider active power modulation. In [30], Harnefors *et al.* investigate POD in asynchronous ac networks interconnected by a single point-to-point HVDC link. Modulation of HVDC active power using local frequency measurement is shown to be a robust control strategy both for the sharing of FCR and for improving the POD. In Chapter 4 we investigate to what extent oscillation damping in the HVDC-interconnected system can be improved. With active power modulation of the HVDC link, the interconnected ac systems will interact. This affects the control performance and may limit the achievable POD improvement.

Part I

Interarea Oscillation Damping

Chapter 3

Zero Dynamics Coupled to High-Speed Excitation Control

This chapter considers fundamental control limitations for rotor angle stability. Limitations are identified by characterizing open-loop transfer function zeros for input-output combinations of certain power system configurations. Of particular interest are non-minimum phase (NMP) zeros that limit the achievable performance of the closed-loop system. By studying a single-machine infinite bus (SMIB) power system model, analytic conditions for the presence of NMP zeros are derived. They are shown to be closely linked to the destabilizing effect of automatic voltage regulators (AVRs). Depending on the control loop, it is found that NMP zeros may persist in the system even if the closed-loop system is stabilized through feedback control. A simulation study shows that NMP zeros introduced by AVR limit the achievable performance and stabilization using feedback control.

The study of fundamental limitations in filtering and control design dates back to the ground breaking work of Bode in the 1940s [111]. In this chapter, we consider the feedback control limitations associated with NMP zeros. With increasing feedback gain, the closed-loop poles tends to the position of the open-loop zeros. NMP zeros therefore introduce a limitation on the achievable performance of the closed-loop system. For an overview of control limitations associated with NMP zeros see for instance [112–117]. When designing a power system stabilizer (PSS) we typically only care about a bandwidth window around poorly damped poles. Thus only NMP zeros close to the considered poles impose limitations on the closed-loop system. Since zero positions highly depend on the operating condition, they need to be carefully analyzed. An example is the modulation control of the Pacific DC Intertie in the 1970s. The modulation control considerably improved stability of the north–south interarea mode in the western North American power system. However, using local ac power flow as feedback signal, the open-loop system showed an NMP zero that caused the modulation to introduce a 0.7 Hz oscillation under certain operating conditions [16]. This was one of the primary reasons that the control

method eventually got rejected [17].

Rigorous numerical case studies are required to identify troublesome zero dynamics and to gain insight into the control problem at hand [118]. Today, efficient methods are available to identify transfer function zeros even in large power system models [119]. In [20], trade-offs between local measurements and wide-area measurements are studied in the general control configuration. Limitations due to NMP zeros and time-delays are taken into account to identify suitable input-output pairs. Resorting to a numerical solution, however, loses valuable physical insight into the problem at hand.

The contribution of this chapter is to identify fundamental control limitations for POD by characterizing the open-loop transfer function zero dynamics for different input-output combinations in the system. To obtain useful analytical results, the focus is on a SMIB model. For this model, it is explicitly shown how AVR destabilizes the electromechanical mode. For some transfer functions, NMP zeros are found to be caused by interaction with the AVR. Depending on the control-loop, it is shown that the NMP zeros persist in the system even if the closed-loop system is stabilized. The analysis gives insight into where in the system NMP zeros are likely to occur, and where they may impose a problem for POD control design.

The remainder of this chapter is organized as follows. In Section 3.1 a linearized SMIB model is presented. In Section 3.2 control limitations are derived and in Section 3.3 the results are validated on a detailed nonlinear power system model. Section 3.4 concludes the work.

3.1 Dynamic Modeling of Multi-Machine Power Systems

We consider a nonlinear differential algebraic power network model on the form

$$\dot{x}(t) = f\big(x(t), \gamma(t), u(t)\big) \tag{3.1a}$$

$$0 = g\big(x(t), \gamma(t), u(t)\big) \tag{3.1b}$$

$$y(t) = h\big(x(t), \gamma(t), u(t)\big) \tag{3.1c}$$

where $x(t) \in \mathbb{R}^{n_x}$ constitute the states, $\gamma(t) \in \mathbb{R}^{n_\gamma}$ are time-varying parameters, $u(t) \in \mathbb{R}^{n_u}$ external inputs, and $y(t) \in \mathbb{R}^{n_y}$ some outputs of the system.

For small-signal analysis, the system is linearized at a stationary operating point $x(t) = x^*$, $\gamma(t) = \gamma^*$, and $u(t) = u^*$, resulting in the linear state-space model

$$\begin{aligned} \dot{x}(t) &= Ax(t) + Bu(t) \\ y(t) &= Cx(t) + Du(t). \end{aligned} \tag{3.2}$$

Since the time constants in (3.2) depend on the current operating point, the model can only be considered accurate for small deviation from this point.

3.1.1 Network Model

Consider a power network and let the system voltages be given by

$$Ue^{j\varphi} = \left[U_1 e^{j\varphi_1}, U_2 e^{j\varphi_2}, \ldots, U_N e^{j\varphi_N}\right]^T \in \mathbb{C}^N \tag{3.3}$$

where $U \in \mathbb{R}^N$ and $\varphi \in \mathbb{R}^N$ are voltage amplitudes at system nodes and the phase angles relative to a constant reference frame rotating at nominal frequency, typically at 50 or 60 Hz. The impedance between two nodes is given by

$$Z_{ik} = R_{ik} + jX_{ik}$$

and corresponding admittance is

$$y_{ik} = 1/Z_{ik} = g_{ik} - jb_{ik}.$$

Nodes are interconnected over a network described by the admittance matrix $Y \in \mathbb{C}^{N\times N}$ with elements

$$Y_{ik} = -y_{ik}, \quad \text{and} \quad Y_{ii} = y_{ii} = y_i + \sum_{k\in\mathcal{N}_i} y_{ik} \tag{3.4}$$

where $y_i = g_i - jb_i$ is the shunt admittance at node i and $\mathcal{N}_i$ is the set of nodes directly connected to node i. Power injected at the nodes are given by

$$S = P + jQ = \operatorname{diag}(Ue^{j\varphi})\bar{Y}Ue^{-j\varphi} \in \mathbb{C}^N, \tag{3.5}$$

where $\bar{Y}$ is the complex conjugate of Y. Active and reactive power injected at node i give the two algebraic equations

$$\begin{aligned} P_i &= g_{ii}U_i^2 + \sum_{k\in\mathcal{N}_i} U_iU_k\Big(b_{ik}\sin(\varphi_i-\varphi_k) - g_{ik}\cos(\varphi_i-\varphi_k)\Big) \\ Q_i &= b_{ii}U_i^2 - \sum_{k\in\mathcal{N}_i} U_iU_k\Big(b_{ik}\cos(\varphi_i-\varphi_k) + g_{ik}\sin(\varphi_i-\varphi_k)\Big). \end{aligned}$$

For the analysis it is convenient to write (3.5) as $S = \boldsymbol{Y}\mathbf{1}$, where $\mathbf{1} \in \mathbb{R}^N$ is a vector of ones and $\boldsymbol{Y} \in \mathbb{C}^{N\times N}$ is a *weighted* admittance matrix with elements

$$\boldsymbol{Y}_{ik} = -\bar{y}_{ik}U_iU_ke^{j(\varphi_i-\varphi_k)}, \quad \text{and} \quad \boldsymbol{Y}_{ii} = \bar{y}_{ii}U_i^2. \tag{3.6}$$

We partition (3.3) as

$$Ue^{j\varphi} = \big[\underbrace{(Ee^{j\delta})^T}_{\text{Dynamic nodes.}}, \underbrace{(Ve^{j\theta})^T}_{\text{Algebraic network nodes.}}\big]^T \in \mathbb{C}^N,$$

to differentiate between nodes where voltages $Ee^{j\delta} \in \mathbb{C}^{n_\delta}$ are determined by differential equations (3.1a), and nodes where voltages $Ve^{j\theta} \in \mathbb{C}^{n_\theta}$ are determined by algebraic equations (3.1b).

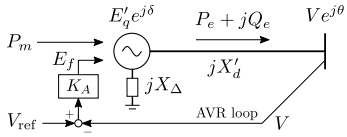

Figure 3.1: One-axis synchronous machine with AVR.

3.1.2 One-Axis Synchronous Machine Model

For study of electromechanical dynamics, the synchronous machines in the system are often described using the one-axis model, with notation from [52],

$$\begin{aligned}\dot{\delta} &= \omega \\ M\dot{\omega} &= -\frac{1}{X'_d}E'_q V\sin(\delta-\theta) + D\omega + P_m \\ T'_{do}\dot{E}'_q &= -\frac{X_d}{X'_d}E'_q + \frac{X_d - X'_d}{X'_d}V\cos(\delta-\theta) + E_f,\end{aligned} \tag{3.7}$$

where state variables δ, ω, and E'_q represent the rotor phase angle, rotor speed deviation from nominal speed, and q-axis transient voltage, respectively. Parameter M represent the machine inertia, D a small non-negative machine damping constant, T'_{do} the d-axis transient open-circuit time constant, and X'_d and X_d the d-axis transient reactance and synchronous reactance respectively.[1] External inputs P_m and E_f are the mechanical power from the turbine and the field voltage. Variables V and θ represent the voltage amplitude and phase angle at the adjacent network node. The node adjacent to the machine node will typically be referred to as the machine terminal. The total series reactance between the machine node and the machine terminal include transformers, line reactances etc.

Let P_e and Q_e be the active and reactive power exported from the machine node to the network as shown in Figure 3.1. The second line in (3.7) corresponds to $M\dot{\omega} = -P_e + D\omega + P_m$, i.e., rotor angular acceleration depends on the active power balance at the machine node. Similarly the third line is a function of the reactive power. Let $X_\Delta = X_d - X'_d$, $b'_d = 1/X'_d$, and $b_\Delta = 1/X_\Delta$. The third line in (3.7) can then be rewritten as

$$T'_{do}b_\Delta\dot{E}'_q = -b_\Delta E'_q \underbrace{-b'_d E'_q + b'_d V\cos(\delta-\theta)}_{-Q_e/E'_q} + b_\Delta E_f.$$

Note that b_Δ represents the shunt susceptance at the machine node. Thus, we can describe the machine node as a dynamical node connected to an algebraic network node.

[1] The prime notation is used to emphasize that the model assumes parameters linearized at a fixed speed and that the model is accurate only for a transient time period. Faster *subtransient* dynamics are often noted with double prime. In the one-axis model, the subtransient and d-axis dynamics have been neglected by setting the corresponding time constants $T''_{do} = T''_{qo} = T'_{qo} = 0$ [52].

3.1.3 Excitation Control of Synchronous Machine

The excitation system performs control and protective functions essential to satisfactory performance of the power system by controlling the field voltage, E_f. High-speed excitation systems with AVRs are commonly installed at generators as it is by far the most effective and economical method to improve transient stability [25]. AVRs are typically modeled using the first-order model

$$T_e \dot{E}_f = -E_f + K_A(V_{\text{ref}} - V), \tag{3.8}$$

where V is typically measured at the machine terminal. Here however, it is assumed that the fast dynamics of the excitation system can be neglected, so

$$E_f = K_A(V_{\text{ref}} - V), \tag{3.9}$$

as shown in Figure 3.1.

3.1.4 Linearized Multi-Machine Model

Consider a multi-machine power system, as shown in Figure 3.2, with n_δ machines represented using the one-axis model (3.7). Let state variables $x = [\delta^T, \omega^T, E_q'^T]^T \in \mathbb{R}^{3n_\delta}$ represent the generator states and algebraic variables $\gamma = [\theta^T, V^T]^T \in \mathbb{R}^{2n_\theta}$ voltages at the n_θ network nodes.

Partition the weighted network admittance matrix (3.6) as

$$\boldsymbol{Y} = \left[\begin{array}{c|c} \boldsymbol{Y}_{\delta\delta} & \boldsymbol{Y}_{\delta\theta} \\ \hline \boldsymbol{Y}_{\theta\delta} & \boldsymbol{Y}_{\theta\theta} \end{array}\right] \in \mathbb{C}^{N\times N}$$

where $\boldsymbol{Y}_{\delta\delta} \in \mathbb{C}^{n_\delta \times n_\delta}$. If the machine terminals are modeled, as shown in Figure 3.2, the corresponding *unweighted* admittance matrix (3.4) is given by $Y_{\delta\delta} = -j\,\text{diag}(b_d' + b_\Delta)$. Network matrix $\boldsymbol{Y}_{\theta\theta} \in \mathbb{C}^{n_\theta \times n_\theta}$ connects network nodes where voltages are determined by the algebraic equation (3.1b). Off-diagonal blocks $\boldsymbol{Y}_{\delta\theta} \in \mathbb{C}^{n_\delta \times n_\theta}$ and $\boldsymbol{Y}_{\theta\delta} \in \mathbb{C}^{n_\theta \times n_\delta}$ models the connection between the machine and network nodes. Constant power inputs are assumed to be zero at the algebraic network nodes, whereas constant impedance loads can be incorporated as shunt elements in (3.4).

Following the modeling above and excluding the AVR, the state matrix of (3.2) becomes

$$A_0 = \begin{bmatrix} 0 & I & 0 \\ -\mathcal{M}^{-1}\,\text{Im}(\boldsymbol{Y}_A) & -\mathcal{M}^{-1}\mathcal{D} & -\mathcal{M}^{-1}\,\text{Re}(\boldsymbol{Y}_A + 2\boldsymbol{Y}_{\text{sh}})E^{-1} \\ T^{-1}\,\text{Re}(\boldsymbol{Y}_A) & 0 & -T^{-1}\,\text{Im}(\boldsymbol{Y}_A + \boldsymbol{Y}_{\text{sh}})E^{-1} \end{bmatrix}, \tag{3.10}$$

where 0 and I are appropriately sized zero and identity matrices, $\mathcal{M} = \text{diag}(M_1, \ldots, M_{n_\delta})$, $\mathcal{D} = \text{diag}(D_1, \ldots, D_{n_\delta})$, $E = \text{diag}(E'^*_{q,1}, \ldots, E'^*_{q,n_\delta}) \in \mathbb{R}^{n_\delta \times n_\delta}$, and $T = \text{diag}(T'_{do,1} b_{\Delta 1} E'^*_{q,1}, \ldots, T'_{do,n_\delta} b_{\Delta n_\delta} E'^*_{q,n_\delta})$.

The network matrix $\boldsymbol{Y}_A$ is obtained from $\boldsymbol{Y}_{\text{red}} = \boldsymbol{Y}_{\delta\delta} - \boldsymbol{Y}_{\delta\theta}\boldsymbol{Y}_{\theta\theta}^{-1}\boldsymbol{Y}_{\theta\delta}$ and $\boldsymbol{Y}_{\text{sh}} = \text{diag}(\boldsymbol{Y}_{\text{red}}\mathbf{1})$, as $\boldsymbol{Y}_A = \boldsymbol{Y}_{\text{red}} - \boldsymbol{Y}_{\text{sh}}$, evaluated around a steady-state operating point.

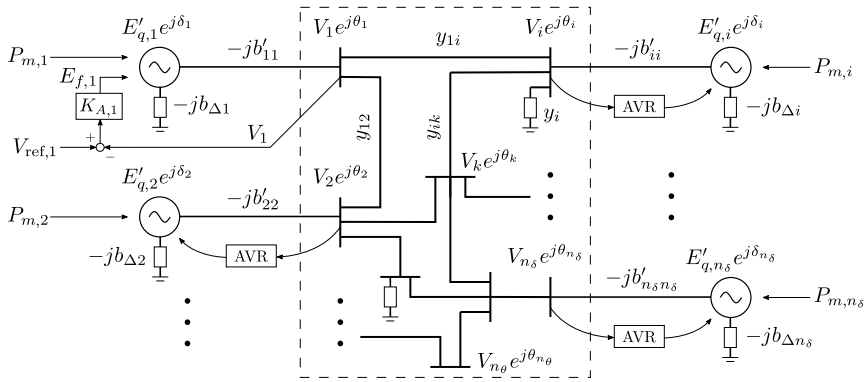

Figure 3.2: Multi-machine power system with n_δ machines interconnected over a network with $n_\theta \geq n_\delta$ nodes.

Note that $\boldsymbol{Y}_{\text{sh}}$ contains the power injected by turbines and excitation system at the machine nodes.

Considering constant power inputs $u = [P^\intercal, Q^\intercal]^\intercal \in \mathbb{R}^{2n_\theta}$ and outputs $y = \gamma$ at network nodes, we have input matrix, excluding AVR and with $u^* = 0$,

$$B_0 = \begin{bmatrix} 0 & 0 \\ \mathcal{M}^{-1}\operatorname{Re}(\boldsymbol{Y}_B) & -\mathcal{M}^{-1}\operatorname{Im}(\boldsymbol{Y}_B) \\ T^{-1}\operatorname{Im}(\boldsymbol{Y}_B) & T^{-1}\operatorname{Re}(\boldsymbol{Y}_B) \end{bmatrix}, \tag{3.11}$$

output matrix

$$C = \begin{bmatrix} \operatorname{Re}(\boldsymbol{Y}_C) & 0 & -\operatorname{Im}(\boldsymbol{Y}_C)E^{-1} \\ \boldsymbol{V}\operatorname{Im}(\boldsymbol{Y}_C) & 0 & \boldsymbol{V}\operatorname{Re}(\boldsymbol{Y}_C)E^{-1} \end{bmatrix},$$

and direct feed-through matrix

$$D = \begin{bmatrix} \operatorname{Im}(\boldsymbol{Y}_D) & \operatorname{Re}(\boldsymbol{Y}_D) \\ -\boldsymbol{V}\operatorname{Re}(\boldsymbol{Y}_D) & \boldsymbol{V}\operatorname{Im}(\boldsymbol{Y}_D) \end{bmatrix}, \tag{3.12}$$

where $\boldsymbol{Y}_D = -\boldsymbol{Y}_{\theta\theta}^{-1}$, $\boldsymbol{Y}_B = \boldsymbol{Y}_{\delta\theta}\boldsymbol{Y}_D$, $\boldsymbol{Y}_C = \boldsymbol{Y}_D\boldsymbol{Y}_{\theta\delta}$, and $\boldsymbol{V} = \operatorname{diag}(V_1^*, \ldots, V_{n_\theta}^*)$.

With AVR modeled using (3.9), the state matrix of (3.2) is instead given by

$$A = A_0 - K_{\text{AVR}} \begin{bmatrix} 0 & 0 & 0 \\ 0 & 0 & 0 \\ \boldsymbol{V}\operatorname{Im}(\boldsymbol{Y}_C) & 0 & \boldsymbol{V}\operatorname{Re}(\boldsymbol{Y}_C)E^{-1} \end{bmatrix},$$

and the input matrix by

$$B = B_0 - K_{\text{AVR}} \begin{bmatrix} 0 & 0 \\ 0 & 0 \\ -\boldsymbol{V}\operatorname{Re}(\boldsymbol{Y}_D) & \boldsymbol{V}\operatorname{Im}(\boldsymbol{Y}_D) \end{bmatrix}, \tag{3.13}$$

where $K_{\text{AVR}} = \operatorname{diag}(K_{A,1}, \ldots, K_{A,n_\delta}) \operatorname{diag}(T'_{do,1}, \ldots, T'_{do,n_\delta})^{-1}$.

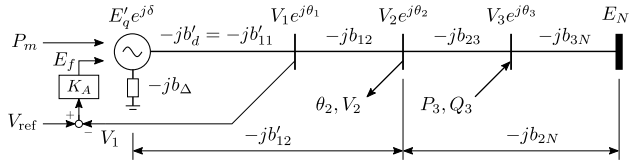

Figure 3.3: SMIB model with three network nodes.

3.2 Zero Dynamics and Control Limitations

Consider the SMIB model in Figure 3.3. At the machine terminal, V_1 is measured for the AVR. We will first show how interaction between the electromechanical and voltage dynamics have a destabilizing effect on the electromechanical mode. Then we study the control performance limitations in stabilizing this mode. This is done by studying the open-loop zeros in the single-input single-output (SISO) transfer function $G_{yu}(s)$ from inputs $u = P_3$ or Q_3 at a control bus to measurements $y = \theta_2$ or V_2 at a measurement bus.[2] To limit the number of possible scenarios, the following standing assumption is made.

3.2.1 SMIB Model

The SMIB model shown in Figure 3.3 is commonly used for analyzing generators connected to the grid. The machine is connected to a strong (infinite) bus that represent the rest of the system. Here, the voltage E_N can be considered as a constant voltage rotating at the nominal system frequency. We introduce three network nodes as shown in Figure 3.3. The system voltages are given by

$$U e^{j\varphi} = \left[E'_q e^{j\delta} \;\; E_N \;\; V_1 e^{j\theta_1} \;\; V_2 e^{j\theta_2} \;\; V_3 e^{j\theta_3}\right]^T,$$

where V_1 is measured for the AVR. The linearized state-space model (3.2) is obtained as above with the unforced dynamics for the states $x = [\delta, \omega, E'_q]^T$ given by[3]

$$\dot{x} - \dot{x}^* = A(x - x^*) = \begin{bmatrix} 0 & 1 & 0 \\ -a_{21} & -a_{22} & -a_{23} \\ -a_{31} & 0 & -a_{33} \end{bmatrix} (x - x^*) \tag{3.14}$$

with elements

$$\begin{aligned} a_{21} &= \frac{b_\Sigma}{M} E'^*_q E_N \cos\delta^*, \quad a_{22} = \frac{D}{M}, \quad a_{23} = \frac{b_\Sigma}{M} E_N \sin\delta^*, \\ a_{31} &= \frac{b_\Sigma}{T'_{do} b_\Delta} E_N \sin\delta^* - \frac{K_A}{T'_{do}} \beta_1 E'^*_q \sin\varepsilon^*_1, \\ a_{33} &= \frac{b_\Delta + b_\Sigma}{T'_{do} b_\Delta} + \frac{K_A}{T'_{do}} \beta_1 \cos\varepsilon^*_1, \end{aligned} \tag{3.15}$$

[2] For PSS, the control bus coincide with the machine node.

[3] Dynamics at the infinite bus are truncated since $\dot{E}_N = \dot{\delta}_N = 0$.

where b_Σ is the total series susceptance between the machine node and the infinite bus. Note that element a_{31} and a_{33} are affected by the AVR using measurements at the machine terminal. At network nodes $i = 1, 2, 3$,

$$\begin{bmatrix} \theta_i - \theta_i^* \\ V_i - V_i^* \end{bmatrix} = \beta_i \begin{bmatrix} \frac{E_q'^*}{V_i^*} \cos \varepsilon_i^* & 0 & \frac{1}{V_i^*} \sin \varepsilon_i^* \\ -E_q'^* \sin \varepsilon_i^* & 0 & \cos \varepsilon_i^* \end{bmatrix} (x - x^*), \tag{3.16}$$

where $\beta_i = b'_{1i}/(b'_{1i} + b_{iN}) \in [0, 1]$ is the relative electrical position of the network node and $\varepsilon_i^* = \delta^* - \theta_i^*$. The input matrix (3.11) can be derived similar to (3.16). With AVR, a direct feed-through between the input and voltage measurement at the machine terminal are introduced as shown in (3.13). The direct feed-through (3.12) between nodes are given in Appendix 3.A.

Assumption 3.1 Active power flows in a uniform direction between the machine node and the infinite bus. The load angles $\varepsilon_i^* = \delta^* - \theta_i^*$, $i = 1, 2, 3$, therefore have the same sign. The network nodes may coincide or be placed in any order between the machine node and the infinite bus.

3.2.2 AVR Influence on Stability

In this section we consider the influence of the AVR on the dynamics. A common simplifying assumption is that the load angle $\delta^* \approx \theta_i^* \approx 0$. Under this assumption $a_{23} = a_{31} = 0$ and (3.14) has three eigenvalues: $\lambda_{1,2} \approx -a_{22}/2 \pm j\sqrt{a_{21}}$ (assuming $a_{21} \gg {a_{22}}$[4]) and $\lambda_3 = -a_{33}$ associated with $[\delta, \omega]$ and E'_q respectively.

Now as $\delta \neq 0$ the voltage mode λ_3 will start to interact with the electromechanical mode λ_1, λ_2. If $K_A = 0$, or if $\theta_1^* = \delta^*$, then since $\operatorname{sgn}(a_{31}) = \operatorname{sgn}(a_{23})$ the eigenvalues will attract each other, thus stabilizing the electromechanical mode. However, usually with AVR, $K_A \gg 0$ and $\theta_1^* \neq \delta^*$. In this case λ_3 moves further into the left half plane (LHP) and is mostly unaffected by the interaction. This does not hold true for the electromechanical mode, however. We notice that if

$$\left| \frac{b_\Sigma}{b_\Delta} E_N \sin \delta^* \right| > \left| K_A \beta_1 E_q'^* \sin \varepsilon_1^* \right|, \tag{3.17}$$

is violated, then a_{31} changes sign. Therefore, the eigenvalues will repel each other. The interaction thus destabilizes the electromechanical mode.

The same conclusion can be draw from studying the characteristic polynomial of (3.14):

$$p(s) = s^3 + (a_{22} + a_{33})s^2 + (a_{22}a_{33} + a_{21})s + a_{21}a_{33} - a_{23}a_{31}. \tag{3.18}$$

This polynomial is stable if

$$\beta_1 K_A \left(\cos \delta^* \cos \varepsilon_1^* + \sin \delta^* \sin \varepsilon_1^* \right) + \frac{b_\Delta + b_\Sigma}{b_\Delta} \left(\cos \delta^* - \frac{E_N}{E_q'^*} \sin^2 \delta^* \right) > 0,$$

[4]With machine speed in rad/s, typically $D \in [0,\ 3/2\pi 50]$ or $D \in [0,\ 3/(2\pi 60)]$. Thus $a_{21} \gg a_{22}$.

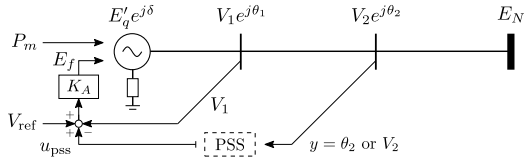

Figure 3.4: SMIB model with PSS. Note that network node 2 may coincide directly with the machine node.

which holds true for reasonable load angles and large K_A, and if

$$a_{22}(a_{22}a_{33} + a_{21} + a_{33}^2) + a_{23}a_{31} > 0.$$

For the remainder of the section, we make the simplifying assumption that the direct machine damping $D = 0$. Hence, $a_{22} = 0$, so the stability criterion becomes

$$a_{23}a_{31} > 0,$$

which is equivalent to (3.17).

3.2.3 Auxiliary Excitation Control

A common way to improve stability is to combine AVR with PSS. With input u_{pss} in Figure 3.4, the transfer function to system states becomes

$$(sI - A)^{-1} \begin{bmatrix} 0 \\ 0 \\ K_A \end{bmatrix} = \frac{K_A}{p(s)} \begin{bmatrix} -a_{23} \\ -sa_{23} \\ s^2 + a_{21} \end{bmatrix}, \tag{3.19}$$

where $p(s)$ is given by (3.18). Note that zeros in (3.19) are unaffected by the AVR.

Using (3.16), the open-loop zeros of the transfer function from u_{pss} to θ_2, $G_{\theta_2,u_{\text{pss}}}(s)$ are

$$q_{1,2}^{(\theta_2,u_{\text{pss}})} = \pm\sqrt{\frac{b_\Sigma}{M} E'^*_q E_N \left(\sin\delta^* \frac{\cos\varepsilon_2^*}{\sin\varepsilon_2^*} - \cos\delta^*\right)}. \tag{3.20}$$

Since $\operatorname{sgn}(\delta^*) = \operatorname{sgn}(\varepsilon_2^*)$ and $|\delta^*| \geq |\varepsilon_2^*|$, the zeros are real if $\delta^* \neq 0$. For PSS, rotor frequency are typically measured directly, in which case $q_{1,2}^{(\theta_2,u_{\text{pss}})} \to \pm\infty$ as $|\varepsilon_2^*| \to 0$.

The open-loop zeros of $G_{V_2,u_{\text{pss}}}(s)$ are

$$q_{1,2}^{(V_2,u_{\text{pss}})} = \pm j\sqrt{\frac{b_\Sigma}{M} E'^*_q E_N \left(\cos\delta^* + \sin\delta^* \frac{\sin\varepsilon_2^*}{\cos\varepsilon_2^*}\right)}. \tag{3.21}$$

With direct machine damping $a_{22} > 0$, both zero pairs in (3.20) and (3.21) will move in the negative real direction with increased damping gain.

Remark 3.1 (Observability) The zeros (3.21) are very close to the undamped frequency of the electromechanical mode

$$\Omega = \sqrt{\frac{b_\Sigma}{M} E'^*_q E_N \cos\delta^*}, \tag{3.22}$$

making this an unsuitable loop to close.

Remark 3.2 (Power measurement) In the SMIB model, active power measurement can be considered a special case of phase angle measurements, where $\varepsilon_2^* = \delta^*$ and $\beta_2 = b_\Sigma$ in (3.16). By (3.20), this results in two zeros in the origin.

3.2.4 Auxiliary Governor Control

In [93], Smed and Andersson show that active power injections close to the machine node are ideal for controlling the electromechanical mode. Assuming that the governor is fast enough so that its dynamics can be ignored, the transfer function to system states becomes

$$(sI - A)^{-1} \begin{bmatrix} 0 \\ 1 \\ 0 \end{bmatrix} = \frac{1}{p(s)} \begin{bmatrix} s + a_{33} \\ s(s + a_{33}) \\ -a_{31} \end{bmatrix}. \tag{3.23}$$

The transfer function $G_{\theta_2,P_m}(s)$ has one open-loop zero

$$q^{(\theta_2,P_m)} = \frac{-1}{T'_{do} b_\Delta} \left(b_\Delta + b_\Sigma \Big(1 - \frac{E_N}{E'^*_q} \frac{\sin\varepsilon_2^*}{\cos\varepsilon_2^*} \sin\delta^* \Big) \right) - \frac{K_A}{T'_{do}} \beta_1 \left(\cos\varepsilon_1^* + \frac{\sin\varepsilon_2^*}{\cos\varepsilon_2^*} \sin\varepsilon_1^* \right),$$

which is minimum phase. Similarly, for $G_{V_2,P_m}(s)$

$$q^{(V_2,P_m)} = \frac{-1}{T'_{do} b_\Delta} \left(b_\Delta + b_\Sigma \Big(1 + \frac{E_N}{E'^*_q} \frac{\cos\varepsilon_2^*}{\sin\varepsilon_2^*} \sin\delta^* \Big) \right) - \frac{K_A}{T'_{do}} \beta_1 \left(\cos\varepsilon_1^* - \frac{\cos\varepsilon_2^*}{\sin\varepsilon_2^*} \sin\varepsilon_1^* \right).$$

With high load angles, and if the voltage V_2 is measured closer to the machine node than the machine terminal $|\varepsilon_2^*| < |\varepsilon_1^*|$, the zero, $q^{(V_2,P_m)}$ may potentially move into the right half-plane.

3.2.5 Active Power Injection and Phase Angle Measurement

Power electronic devises can be used to improve the stability of electromechanical modes. If fast and strong enough, power oscillations can be controlled directly by

controlling active power injections. The difference from the governor control in Section 3.2.4 is that the input is not directly acting on the state ω. The transfer function to system states

$$(sI - A)^{-1} \begin{bmatrix} 0 \\ b_2 \\ b_3 \end{bmatrix} = \frac{1}{p(s)} \begin{bmatrix} (s + a_{33})b_2 - a_{23}b_3 \\ s(s + a_{33})b_2 - sa_{23}b_3 \\ -a_{31}b_2 + (s^2 + a_{21})b_3 \end{bmatrix},$$

is a combination of (3.19) and (3.23) where from (3.11)

$$b_2 = \frac{\beta_3 E_q'^*}{MV_3^*} \cos\varepsilon_3^*, \text{ and } b_3 = \frac{\beta_3}{T_{do}' b_\Delta V_3^*} \left(\sin\varepsilon_3^* - b_3^{\text{AVR}}\right). \tag{3.24}$$

The term b_3^{AVR} in (3.24) is introduced by the AVR due to direct feed-through between the input bus and the machine terminal as shown in (3.13).

Remark 3.3 The input matrix elements, b_2 and b_3 in (3.24), are not to be confused with susceptance.

From calculations in Appendix 3.A we find that

$$b_3^{\text{AVR}} = \frac{b_\Delta K_A}{\beta_3 \hat{b}_{13}} \sin\varepsilon_{13}^*, \tag{3.25}$$

where $\hat{b}_{13} = b_{11}' + \frac{b_{11}' b_{3N}}{b_{13}} + b_{3N}$ and $\varepsilon_{13}^* = \theta_1^* - \theta_3^*$. Thus

$$b_3 = \frac{\beta_3}{T_{do}' b_\Delta V_3^*} \left(\sin\varepsilon_3^* - \frac{b_\Delta K_A}{\beta_3 \hat{b}_{13}} \sin\varepsilon_{13}^*\right). \tag{3.26}$$

The transfer function $G_{\theta_2, P_3}(s)$ becomes

$$G_{\theta_2, P_3}(s) = \frac{c_1\big((s + a_{33})b_2 - a_{23}b_3\big) + c_3\big((s^2 + a_{21})b_3 - a_{31}b_2\big) + dp(s)}{p(s)}, \tag{3.27}$$

where from (3.16)

$$c_1 = \beta_2 \frac{E_q'^*}{V_2^*} \cos\varepsilon_2^*, \quad c_3 = \beta_2 \frac{1}{V_2^*} \sin\varepsilon_2^*, \tag{3.28}$$

and from Appendix 3.A, the direct feed-through term

$$d = \frac{\cos\varepsilon_{23}^*}{\hat{b}_{23} V_2^* V_3^*}. \tag{3.29}$$

Substituting (3.18) in (3.27), the zero polynomial of $G_{\theta_2, P_3}(s)$ becomes

$$\begin{aligned} s^3 d + s^2(da_{33} + c_3 b_3) + s(da_{21} + c_1 b_2) + da_{21}a_{33} - da_{23}a_{31} \\ + c_1 a_{33} b_2 - c_1 a_{23} b_3 + c_3 a_{21} b_3 - c_3 a_{31} b_2, \end{aligned} \tag{3.30}$$

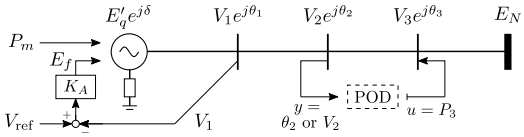

Figure 3.5: SMIB model with POD controller.

which similar to (3.18), for reasonable load angles and large K_A, is stable if

$$(c_3 b_2 + d a_{23})(c_1 b_3 + d a_{31}) > 0. \tag{3.31}$$

Under Assumption 3.1, all load angles have the same sign, so (3.31) reduces to

$$\sin \delta^* (c_1 b_3 + d a_{31}) > 0. \tag{3.32}$$

Combining (3.26) with (3.28),

$$c_1 b_3 = \beta_2 \frac{E'^*_q}{V^*_2} \cos \varepsilon^*_2 \frac{1}{T'_{do} V^*_3} \left(\frac{\beta_3}{b_\Delta} \sin \varepsilon^*_3 - \frac{K_A}{\hat{b}_{13}} \sin \varepsilon^*_{13} \right) \tag{3.33}$$

and (3.15) with (3.29),

$$d a_{31} = \frac{\cos \varepsilon^*_{23}}{\hat{b}_{23} V^*_2 V^*_3} \left(\frac{b_\Sigma}{T'_{do} b_\Delta} E_N \sin \delta^* - \frac{K_A}{T'_{do}} \beta_1 E'^*_q \sin \varepsilon^*_1 \right).$$

It now follows that if (3.17) is fulfilled, then $G_{\theta_2, P_3}(s)$ is minimum phase. Conditions (3.17) and (3.32) are similar but with an extra term from (3.33) that relaxes the condition in (3.32) as long as $|\beta_3 \sin \varepsilon^*_3 / b_\Delta - K_A \sin \varepsilon^*_{13} / \hat{b}_{13}| > 0$, which holds true for $\varepsilon^*_{13} \operatorname{sgn}(\delta^*) < 0$ and for small $|\varepsilon^*_{13}| \ll |\varepsilon^*_3|$. The system can therefore be minimum phase even if it is unstable.

Remark 3.4 The zero of interest in $G_{\theta_2, P_3}(s)$ is a complex conjugated zero pair associated with the electromechanical dynamics of the rotor. The undamped frequency of the electromechanical mode (3.22) is $\Omega = \sqrt{b_\Sigma E'^*_q E_N \cos \delta^* / M}$. Assuming that interaction between the electromechanical and voltage dynamics can be neglected, i.e. if we have low load angles and no AVR, then the electromechanical zero pair is given by, $\pm j \sqrt{a_{21} + c_1 b_2 / d}$ assuming that $E'_q \approx E_N$, $\varepsilon^*_2 \approx \varepsilon^*_3$, and $\cos \delta^* \approx \cos \varepsilon^*_2 \cos \varepsilon^*_3$ then

$$\operatorname{Im} q^{(\theta_2, P_3)}_{1,2} \approx \pm \sqrt{\frac{b'_{12}}{M} E'^{*2}_q \cos \delta^*}, \quad \text{where} \quad \left| q^{(\theta_2, P_3)}_{1,2} \right| \geq \Omega.$$

The closer the control and measurement are to the machine node, the faster the zero. The mode is unobservable at the infinite bus, where $b'_{12} = b_\Sigma$.

3.2.6 Active Power Injection and Voltage Measurement

Consider active power injections as in Section 3.2.5, but with voltage amplitude at a network node as the measured output. The zero polynomial in the transfer function from P_3 to V_2 will be the same as (3.30) but with

$$c_1' = -\beta_2 E_q'^* \sin\varepsilon_2^*, \quad c_3' = \beta_2 \cos\varepsilon_2^*, \tag{3.34}$$

and direct feed-through term

$$d' = \frac{\sin\varepsilon_{23}^*}{\hat{b}_{23} V_3^*}. \tag{3.35}$$

Here the step from (3.31) to (3.32) is no longer valid. To analyze the presence of NMP zeros, we first make the following assumptions.

Assumption 3.2 ($\boldsymbol{\theta_2 = \theta_3}$) Control and measurement occur at the same bus. Therefore, the direct term (3.35) is zero.

The zero polynomial of $G_{V_2,P_3}(s)$ become

$$s^2 c_3' b_3 + s c_1' b_2 + c_1'(a_{33} b_2 - a_{23} b_3) + c_3'(a_{21} b_3 - a_{31} b_2),$$

which divided by $c_3' b_3$ gives us the zero polynomial

$$s^2 + s\alpha_1 + \alpha_2. \tag{3.36}$$

Assumption 3.3 ($\boldsymbol{\theta_1 = \theta_2 = \theta_3}$) Control and measurement both occur at the machine terminal.

Substituting (3.24), (3.26) and (3.34) in (3.36) we find that

$$\alpha_1 = -\frac{E_q'^{*2} T_{do}' b_\Delta \sin\varepsilon_2^* \cos\varepsilon_3^*}{M \cos\varepsilon_2^* \left(\sin\varepsilon_3^* - \frac{b_\Delta K_A}{\beta_3 \hat{b}_{13}} \sin\varepsilon_{13}^*\right)} = -\frac{E_q'^{*2} T_{do}' b_\Delta}{M}$$

where the 2nd equality follows due to Assumption 3.3. As shown in Appendix 3.B this also mean that

$$\alpha_2 \approx -\frac{E_q'^{*2}(b_\Sigma + b_\Delta)}{M}.$$

Assumption 3.4 ($\boldsymbol{|\alpha_1| \gg |\alpha_2|}$) With parameters in p.u. it is reasonable that $T_{do}' \approx 10\,\mathrm{s}$ and that $b_\Delta > b_\Sigma$ [25]. Therefore, α_1 dominates α_2 in (3.36).

Under Assumption 3.4, the transfer function $G_{V_1,P_1}(s)$ have an open-loop NMP zero at $-\alpha_1$. Note also that the undamped frequency of the electromechanical mode

$$\Omega = \sqrt{\frac{b_\Sigma}{M} E_q'^* E_N \cos\delta^*} \ll \frac{E_q'^{*2} T_{do}' b_\Delta}{M}. \tag{3.37}$$

Thus, the NMP zero does not indicate any damping control limitations. If we relax Assumption 3.3 but still assume that α_1 dominates α_2, then $G_{V_i,P_i}(s)$, $i = 1, 2, 3$, has an open-loop zero

$$q^{(V_i,P_i)} \approx \frac{E_q'^{*2} T_{do}' b_\Delta \sin \varepsilon_i^*}{M\left(\sin \varepsilon_i^* - \frac{b_\Delta K_A}{\beta_i \tilde{b}_{1i}} \sin \varepsilon_{1i}^*\right)}. \tag{3.38}$$

Remark 3.5 If $\varepsilon_{1i}^* \operatorname{sgn}(\delta^*) < 0$ the NMP zero moves towards the origin. This may limit damping control design. If $\varepsilon_{1i}^* \operatorname{sgn}(\delta^*) > 0$ the zero moves further into the right half-plane and eventually crosses over into the LHP where it goes towards the origin. Typically however, $|\varepsilon_i^*| > |\varepsilon_{1i}^*| \approx 0$ and thus (3.38) is insensitive to both AVR and the control bus location.

If we relax Assumption 3.2 and allow $\theta_2 \neq \theta_3$ then $G_{V_2,P_3}(s)$ has an open-loop right half-plane zero

$$q^{(V_2,P_3)} \approx \frac{E_q'^{*2} T_{do}' b_\Delta}{M} \frac{\tan \varepsilon_2^*}{\tan \varepsilon_3^*}. \tag{3.39}$$

Thus if the measurement bus is closer to the machine than the control bus, the NMP zero moves closer to the origin.

3.2.7 Summary

In this section, fundamental control limitations in a SMIB power system have been analyzed by studying the presence of NMP zeros in open-loop transfer functions.

The P-θ transfer function $G_{\theta_2,P_3}(s)$ has a zero pair

$$q_{1,2}^{(\theta_2,P_3)} \approx \sigma \pm j\sqrt{\frac{b_{12}'}{M} E_q'^{*2} \cos \delta^*}.$$

The condition for $\sigma < 0$ is that

$$\left| \frac{T_{do}'}{d} c_1 b_3 + \frac{b_\Sigma}{b_\Delta} E_N \sin \delta^* \right| > \left| K_A \beta_1 E_q'^* \sin \varepsilon_1^* \right|,$$

where $c_1 b_3$ from (3.33) depends on the location of the measurement and control bus respectively. The sign of σ is closely linked to the destabilizing effect that the AVR has on the electromechanical mode. The closer the control and measurement is to the machine node, however, the less sensitive the system is to the effect of the AVR.

The P-V transfer function is less sensitive to the AVR. Its NMP zero (3.39) tells us that control input should preferably be close to the machine node and that the measurement is best located further out in the system. This agrees with [93] where active power controllability and phase angle observability was found most effective far away from mass-weighted electrical midpoint, which for the SMIB model means far away from the infinite bus. On the contrary, reactive power controllability and

voltage observability is shown to be the most effective at the midpoint. However, since the voltage at the infinity bus is assumed fixed, this makes the SMIB model unsuitable for the study of Q-V control, as noted in Remark 3.1.

3.3 Simulation Study

In this section we study the control limitations imposed by zero dynamics using a more detailed power system model implemented in Simulink. The considered SMIB system shown in Figure 3.6 has a 6^{th} order synchronous machine model and fast, but not neglected, exciter dynamics. The model is described in detail in [25, Example 13.2], where it is used to study the effect of AVR and PSS. The machine, representing the aggregation of four synchronous machines, feeds 0.9 p.u. active power into an infinite bus.

3.3.1 Active Power Injection and Phase Angle Measurement

To test the transient and steady-state rotor angle stability, we consider a three phase ground fault at time $t = 1$ s. The fault occurs in the lower circuit close to bus 2 as shown in Figure 3.6. The fault is cleared by disconnecting the affected line at both ends within 0.10 s.

Following the numbers listed in Figures 3.7 to 3.9.

① With constant field voltage, the system fails to maintain synchrony following the fault in Figure 3.7. To enhance the transient stability, AVR is implemented. As seen in Figure 3.8 this moves the poles associated to the voltage dynamics further into the LHP, increasing the synchronizing torque of the machine.

The presence of an extra pole on the real axis in Figure 3.8 stems from the fact that the electrical dynamics of the synchronous machine is represented by a 6^{th} order model.

② Although the AVR achieves initial transient stability the system goes unstable in the second swing in Figure 3.7. This is because the AVR has moved the pole of the electromechanical mode into the right half-plane as seen in Figure 3.8.

To stabilize the system we consider active power injections using local phase angle measurements at buses 2–3 in Figure 3.6.

③ As shown in Section 3.2.5, the presence of NMP zeros are closely linked to the destabilizing effect of the AVR. For nodes closer to the machine, the zeros are shifted further into the LHP. This can be seen in Figure 3.9a where the open-loop zeros are plotted alongside the electromechanical mode.

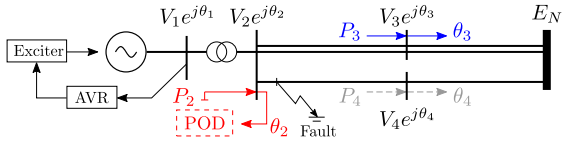

Figure 3.6: SMIB network from [25, Example 13.2].

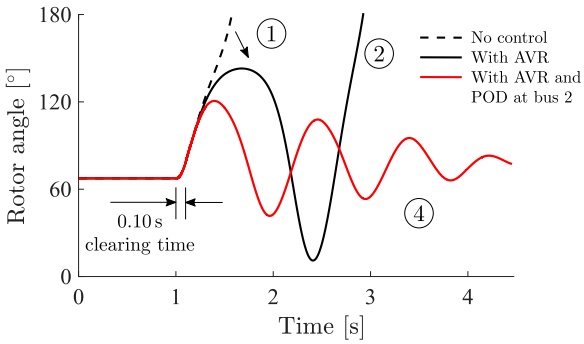

Figure 3.7: Rotor angle response with fault cleared in 0.10 s.

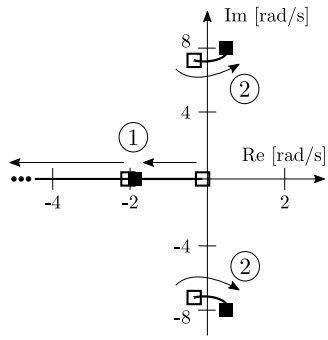

Figure 3.8: Root locus with AVR at bus 1.

We consider a classical POD design using the residue method. Let $P_i = -K(s)\theta_i$, where the feedback controller

$$K(s) = \underbrace{\frac{s+T_1}{s+T_2}}_{\text{Phase compensation}} s \underbrace{\left(\frac{100}{s+100}\right)^2}_{\text{Low-pass}} \underbrace{\frac{s}{s+1/1.5}}_{\text{Wash-out}} k_{\text{POD}}. \tag{3.40}$$

The eigenvalue sensitivity to changes in $K(s)$ is given by the residue [45]

$$R(\lambda) = -\frac{\partial \lambda}{\partial K(s)}. \tag{3.41}$$

The phase compensation in (3.40) is tuned so that $\arg\big(R(\lambda)K(\lambda)\big) = -\pi$ for the electromechanical mode. Thus, feedback moves the eigenvalue in the negative real direction as seen in Figures 3.9b and 3.9c. However, as the gain k_{POD} increases, the trajectory of the closed-loop eigenvalue changes and it eventually approaches the position of the nearby open-loop zero.

④ With POD at bus 2, the control achieves an optimal damping of 13 % as shown in Figure 3.9b. With POD and AVR, the system achieves both transient and steady-state stability as seen in Figure 3.7.

Note that the zero $q^{(\theta_2,P_2)}$ does not move in Figure 3.9b. This is natural since closed-loop zeros in a SISO system cannot be moved by feedback control [112].

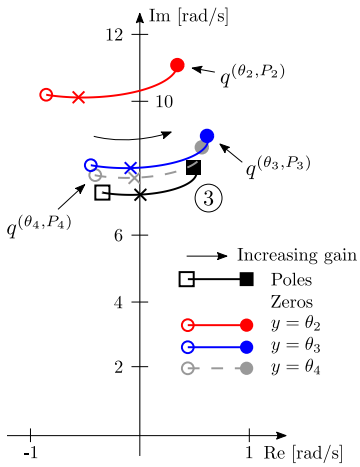

(a) AVR at bus 1.

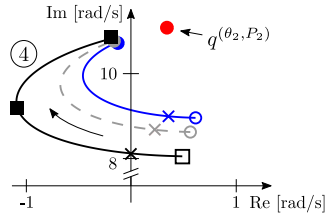

(b) POD at bus 2.

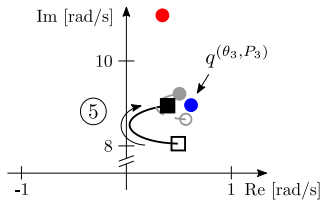

(c) POD at bus 3.

Figure 3.9: Poles and zeros of $G_{\theta_i,P_i}(s)$, $i \in \{2,3,4\}$, with AVR or AVR plus POD control. The "×" marks the feedback gain level where the pole crosses the imaginary axis.

⑤ With an increasing feedback gain, the closed-loop poles approaches the open-loop zeros. In Figure 3.9c we see that this impose a limitation for control at bus 3 that fails to achieve stability for any k_{POD}.

The residue (3.41) is useful to find suitable input-output pairs as it is a measure of the controllability and observability of the considered mode [45]. In general λ can be stabilized as long as $|R(\lambda)| \neq 0$. With nearby NMP zeros however, robustness deteriorates, increasing the sensitivity to changes in the system [112].

3.3.2 Active Power Injection and Voltage Measurement

Consider the system in Figure 3.6 as in Section 3.3.1 but now with voltage as the measured output. According to (3.39), the transfer function $G_{V_i,P_k}(s)$ should have a zero on the positive real axis. The zero should be roughly at the same point for all local measurement loops $G_{V_i,P_i}(s)$. In Figure 3.10 we see that these zeros appear at 50 rad/s which, in agreement with (3.37), is much larger than the electromechanical mode. With external measurement, the NMP zero moves closer to the origin if the measurement is closer to the machine and vice versa. As shown in Section 3.2.6, all NMP zeros are insensitive to the AVR.

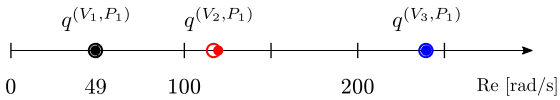

(a) Active power injection at bus 1.

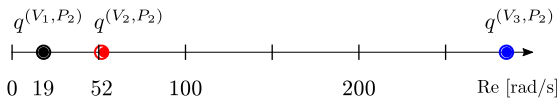

(b) Active power injection at bus 2.

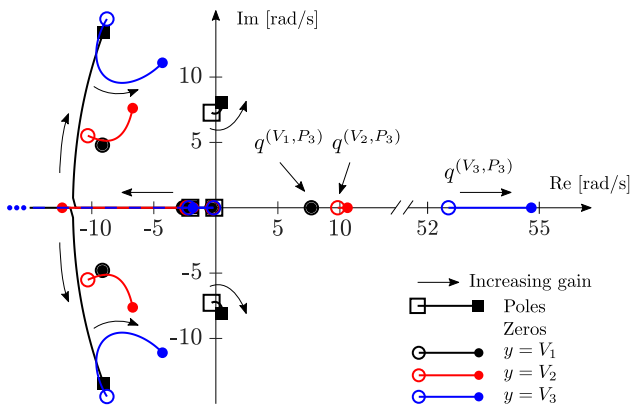

(c) Active power injection at bus 3.

Figure 3.10: Poles and zeros of $G_{V_i,P_k}(s)$, $i \in \{1,2,3\}$, with AVR.

3.4 Summary

The presence of open-loop transfer function zeros have been characterized for different input-output configurations in power systems. It was shown, using a SMIB model, that NMP zeros are closely linked to the destabilizing effect of AVR. Depending on input-output combination chosen for feedback control, these NMP zeros may persist in the system. Right half-plane zeros close to an unstable electromechanical mode was shown to prevent stabilization using feedback control.

The SMIB model have been used since it allows for an analytically tractable solution to the problem. The model detail will of course have an impact on the pole-zero locations of the system. For instance, the approximation from the dynamical AVR model (3.8) to the simple proportional model (3.9) is only accurate if the AVR is fast compared to the electromechanical dynamics. However, reducing the bandwidth of the AVR also means that the intended transient stability improvement will be reduced. So there will still be a trade-off between transient and small-signal stability as described in Section 3.2.2.

Appendix

3.A Direct Feed-Through

The admittance matrix interconnecting network nodes i and k in Figure 3.3 is given by

$$Y_{\theta\theta} = j \begin{bmatrix} -b'_{1i} - b_{ik} & b_{ik} \\ b_{ik} & -b_{ik} - b_{kN} \end{bmatrix},$$

with nodes ordered so that $b'_{1i} \geq b'_{1k}$, i.e., node i is closer to the machine node. By (3.6), the weighted admittance matrix

$$\boldsymbol{Y}_{\theta\theta} = j \begin{bmatrix} (b'_{1i} + b_{ik})V_i^2 & -b_{ik}V_iV_ke^{j\varepsilon_{ik}} \\ -b_{ik}V_iV_ke^{-j\varepsilon_{ik}} & (b_{ik} + b_{kN})V_k^2 \end{bmatrix},$$

where $\varepsilon_{ik} = \theta_i - \theta_k$. With $\boldsymbol{Y}_D =$

$$-\boldsymbol{Y}_{\theta\theta}^{-1} = j\frac{1}{V_i^2V_k^2}\frac{1/b_{ik}}{\hat{b}_{ik}} \begin{bmatrix} (b_{ik} + b_{kN})V_k^2 & b_{ik}V_iV_ke^{j\varepsilon_{ik}} \\ b_{ik}V_iV_ke^{-j\varepsilon_{ik}} & (b'_{1i} + b_{ik})V_i^2 \end{bmatrix},$$

where $\hat{b}_{ik} = b'_{1i} + \frac{b'_{1i}b_{kN}}{b_{ik}} + b_{kN}$, the direct feed-through between the network nodes are then obtained using (3.12).

3.B Zero Polynomial Coefficient

Substituting (3.15), (3.24), (3.26) and (3.34) in (3.36) we find that

$$\begin{aligned}\alpha_2 = \Big(-c'_1a_{23}b_3 + c'_3a_{21}b_3 + c'_1a_{33}b_2 - c'_3a_{31}b_2\Big)\Big/c'_3b_3 = \\ \frac{E_q'^{*2}b_\Sigma}{M}\frac{1}{\cos\varepsilon_2^*\left(\sin\varepsilon_3^* - b_3^{\mathrm{AVR}}\right)}\Bigg(\frac{E_N}{E'^*_q}\sin\delta^*\sin\varepsilon_2^*\left(\sin\varepsilon_3^* - b_3^{\mathrm{AVR}}\right) \\ + \frac{E_N}{E'^*_q}\cos\delta^*\cos\varepsilon_2^*\left(\sin\varepsilon_3^* - b_3^{\mathrm{AVR}}\right) - \frac{b_\Sigma + b_\Delta}{b_\Sigma}\sin\varepsilon_2^*\cos\varepsilon_3^* \\ - \frac{b_\Delta}{b_\Sigma}K_A\beta_1\cos\varepsilon_1^*\sin\varepsilon_2^*\cos\varepsilon_3^* - \frac{E_N}{E'^*_q}\sin\delta^*\cos\varepsilon_2^*\cos\varepsilon_3^* \\ + \frac{b_\Delta}{b_\Sigma}K_A\beta_1\sin\varepsilon_1^*\cos\varepsilon_2^*\cos\varepsilon_3^*\Bigg) \approx -\frac{E_q'^{*2}(b_\Sigma + b_\Delta)}{M},\end{aligned}$$

where from (3.25), $b_3^{\mathrm{AVR}} = \frac{b_\Delta K_A}{\beta_3\hat{b}_{13}}\sin\varepsilon_{13}^*$. Note that all effects from the AVR cancel out due to Assumption 3.3.

Chapter 4

Single-Line HVDC Control Limitations

This chapter considers power oscillation damping (POD) by modulating the active power of a high-voltage direct current (HVDC) transmission line. An analytical study of how the proximity between interarea modal frequencies in two interconnected asynchronous grids puts a fundamental limit to the achievable performance is presented. It is shown that the ratio between the modal frequencies is the sole factor determining the achievable performance. This is of course assuming that the HVDC can provide the desired power and that the ac buses are strong enough to receive the power injections. Since the control cannot exceed rated HVDC power the latter of these points should not be an issue for a properly installed HVDC link. The phenomenon is a physical limitation caused by the two interconnected ac grids, and cannot be circumvented by better control design or by the use of wide-area measurements. To validate the derived limitations, simulations using a wide-area controller tuned to optimize performance in terms of POD are done. The influence of limited system information and unmodeled dynamics is shown on a simplified two-machine model. The analytical result is then tested on a realistic model with two interconnected 32-bus networks. The result shows that the analytical result are useful for assessing the fundamental performance limitations also as networks grow in complexity.

The proximity in frequency of two poorly damped oscillatory modes can be troublesome. It greatly affects the controllability of the interarea modes and therefore impairs the achievable POD from HVDC active power modulation. This *modal interaction* is the main focus of this chapter. In [30] it is shown that HVDC primary frequency control never decreases POD under some simplifying assumptions. This is proven by using a simple proportional droop controller, phase compensated for the HVDC active power actuation lag, with feedback from local frequency measurements at the two HVDC terminals. Such a control allows for efficient sharing of inertia response and primary reserves between the connected systems using only local measurements. In general, dc dynamics are orders of magnitude faster than interarea modes (see Section 2.6.3). For the remainder of this work, a residualized model [120]

will be used, where faster dc dynamics are neglected. Instead, the focus will be on interactions occurring between ac systems interconnected with HVDC.

The main contribution of this chapter is to show how modal interaction limits the achievable POD from HVDC active power modulation. This is done by extending the work of [21, 30, 93]. In our analysis, the well-known controllability Gramian [121, 122] is used to assess the controllability of the system. The Gramian gives a fundamental measure for how hard it is to control the interarea oscillations, independent of control structure.

The remainder of this chapter is organized as follows. In Section 4.1 nonlinear and linear models of the HVDC-interconnected system are defined. In Section 4.2, reduction of the linear model is done along with an energy interpretation. In Section 4.3, controllability analysis of the reduced model is made. In Sections 4.4 and 4.5 a droop controller is synthesized and implemented in simulations to show POD performance and sensitivity. The chapter is summarized in Section 4.6.

4.1 Model of the HVDC-Interconnected System

Consider the HVDC-interconnected system in Figure 4.1. We let the dominant interarea mode in Network 1 (top) and Network 2 (bottom) be represented by two synchronous machines connected by an ac transmission line. The grouping of power system buses into regions that model the dominant slow interarea modes is an analysis method validated by slow coherency theory [44, 123]. The method gives a simplified model that facilitates analysis. It should be noted that fast dynamics inside the regions have been neglected. Because of this, results derived from the reduced-order model need to be validated in more realistic detailed models.

Machines are modeled, using the classical machine model, as a stiff electromotive force behind a transient reactance. Higher-order ac dynamics such as impact from machine damper windings, voltage regulators and system loads, governors etc. are lumped into the damping constant D_{ij}. In addition, transmission is assumed lossless and the electrical distance between machine ij and dc bus i is represented by the reactance X_{ij}, consisting of transient machine reactance, transformers, and transmission lines [25]. Thus, the electromechanical dynamics for network $i \in \{1, 2\}$ is given by the swing equation

$$\begin{aligned} \dot{\delta}_{ij} &= \omega_{ij} \\ M_{ij}\dot{\omega}_{ij} &= \underbrace{P_{m,ij} - P_{\text{load},ij}}_{\Delta P_{ij}} - \underbrace{\frac{V_{ij}V_i}{X_{ij}}\sin(\delta_{ij} - \theta_i)}_{P_{e,ij}} - D_{ij}\omega_{ij} \end{aligned} \tag{4.1}$$

for machines $j \in \{1, 2\}$, where δ_{ij} is the machine busbar-voltage, ω_{ij} represents machine ij's deviation from the nominal frequency ω_{nom}. The constant M_{ij} represents the frequency and pole-pair scaled inertia of each machine.

The difference between the mechanical input power from the machines and the local loads is given by ΔP_{ij}. Since load dynamics are not of interest in the analysis,

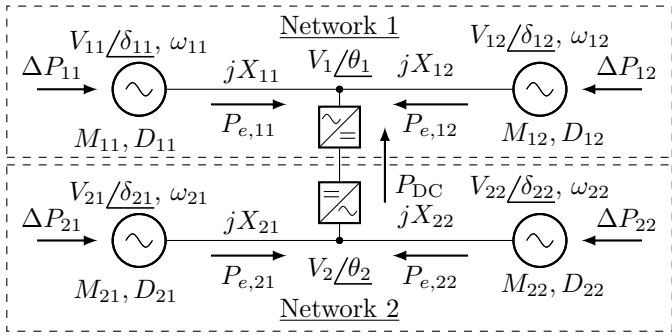

Figure 4.1: The HVDC-interconnected system used to study modal interaction, between two ac networks.

loads are assumed to act directly on generator states. DC busbar-voltage phase angle θ_i is given by the active power

$$P_{\mathrm{DC}} + \sum_{j=1}^{2} \frac{V_{ij} V_i}{X_{ij}} \sin(\delta_{ij} - \theta_i) = 0 \tag{4.2}$$

and reactive power balance

$$Q_{\mathrm{DC}} + \sum_{j=1}^{2} \frac{V_{ij} V_i \cos(\delta_{ij} - \theta_i) - V_i^2}{X_{ij}} = 0 \tag{4.3}$$

where P_{DC} and Q_{DC} is active and reactive power injected at the HVDC terminal. In addition we make the simplifying assumption that machine excitation and reactive power at the HVDC terminal are controlled (using, e.g., a voltage source converter HVDC terminal, a static var compensator, or a variable shunt capacitor bank) so that all buses have the voltage amplitude V for the time frame of interest [30].

Linearization and further simplifications commonly done in small-signal studies of power systems are made next. The second machine is set as phase reference in each network. Without loss of generality: $\delta_{i2} = 0$, $\Delta\delta_i = \delta_{i1} - \delta_{i2}$, and $\Delta\dot{\delta}_i = \omega_{i1} - \omega_{i2}$. Assuming small power flows, with $\Delta P_{ij} \approx 0$, gives small voltage phase-angle differences between buses. This implies that $\cos(\delta_{ij} - \theta) \approx 1$. If we let $Q_{\mathrm{DC}} = 0$ then (4.3) does not play a role in the small-signal dynamics. The assumption of small voltage phase-angle differences also implies $\sin(\delta_{ij} - \theta) \approx \delta_{ij} - \theta$ in (4.1) and, similarly, from (4.2) then approximately

$$\theta_i = \frac{X_{i2}}{X_{\Sigma,i}} \delta + \frac{X_{i1} X_{i2}}{V^2 X_{\Sigma,i}} P_{\mathrm{DC}}$$

where $X_{\Sigma,i} := X_{i1} + X_{i2}$ is the total series impedance in Network i. These simplifi-

cations result in the linear state-space model

$$\begin{aligned} \dot{x}_i &= A_i' x_i + B_i' u \\ y_i &= C_i' x_i \end{aligned} \tag{4.4}$$

with state vector $x_i = [\Delta\delta_i,\ \omega_{i1},\ \omega_{i2}]^T$, input $u = P_{\mathrm{DC}}$, and y some general output.

For the study of POD and modal interaction, additional simplifications are possible without loss of relevant dynamics. This is essential for facilitating the analysis of the HVDC-interconnected system. Only the electromechanical oscillations between the two machines are of interest. Therefore, only frequency in relation to the center of inertia (COI) frequency

$$\omega_{\mathrm{COI},i} = \frac{M_{i1}}{M_{\Sigma,i}}\omega_{i1} + \frac{M_{i2}}{M_{\Sigma,i}}\omega_{i2}$$

where $M_{\Sigma,i} = M_{i1} + M_{i2}$, needs to be considered. We therefore let the output vector be $y_i = [\Delta\delta_i,\ \omega_{i1} - \omega_{\mathrm{COI},i},\ \omega_{i2} - \omega_{\mathrm{COI},i}]^T$. Additionally, we make the following assumption that will let us reduce the system.

Assumption 4.1 (Damping Proportional to Inertia) The machine damping is evenly distributed and proportional to the machine inertia constant (which in turn is proportional to rated power)

$$D_{ij} = D_i \frac{M_{ij}}{M_{\Sigma,i}}$$

such that the machines become scaled versions of each other.

Remark 4.1 Since the mode (corresponding eigenvalue λ) is assumed poorly damped ($|\operatorname{Re}(\lambda)| \ll |\lambda|$) Assumption 4.1 has little effect on model accuracy. This is further discussed in the Section 4.2.

With Assumption 4.1, the system matrices in (4.4) becomes

$$A_i' = \begin{bmatrix} 0 & 1 & -1 \\ \frac{-V^2}{M_{i1}X_{\Sigma,i}} & \frac{-D_i}{M_{\Sigma,i}} & 0 \\ \frac{V^2}{M_{i2}X_{\Sigma,i}} & 0 & \frac{-D_i}{M_{\Sigma,i}} \end{bmatrix},\ B_i' = \begin{bmatrix} 0 \\ \frac{X_{i2}}{M_{i1}X_{\Sigma,i}} \\ \frac{X_{i1}}{M_{i2}X_{\Sigma,i}} \end{bmatrix} \tag{4.5}$$

and since

$$\omega_{i1} - \omega_{\mathrm{COI},i} = \left(1 - \frac{M_{i1}}{M_{\Sigma,i}}\right)\omega_{i1} - \frac{M_{i2}}{M_{\Sigma,i}}\omega_{i2} = \frac{M_{i2}}{M_{\Sigma,i}}\omega_{i1} - \frac{M_{i2}}{M_{\Sigma,i}}\omega_{i2}$$

the output matrix becomes

$$C_i' = \begin{bmatrix} 1 & 0 & 0 \\ 0 & \frac{M_{i2}}{M_{\Sigma,i}} & \frac{-M_{i2}}{M_{\Sigma,i}} \\ 0 & \frac{-M_{i1}}{M_{\Sigma,i}} & \frac{M_{i1}}{M_{\Sigma,i}} \end{bmatrix}. \tag{4.6}$$

4.2 Model Reduction and Energy Interpretation

In this section we discuss how to reduce the state dimension of the model introduced previously, and how to make a useful energy interpretation of the model.

Due to Assumption 4.1, the two machines are linearly scaled versions of each other. Therefore, only machine frequency deviations, scaled by M_{i1} or M_{i2}, around $\omega_{\mathrm{COI},i}$ are observable in y_i. Hence, only the difference $\omega_{i1} - \omega_{i2}$ (and not the absolute states) is observable. Thus, (4.4) to (4.6) is not a minimal realization but can be reduced further without losing additional control information [121].

4.2.1 Model Reduction

Let z_i be a reduced state vector that represents the observable subspace of (4.4) to (4.6) given by $z_i = P^\dagger x_i$. The transformation matrix P is time invariant and $P^\dagger$ is its Moore-Penrose pseudoinverse. A minimal (observable and controllable) realization of (4.4) to (4.6) is then

$$\begin{aligned} \dot{z}_i &= A_i z_i + B_i u \\ y_i &= C_i z_i \end{aligned} \tag{4.7}$$

where $A_i = P^\dagger A_i' P$, $B_i = P^\dagger B_i'$ and $C_i = C_i' P$ [121, Theorem 10.13].

For the analysis, it is convenient to let the reduced state vector $z_i = [\Delta\delta_i,\, \Delta\omega_i]^T$ where $\Delta\omega_i = \omega_{i1} - \omega_{i2}$. This is achieved by choosing

$$P^\dagger := \begin{bmatrix} 1 & 0 & 0 \\ 0 & 1 & -1 \end{bmatrix}. \tag{4.8}$$

The matrices in (4.7) thus become

$$A_i = \begin{bmatrix} 0 & 1 \\ \frac{-V^2 M_{\Sigma,i}}{M_{i1} M_{i2} X_{\Sigma,i}} & \frac{-D_i}{M_{\Sigma,i}} \end{bmatrix}, \quad B_i = \begin{bmatrix} 0 \\ \frac{M_{i2} X_{i2} - M_{i1} X_{i1}}{M_{i1} M_{i2} X_{\Sigma,i}} \end{bmatrix}, \quad C_i = \begin{bmatrix} 1 & 0 \\ 0 & \frac{M_{i2}}{M_{\Sigma,i}} \\ 0 & \frac{-M_{i1}}{M_{\Sigma,i}} \end{bmatrix} \tag{4.9}$$

where the undamped frequency of the interarea mode is given by

$$\Omega_i = \sqrt{\frac{V^2 M_{\Sigma,i}}{M_{i1} M_{i2} X_{\Sigma,i}}}. \tag{4.10}$$

This construction can be compared to the classical two-body problem of Newtonian mechanics [124]. From (4.9) it is easily seen that the interarea mode is controllable using active power injection, as long the HVDC terminal is not located at the mass-scaled electrical midpoint between the two machines, i.e., as long as $M_{i1} X_{i1} \neq M_{i2} X_{i2}$. This result is also found in [21, 30, 93]. To simplify the analysis further,

consider the special case $M_{i1} = M_{i2} = M_i$, which we refer to as a *symmetric network*. The system matrices become

$$A_i = \begin{bmatrix} 0 & 1 \\ \frac{-2V^2}{M_i X_{\Sigma,i}} & \frac{-D_i}{2M_i} \end{bmatrix}, \quad B_i = \begin{bmatrix} 0 \\ \frac{X_{B,i}}{M_i} \end{bmatrix}, \quad C_i = \begin{bmatrix} 1 & 0 \\ 0 & 0.5 \\ 0 & -0.5 \end{bmatrix}, \tag{4.11}$$

where $X_{B,i} = \frac{X_{i2} - X_{i1}}{X_{\Sigma,i}} \in [-1, 1]$ is the electric position of the dc bus in network i w.r.t. line impedance.

For system (4.9) to be a minimal realization of (4.4) it is required that the machines are scaled versions of each other according to Assumption 4.1. In the following example we study the effects of this assumption.

Example 4.1 (Consequence of Assumption 4.1) Consider a nominal network G_0 where Assumption 4.1 holds and a perturbed network G where there is no damping at the second machine.

- *Nominal network*, G_0. The nominal network is defined with $f_{\text{nom}} = 50\,\text{Hz}$, unit voltage, unit line impedance and an undamped modal frequency set to $\Omega_i/2\pi = 0.5\,\text{Hz}$. From (4.10), $\Omega_i = \sqrt{2/M_i}$ and thus $M_i = 2/\Omega_i^2$. The damping constant D_i at both machines are chosen such that the 0.5 Hz interarea mode in the nominal network have a damping ratio of 8 % as shown in Appendix 4.F.
- *Perturbed network*, G. In the perturbed network we let system damping be concentrated in machine 1. That is, let $D_{i1} = 2D_i$ and $D_{i2} = 0$.

In the reduced model (4.9) original state variables $[\Delta\delta_i,\, \omega_{i1},\, \omega_{i1}]^T$ are approximated to $[\Delta\delta_i,\, \Delta\omega_i = \omega_{i1} - \omega_{i1}]^T$. This reduction requires that Assumption 4.1 holds. In Figure 4.2 we study the accuracy of this reduction. The bode plot of the transfer function from input u to output $\Delta\omega_i$ are shown for the nominal and perturbed system respectively.

In Figure 4.2a we consider a system with $X_{B_i} = 0.5$, i.e., the dc bus is located close to machine 1. Here, the phase angle differs between G and G_0 at lower frequencies. In Figure 4.2b we consider a system with $X_{B_i} = -0.5$, thus the dc bus is closer to the machine without damping. In this case, the amplitude of $|G|$ and $|G_0|$ differ at lower frequencies. However, for both of these cases, the system gain $|G|$ and $|G_0|$ is already comparatively low at these frequencies. We see that in the relevant bandwidth window around the modal frequency, perturbations have little effect on the system response. Thus, the proposed model reduction is fairly accurate also when Assumption 4.1 does not hold.

Remark 4.2 In modal analysis of power systems, it is common practice to describe system dynamics in terms of eigenvalues [25, 125] as shown in Appendix 4.A. The resulting system matrix is diagonal and thus the dynamics of the system states are

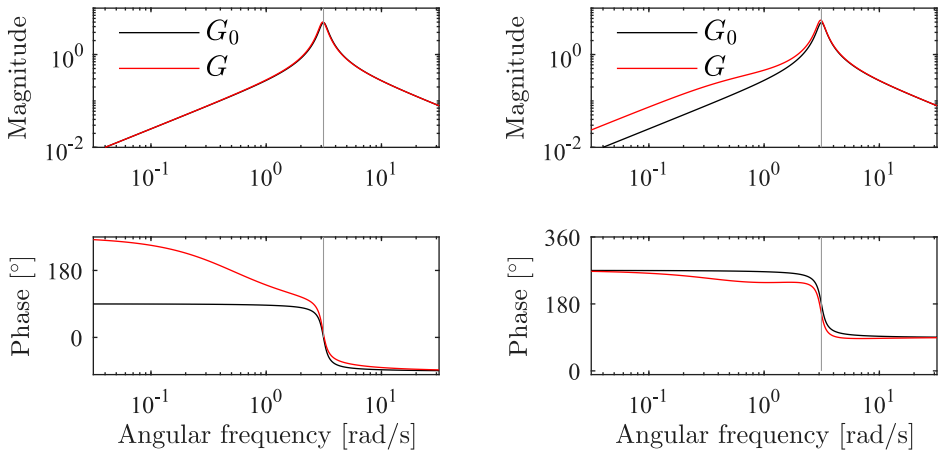

(a) DC bus location $X_B = 0.5$

(b) DC bus location $X_B = -0.5$

Figure 4.2: Transfer function of nominal (G_0) and perturbed system (G) from input u to output $\Delta\omega_i$ considering two different dc bus locations. Around the modal frequency 0.5 Hz (gray line) the system perturbation has little effect.

decoupled from each other. Therefore, the system can easily be reduced. However, as the representation result in complex valued system matrices it is not useful for the purpose of our analysis. As shown in Appendix 4.C, a diagonal modal matrix can be transformed into a real Jordan form [126]. Here the system is represented in block diagonal form where complex conjugated eigenvalue pairs $\lambda_l = -\gamma_l \pm j\omega_{e,l}$, corresponding to modes of oscillation, are represented by real 2×2 blocks on the form

$$\begin{bmatrix} \gamma_l & \omega_{e,l} \\ -\omega_{e,l} & \gamma_l \end{bmatrix}.$$

If Assumption 4.1 holds then transformation with (4.8) also preserves the dynamics of the interarea oscillations. This, since the transformation matrix is a linear combination of the relevant eigenvectors. The benefit of the proposed reduction method is that the states of the new model reflects properties of the original system that are easy to study and interpret. If the assumption does not hold, the system can still be reduced but the new states are going to be a combination of original state variables, thus making further analysis cumbersome.

4.2.2 Energy Interpretation

In this section we derive an expression for the *oscillatory energy* stored in Network i at state $\left[\Delta\delta_i,\, \Delta\omega_i\right]^T = \left[\delta_{0,i},\, \omega_{0,i}\right]^T$.

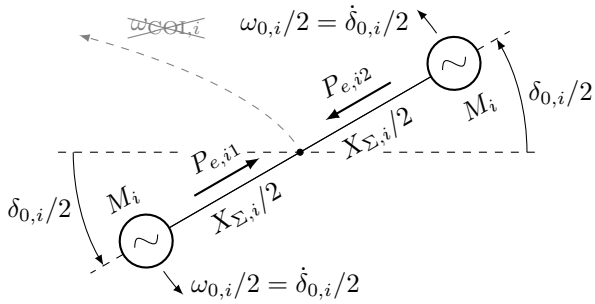

Figure 4.3: Visualization of a reduced two-machine ac network.

Interarea oscillations (or power oscillations) are electric power being transfered between machines. Consider the unforced, undamped symmetrical ac network shown in Figure 4.3, where the swing equation (4.1) gives

$$M_i \dot{\omega}_{0,i} = -2P_{e,i1} = -\frac{V^2}{X_{\Sigma,i}/2}\delta_{0,i}. \tag{4.12}$$

Work is the conversion between mechanical kinetic energy and electrical potential energy. Hence, power oscillations are an electromechanical phenomenon. Multiplying both sides in (4.12) by $d\Delta\delta_i/dt = \Delta\omega_i$ and deriving work done to both machines as the integral of power over time, t, we get

$$2\int M\omega_{0,i}\frac{d\omega_{0,i}}{dt}dt = -2\int \frac{V^2}{X_{\Sigma,i}/2}\delta_{i,0}\frac{d\delta_{0,i}}{dt}dt \tag{4.13}$$

or

$$\frac{2V^2}{X_{\Sigma,i}}\delta_{0,i}^2 + M\omega_{0,i}^2 = E_{\mathrm{p},i} + E_{\mathrm{k},i} =: E_{0,i} \tag{4.14}$$

where, since we are dealing with a conservative system, the sum of kinetic $E_{\mathrm{k},i} = M_i\omega_{0,i}^2$ and potential energy $E_{\mathrm{p},i} = \frac{2V^2}{X_{\Sigma,i}}\delta_{0,i}^2$ is constant over time [124]. This sum is referred to as the oscillatory energy $E_{0,i}$, which is the quantity we are interested in controlling using active power injection at the dc terminal.

4.2.3 Modeling the HVDC-Interconnected System

Using (4.7) together with (4.9) or (4.11), the HVDC-interconnected system in Figure 4.1 can now be described by

$$\dot{z} := \begin{bmatrix}\dot{z}_1\\ \dot{z}_2\end{bmatrix} = \begin{bmatrix}A_1 & 0\\ 0 & A_2\end{bmatrix}\begin{bmatrix}z_1\\ z_2\end{bmatrix} + \begin{bmatrix}B_1\\ -B_2\end{bmatrix}u =: Az + Bu. \tag{4.15}$$

4.3 Controllability Analysis

In this section we introduce some mathematical tool that are commonly known in control theory. These will be useful for the analysis of the system.

Consider a n-dimensional linear time-invariant (LTI) system. As long as the controllability matrix

$$\mathcal{C} = \begin{bmatrix} B\, AB\, A^2B \cdots A^{n-1}B \end{bmatrix} \tag{4.16}$$

has full rank, the system is controllable.

Theorem 4.1 (Controllability Gramian [122]) *The LTI system* (4.15) *is controllable if and only if the controllability Gramian*

$$W_C = \int_0^T e^{At} B B^T e^{A^T t} dt. \tag{4.17}$$

is nonsingular for any $T > 0$.

Theorem 4.1 is equivalent to the controllability matrix (4.16) having full rank [122, Theorem 6.1]. However, the controllability Gramian has more uses as it gives us information on how hard the system is to control.

If damping constants D_1, $D_2 > 0$ then A is strictly Hurwitz, i.e., its eigenvalues have strictly negative real part. The controllability Gramian W_C over infinite time, $T = \infty$, can then be obtained by solving a Lyapunov equation.

Theorem 4.2 (Controllability Gramian $t \to \infty$ [122]) *If A is strictly Hurwitz, then the controllability Gramian, with $t \to \infty$, is given by the unique solution to the Lyapunov equation*

$$AW_C + W_C A^T + BB^T = 0. \tag{4.18}$$

The controllability Gramian gives us the minimal energy control, or *control effort*, required to transfer the system from one state to another.

Theorem 4.3 (Control Effort [122]) *The control effort required to transfer an initially disturbed system state, $z(t = 0) = z_0$, to the origin, $\lim_{t\to\infty} z(t) = 0$, is given by*

$$\|u\|_2^2 = z_0^T W_C^{-1} z_0$$

where $u \in L_2[0,\ \infty)$.

Definition 4.1 (Unitary Matrix [127]) A (complex) matrix $\mathcal{V}$ is unitary if its complex conjugate transpose

$$\mathcal{V}^H = \mathcal{V}^{-1}.$$

Definition 4.2 (Singular Value Decomposition (SVD) [127]) The SVD of a matrix $W \in \mathbb{C}^{n\times n}$ is based on the existence of unitary matrices $\mathcal{U}, \mathcal{V} \in \mathbb{C}^{n\times n}$ such that

$$W = \mathcal{U}\Sigma\mathcal{V}^H$$

where

$$\Sigma = \mathrm{diag}(\sigma_1, \sigma_2, \dots \sigma_n)$$

and

$$\bar{\sigma} := \sigma_1 \geq \sigma_2 \geq \cdots \geq \sigma_n =: \underline{\sigma}$$

are the singular values of W. SVD is also applicable to non-square matrices.

Since W_C is created from the square of two matrices (4.17) $W_C \geq 0$ and $W_C = W_C^T$. In addition W_C and thus $\mathcal{U}$ and $\mathcal{V}$ are real. This means that

$$W_C = \mathcal{U}\Sigma\mathcal{V}^T \Leftrightarrow W_C^T = \left(\mathcal{U}\Sigma\mathcal{V}^T\right)^T = \mathcal{V}\Sigma\mathcal{U}^T.$$

Consequently $\mathcal{V} = \mathcal{U}$, and $\sigma_l(W_C)$ is the same as the eigenvalue $\lambda_l(W_C)$.

With $z_l := v_l^T z_0$, where singular vectors v_l are the columns in $\mathcal{V}$, it follows that the control effort can be computed as

$$\|u\|_2^2 = z_0^T \mathcal{V}\Sigma^{-1}\mathcal{V}^T z_0 = \sum_{l=1}^{n} \frac{z_l^2}{\sigma_l}. \tag{4.19}$$

4.3.1 Assessing Controllability of an Isolated AC Network

Consider the single ac network i in (4.11) with $D_i > 0$, controlled with an arbitrary active power injection at the dc bus from a source with negligible dynamics, e.g., a large battery storage. By Theorem 4.2, the controllability Gramian for the two-machine network is (see Appendix 4.E)

$$W_{C,i} = \frac{X_{B,i}^2}{D_i} \begin{bmatrix} \frac{X_{\Sigma,i}}{2V^2} & 0 \\ 0 & \frac{1}{M_i} \end{bmatrix}. \tag{4.20}$$

According to (4.19), the control effort required to transfer the system from an initially disturbed state to zero is given by

$$\|u\|_2^2 = z_{0,i}^T W_{C,i}^{-1} z_{0,i} = \frac{D_i}{X_{B,i}^2}\frac{2V^2}{X_{\Sigma,i}}\delta_{0,i}^2 + \frac{D_i}{X_{B,i}^2} M_i \omega_{0,i}^2. \tag{4.21}$$

Expressing (4.21) in the terms of oscillatory energy (4.14), we get

$$\|u_i\|_2^2 = \frac{D_i}{X_{B,i}^2}(E_{\mathrm{p},i} + E_{\mathrm{k},i}) = \frac{D_i}{X_{B,i}^2} E_{0,i}. \tag{4.22}$$

Here it is seen that control effort is inversely proportional to the squared (mass-weighted) electric position, $X_{B,i}^2$, of the dc terminal. This agrees with the findings of [21, 30, 93].

Remark 4.3 If we let $D_i = 0$, then the finite-time controllability Gramian (Theorem 4.1) gives us an intuitive interpretation of the required control effort (Theorem 4.3). The time, T, is a measure of the control aggressiveness.

For large T, we have (see Appendix 4.D)

$$W_{C,i} \approx X_{B,i}^2 \frac{T}{2M_i} \begin{bmatrix} \frac{X_{\Sigma,i}}{2V^2} & 0 \\ 0 & \frac{1}{M_i} \end{bmatrix}$$

which is the same as (4.20) with

$$D_i = \frac{2M_i}{T}.$$

Thus, (4.18) is considered a good controllability estimate with $D_i > 0$ representing the control aggressiveness.

The finite-time controllability Gramian becomes impractical as the dimension of the system increases. Therefore, Theorem 4.2 will be used to analyze the HVDC-interconnected system.

4.3.2 Computing the Gramian W_C

The controllability Gramian (4.18) for the HVDC-interconnected system, computed using Kronecker products [128] (see Appendix 4.E) yields

$$W_C = \begin{bmatrix} a_1 & -\alpha & 0 & -\gamma \\ -\alpha & a_2 & \gamma & 0 \\ 0 & \gamma & b_1 & -\beta \\ -\gamma & 0 & -\beta & b_2 \end{bmatrix} \tag{4.23}$$

with state variables ordered

$$z = \left[\Delta\delta_1,\, \Delta\delta_2,\, \Delta\omega_1,\, \Delta\omega_2\right].$$

The elements of (4.23) depend on the parameters of Network 1 and 2. The main factor determining controllability is the undamped modal frequencies Ω_1 and Ω_2 in (4.10).

Assumption 4.2 (Identical Networks, Except for the Inertia Constant) For the following analysis we choose $M := M_1$, $M_2 := M + \epsilon$ and let the systems be identical in all other aspects, i.e., let $D_1 = D_2 =: D$ and $X_{\Sigma,1} = X_{\Sigma,2} =: X_\Sigma$. Note that $\Omega_1 \neq \Omega_2$ if $\epsilon \neq 0$.

The elements of (4.23) are then given by

$$\begin{aligned} a_1 &= a_2 = \frac{X_B^2}{D}\frac{X_\Sigma}{2V^2} =: a \\ b_1 &= \frac{X_B^2}{D}\frac{1}{M} =: b \\ b_2 &= b\frac{M}{M+\epsilon} \\ \alpha &= a\frac{2M+\epsilon}{2M+\epsilon+2c\epsilon^2} \\ \beta &= b\frac{2M}{2M+\epsilon+2c\epsilon^2} \\ \gamma &= \frac{X_B^2}{D^2}\frac{2\epsilon}{2M+\epsilon+2c\epsilon^2} \\ c &= \frac{2V^2}{D^2 X_\Sigma}. \end{aligned} \tag{4.24}$$

Here we note that $\alpha \to a$, $\beta \to b$, $b_2 \to b$, and $\gamma \to 0$, as $\epsilon \to 0$, which make W_C rank deficient. Moreover, the matrix of singular vectors is given by

$$\lim_{\epsilon\to 0} \mathcal{V} = \frac{1}{\sqrt{2}}\begin{bmatrix} 0 & 1 & 0 & 1 \\ 0 & -1 & 0 & 1 \\ 1 & 0 & 1 & 0 \\ -1 & 0 & 1 & 0 \end{bmatrix} \tag{4.25}$$

As can be expected for the control of a multivariable system, *directionality* will have to be considered [115]. With state variables ordered $z = \left[\Delta\delta_1,\, \Delta\delta_2,\, \Delta\omega_1,\, \Delta\omega_2\right]$ we see (according to (4.14)) that the interesting singular vectors corresponding to the least controllable directions represent potential energy, $E_\mathrm{p} := E_{\mathrm{p}1} + E_{\mathrm{p}2}$, $z_0 \in \mathrm{span}(v_4)$; and kinetic energy, $E_\mathrm{k} := E_{\mathrm{k}1} + E_{\mathrm{k}2}$, $z_0 \in \mathrm{span}(v_3)$. Interpreted as oscillatory energy, this becomes $E_0 := E_\mathrm{p} + E_\mathrm{k}$, $z_0 \in \mathrm{span}(v_3, v_4)$.

For small ϵ, networks will have similar modal frequencies, and controllability is going to be greatly affected by system interactions α, β and γ. The two smallest singular values of W_C corresponding to directions v_l with highest required control effort are the most interesting ones. Approximating these gives an analytical estimate of the controllability.

Making a Maclaurin series expansion of matrix elements (4.24) with respect to ϵ (see Appendix 4.G) shows that for small ϵ

$$\left|\frac{d\alpha(\epsilon)}{d\epsilon}\right| < \left|\frac{d\beta(\epsilon)}{d\epsilon}\right| < \left|\frac{db_2(\epsilon)}{d\epsilon}\right| < \left|\frac{d\gamma(\epsilon)}{d\epsilon}\right|.$$

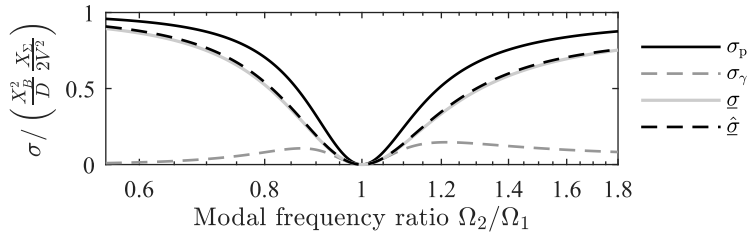

Figure 4.4: Controllability of the two HVDC-interconnected networks in Example 4.2. Estimated singular values σ_γ, σ_{p}, and $\underline{\hat{\sigma}}$ together with numerically calculated $\underline{\sigma}$.

A simplification of W_C, accurate for small ϵ, is then

$$W_C^\gamma := \begin{bmatrix} a & -a & 0 & -\gamma \\ -a & a & \gamma & 0 \\ 0 & \gamma & b & -b \\ -\gamma & 0 & -b & b \end{bmatrix}$$

where the smallest singular value becomes

$$\sigma_\gamma := \min\left(\mathrm{svd}(W_C^\gamma)\right) = \left| b - \sqrt{(b^2+\gamma^2)} \right|. \tag{4.26}$$

Maclaurin series expansion of σ_γ gives the estimate

$$\sigma_\gamma(\epsilon) = \frac{X_B^2}{D} \frac{1}{2D^2 M} \epsilon^2 + \mathcal{O}(\epsilon^3). \tag{4.27}$$

Example 4.2 In Figure 4.4 we let the networks 1 and 2 be defined with $f_{\mathrm{nom}} = 50\,\mathrm{Hz}$, $X_B = 0.5$, unit voltage, unit line impedance and the undamped modal frequency are set to $\Omega_1/2\pi = 0.5\,\mathrm{Hz}$. From (4.10), $\Omega_1 = \sqrt{2/M}$ and thus $M = 2/\Omega_1^2$.

To study how modal interaction affects controllability, the undamped modal frequency in Network 2 is set to $\Omega_2 = \sqrt{2/(M+\epsilon)}$ according to Assumption 4.2. The damping constant D are chosen such that the 0.5 Hz interarea mode in Network 1 have a damping ratio of 8 % as shown in the Appendix 4.F.

As seen in Figure 4.4, the estimate (4.26) is only accurate for small ϵ. For slightly larger ϵ the properties of W_C is dominated by the diagonal blocks

$$W_C^{\mathrm{p}} := \begin{bmatrix} a & -\alpha \\ -\alpha & a \end{bmatrix} \quad \text{and} \quad W_C^{\mathrm{k}} := \begin{bmatrix} b & -\beta \\ -\beta & b_2 \end{bmatrix}$$

in (4.23), where, the smallest singular value

$$\sigma_{\mathrm{p}} := \min\left(\mathrm{svd}(W_C^{\mathrm{p}})\right) = |a - \alpha|$$

together with (4.24) becomes

$$\sigma_{\mathrm{p}}(\epsilon) = \frac{X_B^2}{D}\frac{X_\Sigma}{2V^2}\frac{2c\epsilon^2}{2M+\epsilon+2c\epsilon^2}. \tag{4.28}$$

Maclaurin series expansion of (4.28) yields

$$\sigma_{\mathrm{p}} = \frac{X_B^2}{D}\frac{cX_\Sigma}{2D^2M}\epsilon^2 + \mathcal{O}(\epsilon^3).$$

With $c = \frac{2V^2}{D^2X_\Sigma}$ according to (4.24) (4.28) becomes

$$\sigma_{\mathrm{p}}(\epsilon) \approx \frac{X_B^2}{D}\frac{1}{D^2M}\epsilon^2. \tag{4.29}$$

From (4.27) we have that that for small ϵ

$$\sigma_\gamma(\epsilon) \approx \frac{X_B^2}{D}\frac{1}{2D^2M}\epsilon^2. \tag{4.30}$$

For the second-order term of (4.29) to match that of (4.30), c in (4.28) needs to be replaced by $c/2$, suggesting the estimate

$$\hat{\underline{\sigma}}(\epsilon) = \frac{X_B^2}{D}\frac{X_\Sigma}{2V^2}\frac{c\epsilon^2}{2M+\epsilon+c\epsilon^2}. \tag{4.31}$$

As seen in Figure 4.4 this is a fairly accurate analytical estimate of the real singular value.

4.3.3 Modal Interaction and Energy Interpretation

From (4.10) and Assumption 4.2 it follows that

$$\epsilon = \frac{2V^2}{X_\Sigma\Omega_2^2} - M. \tag{4.32}$$

Substituting (4.32) in (4.31) yields

$$\hat{\underline{\sigma}}(\epsilon) = \frac{2V^2}{X_\Sigma}\frac{D}{X_B^2}\left(1 + D^2\frac{1+\Omega_1^2/\Omega_2^2}{\frac{2V^2M}{X_\Sigma}(1-\Omega_1^2/\Omega_2^2)^2}\right).$$

The control effort required for an initial disturbed state, $z_0 \in \mathrm{span}(v_4)$ and $E_{\mathrm{p}} = v_4^T\frac{2V^2}{X_\Sigma}v_4$ becomes

$$\|u\|_2^2 \approx E_{\mathrm{p}}\frac{D}{X_B^2}\left(1 + D^2\frac{1+\Omega_1^2/\Omega_2^2}{\frac{2V^2M}{X_\Sigma}(1-\Omega_1^2/\Omega_2^2)^2}\right) \tag{4.33}$$

However, as implied by (4.22) and (4.25), (4.33) holds for any $z_0 \in \text{span}(v_3, v_4)$ thus E_p can be replaced by E_0. This allows us to express the worst-case required control effort due to modal interaction between the HVDC-interconnected ac networks as

$$\|u_D\|_2^2 := E_0 \frac{D}{X_B^2} \left(1 + D^2 \frac{1 + \Omega_1^2/\Omega_2^2}{\frac{2V^2M}{X_\Sigma}(1 - \Omega_1^2/\Omega_2^2)^2} \right). \tag{4.34}$$

The subscript D indicates that the controllability Gramian is calculated using Theorem 4.2 and thus depends on the damping constant.

Remark 4.4 For differences in the HVDC-interconnected networks parameters, some adjustments to (4.34) is needed to get an accurate estimate (see Appendix 4.H). This is however left out here for the sake of readability.

In Figure 4.5 the estimate (4.34) is compared with numerical results using a finite-time controllability Gramian (4.17) for an undamped system

$$\|u_T\|_2^2 := z_0^T \left(\int_0^T e^{At} B B^T e^{A^T t} dt \right)^{-1} z_0 \tag{4.35}$$

where $z_0 \in \text{span}(v_3, v_4)$ and we let $T \propto 1/D$ used in (4.34). For the graphical comparison in Figure 4.5, the measures (4.34) and (4.35) are normalized as

$$\|\bar{u}_D\|_2 := \left(1 + D^2 \frac{1 + \Omega_1^2/\Omega_2^2}{\frac{2V^2M}{X_\Sigma}(1 - \Omega_1^2/\Omega_2^2)^2} \right) \tag{4.36}$$

and

$$\|\bar{u}_T\|_2 := \sqrt{\frac{\|u_T\|_2^2}{\|u_{T,1}\|_2^2 + \|u_{T,2}\|_2^2}} \tag{4.37}$$

where $\|u_{T,1}\|_2^2$ and $\|u_{T,2}\|_2^2$ are the corresponding finite-time minimal control effort for Network 1 and Network 2, respectively.

Remark 4.5 In Figure 4.5 it is shown how the modal interaction puts a limit to how aggressive the control action can be. As for a single ac network (see Remark 4.3) an inverse relation between D and T is seen. This indicates that D is a reasonable representation of control aggressiveness also for the interconnected system.

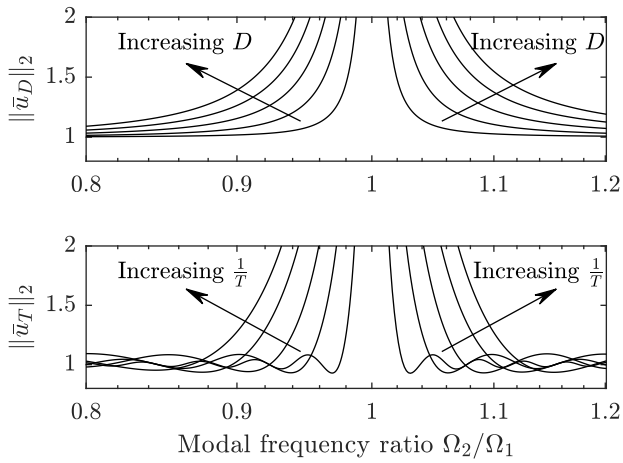

Figure 4.5: The normalized minimal energy control calculated using (4.36)(top) with D chosen to give damping factor $\zeta = \{2, 4, 6, 8, 10\,\%\}$ and (4.37) (bottom) with no inherent damping and $T = 1/D$. It follows that a more aggressive control comes at the cost of increased sensitivity to modal interaction.

4.4 Control Synthesis

As seen in Section 2.2, oscillatory instability is caused by a lack of damping torque. In this section, a controller designed to optimize achievable damping torque by maximizing the minimal system damping ratio is proposed.

First consider an individual network

$$\dot{z}_i \begin{bmatrix} 0 & 1 \\ \frac{-2V^2}{M_i X_{\Sigma,i}} & \frac{-D_i}{2M_i} \end{bmatrix} z_i + \begin{bmatrix} 0 \\ \frac{X_{B,i}}{M_i} \end{bmatrix} u.$$

With $u = -K_i \Delta\omega_i,\ K_i > 0$ we see that damping torque is improved as the complex eigenvalue pair is moved left in the complex plane [93]. With an increasing gain K_i system performance in terms of POD is improved if controlled from a source with negligible dynamics, e.g., a large battery storage. However, as shown in Section 4.3, modal interaction will put a limit to achievable POD performance in the HVDC-interconnected system.

Consider the HVDC-interconnected system depicted in Figure 4.1. The input $u = P_{\mathrm{DC}}$ is controlled with proportional feedback. Neglecting the HVDC actuation lag, the following control law is used:

$$u = P^0_{\mathrm{DC}} - Ky. \tag{4.38}$$

Here we propose the output signal

$$y = \begin{bmatrix} \Delta\omega_1 \\ \Delta\omega_2 \end{bmatrix} := \begin{bmatrix} \omega_{11} - \omega_{12} \\ \omega_{21} - \omega_{22} \end{bmatrix} \tag{4.39}$$

to increase the damping torque and to target the oscillatory energy in each system. For simplicity a proportional droop controller, $K = \begin{bmatrix} K_1, -K_2 \end{bmatrix}$ is considered.

Let λ_l, $l \in \{1, \ldots, n\}$ be the eigenvalues of the closed-loop system

$$\dot{z} = Az - BKy. \tag{4.40}$$

The damping ratio of the modes is given by

$$\zeta_l = -\operatorname{Re}(\lambda_l)/|\lambda_l| \tag{4.41}$$

with the minimal damping ratio for all N modes given by

$$\zeta_{\min} := \min_{l \in \{1,\ldots,n\}} \zeta_l.$$

For optimal performance in terms of POD, we seek K such that

$$\max_K \ \zeta_{\min}. \tag{4.42}$$

This control strategy requires that a good estimate of y is available, which for practical application could be obtained using local or external measurements [129].

4.4.1 Detailed Model Specification

To illustrate the control strategy on a more detailed system, we consider a HVDC-interconnected system as seen in Figure 4.1 where each network $i \in \{1, 2\}$ is represented using two synchronous machines $j \in \{1, 2\}$ where

- the nonlinear dynamics given by (4.1), (4.2) are considered;
- we allow asymmetric networks with $X_{B,1} \neq X_{B,2}$ and

$$M_{i1} := M_i, \ M_{i2} := \alpha_i M_i;$$

- each machine is participating in the frequency containment reserves (FCR). The active power injection is given by the first-order governor

$$P_{m,ij} = P^0_{m,ij} - \frac{1}{sT_g + 1} \frac{R_g}{\omega_{\text{nom}}} \omega_{ij} \tag{4.43}$$

with time constant $T_g = 2\,\text{s}$ and droop gain $R_g = 25\,\text{p.u.}$ for all machines;

Table 4.1: The four considered cases together with optimal gain and damping obtained for simplified and detailed model.

Case	1		2		3		4	
Network	1	2	1	2	1	2	1	2
$\Omega/2\pi$ [Hz]	0.5	0.525	0.5	0.6	0.5	0.6	0.5	0.6
H [s]	6	6	6	6	4	6	6	6
X_B	0.5	0.5	0.5	0.5	0.5	0.5	0.8	0.5

- HVDC is utilized to share primary frequency reserves by adding FCR control to (4.38)

$$u = P_{\mathrm{DC}}^0 - Ky + \frac{1}{sT_{\mathrm{DC}}+1}\frac{R_{\mathrm{DC}}}{\omega_{\mathrm{nom}}}(\omega_{\mathrm{COI},1} - \omega_{\mathrm{COI},2}) \tag{4.44}$$

  where $T_{\mathrm{DC}} = 2\,\mathrm{s}$ and $R_{\mathrm{DC}} = 50\,\mathrm{p.u.}$

Four cases of HVDC-interconnected ac networks as specified in Table 4.1 are considered. The system parameters are given in per unit (p.u.). Common to all cases is that we let $D_1 = D_2 = 2/\omega_{\mathrm{nom}}$, $\alpha_1 = \alpha_2 = 1$, and FCR control at machines and dc terminals as specified by (4.43) and (4.44). The machine inertia constant $M_i = 2H_iS_r/\omega_{\mathrm{nom}}$ are based on the inertia time constant H, which usually falls within 3–8 s for a power system dominated by synchronous machines [25]. The rated power of each machine is set to $S_r = 4\,\mathrm{p.u.}$, $f_{\mathrm{nom}} = 50\,\mathrm{Hz}$, and $V_1 = V_2 = 1\,\mathrm{p.u.}$ The network impedance is given by (4.10) such that $\Omega_i, i \in \{1,2\}$ are obtained for the cases in Table 4.1. As an example, $\left[X_{\Sigma,1},\, X_{\Sigma,2}\right] \approx \left[1.3,\, 1.2\right]$ for Case 1. The active power injection is consumed locally at each machine bus. Hence, $\Delta P_i = P_{e,i} = P_{\mathrm{DC}}^0 = 0,\ \forall i$.

4.4.2 Reconstructing a Simplified Model

The controllability analysis done in Section 4.3 and the control strategy (4.42) are based on a simplified model where higher-order dynamics such as FCR control, (4.43) and (4.44), are lumped into the damping constant D. The effect of the unmodeled dynamics is studied by synthesizing a controller based on the simplified forth order HVDC-interconnected system model (4.11). Performance, in terms of POD, is then compared between the simplified and the detailed model.

To investigate the sensitivity to unmodeled dynamics we assume that the only information available is the estimated eigenvalues $\hat{\lambda}_l = -\hat{\gamma}_l \pm j\hat{\omega}_{e,l}$. In particular interest are the eigenvalues representing the poorly damped interarea mode in Network 1 and Network 2, respectively. Using this information, a model of the reduced networks in (4.9) is reconstructed by solving the characteristic equation

of A_i:

$$\Delta\ddot{\delta}_i + \underbrace{\frac{D_i}{M_{\Sigma,i}}}_{2\gamma_i}\Delta\dot{\delta}_i + \underbrace{\frac{V_i^2 M_{\Sigma,i}}{M_{i1}M_{i2}X_{\Sigma,i}}}_{\Omega_i^2}\Delta\delta_i = 0. \tag{4.45}$$

Remark 4.6 From the characteristic equation (4.45), and the state-space representation (4.9), we see that proportional (negative) feedback of $\Delta\omega_i = \Delta\dot{\delta}_i$ will move the pole straight in the negative real direction. This will increase the damping torque (in phase with $\Delta\omega_i$) of the electromechanical mode.

Since the mode is poorly damped, we assume $\omega_{e,i} \approx \Omega_i$. Proposing some parameter estimates $\hat{H}_i$, $\hat{X}_{B,i}$, and $\hat{\alpha}_i$ allows us to reconstruct the second order state-space representation (4.9)

$$\hat{G}_i \overset{s}{=} \left[\begin{array}{c|c} \hat{A}_i & \hat{B}_i \\ \hline \hat{C}_i & 0 \end{array}\right]$$

of each network. The HVDC controller is then tuned on the interconnected model

$$\hat{G} = \begin{bmatrix} \hat{G}_1 \\ -\hat{G}_2 \end{bmatrix}$$

using (4.42).

4.4.3 Tuning Result Using Reconstructed Model

In this section we compare the result using the reconstructed and the detailed model for tuning. In Table 4.2 it is seen that the controller gains $\hat{K}$ result in slightly lower POD when applied to the detailed model ($\zeta_{\min} < \hat{\zeta}_{\min}$). Comparing $\hat{K}$ with the optimal gain obtained for the detailed system K^*, we see that a good conservative approach to account for these unmodeled dynamics would be to scale $\hat{K}$ with some factor smaller than one. The main reason for POD deterioration is the HVDC FCR control (4.44), which could be taken into account in the tuning process. In Figure 4.6 the minimal system damping ratio $\zeta_{\min}$ for Case 3 is shown as a function of both K_1 and K_2 while Figure 4.7 shows the highest $\zeta_{\min}$ achieved at each given K_1. In Figure 4.7 it is seen that lowering the inertia, or moving the dc bus location closer to one of the generator as in 3 and 4, respectively, makes Network 1 more controllable. Feedback gain K_1 consequently has a higher effect on POD in Network 1. However, its seen that only the modal frequency ratio Ω_1/Ω_2 will have a significant effect on optimal performance as indicated in Section 4.3.3. Consequently, this means a lower optimal K_1 for the more controllable cases.

Root Locus

Let the HVDC POD controller be $K = kK'$, where K' is either or $\hat{K}$ or K^* obtained from the reconstructed or detailed model respectively. In Figure 4.8 the root locus

Table 4.2: Feedback gain $\hat{K}$ and $\hat{\zeta}_{\min}$ are obtained by solving (4.42) for a reconstructed simplified model (see Section 4.4.2) while $\zeta_{\min}$ is the actual damping ratio achieved using $\hat{K}$ on the complete detailed model. Optimal gain feedback gain K^* and $\zeta^*_{\min}$ are obtained by solving (4.42) with complete knowledge of the system.

	Case	1		2		3		4	
	Network	1	2	1	2	1	2	1	2
Reconstructed simplified model	$\hat{K}$ [1/Hz]	0.27	0.29	1.02	1.23	0.64	1.18	0.64	1.24
	$\hat{\zeta}_{\min}$ [%]	2.9		9.4		9.2		9.4	
	$\zeta_{\min}$ [%]	2.2		7.0		6.9		7.0	
Complete model	K^* [1/Hz]	0.26	0.29	1.02	1.22	0.64	1.18	0.64	1.23
	$\zeta^*_{\min}$ [%]	2.7		9.1		9.0		9.2	

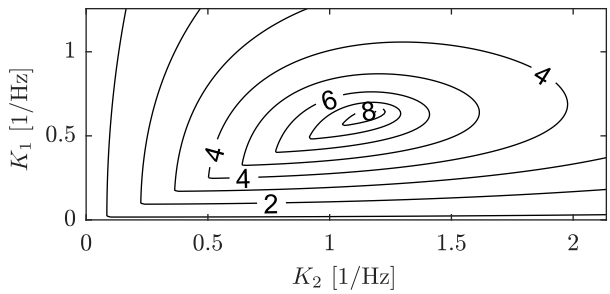

Figure 4.6: Case 3: Level curves for the minimal system damping ratio $\zeta_{\min}$ [%] as a function of both K_1 and K_2.

of the HVDC-interconnected system is drawn showing poles of the poorly damped interarea modes as k goes from zero to infinity. Note that oscillatory modes appear as complex conjugates. For clarity only the eigenvalues with positive imaginary part are shown in Figure 4.8. Their conjugate counterparts are mirrored over the real axis.

As the gain increases the poles move towards each other until they diverge. At the bifurcation point the eigenvalues of the two system are identical. Afterwards they split up into two new eigenvalues pairs. The pair corresponding to the easily controllable system direction (which in Section 4.3 corresponds to state variables in $\text{span}(v_1, v_2)$) continues into the left half-plane (LHP). The pair that corresponds to the least controllable directions $\text{span}(v_3, v_4)$ moves back towards the imaginary axis until all additional damping from the HVDC control is lost. This might be a problem if one of the ac networks are inherently unstable. The inaccuracy of the reconstructed model causes the poles to diverge when they are further apart, as seen in Figure 4.8a.

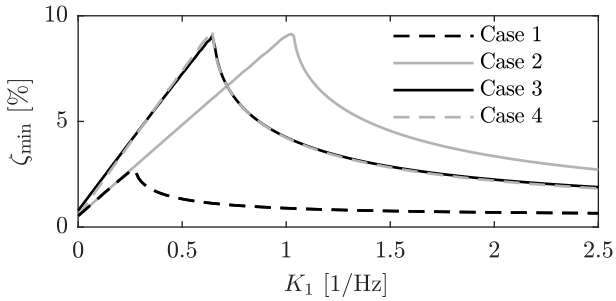

Figure 4.7: The highest minimal system damping ratio $\zeta_{\min}$ as a function of K_1.

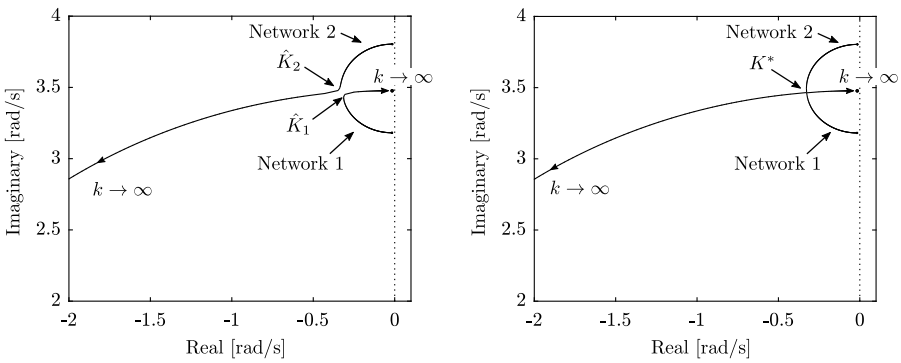

(a) Controller tuned using reconstructed model, $K = k\hat{K}$

(b) Controller tuned using detailed model, $K = kK^*$

Figure 4.8: Case 2: Root locus of the electromechanical mode in each of the HVDC-interconnected systems using HVDC POD control.

4.4.4 Step Response

Simulations using the model considered in Section 4.4.1 are presented next. A disturbance in the form of a sudden 0.4 p.u. load increase at machine-bus 1 in Network 1 is the considered scenario.

Machine speeds with feedback gain $\hat{K}$ obtained from the simplified model, using the procedure introduced in Section 4.4.2, are presented in Figures 4.9 and 4.10 for Case 1 and 2, respectively.

An immediate frequency fall can be seen at machine-bus 1 in Network 1 where the load increase occurs. The load imbalance causes a separation in machine speeds and an ensuing power oscillation between the two machines. The proposed control scheme (4.40) is implemented to increase POD, consequently spreading the power oscillation to the assisting network. A larger difference between Ω_1 and Ω_2 gives a lower modal interaction between the networks according to Section 4.3.3. Hence,

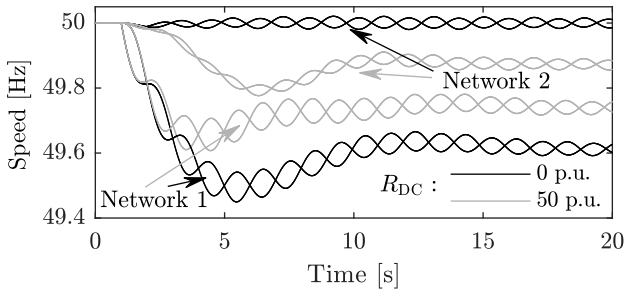

Figure 4.9: Case 1: Machine speeds for the HVDC-interconnected two-machine networks following a 0.4 p.u. load increase in Network 1 (bottom line-pair) aided by Network 2 (top line-pair). Gray and black lines shows performance with and without sharing of primary reserves through the HVDC link (4.44), respectively.

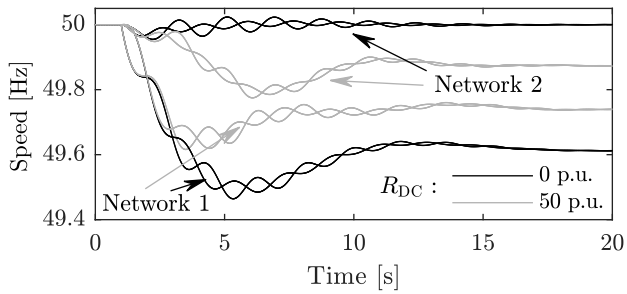

Figure 4.10: Case 2: Scenario identical to Figure 4.9.

Case 2 facilitates a higher POD performance compared to Case 1. A higher feedback gain moves Ω_1 and Ω_2 closer to each other as seen in Figure 4.8. As the modal frequencies move closer to each other, controllability and thus, POD benefits are reduced.

To illustrate the effect of FCR control (4.44) we also consider a model with $R_{\mathrm{DC}} = 0$ in both cases. Comparing the cases with FCR control (gray lines), to those without (black lines) we see that sharing of primary reserves, to reduce nadir and steady-state frequency deviation, can be implemented independent of POD control.

4.4.5 Sensitivity to Parameter Estimates

To show the effect of misjudging the dc busbar location in the tuning process, we consider Case 2 (see Table 4.1) with two different estimates of $\hat{X}_B$, given in Table 4.3. Here we let $R_{\mathrm{DC}} = 0$ so as to not get interference from FCR control.

Table 4.3: Sensitivity to parameter estimate $\hat{X}_B$ using ideal feedback $\Delta\omega$ (4.46) and estimate $\Delta\hat{\omega}$ (4.47) from local frequency measurements.

			Feedback Signal		$\Delta\omega$		$\Delta\hat{\omega}$	
Case	$\hat{X}_B$	$\hat{K}_1$	$\hat{K}_2$ [1/Hz]	$\hat{\zeta}_{\min}$	ζ_1	ζ_2	ζ_1	ζ_2 [%]
2	0.5	1.08	1.31	9.4	9.9	8.8	9.9	8.8
2.a	0.25	2.16	1.31	9.4	24	3.2	44	1.5
2.b	0.75	0.72	1.31	9.4	5.5	10	3.8	10
2.0	-	-	-	-	0.52	0.39	0.52	0.39

External Measurement

First we study the case where the ideal feedback signal from (4.39)

$$y = \begin{bmatrix} \Delta\omega_1 \\ \Delta\omega_2 \end{bmatrix} \tag{4.46}$$

is available using communication from remote phasor measurement units at the machine busbars.

Local Measurement

Assume that $\Delta\omega_i$ is estimated using local frequency measurements at the dc terminals. A good estimate, $\Delta\hat{\omega}_i$, will require accurate knowledge of the model. Miss-judging the observability (which for this case is the same as the controllability $X_{B,i}$) will affect the magnitude of the estimate and will therefore give the same effect as an incorrectly tuned feedback gain. Since the focus of this chapter is not on observer design we are here assuming that

$$\Delta\hat{\omega}_i = \Delta\omega_i \frac{X_{B,i}}{\hat{X}_{B,i}} \tag{4.47}$$

i.e., if the observability is underestimated we are going to have an overestimate of $\Delta\omega_i$. In Table 4.3 we see how the use of local measurements makes the control method more sensitive to model error.

Remark 4.7 In practice $\Delta\hat{\omega}_i$ could be obtained using a wash-out or band-pass filter, in which case transient response and phase would be affected by model error and filter tuning. To achieve a more robust estimate, additional feedback signals such as ac power flow and voltage could be used.

Simulation of Oscillatory Energy Following a Load Step

In Case 2.a, where controllability and observability is underestimated, an overestimated $\hat{K}_1$ greatly increases POD performance in Network 1 at the cost of overall system performance, measured by $\zeta_{\min}$. In Figures 4.11 and 4.12 the oscillatory

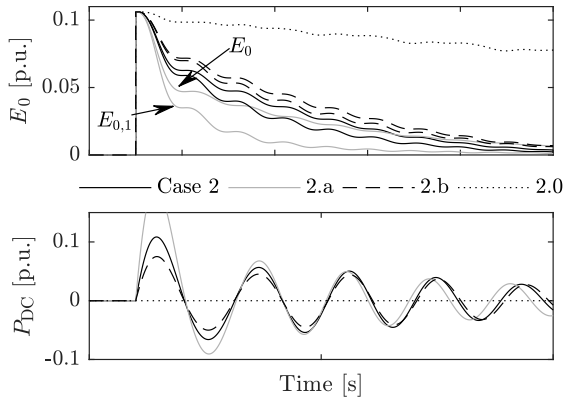

Figure 4.11: Oscillatory energy (top) following a 0.4 p.u. load increase in Network 1 for the cases specified in Table 4.3, with the resulting P_{DC} (bottom). Per unit energy is calculated using (4.13), where the potential energy is in relation to pre- and post-disturbed steady-state. Control is implemented using ideal feedback $\Delta\omega$.

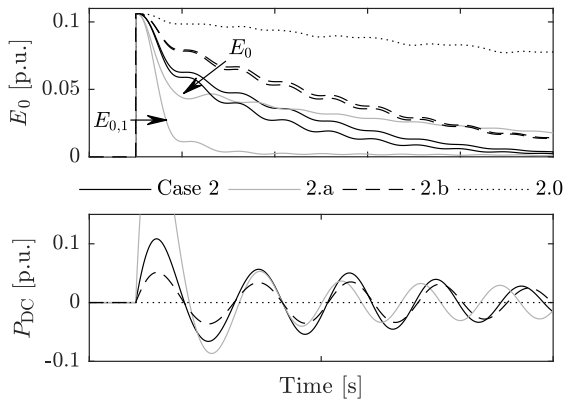

Figure 4.12: Same scenario as in Figure 4.11 but with feedback signal $\Delta\hat{\omega}$ (4.47). We see that the dependency on observability of $\Delta\omega$ from local measurements gives increased sensitivity to model error.

energy (4.13), $E_0 = E_{0,1} + E_{0,2}$, following a sudden 0.4 p.u. load increase at machine-bus 1 is shown. The oscillatory energy $E_{0,1}$ in the disturbed network is greatly reduced due to a high initial P_{DC}. This however, introduce a large oscillatory energy $E_{0,2}$ in the assisting network where the POD is lower, reducing overall system performance. Comparing Figure 4.11 with Figure 4.12 we see that the negative impact of model error increases if we also considers the effect on observability. As

can be seen, underestimating $\hat{K}$ in Case 2.b gives the opposite result. For comparison Case 2.0 gives an base reference where POD control is not utilized. From Case 2.0 we see that even though badly tuned K gives poor POD, we can always expect an improvement from the case without POD control.

4.5 Simulation Study

To improve the confidence in the analytical results, simulations on more detailed power system models are made in Simulink. We consider the Nordic 32-bus Cigré test system (N32) [43]. The model is implemented in Simulink Simscape Electrical [51] with synchronous machines, excitation systems, governors, transmission, transformers, and load characteristics as specified in [43]. The N32 model is a system with large power transfers from the hydro dominated north and external areas (lumped into north area) to loads in the central and southwestern areas (lumped into the south area) where a large amount of thermal power is installed. The implemented N32 model shows a 0.5 Hz interarea mode Ω between the north and south areas. For illustrative purposes, the damping of this mode is reduced to roughly 1% by modifying the PSS at machines 4072 and 1042.

For the study, an artificial system is created by interconnecting two separate N32 networks with a point-to-point HVDC link as shown in Figure 4.13. Four cases with different system topologies are considered. In Cases 1 and 2 the dc link is located at bus 4045 in both ac networks. In Cases 3 and 4 the dc terminal is moved to bus 4072 in Network 1. To illustrate limitations imposed by modal interaction, the inertia time constants are scaled to modify modal frequencies (4.10) of Network 2. The cases are summarized in Table 4.4.

4.5.1 HVDC POD Controller

The HVDC active power is modulated using (4.40) with the relative frequency difference

$$y_i = \frac{\sum_{j\in\text{south}} M_{ij}\omega_{ij}}{\sum_{j\in\text{south}} M_{ij}} - \frac{\sum_{j\in\text{north}} M_{ij}\omega_{ij}}{\sum_{j\in\text{north}} M_{ij}} \tag{4.48}$$

as a single-machine equivalent (SIME) [57, 130] feedback signal from each network.

The signal is obtained by communicating the machine measurements to the dc controller. A proportional controller is implemented using the tuning procedure introduced in Section 4.4. The second-order system representation (4.9), used in the tuning process, is obtained using Simulink's Linear Analysis Tool.

The result shown in Table 4.5 confirms the analytic result that modal interaction limits the potential POD benefits from active power modulation. The control, tuned to each specific case, exploits the modal frequency differences. With higher gains, the modal frequencies move closer to each other and the system lose controllability of the interarea modes. Moving the dc terminal to the more controllable position

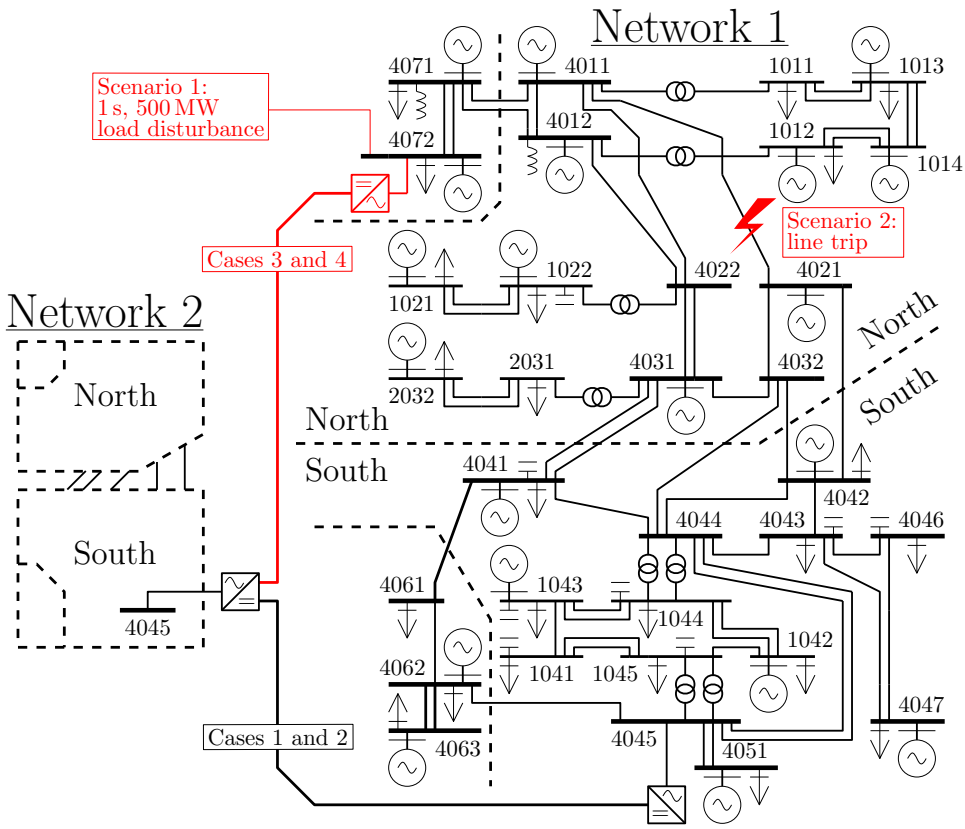

Figure 4.13: The artificial network model consisting of two HVDC-interconnected N32 networks [43].

Table 4.4: Modal frequencies and dc buses of the four considered cases of HVDC-interconnected N32 networks.

Case	1		2		3		4	
Network	1	2	1	2	1	2	1	2
$\Omega/2\pi$ [Hz]	0.51	0.53	0.51	0.60	0.51	0.53	0.51	0.60
DC Bus	4045	4045	4045	4045	4072	4045	4072	4045

at bus 4072 in Cases 3 and 4 reduces the required dc power actuation but have negligible effect on resulting POD performance.

Remark 4.8 The damping ratio $\hat{\zeta}_{\min}$ is obtained in the tuning process by solving (4.42) for the reduced second-order model (4.9). Naturally, the minimal damping ratio $\zeta_{\min}$ achieved in the full-scale model will deviate slightly. Notably, we see that

Table 4.5: Resulting POD of the HVDC-interconnected N32 networks. Controller K_i is tuned to the corresponding Case i.

Controller	K_1	K_2	K_3	K_4
Gain [MW/Hz]	453 617	1558 1675	190 514	663 1410
$\hat{\zeta}_{\min}$ [%]	3.4	9.4	3.2	8.6
$\zeta_{\min}$(Case 1) [%]	2.9	1.4	1.8	1.6
$\zeta_{\min}$(Case 2) [%]	3.0	6.9	1.8	3.7
$\zeta_{\min}$(Case 3) [%]	1.5	0.9	2.9	1.1
$\zeta_{\min}$(Case 4) [%]	4.2	3.0	3.0	7.1

the $\zeta_{\min} < \hat{\zeta}_{\min}$. This is because the damping ratio is tuned to optimize the POD in both systems, modeling both networks as SIMEs (4.9). Any change from this ideal model will either reduce controllability, making the controller gain K_i to small; or increase controllability, increasing the modal interaction between the two systems. Both of these effects lead to $\zeta_{\min} < \hat{\zeta}_{\min}$.

4.5.2 Simulation Results

To validate the results, we simulate the nonlinear system.

Scenario 1) Load Disturbance, HVDC-Configuration Case 1, Controller K_1

A 500 MW load disturbance occur at the time interval $t = [1,2]$ s at bus 4072 in Network 1. As shown in Figure 4.14 the load disturbance reduces the initial machine speed at bus 4072 ensuing in a north–south interarea oscillation.

Scenario 2) Line Trip, HVDC-Configuration Case 2, Controller K_2

The transmission line between buses 4011 and 4021 is tripped at time $t = 1$ s. Since there is a large power transfer from the north to the south, the initial loss of transfer capacity causes machines in the north area to accelerate while the southern machines decelerate. As seen in Figure 4.16 a local mode within the north area is also excited by the disturbance. However, the local mode is well damped and after a while the response is dominated by the north–south interarea mode.

The resulting HVDC active power for the two scenarios is shown in Figure 4.15. In agreement with the analysis, HVDC active power modulation is shown to be more effective in Scenario 2, where we consider the network topology with higher modal ratio. This allows for a large feedback gain and a damping improvement from 1 % to 6.9 %. As a comparison, Scenario 1, where we consider a network topology with a low modal ratio, allows for a comparatively smaller feedback gain, as shown in Table 4.5. As a result, the damping can only be improved to around 2.9 %.

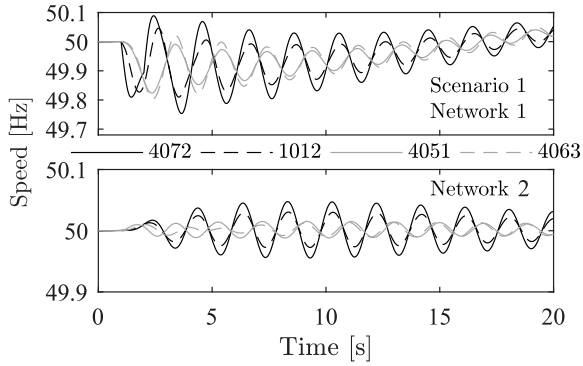

Figure 4.14: Scenario 1: Machine speeds at buses 4072 and 1012 in the northern areas and 4051 and 4063 in the southern areas following a 500 MW load disturbance at bus 4072 in Network 1.

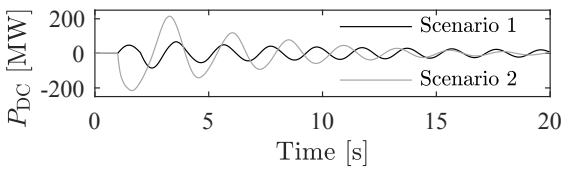

Figure 4.15: HVDC active power following the disturbance of the two scenarios in Figures 4.14 and 4.16.

Remark 4.9 The control design method used in this chapter is designed to optimize POD using a simplistic proportional feedback controller. However, this assumes that a good representation of the relative frequency difference (4.48) is available as a feedback signal, for instance using wide-area measurements. It also assumes that the SIME model (4.9) is a good estimate of the system. If this is not the case, e.g., if Assumption 4.1 is not justified due to a disproportionate distribution of frequency dependent loads and governors, then a dynamic controller will likely be necessary to achieve optimal POD. A more sophisticated control design method, is then needed. A controller dealing with these issues can be designed, e.g., using the modal linear quadratic Gaussian control design presented in [28, 99] or the signal based $\mathcal{H}_2$ optimal control presented later in Section 6.4.

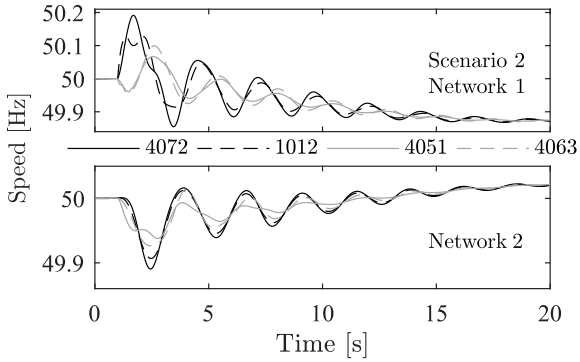

Figure 4.16: Scenario 2: Machine speeds at buses 4072 and 1012 in the northern areas and 4051 and 4063 in the southern areas following a line trip in the northern area of Network 1.

4.6 Summary

Oscillatory stability has become an increasing concern in the modern power system. Stability of interarea modes often limits the transfer capacity over weak transmission corridors. In this chapter we have studied how HVDC active power modulation between two asynchronous ac networks can be used to improve POD. It was shown that the location of the dc terminal affects the controllability, and thus the size of the required control action. However, if POD improvements are desired in both ac networks, then the ratio between the modal frequencies is the sole factor determining the achievable nominal performance. If the modal frequencies moves closer to each other, e.g., due to operational changes in any of the interconnected networks, then the damping contribution from the HVDC POD will deteriorate due to an increased modal interaction. With a reduced modal ratio, lower feedback gains are required, to avoid issues with modal interaction. The analytical results were validated by simulating on a simple test case as well as on a detailed model of two HVDC-interconnected 32-bus networks.

Appendix

4.A Eigenvalue Decomposition of a Matrix

Consider a diagonalizable matrix A (with complete basis of eigenvectors). Let

$$\Lambda = \text{diag}(\lambda_1, \ldots, \lambda_n)$$

where λ_i, $i \in \{1, \ldots, n\}$ are the i^{th} eigenvalue of A. Then

$$\begin{aligned} A\mathcal{U} &= \mathcal{U}\Lambda \\ \mathcal{V}^H A &= \Lambda \mathcal{V}^H \\ \mathcal{V}^H &= \mathcal{U}^{-1}, \end{aligned}$$

where the left modal matrix $\mathcal{V} = [v_1, \ldots, v_n]$ and the right modal matrix $\mathcal{U} = [u_1, \ldots, u_n]$. The factorization

$$A = \mathcal{U}\Lambda\mathcal{V}^H.$$

is useful for calculating matrix exponentials as

$$e^A = \mathcal{U}\, e^{\Lambda}\, \mathcal{V}^H = \mathcal{U}\ \text{diag}(e^{\lambda_1}, \ldots, e^{\lambda_n})\, \mathcal{V}^H. \tag{4.49}$$

4.B State-Space Equation on Modal Form

Let ξ be a vector given by the linear transformation

$$\xi = \mathcal{V}^H x.$$

The new variables ξ_n, $n \in \{1, \ldots, n\}$ are complex variables describing the modes of the original system. The dynamic of the system modes are described by the state equation

$$\dot{\xi}(t) = \mathcal{V}^H A\mathcal{U}\xi(t) + \mathcal{V}^H B u(t) = \Lambda\xi(t) + \mathcal{V}^H B u(t). \tag{4.50}$$

Since the state matrix Λ is diagonal, system dynamics are decoupled. The solution to (4.50) are thus given by

$$\xi_l(t) = e^{\lambda_l}\xi(t_0) + \int_{t_0}^{t} e^{\lambda_l(t-\tau)} v_l^H B u(\tau) d\tau.$$

Remark 4.10 The diagonal state matrix Λ makes this a practical system to analyze. However, for oscillatory modes (which appear as complex conjugated eigenvalue pairs) the resulting state variables and system matrices become complex.

4.C Real Jordan Form

Let $\boldsymbol{V} = \begin{bmatrix}\boldsymbol{v}_1, \ldots, \boldsymbol{v}_n\end{bmatrix} \in \mathbb{R}^{n\times n}$ be a transformation matrix with

- $\begin{bmatrix}\boldsymbol{v}_i, \boldsymbol{v}_{i+1}\end{bmatrix} = \begin{bmatrix}\mathrm{Re}(v_i), \mathrm{Im}(v_i)\end{bmatrix}$ if $\lambda_i = \bar{\lambda}_{i+1}$, and
- $\boldsymbol{v}_i = v_i$ if λ_i is real.

With the linear transformation, $z = \boldsymbol{V}^T x$ the state-space representation of the system becomes

$$G_y \overset{s}{=} \left[\begin{array}{c|c} J & \boldsymbol{V}^T B \\ \hline C_y & 0 \end{array}\right] \tag{4.51}$$

where, $J = \boldsymbol{V}^T A \left(\boldsymbol{V}^T\right)^{-1}$ is the block diagonal matrix[1]

$$J = \begin{bmatrix} \lambda_1 & 0 & \cdots & 0 \\ 0 & \ddots & & \vdots \\ \vdots & & \begin{bmatrix} a_i & b_i \\ -b_i & a_i \end{bmatrix} & 0 \\ 0 & \cdots & 0 & \ddots \end{bmatrix} \tag{4.52}$$

where complex eigenvalues $\lambda_i = -a_i \pm jb_i$.

Model Reduction in Section 4.2

Let z_l be the reduced state vector representing the observable subspace $z_i = P^\dagger x$. If the transformation matrix $P^\dagger$ is chosen as a linear combination of left eigenvectors as

$$P^\dagger = S \begin{bmatrix} \mathrm{Re}(v_l^H) \\ \mathrm{Im}(v_l^H) \end{bmatrix}$$

where S is an invertible square matrix of appropriate dimension. Then the model reduction $A_i = P^\dagger A_i' P$, $B_i = P^\dagger B_i'$ and $C_i = C_i' P$ results in a minimal (observable and controllable) realization of the oscillatory mode l in the original system. The new 2×2 state matrix A_i is similar (same characteristic polynomial, i.e., same eigenvalues, counting multiplicity [126]) to the corresponding 2×2 block in (4.52).

[1] The modal form (5.10) is on complex Jordan form. Here we have assumed that A is diagonalizable, i.e. that all eigenvectors are linearly independent. If this is not the case, both Λ and J will have ones on the super-diagonal at positions corresponding to linearly dependent eigenvectors [126].

4.D Solving the Controllability Gramian

Consider the LTI system (4.9) describing the electromechanical mode of an ac network with system state matrix and input matrix

$$A = \begin{bmatrix} 0 & 1 \\ \frac{-2V^2}{MX_\Sigma} & \frac{-D}{2M} \end{bmatrix}, \quad B = \begin{bmatrix} 0 \\ \frac{X_B}{M} \end{bmatrix}. \tag{4.53}$$

For ease of notation we rewrite (4.53) as

$$A = \begin{bmatrix} 0 & 1 \\ -\Omega^2 & -2\gamma \end{bmatrix}, \quad B = \begin{bmatrix} 0 \\ b \end{bmatrix}. \tag{4.54}$$

Finite-Time Controllability Gramian

The finite time ($T < \infty$) controllability Gramian (Theorem 4.1) is given by

$$W_C = \int_0^T e^{At} B B^T e^{A^T t} dt. \tag{4.17}$$

Calculating the finite-time Gramian for the Undamped 2×2 System

Using (4.49), W_C can be calculated as

$$W_C = \int_0^T \mathcal{V}^H e^{\Lambda t} \mathcal{U} B B^T \mathcal{U}^H e^{\Lambda^H t} \mathcal{V}^H dt. \tag{4.55}$$

For the 2×2 system 4.54 we have

$$\begin{aligned}
\Lambda &= \begin{bmatrix} -j\Omega & 0 \\ 0 & j\Omega \end{bmatrix} \\
e^{\Lambda t} &= \begin{bmatrix} \cos(\Omega t) - j\sin(\Omega t) & 0 \\ 0 & \cos(\Omega t) + j\sin(\Omega t) \end{bmatrix} \\
\mathcal{V}^H &= \begin{bmatrix} -j\frac{\Omega}{2} & \frac{1}{2} \\ j\frac{\Omega}{2} & \frac{1}{2} \end{bmatrix} \\
\mathcal{U} &= \begin{bmatrix} j\frac{1}{\Omega} & -j\frac{1}{\Omega} \\ 1 & 1 \end{bmatrix} \\
\mathcal{U} e^{\Lambda t} \mathcal{V}^H &= \begin{bmatrix} \cos(\Omega t) & \frac{\sin(\Omega t)}{\Omega^2} \\ \frac{\sin(\Omega t)}{\Omega^2} & \cos(\Omega t) \end{bmatrix}.
\end{aligned}$$

thus the integral (4.55) becomes

$$\begin{aligned}
W_C &= b^2 \int_0^T \begin{bmatrix} \frac{\sin^2(\Omega t)}{\Omega^2} & \frac{\cos(\Omega t)\sin(\Omega t)}{\Omega} \\ \frac{\cos(\Omega t)\sin(\Omega t)}{\Omega} & \cos^2(\Omega t) \end{bmatrix} dt \\
&= b^2 \begin{bmatrix} \frac{2\Omega T - \sin(2\Omega T)}{4\Omega^3} & \frac{\sin^2(\Omega T)}{2\Omega^2} \\ \frac{\sin^2(\Omega T)}{2\Omega^2} & \frac{2T - \sin(2\Omega T)}{4\Omega} \end{bmatrix}
\end{aligned}$$

Substituting in $\Omega = \sqrt{\frac{2V^2}{MX_\Sigma}}$ and $b = \frac{X_B}{M}$ gives

$$W_C = \begin{bmatrix} w_{11} & w_{12} \\ w_{21} & w_{22} \end{bmatrix}$$

where

$$w_{11} = \frac{X_B^2 T}{2M}\frac{X_\Sigma}{2V^2} - \sqrt{\frac{2X_\Sigma}{MV^2}}\frac{X_B^2}{8}\frac{X_\Sigma}{2V^2}\sin\sqrt{\frac{8T^2V^2}{MX_\Sigma^2}}$$

$$w_{12} = w_{21} = \frac{X_B^2 X_\Sigma}{4MV^2}\sin\sqrt{\frac{2T^2V^2}{MX_\Sigma^2}}$$

$$w_{22} = \frac{X_B^2 T}{2M}\frac{1}{M} + \sqrt{\frac{2X_\Sigma}{MV^2}}\frac{X_B^2}{8}\frac{1}{M}\sin\sqrt{\frac{8T^2V^2}{MX_\Sigma^2}}.$$

For large T, this simplifies to

$$W_C \approx X_B^2\frac{T}{2M}\begin{bmatrix} \frac{X_\Sigma}{2V^2} & 0 \\ 0 & \frac{1}{M} \end{bmatrix}$$

Calculating the finite-time Gramian for Higher Order Systems

As system dimension increases, solving the integral (4.17) analytically becomes harder. For low-order systems ($n = 2$) or a numerical solution of higher order systems, the integral can conveniently be solved using matrix exponentials.

Theorem 4.4 ([131, Theorem 1]) *Consider the system*

$$\dot{x}(t) = Ax(t) + Bu(t).$$

Let

$$\exp\left(\begin{bmatrix} -A & BB^\intercal \\ 0 & A^\intercal \end{bmatrix} T\right) = \begin{bmatrix} F_1(T) & G(T) \\ 0 & F_2(T) \end{bmatrix},$$

where

$$F_1(T) = e^{-AT},\ F_2(T) = e^{A^\intercal T}$$

and

$$G(T) = \int_0^T e^{-A(T-t)}BB^\intercal e^{A^\intercal t}dt = e^{-AT}\int_0^T e^{At}BB^\intercal e^{A^\intercal t}dt.$$

The finite-time controllability Gramian is given by

$$W_C(T) = F_2^\intercal(T)G(T).$$

4.E Infinite-Time Controllability Gramian

If A is strictly Hurwitz, then the controllability Gramian (Theorem 4.2) is given by the unique solution to the Lyapunov equation

$$AW_C + W_C A^T + BB^T = 0. \tag{4.18}$$

Calculating the infinite-time Gramian for the 2×2 System

For the 2×2 system 4.54 we have

$$\begin{bmatrix} 0 & 1 \\ -\Omega^2 & -2\gamma \end{bmatrix} W_C + W_C \begin{bmatrix} 0 & -\Omega_2 \\ 1 & -2\gamma \end{bmatrix} + \begin{bmatrix} 0 & 0 \\ 0 & b^2 \end{bmatrix} = 0$$

with

$$W_C = W_C^T = \begin{bmatrix} w_{11} & w_{12} \\ w_{12} & w_{22} \end{bmatrix}$$

the controllability Gramian obtained by solving the equations

$$\begin{aligned} w_{12} + w_{12} &= 0 \\ w_{22} - \Omega^2 w_{11} &= 0 \\ w_{11} &= \frac{w_{22}}{\Omega^2} \\ -2\gamma w_{22} - 2\gamma w_{22} + b^2 &= 0 \\ w_{22} &= \frac{b_2^2}{4\gamma} \end{aligned}$$

Substituting in $\Omega = \sqrt{\frac{2V^2}{MX_\Sigma}}$, $\gamma = \frac{D}{4M}$, and $b = \frac{X_B}{M}$ gives

$$W_C = \frac{X_B}{D} \begin{bmatrix} \frac{X_\Sigma}{2V^2} & 0 \\ 0 & \frac{1}{M} \end{bmatrix}.$$

Calculating the infinite-time Gramian for Higher Order Systems

The Lyapunov equation (4.18) can be solved using Kronecker products [128]

$$(A \otimes I + I \otimes A^T)\boldsymbol{w}_c = -\boldsymbol{b}$$

where

- I is a identity matrix with the same dimensions as A;
- $\boldsymbol{b}$ is a column vector with the rows of BB^T stacked on top of each other;
- $\boldsymbol{w}_c$ is a column vector to be solved with the columns of W_C stacked on top of each other.

4.F Damping Constant in Examples 4.1 and 4.2

The complex conjugated eigenvalue pair of A_i in (4.11) is given by

$$\lambda_i = \gamma_i \pm \omega_{e,i} = -\frac{D_i}{4M_i} \pm \sqrt{\left(\frac{D_i}{4M_i}\right)^2 - \frac{2}{M_i}}. \tag{4.56}$$

The damping ratio is defined as

$$\zeta_i := \frac{-\operatorname{Re}(\lambda_i)}{|\lambda_i|} = \frac{-\gamma_i}{\sqrt{\gamma_i^2 + \omega_{e,i}^2}}$$

and thus

$$|\gamma_i| = \omega_{e,i}\sqrt{\frac{\zeta_i^2}{1-\zeta_i^2}} \approx \Omega_i \sqrt{\frac{\zeta_i^2}{1-\zeta_i^2}}.$$

where we have assumed that the mode is poorly damped. Using (4.56) the damping constant is then given by

$$D_i \approx 4M_i\Omega_i\sqrt{\frac{\zeta_i^2}{1-\zeta_i^2}} = \frac{8}{\Omega_i}\sqrt{\frac{\zeta_i^2}{1-\zeta_i^2}} \approx 8\frac{\zeta_i}{\Omega_i}$$

4.G Maclaurin Series Expansion for Small $|\epsilon|$

The Maclaurin series expansion of (4.23) becomes

$$\begin{aligned}
a &= \frac{X_B^2}{D}\frac{X_\Sigma}{2V^2} \\
\alpha &= a\left(1 - \frac{c}{M}\epsilon^2\right) + \mathcal{O}(\epsilon^3) \\
b &= \frac{X_B^2}{D}\frac{1}{M} \\
b_2 &= b\left(1 - \frac{\epsilon}{M} + \frac{\epsilon^2}{M^2}\right) + \mathcal{O}(\epsilon^3) \\
\beta &= b\frac{1}{4M^2}\left(4M^2 - 2M\epsilon + (1-4cM)\epsilon^2\right) + \mathcal{O}(\epsilon^3) \\
\gamma &= \frac{X_B^2}{D^2}\left(\frac{\epsilon}{M} - \frac{\epsilon^2}{2M^2}\right) + \mathcal{O}(\epsilon^3).
\end{aligned}$$

Taking derivatives with respect to ϵ

$$\begin{aligned}\frac{d\alpha(\epsilon)}{d\epsilon} &= 0 + \mathcal{O}(\epsilon^2)\\ \frac{db_2(\epsilon)}{d\epsilon} &= -\frac{b}{M}\epsilon + \mathcal{O}(\epsilon^2)\\ \frac{d\beta(\epsilon)}{d\epsilon} &= -\frac{b}{2M}\epsilon + \mathcal{O}(\epsilon^2)\\ \frac{d\gamma(\epsilon)}{d\epsilon} &= \frac{b}{D}\epsilon + \mathcal{O}(\epsilon^2).\end{aligned}$$

For the weakly damped system in Example 4.2, $M \gg D$, and therefore

$$\left|\frac{d\alpha(\epsilon)}{d\epsilon}\right| \leq \left|\frac{d\beta(\epsilon)}{d\epsilon}\right| \leq \left|\frac{db_2(\epsilon)}{d\epsilon}\right| \leq \left|\frac{d\gamma(\epsilon)}{d\epsilon}\right|.$$

4.H Improved Control Effort Estimate

The control effort estimate (4.34) holds for any network parameterizations. Defining

$$\begin{aligned}\rho &:= 2\sqrt{\frac{V_1^2 M_1}{X_{\Sigma,1}}\frac{V_2^2 M_2}{X_{\Sigma,2}}}\\ \Psi_1 &:= 1 + D^2\frac{1+\Omega_1^2/\Omega_2^2}{\rho(1-\Omega_1^2/\Omega_2^2)^2}\\ \Psi_2 &:= 1 + D^2\frac{1+\Omega_2^2/\Omega_1^2}{\rho(1-\Omega_2^2/\Omega_1^2)^2}\end{aligned}$$

gives the estimate

$$\|u\|_2^2 \approx E_\infty^2(D) := E_0\frac{D}{X_B^2}\sqrt{\Psi_1\Psi_2},$$

which is more accurate for parameter differences between the HVDC-interconnected networks.

Chapter 5

Coordinated HVDC Control

In this chapter, coordination of multiple point-to-point high-voltage direct current (HVDC) lines interconnecting asynchronous ac systems is considered. As shown in Chapter 4, when controlling a single HVDC link, achievable performance is limited since control actions may excite modes of similar frequencies in the assisting networks. However, with coordinated control of two or more HVDC links, the limitations can be circumvented. And with decoupling control, the system interactions can be avoided altogether. In this chapter, conditions suitable for decoupling control are investigated. It is shown that decoupling between system modes can be achieved using a proportional controller. The control method is compared to decentralized and centralized optimal control. The best control method for different system topologies is investigated by looking at input usage and stability following actuator or measurement failures. The results are validated on a realistic model with two interconnected 32-bus networks.

One concern that arises when utilizing HVDC active power control for power oscillation damping (POD) is that interarea modes of the assisting network may be excited [30]. Since poorly damped interarea modes usually fall in the same frequency ranges [25], control methods should avoid unnecessary excitation of weekly damped modes. Interactions can be mitigated by incorporating energy storage from integrated wind power or large capacitor banks in the dc system [76, 84]. In this work, a solution that does not require dc energy storage is proposed. In [30] it was shown that through HVDC active power control, although propagating the disturbance to the assisting network, the overall POD can be improved in both of the HVDC-interconnected ac networks. In Chapter 4 it has been shown that the limiting performance factor for such a control strategy is the proximity of interarea modal frequencies between the two ac networks. A higher feedback gain improves POD of the two ac networks, but also moves the frequency of their interarea modes, and their eigenvalues, closer to each other thereby reducing controllability through modal interaction. This limitation is independent of the inertia and dc bus location[1] in each respective

[1] As long as the dc bus is not exactly at the mass-weighted electrical midpoint.

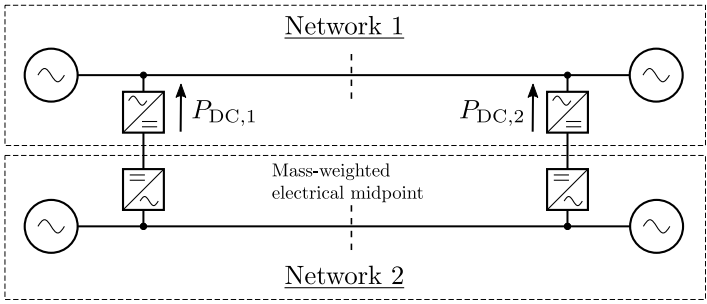

Figure 5.1: Two-sided HVDC-configuration between two asynchronous two-machine networks. Power oscillation damping of one network can be improved by controlling the two links in anti-phase, using the other ac network as a power sink.

network, provided that the measurement quality allows for sufficiently high feedback gains, and that the actuator capacity is sufficient for realizing the desired control.

With additional HVDC lines, the limitations imposed by modal interactions can be circumvented. In [110] it was shown that by controlling two distant HVDC links (as seen in Figure 5.1) in anti-phase, the link resembles a long HVDC link interconnecting the two areas. Oscillation damping is then improved by injecting power between the two areas, using the asynchronous ac network to which the HVDC links is connected, as a power sink. Since multiple HVDC connections between asynchronous ac networks are common today, improvement of dynamic performance using coordinated control can be achieved without the need for any additional hardware installations.

The main contribution of this chapter is to show how the system topology affects multivariable interactions in a HVDC-interconnected system where both ac networks have poorly damped interarea modes. A decentralized control method is compared to decoupling control. It is shown that decoupling control, that avoid interaction between selected interarea modes, can be achieved using a proportional controller. The decentralized and decoupling controllers are compared to a single-line equivalent where the links are controlled as one, as well as a centralized optimal controller. Suitability of the different control methods is analyzed with respect to network topology and sensitivity to dc link failures.

The remainder of the chapter is organized as follows. In Section 5.1 a generalized linear model representation of a power system with arbitrary many buses and HVDC links is presented. In Section 5.2 test systems with different HVDC-configurations are specified. In Section 5.3 some useful tools for analyzing multiple-input multiple-output (MIMO) systems are introduced. In Section 5.4 coordinated control methods are designed for the test cases of interest defined in Section 5.2. In Section 5.5 closed-loop stability properties of the control methods with respect to communication, measurement and actuator failure is discussed. In Section 5.6 it is shown how to implement decoupling control in a system with arbitrary number of states and input-output combinations. In Section 5.7 and Section 5.7 simulations on more

detailed power system models are performed to validate the analytical findings. Section 5.9 summaries the chapter.

5.1 Model of System with Multiple HVDC Links

With multiple HVDC links, the limitations imposed by modal interactions may be circumvented. To obtain insight into how additional controllable HVDC links may improve achievable system we first introduce a more general system description.

5.1.1 General Model of an HVDC-Interconnected System

The model of an ac network with arbitrary many machine and buses, linearized in the same manner as in Section 4.1, can be described as

$$\begin{bmatrix} I & 0 & 0 \\ 0 & \mathcal{M} & 0 \\ 0 & 0 & 0 \end{bmatrix} \begin{bmatrix} \dot{\boldsymbol{\delta}} \\ \dot{\boldsymbol{\omega}} \\ \dot{\boldsymbol{\theta}} \end{bmatrix} = \begin{bmatrix} 0 & I & 0 \\ -\mathcal{L}_{\delta\delta} & -\mathcal{D} & -\mathcal{L}_{\delta\theta} \\ -\mathcal{L}_{\theta\delta} & 0 & -\mathcal{L}_{\theta\theta} \end{bmatrix} \begin{bmatrix} \boldsymbol{\delta} \\ \boldsymbol{\omega} \\ \boldsymbol{\theta} \end{bmatrix} + \begin{bmatrix} 0 & 0 \\ I & 0 \\ 0 & I \end{bmatrix} \begin{bmatrix} P_\delta \\ P_\theta \end{bmatrix}$$

where 0 and I are zero and identity matrices of appropriate sizes, $\mathcal{M} = \mathrm{diag}(M_1, \ldots, M_n)$ and $\mathcal{D} = \mathrm{diag}(D_1, \ldots, D_n)$ are diagonal matrices containing machine inertia and damping constants, respectively. Vectors $\boldsymbol{\delta} = [\delta_1, \ldots, \delta_{n_\delta}]^T$ and $\boldsymbol{\theta} = [\theta_1, \ldots, \theta_{n_\theta}]^T$, represent the voltage phase angle at machine and dc buses, respectively, and $\boldsymbol{\omega} = [\omega_1, \ldots, \omega_{n_\delta}]^T$ represent the machine speeds. This model representation, is also known as the multi-machine classical model [52]. It is obtained following the same reasoning as in Section 3.1, but by truncating the dynamics of the q-axis transient voltage E'_q in (3.7), thereby neglecting all voltage dynamics. Consequently, only rotor angle dynamics and the effect of constant power loads and active power injections can be studied.

Let the external input $P_\delta = P_m - P_{\mathrm{load}} \in \mathbb{R}^{n_\delta}$ be the active power injected to the system from machine buses and let $P_\theta \in \mathbb{R}^{n_\theta}$ be the power injected at other buses e.g. from constant power loads or HVDC power injections. The linearized ac power flow is given by

$$\begin{bmatrix} P_\delta \\ P_\theta \end{bmatrix} = \mathcal{L} \begin{bmatrix} \boldsymbol{\delta} \\ \boldsymbol{\theta} \end{bmatrix} = \begin{bmatrix} \mathcal{L}_{\delta\delta} & \mathcal{L}_{\delta\theta} \\ \mathcal{L}_{\theta\delta} & \mathcal{L}_{\theta\theta} \end{bmatrix} \begin{bmatrix} \boldsymbol{\delta} \\ \boldsymbol{\theta} \end{bmatrix}$$

where $\mathcal{L}$ is the linearized susceptance matrix of the network, $\mathcal{L} = \mathrm{Im}(\boldsymbol{Y}_A)$ in (3.10). The susceptance matrix $\mathcal{L}$ is a Laplacian matrix, $\mathcal{L}_{\delta\delta}$ is diagonal, $\mathcal{L}_{\theta\theta}$ is assumed to be invertible, and $\mathcal{L}_{\delta\theta} = \mathcal{L}_{\theta\delta}^T$.

Machine rotor dynamics, is given by the swing equation (4.1)

$$\mathcal{M}\dot{\boldsymbol{\omega}} = P_m - P_{\mathrm{load}} - P_e - \mathcal{D}\boldsymbol{\omega}.$$

Using Kron reduction [10, 132], P_e can be reduced to a function of state variables $\boldsymbol{\delta}$ and active power injection P_θ at the dc buses:

$$P_e = \mathcal{L}_\delta \boldsymbol{\delta} + \mathcal{L}_\theta P_\theta$$

where $\mathcal{L}_\delta = \mathcal{L}_{\delta\delta} - \mathcal{L}_{\delta\theta}\mathcal{L}_{\theta\theta}^{-1}\mathcal{L}_{\theta\delta}$ and $\mathcal{L}_\theta = \mathcal{L}_{\delta\theta}\mathcal{L}_{\theta\theta}^{-1}$. Note that both $\mathcal{L}$ and $\mathcal{L}_\delta$ are Laplacian matrices.

Assuming that there are no loads at the dc buses we have $P_\theta = P_{\mathrm{DC}}$. The dynamics of the power system, linearized around an initial operating point, is then given by

$$\begin{bmatrix}\dot{\boldsymbol{\delta}}\\ \dot{\boldsymbol{\omega}}\end{bmatrix} = \begin{bmatrix}0 & I\\ -\mathcal{M}^{-1}\mathcal{L}_\delta & -\mathcal{M}^{-1}\mathcal{D}\end{bmatrix}\begin{bmatrix}\boldsymbol{\delta}\\ \boldsymbol{\omega}\end{bmatrix} + \begin{bmatrix}0 & 0\\ \mathcal{M}^{-1} & \mathcal{M}^{-1}\mathcal{L}_\theta\end{bmatrix}\begin{bmatrix}P_m - P_{\mathrm{load}}\\ P_{\mathrm{DC}}\end{bmatrix}.$$

Similarly, voltage phase angle or frequency measurements at non generator buses is given by $\mathcal{L}_\theta^T\boldsymbol{\delta}$ and $\mathcal{L}_\theta^T\boldsymbol{\omega}$ respectively [133].

5.1.2 Two-Machine Networks Interconnected by Two HVDC Lines

To simplify the analysis we make the following assumption:

Assumption 5.1 (Damping Proportional to Inertia) The machine damping is evenly distributed and proportional to the machine inertia constant (which in turn is proportional to rated power)

$$D_{ij} = D_i\frac{M_{ij}}{M_{\Sigma,i}}$$

such that the machines become scaled versions of each other.

Remark 5.1 Since the mode (corresponding to eigenvalue λ) is assumed poorly damped ($|\operatorname{Re}(\lambda)| \ll |\lambda|$) Assumption 5.1 has little effect on model accuracy. This is further discussed in the Section 4.2.

As shown in Section 4.2, the swing mode of a two-machine system can then be represented using the relative phase and machine speeds $\Delta\delta_i = \delta_{i1} - \delta_{i2}$ and $\Delta\omega_i = \omega_{i1} - \omega_{i2}$, respectively. The linearized dynamics of the system is given by

$$\begin{bmatrix}\Delta\dot{\delta}_i\\ \Delta\dot{\omega}_i\end{bmatrix} = \underbrace{\begin{bmatrix}0 & 1\\ \frac{-V_i^2 M_{\Sigma,i}}{M_{i1}M_{i2}X_{\Sigma,i}} & \frac{-D_i}{M_{\Sigma,i}}\end{bmatrix}}_{A_i}\begin{bmatrix}\Delta\delta_i\\ \Delta\omega_i\end{bmatrix} + \underbrace{\begin{bmatrix}0 & 0\\ b_{i1} & b_{i2}\end{bmatrix}}_{B_i}\underbrace{\begin{bmatrix}P_{\mathrm{DC1}}\\ P_{\mathrm{DC2}}\end{bmatrix}}_{u}$$

where $X_{\Sigma,i}$ is the series reactance between the machine buses in Network i, A_i, and B_i is the system state and input matrix respectively. The input u are the controlled active power injections of the two dc links. As an example, the input matrix

$$B_1 = \begin{bmatrix}0 & 0\\ \frac{M_{12}(X_{12}+X_{13})-M_{11}X_{11}}{M_{11}M_{12}X_{\Sigma,1}} & \frac{M_{12}X_{12}-M_{11}(X_{11}+X_{13})}{M_{11}M_{12}X_{\Sigma,1}}\end{bmatrix} \tag{5.1}$$

is obtained for Network 1 in Figure 5.2.

Let $y_i = \Delta\omega_i$ be the measured output signal. The transfer function $G_i(s)$ from u to y_i then becomes

$$G_i = \begin{bmatrix} 0 & 1 \end{bmatrix} (sI - A_i)^{-1} B_i = \frac{s}{s^2 + s2\gamma_i + \Omega_i^2} \begin{bmatrix} b_{i1} & b_{i2} \end{bmatrix}$$

where

$$\Omega_i = \sqrt{\frac{V_i^2 M_{\Sigma,i}}{M_{i1} M_{i2} X_{\Sigma,i}}}$$

is the undamped frequency of Network i and

$$\gamma_i = \frac{1}{2} \frac{D_i}{M_{\Sigma,i}}.$$

The HVDC-interconnected system to be controlled, is thus represented by the transfer function

$$G = \begin{bmatrix} G_1 \\ -G_2 \end{bmatrix} = \begin{bmatrix} \frac{s}{s^2+s2\gamma_1+\Omega_1^2} & 0 \\ 0 & \frac{s}{s^2+s2\gamma_2+\Omega_2^2} \end{bmatrix} \begin{bmatrix} b_{11} & b_{12} \\ -b_{21} & -b_{22} \end{bmatrix}. \tag{5.2}$$

5.2 Model Specifications

The mutual placement of the HVDC terminals determine the interaction of the two ac networks due to HVDC active power modulation. Thus it will play a big role in POD control design. If we consider the damping of one dominant interarea mode in each of the asynchronous ac networks there are essentially three relevant configurations possible using two HVDC links.

Two-Sided HVDC-Configuration

In a *two-sided* HVDC-configuration the HVDC terminals are located on each side of the mass-weighted electrical midpoint in each system, as seen in Figure 5.1. The mass-weighted electrical midpoint is the location where the interarea mode is uncontrollable using HVDC active power injection. At this location, the corresponding element in the input matrix (5.1) is zero.

Remark 5.2 In a meshed grid, such as the N32 network shown in Figure 4.13, it is hard to identify the exact location of the mass-weighted electrical midpoint. However, the exact location of the midpoint is only interesting for a theoretical understanding of the control problem. In practice, we only consider dc buses with reasonable controllability of the mode. That is, we only consider HVDC links with at least one of its terminals clearly separated from the electric midpoint.

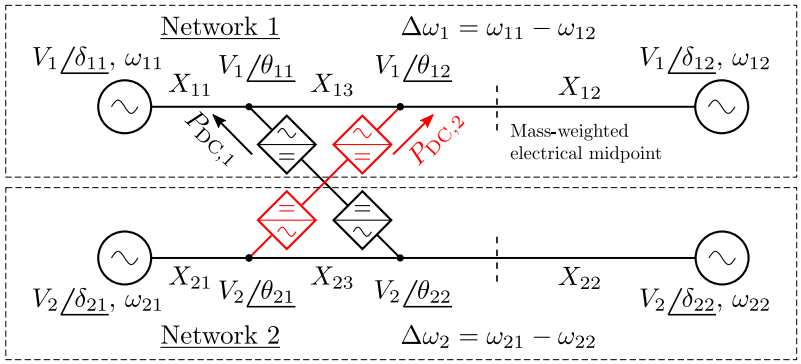

Figure 5.2: One-sided HVDC-configuration between two asynchronous two-machine networks.

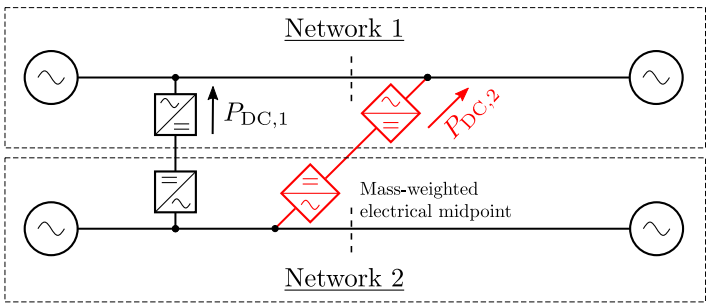

Figure 5.3: Uneven HVDC-configuration between two asynchronous two-machine networks.

One-Sided HVDC-Configuration

We use the term *one-sided* to describe a configuration where both HVDC terminals are located on the same side of the mass-weighted electrical midpoint in each system, as seen in Figure 5.2.

Uneven HVDC-Configuration

The term *uneven* will be used to describe the HVDC-configuration seen in Figure 5.3 where the HVDC terminals are located on either side of the mass-weighted electrical midpoint in one of the ac networks, and on the same side in the other network.

A special case of the uneven configuration is when one of the dc terminals is located directly in the mass-weighted electrical midpoint. It is quite intuitive that interaction between oscillatory modes can be avoided when providing POD in such a setup since the centrally placed link will only affect one of the networks. In the following sections we will investigate this further. For this, we first specify three models with the considered HVDC-configurations.

Table 5.1: Electrical positions of HVDC terminals for three different HVDC-configurations.

	Network 1		Network 2	
Configuration	$X_{B,11}$	$X_{B,12}$	$X_{B,21}$	$X_{B,22}$
Two-Sided	0.6	-0.4	0.4	-0.6
One-Sided	0.6	0.4	0.4	0.6
Uneven	0.6	-0.4	0.6	0.4

5.2.1 Model Parameters

To study the effect of multivariable interactions on the HVDC-interconnected system we consider two ac networks, each represented by a two-machine model, interconnected with two point-to-point HVDC lines as seen in Figures 5.1 to 5.3. The (mass-weighted) electrical position[2] $X_{B,ih} \in [-1, 1]$ for the three considered configurations is shown in Table 5.1. To isolate the effect of HVDC-configuration we considered the two networks to be identical in all scenarios. As shown in Chapter 4 the system would therefore not be controllable using only one dc link. For all three configurations, model dynamics are given by (5.2) with

- no inherent damping, $D_1 = D_2 = 0$;
- undamped modal frequencies $\Omega_1 = \Omega_2 = 0.5\,\text{Hz}$;
- constant voltage $V_1 = V_2 = 1\,\text{p.u.}$ assumed at all buses;
- identical machine inertia constants $M_{ij} = 2HS_r/\omega_{\text{nom}}$. For each machine: rated power $S_r = 4\,\text{p.u.}$, inertia time constant $H = 6\,\text{s}$, and $\omega_{\text{nom}} = 2\pi f_{\text{nom}}$ where $f_{\text{nom}} = 50\,\text{Hz}$ is the nominal system frequency. Since the networks are symmetrical, the mass-weighted electrical midpoint is the same as the electrical midpoint given by $X_{B,ih}$.

Transfer Functions

The transfer functions (5.2) of the three systems specified in Table 5.1 becomes

$$G_{\text{two-sided}} = \begin{bmatrix} \frac{s}{s^2+\pi^2} & 0 \\ 0 & \frac{s}{s^2+\pi^2} \end{bmatrix} \begin{bmatrix} 3.9 & -2.6 \\ -2.6 & 3.9 \end{bmatrix}, \tag{5.3}$$

$$G_{\text{one-sided}} = \begin{bmatrix} \frac{s}{s^2+\pi^2} & 0 \\ 0 & \frac{s}{s^2+\pi^2} \end{bmatrix} \begin{bmatrix} 3.9 & 2.6 \\ -2.6 & -3.9 \end{bmatrix}, \tag{5.4}$$

and

$$G_{\text{uneven}} = \begin{bmatrix} \frac{s}{s^2+\pi^2} & 0 \\ 0 & \frac{s}{s^2+\pi^2} \end{bmatrix} \begin{bmatrix} 3.9 & -2.6 \\ -3.9 & -2.6 \end{bmatrix}. \tag{5.5}$$

[2]Calculated according to (5.1), but leaving out machine inertia constants.

The dynamics of the two ac systems are given by the first (diagonal) matrix while the second (input) matrix describe how the corresponding input u_h affect each output y_i.

For the two- and one-sided configuration (5.3) and (5.4) the input have been ordered so that the plant, G, is as diagonal as possible. That is, input u_1 will have most effect on y_1 while u_2 have most effect on y_2. For the uneven configuration (5.5) there is no clear way to order the inputs.

Since the off-diagonal entries of the input matrices are non-zero, each input will affect both outputs. That is, there is *interaction* between the inputs and outputs. How these multivariable interactions affect the potential benefit of adding additional HVDC lines will be studied in the following sections.

5.3 Analysis of Multivariable Interactions

Some of the difficulties in MIMO system control are an increased sensitivity to uncertainties due to directionality and interactions that may occur between the inputs and outputs. Here we introduce two useful measures for quantifying the degree of directionality and the level of interactions.

Definition 5.1 (Condition Number [115]) The condition number of a matrix G is the ratio between the maximum and minimum singular values

$$\kappa(G) := \frac{\bar{\sigma}(G)}{\underline{\sigma}(G)}.$$

A matrix with a large condition number is said to be *ill-conditioned*. If G is a transfer function then the condition number may be frequency dependent.

If the condition number is small, then problems with multivariable interactions are not likely to be serious. If the condition number are large however this may indicate a control problem. The large condition number may also be the result of input and output scalings. To avoid this, we will instead use the minimized condition number over all possible input and output scalings W_1 and W_2 [115]

$$\kappa^*(G) = \min_{W_1, W_2} \kappa(W_1 G W_2).$$

Another useful measure (independent of input and output scaling) is the RGA.

Definition 5.2 (Relative Gain Array (RGA) [115]) The RGA of a non-singular square matrix G is defined as the Hadamard product (element wise product)

$$\mathrm{RGA}(G) := G \times (G^{-1})^T.$$

The RGA matrix indicates the coupling between inputs and outputs. One property of the RGA is that rows and columns all sum up to one. Input-output combination should be selected so that the corresponding RGA element is as close to 1 as possible [115].

Table 5.2: Condition number and RGA for the HVDC-interconnected systems (5.3) to (5.5).

	Two-Sided	One-Sided	Uneven
κ^*	5	5	1
RGA	$\begin{bmatrix} 1.8 & -0.8 \\ -0.8 & 1.8 \end{bmatrix}$	$\begin{bmatrix} 1.8 & -0.8 \\ -0.8 & 1.8 \end{bmatrix}$	$\begin{bmatrix} 0.5 & 0.5 \\ 0.5 & 0.5 \end{bmatrix}$

5.3.1 Analysis of HVDC-Interconnected Systems

The (minimized) condition number and RGA of the three systems specified in Section 5.2 are shown in Table 5.2. Since the dynamics of the systems are given by a diagonal matrix (5.3) to (5.5), the condition number and RGA are the same for all frequencies.

We see that the condition number and RGA is identical for the one- and two-sided systems. This indicates similar issues with respect to multivariable interactions. Because of this we only consider the one-sided configuration in the following control design and simulation study. For the uneven configuration, we find that the minimized condition number $\kappa^*(G_{\text{uneven}}) = 1$. This indicate that directionality does not limit the achievable performance for the uneven configuration.

5.4 Coordinated Control Design

In this Section we study the HVDC-interconnected system defined in Section 5.2. The goal is to see how multivariable interactions and directionality affect system performance when trying to improve POD in both networks. As shown in Table 5.2 the one- and two-sided HVDC-configurations have the same problem with directionality. We therefore choose to leave out the two-sided configuration.

The one-sided configuration is compared to the uneven configuration which according to Table 5.2 should have no issues with multivariable interactions. To see the implications of this we design four different multivariable controllers designed to improve POD in both of the interconnected ac networks. We then present the simulated system response to a 0.4 p.u. load step at machine-bus 1 in Network 1[3].

5.4.1 Single-Line Control

To counteract ac power flows and improve POD, the dc active power is controlled uniformly for the two HVDC links

$$u_1 = u_2 = \begin{bmatrix} -k & k \end{bmatrix} y$$

where we let $k = 1/\text{Hz}$. As shown in Chapter 4, the achievable POD performance will be limited by modal interactions. Increasing the gain will cause system eigenvalues

[3]System is modeled using (4.1) and (4.2) to incorporate nonlinear power flow.

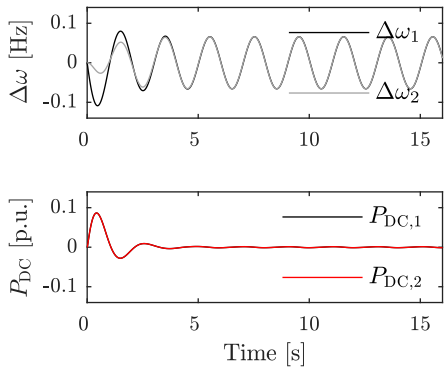

Figure 5.4: Single-line control of the one-sided HVDC-configuration. Relative machine speeds and HVDC active power following a 0.4 p.u. load step at machine-bus 1 in Network 1.

corresponding to the two interarea modes to approach each other (see Figure 4.8). The controllability of the interarea modes are thereby lost. In this case, since $\Omega_1 = \Omega_2$ the interarea modes are uncontrollable no matter the feedback gain. The only achievable benefit is sharing of the disturbance between the two networks as can be seen in Figure 5.4. In this case, performance can be improved using multivariable control methods.

5.4.2 Decentralized Control

The simplest multivariable control approach is to use a diagonal block controller K where each input is paired with one suitable output measurement. Assuming that each actuator is controlled independently using local measurements, this control method can be called decentralized. Decentralized control works well if the condition number of G is small and the controllability from chosen input-output pairings are high relative to the other input-output combinations [115]. For the one-sided (5.4) and uneven (5.5) HVDC-configurations, satisfactory decentralized control is realized with the diagonal controller

$$u = \begin{bmatrix} -k & 0 \\ 0 & \operatorname{sgn}(b_{22})k \end{bmatrix} y, \quad \operatorname{sgn}(b_{11}) := 1. \tag{5.6}$$

In Figure 5.5 it is seen that the decentralized control method manages to circumvent the limitations of the single-line control. For the one-sided configuration in Figure 5.5a however, this comes at the cost of cycling extra power through the HVDC lines. For the uneven configuration in any input-output pairing is suitable, according to the RGA in Table 5.2. We also see in Figure 5.5b that the disturbance is attenuated faster with less input usage. This can be expected since

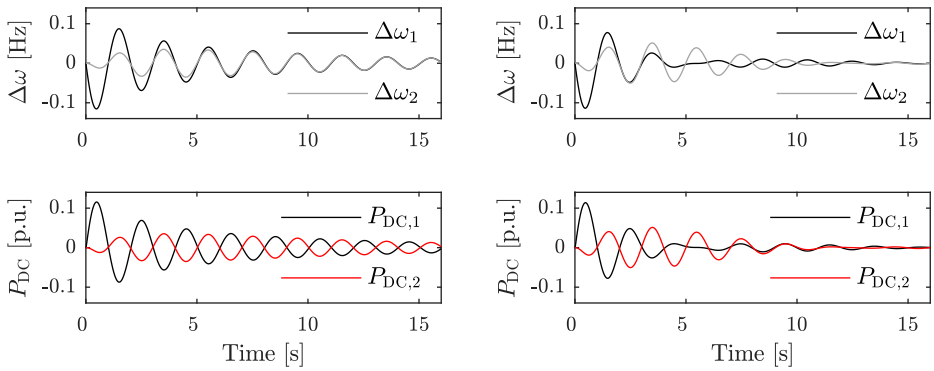

(a) One-sided HVDC-configuration

(b) Uneven HVDC-configuration

Figure 5.5: Decentralized control. Relative machine speeds and HVDC active power following a 0.4 p.u. load step at machine-bus 1 in Network 1.

$\kappa(G_{\text{uneven}}) > \kappa(G_{\text{one-sided}})$ indicates that the uneven configuration has less issues with multivariable interactions.

Since a decentralized control method makes no attempt to cancel interactions in G, resulting performance may be poor if these are considerable. This can be improved by using decoupling control where we attempt to cancel out off-diagonal input-output interactions.

5.4.3 Decoupling Control

By shaping $\tilde{G} = GW$ to be a diagonal system, independent control of each input-output combination can be realized using a diagonal controller. Each control-loop can be tuned independently using single-input single-output (SISO) methods for the corresponding input-output path [115]. The pre-compensator W can be chosen in many ways[4]. Here we choose

$$W = \begin{bmatrix} 1 & \frac{-b_{12}}{b_{11}} \\ \frac{-b_{21}}{b_{22}} & 1 \end{bmatrix} \tag{5.7}$$

and thus

$$\tilde{G} = \begin{bmatrix} \frac{s}{s^2+\Omega_1^2} & 0 \\ 0 & \frac{s}{s^2+\Omega_2^2} \end{bmatrix} \begin{bmatrix} b_{11} - \frac{b_{12}b_{21}}{b_{22}} & 0 \\ 0 & -\left(b_{22} - \frac{b_{12}b_{21}}{b_{11}}\right) \end{bmatrix}.$$

[4]Choosing $W = G^{-1}$ would result in $\tilde{G} = I$. To make the controller proper however, additional poles would have to be added to K.

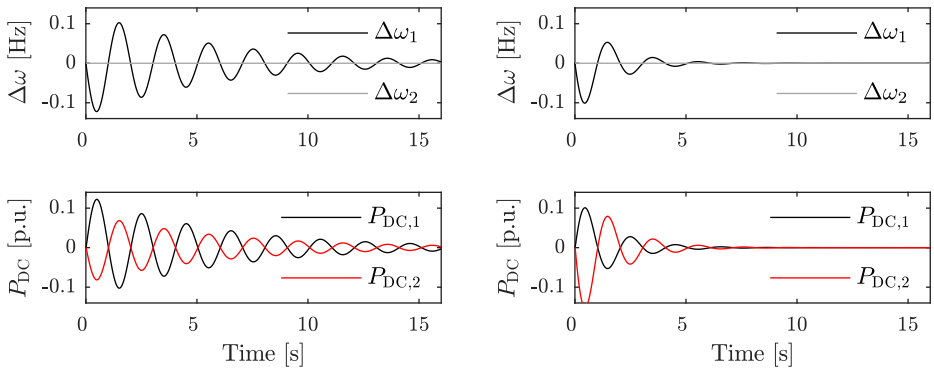

(a) One-sided HVDC-configuration (b) Uneven HVDC-configuration

Figure 5.6: Decoupling control. Relative machine speeds and HVDC active power following a 0.4 p.u. load step at machine-bus 1 in Network 1.

Disturbance rejection, comparable to the decentralized controller (5.6), is achieved using

$$u = W \begin{bmatrix} -k & 0 \\ 0 & \operatorname{sgn}(b_{22})k \end{bmatrix} y = Ky, \quad \operatorname{sgn}(b_{11}) = 1. \tag{5.8}$$

With a decoupling controller, the excitation of the interarea mode in the assisting system is avoided as seen in Figure 5.6. The downside of the decoupling control method may be an increased input usage since one link is controlled to counteract the effect on the assisting network. If G is ill-conditioned, no obvious input-output combination exist to control the multivariable system. This makes it unsuitable for both decoupling and decentralized control.

Decoupling using a constant matrix is possible since we represent the interarea mode using individual state variables and assume that these are available from measurement. Basically, we are decoupling the system at the frequency of the interarea mode. In Section 5.6 we generalize this control method to a higher order system.

Remark 5.3 Asynchronous grids with multiple HVDC-interconnections spread over vast geographical distances are suitable candidates for exploiting the benefits of decoupling control. A possible candidate could for instance be the interconnections between the Nordic synchronous grid and the Baltic region shown in Figure 1.5. Here, the NordBalt link between southern Sweden and Lithuania could potentially be coordinated with the EstLink interconnections between Finland and Estonia, to dampen north–south interarea modes in the Nordic grid, while simultaneously dampening any potential east–west spanning interarea modes in the IPS/UPS grid.

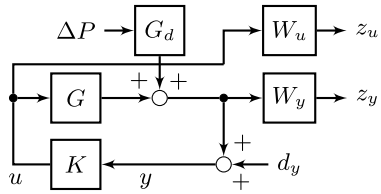

Figure 5.7: The closed-loop feedback system used for $\mathcal{H}_2$ synthesis. Block G_d represents the transfer function from machine bus disturbances to relative machine speeds.

Remark 5.4 Changing ac power flows, system inertia or the connection/disconnection of ac transmission lines may affect the decoupling performance of the controller since the (mass-weighted) electrical midpoint or the HVDC terminals position relative to each other may change. However, such uncertainties are unlikely to be severe enough to cause instability if the system is eligible for decoupling control in the first place.

5.4.4 $\mathcal{H}_2$ Optimal Control

Optimization based methods have been excessively studied for multivariable feedback design in power systems [9, 12]. Such design methods offer a structured way to synthesize multivariable feedback controllers which can potentially yield an better system-performance than a decentralized control design. Here we will consider an $\mathcal{H}_2$ optimal controller. Since the $\mathcal{H}_2$-norm weights the disturbances over all channels and frequencies, a controller yielding satisfactory performance can usually be achieved without too much tuning.

The $\mathcal{H}_2$ controller (essentially a linear quadratic Gaussian (LQG) controller [115]) is obtained as the controller K that minimizes the $\mathcal{H}_2$-norm of the closed-loop system shown in Figure 5.7, from input variables ΔP and d_y to performance variables z_y and z_u. For a dynamic response similar to that of the decentralized and decoupled controller, the controller is tuned with

- external inputs $|\Delta P_{ij}| \leq 0.4\,\text{p.u.}$ and $|d_{yi}| \leq 5\%,\ i, j \in \{1, 2\}$ over all frequencies;
- performance weights $W_z = 1$ and $W_u = 5$.

Comparing Figures 5.5a and 5.8a we see that $\mathcal{H}_2$ synthesis yields a controller similar to that of the decentralized controller (5.6). This is because the decoupling controller in the one-sided configuration decouples the system by controlling one dc link in the wrong direction. Since this decoupling control action counteracts disturbance attenuation this will not be the $\mathcal{H}_2$ optimal control method.

For the uneven HVDC-configuration we find that the $\mathcal{H}_2$ optimal controller resembles a decoupling controller as seen in Figures 5.6b and 5.8b. This is because disturbance attenuation and decoupling requires the same dc power direction as

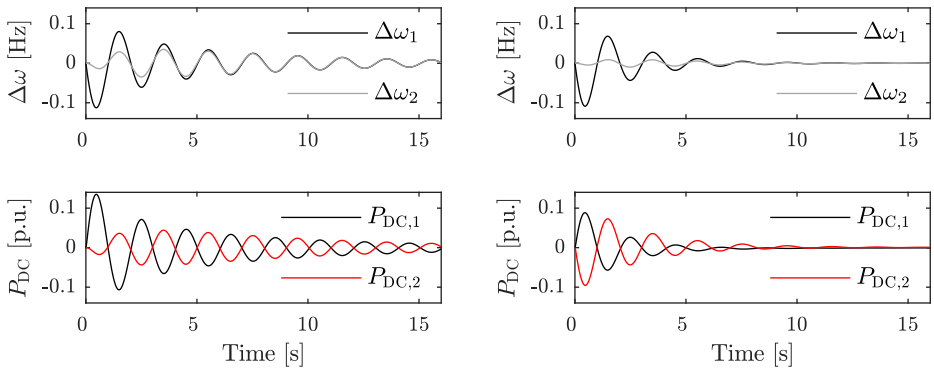

(a) One-sided HVDC-configuration

(b) Uneven HVDC-configuration

Figure 5.8: $\mathcal{H}_2$ optimal control. Relative machine speeds and HVDC active power following a 0.4 p.u. load step at machine-bus 1 in Network 1.

indicated by the RGA in Table 5.2. Similarly, if the system is ill-conditioned, the $\mathcal{H}_2$ optimal controller will resemble the single-line controller since cancellation of multivariable interactions will require too much input usage.

5.5 Closed-Loop Stability Properties: HVDC Link Failure

With single-line control, a disconnection will lead to a weaker control action. In the case of decentralized control, disconnection of one HVDC link will leave one of the networks outside the feedback-loop altogether. Neither of the mentioned contingencies will destabilize the system so the $N-1$ criterion (with respect to the HVDC control) is fulfilled without additional safety actions. With the decoupling controller however, it can be shown (see Appendix 5.A) that if

$$-\operatorname{sgn}(b_{22})b_{21}b_{12} > 0, \quad \operatorname{sgn}(b_{11}), \quad \text{and} \quad \operatorname{sgn}(k) := 1 \tag{5.9}$$

is violated, the system will be destabilized by the HVDC controller following a dc link failure. Equation (5.9) thus represent an $N-1$ stability criterion with respect to dc link (or control actuator) failure. If the inherent damping is weak, then instability is likely to ensue if no safety measures are taken.

The $N-1$ stability criterion (5.9) can also be assessed by studying the RGA. The RGA of a two-by-two matrix is given by [115]

$$\text{RGA} = \begin{bmatrix} q & 1-q \\ 1-q & q \end{bmatrix}$$

where for (5.2)

$$q = \frac{1}{1 - \frac{b_{12}b_{21}}{b_{11}b_{22}}}.$$

Assuming that input and outputs are ordered so that $b_{11}, b_{22} \neq 0$, then if (5.9) holds, $0 < q \leq 1$ and all RGA elements are non-negative.

Measurement Failure

If the system experiencing measurement failure is open-loop stable then instability does not ensue.

Communication Failure

If a measurement signal fails to reach one of the dc link controllers and (5.9) is violated, then one link will provide negative feedback while the other link provides positive feedback. If the communication to the negative feedback link fails then the system will be destabilized.

5.6 Decoupling Control in Higher-Order Systems

The benefit of a decoupling POD controller is that excitation of poorly damped modes in the assisting network can be avoided. The method proposed in Section 5.4.3 achieved this using a proportional controller. In this section we will study how this can be extended to a larger system.

Consider a linear time-invariant (LTI) system

$$G = C(sI - A)^{-1}B \stackrel{s}{=} \left[\begin{array}{c|c} A & B \\ \hline C & 0 \end{array}\right].$$

rewritten on modal form (see Appendix 4.B)

$$G_\mu \stackrel{s}{=} \left[\begin{array}{c|c} \Lambda & \mathcal{V}^H B \\ \hline C_\mu & 0 \end{array}\right] = \left[\begin{array}{c|c} \Lambda & B_\Lambda \\ \hline C_\mu & 0 \end{array}\right] \tag{5.10}$$

where

- $\Lambda = \text{diag}\{\lambda_1, \ldots, \lambda_n\}$ has eigenvalues of A (poles of G) on its diagonal;
- $\mathcal{V} = [v_1, \ldots, v_n]$ is the left modal matrix of A s.t. $\mathcal{V}^H A = \Lambda \mathcal{V}^H$;
- μ is the set of modes $\xi_\mu = \mathcal{V}_\mu^H x$ that we are interested to control.

Since Λ is diagonal, system dynamics are decoupled. The poles, and therefore the stability of each mode, can be controlled individually given that a good estimate of ξ_μ is used as feedback signal [134].

If we design W so that $\mathcal{V}_\mu^H B W = B_\mu^\Lambda W$ is diagonal, then λ_l, $l \in \mu$ can be stabilized without exciting the modes ξ_m, $m \in \mu$, $m \neq l$. If the transfer function from $|\mu|$ inputs to the $|\mu|$ outputs in G_μ is invertible, then the system can be decoupled using a constant pre-compensator matrix $W \in \mathbb{C}^{|\mu| \times |\mu|}$.

Complex modal states appear in complex conjugate pairs s.t. $\xi_{l+1} = \bar{\xi}_l$. If $y = \mathrm{Re}(\mathcal{V}_\mu^H)(\mathcal{V}^H)^{-1}\xi = \mathrm{Re}(\mathcal{V}_\mu^H)x$ is chosen as feedback signal, only one element in each complex conjugated pairs are needed in μ (see Appendix 5.B).

Assumption 5.2 (Phase Condition) Assume that the inputs affect each mode ξ_n with the same phase. Then

$$B_\mu^\Lambda = \Phi\,\mathrm{Re}(\mathcal{V}_\mu^H)B$$

where

$$\Phi = \mathrm{diag}\left(e^{j\varphi_1}, \ldots, e^{j\varphi_{|\mu|}}\right).$$

The selected modes ξ_μ can then decoupled with the pre-compensator

$$W = (\mathrm{Re}(\mathcal{V}_\mu^H)B)^{-1} \in \mathbb{R}^{|\mu|\times|\mu|}. \tag{5.11}$$

Remark 5.5 The eigenvectors are not uniquely defined. When designing (5.11) it is good to align $\mathcal{V}$ so that the condition number $\kappa(\mathrm{Re}(\mathcal{V}_\mu^H)B)$ is small.

A good approach is to set $\angle\mathcal{V}_\mu(\bar{\omega}_\mu) = 0$ or π. The notation $\mathcal{V}_\mu(\bar{\omega}_\mu)$ means that we consider the elements of the left eigenvectors that corresponds to the states representing rotor speeds of the machines with highest participation in each of the modes in μ. The mode shape, as given by rotor speeds, will then be close to the real axis as seen in Figures 5.9b and 5.15.

The proposed decoupling controller is demonstrated in two simulations examples. In Section 5.7 we consider the interconnection of two three-machine networks. This configuration lets us see how the decoupling control targets specific modes in the system. In Section 5.8 we study the $N-1$ stability criterion (5.9) on two HVDC-interconnected 32-bus networks.

5.7 Illustrative Example

To illustrate the selectivity of the decoupling method, we consider the interconnection of two identical ac networks as shown in Figure 5.9a. Each of the networks have an interarea mode Ω_1 at 0.5 Hz and a faster *local* mode Ω_2 at 1.1 Hz. The decoupling controller (designed according to Section 5.6) are then compared to a centralized optimal controller.

5.7.1 Model

The linearized system dynamics (as described in Section 5.1) are given by

$$s\begin{bmatrix}\boldsymbol{\delta}\\ \boldsymbol{\omega}\end{bmatrix} = \underbrace{\begin{bmatrix}0 & I\\ -\mathcal{M}^{-1}\mathcal{L}_\delta & -\mathcal{M}^{-1}\mathcal{D}(s)\end{bmatrix}}_{A}\begin{bmatrix}\boldsymbol{\delta}\\ \boldsymbol{\omega}\end{bmatrix} + \underbrace{\begin{bmatrix}0\\ \mathcal{M}^{-1}\mathcal{L}_\theta\end{bmatrix}}_{B}P_{\mathrm{DC}}$$

where:

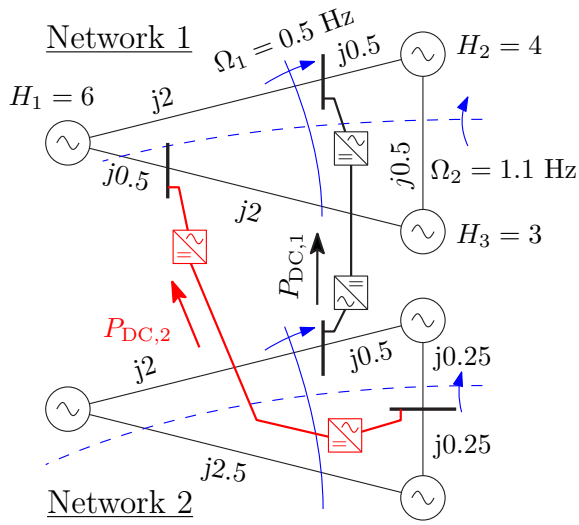

(a) HVDC-interconnected system.

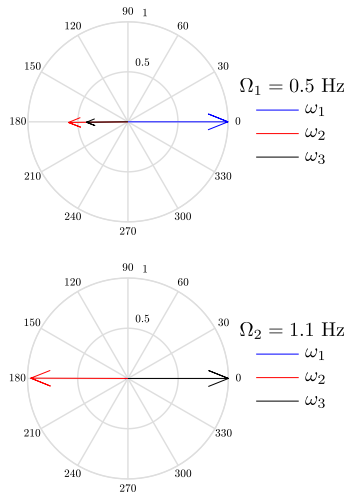

(b) Mode shapes of interarea mode Ω_1 and local mode Ω_2 in each three-machine network.

Figure 5.9: Two identical three-machine networks interconnected by two HVDC links. Line impedances shows electrical position of dc buses in each network.

- Matrix $\mathcal{M}$ is diagonal with the machine inertia constants $2H_iS_r/\omega_{\text{nom}}$, $i \in \{1, \dots, 6\}$ on its diagonal. The machine inertia time constants H_i are shown Figure 5.9a. Rated power of each machine $S_r = 4\,\text{p.u.}$, $\omega_{\text{nom}} = 2\pi f_{\text{nom}}$, and $f_{\text{nom}} = 50\,\text{Hz}$.

- Mechanical input power is affected both by a proportional damping constant as well as a first-order governor (4.43). Diagonal elements in $\mathcal{D}(s)$ are given by the transfer function

$$D_i(s) = \frac{M_i}{M_\Sigma}\left(2 + \frac{25}{4s+1}\right)\frac{1}{\omega_{\text{nom}}}$$

  where M_Σ is the total inertia in each respective network. The machines are thereby scaled versions of each-other and Assumption 5.1 holds.

- Using Kron reduction [132] the network Laplacian matrix and input matrix

are

$$\mathcal{L}_\delta = \begin{bmatrix} 0.8 & -0.4 & -0.4 & 0 & 0 & 0 \\ -0.4 & 2.4 & -2 & 0 & 0 & 0 \\ -0.4 & -2 & 2.4 & 0 & 0 & 0 \\ 0 & 0 & 0 & 0.8 & -0.4 & -0.4 \\ 0 & 0 & 0 & -0.4 & 2.4 & -2 \\ 0 & 0 & 0 & -0.4 & -2 & 2.4 \end{bmatrix}, \text{ and } \mathcal{L}_\theta = \begin{bmatrix} 0.2 & 0.8 \\ 0.8 & 0 \\ 0 & 0.2 \\ -0.2 & 0 \\ -0.8 & -0.5 \\ 0 & -0.5 \end{bmatrix}.$$

5.7.2 Goal

Design a multivariable controller that targets the 0.5 Hz interarea mode in each ac network. The controller should decouple the two modes to avoid exciting the 0.5 Hz mode in the assisting network.

5.7.3 Decoupling Control Design

Let the two eigenvalues (one in each complex conjugated pair) be denoted λ_μ an let the corresponding left eigenvectors be given by $\mathcal{V}_\mu$. We have that

$$\angle(\mathcal{V}_\mu^H B) = \begin{bmatrix} -\pi & 0 \\ 0 & 0 \end{bmatrix}$$

thus Assumption 5.2 holds and adequate decoupling should be achievable with a constant pre-compensator.

With $\boldsymbol{V}_\mu = \mathrm{Re}(\mathcal{V}_\mu)$ we have that

$$B_\mu^\Lambda = \boldsymbol{V}_\mu^T B = \begin{bmatrix} -1.5 & 1.8 \\ 1.5 & 2.6 \end{bmatrix}$$

and

$$\mathrm{RGA}(G_\mu) = B_\mu^\Lambda \times \left((B_\mu^\Lambda)^{-1}\right)^T = \begin{bmatrix} 0.6 & 0.4 \\ 0.4 & 0.6 \end{bmatrix} \tag{5.12}$$

thus we see that the $N-1$ stability criterion (5.9) is fulfilled and the system should be suitable for decoupling control.

The decoupling matrix (with columns scaled to have magnitude one on diagonal) becomes

$$W = \left(B_\mu^\Lambda\right)^{-1} \overset{\text{scale}}{=} \begin{bmatrix} 1 & -1.2 \\ -0.6 & -1 \end{bmatrix}.$$

In practice, $z_\mu = \boldsymbol{V}_\mu x$ is not available and has to be estimated. Here we assume that machine speed measurements are available and base the observer on the corresponding elements in $\boldsymbol{V}_\mu$[5]. To have a feedback signal that is zero in steady

[5] See the mode shape of interarea mode Ω_1 in Figure 5.9b.

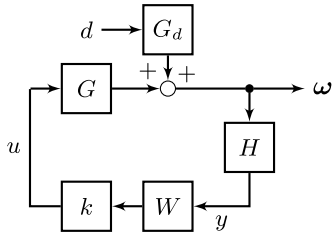

Figure 5.10: Closed-loop system with decoupling POD control.

state we scale the output matrix as in (4.48). Thus the output is given by

$$y = H\boldsymbol{\omega} = \underbrace{\begin{bmatrix} 1 & -0.6 & -0.4 & 0 & 0 & 0 \\ 0 & 0 & 0 & 1 & -0.6 & -0.4 \end{bmatrix}}_{H} \boldsymbol{\omega}.$$

The resulting closed-loop system with

$$u = kWH\boldsymbol{\omega} \tag{5.13}$$

can be seen in in Figure 5.10 where we have added an external input d acting on the system through G_d. For reasonable input usage, we let $k = 0.2\,\text{p.u./Hz}$.

Remark 5.6 In Chapter 4 we designed a controller considering only one link and found that optimal feedback gain is limited by modal interaction. Here, arbitrary high POD can be achieved since the multivariable control circumvents these limitations. This might not be desirable however since this comes at a higher input cost, increased interaction with other modes, and an increased sensitivity to model error. If the eigenvectors are incorrectly estimated, the feedback will affect other eigenvalues and which might destabilize the system. Therefore it is good practice to be conservative when designing the feedback control.

5.7.4 $\mathcal{H}_2$ Optimal Control Design

As shown in Section 5.4.4 similar results can easily be obtain with a $\mathcal{H}_2$ optimal control design. Here we consider the $\mathcal{H}_2$ controller K that minimizes the closed-loop system shown in Figure 5.11, where

- load disturbances at machine-buses, $|\Delta P| \leq 0.4\,\text{p.u.}$,
- measurement noise, $|d_y| \leq 5\,\%$,

are the considered external inputs. To target the interarea mode, we choose Ω_1 from each network as a performance variable. Since we also have observability and controllability of the local modes we add Ω_2 as a performance variable. To get a

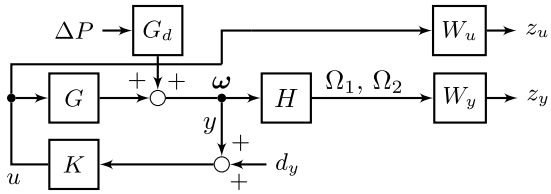

Figure 5.11: The closed-loop feedback system used for $\mathcal{H}_2$ synthesis. Block G_d represents the transfer function from machine bus disturbances to relative machine speeds. Block H gives the mode shapes (Figure 5.9b) of the interarea and local modes in each network.

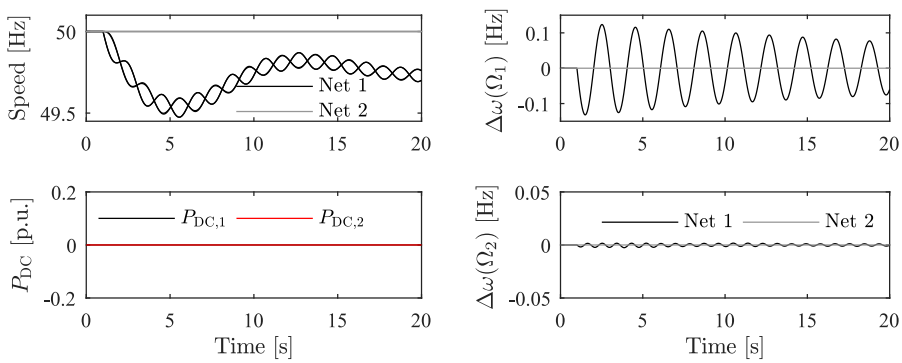

(a) Machine speeds and HVDC active power. (b) Interarea modes Ω_1 and local modes Ω_2 in the two networks.

Figure 5.12: The HVDC-interconnected system in Figure 5.9a following a 0.4 p.u. load increase at machine-bus 1 in Network 1.

POD performance similar to (5.13) we weight the performance variables by $W_y = 1$ and input usage $W_u = 2.5\frac{s+\pi}{s}$. The integrator is added to avoid steady-state input usage. Resulting K is reduced to 10^{th} order[6] using balanced residualization [115].

5.7.5 Simulation Results

The considered scenario is a 0.4 p.u. load increase at machine-bus 1 in Network 1. In Figure 5.12 the system response with no HVDC control is shown. The load step causes a frequency drop in Network 1 and also triggers the interarea mode Ω_1 at 0.5 Hz as seen in Figure 5.12b. The local mode Ω_2 is fairly unaffected by the load disturbance.

We now add the decoupling POD controller (5.13) and consider the same disturbance scenario. As seen in Figure 5.13 the control method greatly improves the

[6]The original controller is 18^{th} order, the same as the open-loop system.

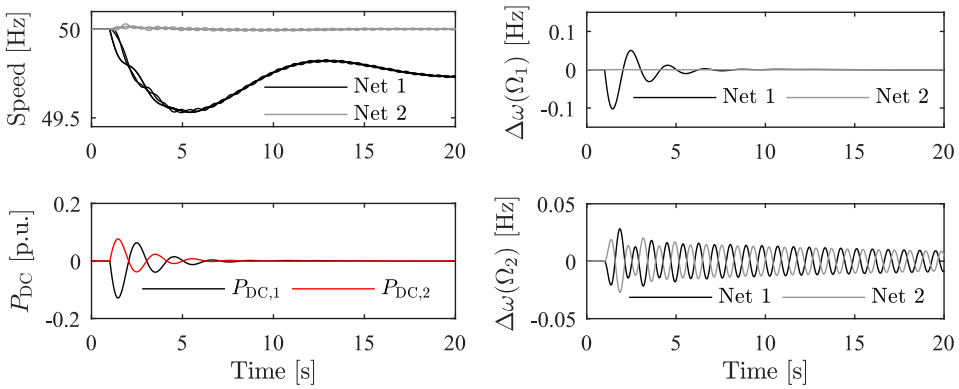

(a) Machine speeds and HVDC active power.

(b) Interarea modes Ω_1 and local modes Ω_2 in the two networks.

Figure 5.13: Same scenario as in Figure 5.12 but with the decoupling POD controller (5.13) and $k = 0.2\,\text{p.u./Hz}$.

damping of Ω_1 in Network 1 without exciting the corresponding interarea mode in Network 2. However, since only decoupling between the interarea modes is implemented, other modes may be affected. For example, we see that the control action excites the local mode Ω_2 in both networks. To include these two modes in the design, and to decouple these with a constant pre-compensator, we would require two more HVDC links. For a design to target all four modes using only two links, it is better to instead opt for a dynamic controller, e.g., using the proposed $\mathcal{H}_2$ optimal control design.

In Figure 5.14 the same disturbance scenario is simulated using the $\mathcal{H}_2$ controller. As indicated by the RGA (5.12) the HVDC-configuration is uneven with respect to the interarea modes Ω_1. The $\mathcal{H}_2$ controller therefore decouples the interarea modes fairly well as seen in Figure 5.14b. In addition to POD of the interarea mode, the controller is also tuned to attenuate oscillations in the local modes Ω_2. The corresponding RGA for the local modes is

$$\text{RGA}(G_{\Omega_2}) = B^{\Lambda}_{\Omega_2} \times \left((B^{\Lambda}_{\Omega_2})^{-1}\right)^T = \begin{bmatrix} 2.9 & -1.9 \\ -1.9 & 2.9 \end{bmatrix}$$

thus the $\mathcal{H}_2$ controller does not attempt to decouple the system at the frequency of the local modes, Ω_2, as seen in Figure 5.14b.

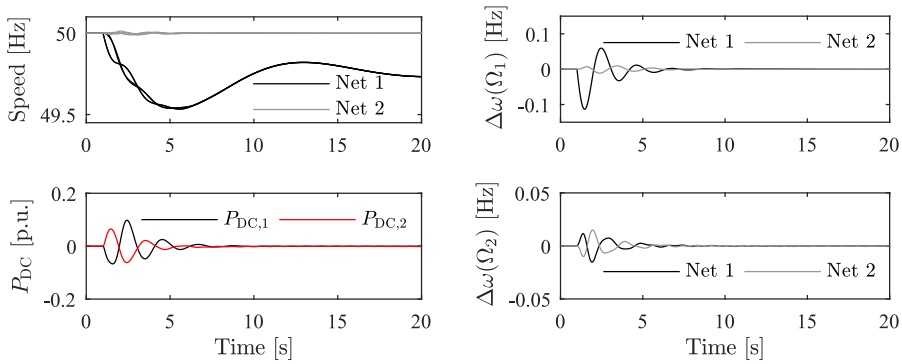

(a) Machine speeds and HVDC active power. (b) Interarea modes Ω_1 and local modes Ω_2 in the two networks.

Figure 5.14: Same scenario as in Figure 5.12 but with a $\mathcal{H}_2$ controller targeting both local and interarea modes.

5.8 Simulation Study

In this section we will analyze $N-1$ stability with respect to failure of one HVDC link while using decoupling control. We consider an artificial system made up by the interconnection of two Nordic 32-bus (N32) Cigré test systems [43] implemented in Simulink[7].

The N32 system has large power transfers from the hydro dominated north and external areas (lumped into north area) to loads in the central and southwestern areas (lumped into the south area) where a large amount of thermal power is installed. The model shows a 0.5 Hz interarea mode between the north and south areas as shown in Figure 5.15. For illustrative purposes, the damping of this mode is reduced to roughly 1% by modifying the PSS of the machines at buses 4072 and 1042. Since we want to investigate stability issues following HVDC link failure, the system needs to be controllable from a single HVDC link. This is achieved by adjusting the interarea mode of Network 2 to 0.6 Hz by scaling down system inertia.

The two N32 models are interconnected using two different HVDC-configurations, as shown in Figure 5.17. The two systems are identical with respect to relative controllability from the dc bus locations. Let $\mathcal{V}_\Omega$ be the left eigenvector corresponding to the north–south interarea mode and let B be the input vector from all considered dc buses (ordered 4072, 4022, 4045, and 4063) then controllability from each input is given by

$$\mathcal{V}_\Omega^H B = \begin{bmatrix} 1\angle 2^\circ & 0.4\angle 8^\circ & 0.4\angle -167^\circ & 0.7\angle -170^\circ \end{bmatrix}.$$

[7]The model was used in Section 4.5 to study controllability.

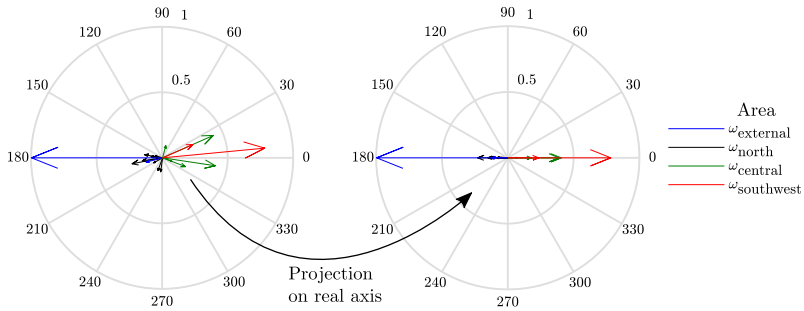

Figure 5.15: Mode shape of the north–south interarea mode in the N32 model given by left eigenvector $\mathcal{V}_\Omega^\omega$ (left). Projection on the real axis, $\boldsymbol{V}_\Omega^\omega$ used for scaling output (right). The notation $\mathcal{V}_\Omega^\omega$ indicates elements of $\mathcal{V}_\Omega$ corresponding to states $\boldsymbol{\omega}$.

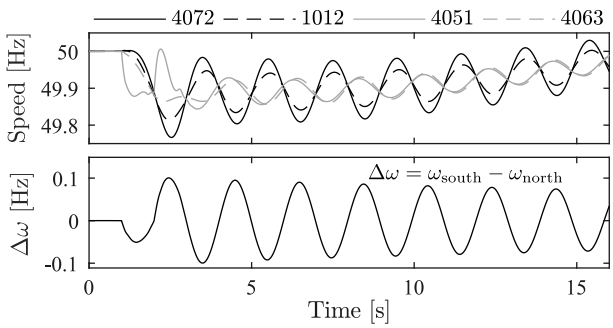

Figure 5.16: Four machine speed measurements (top) following a 500 MW load disturbance without HVDC POD control. The relative speed (bottom) is estimated using (5.14).

This indicates that Assumption 5.2 holds fairly well. Thus, interaction between interarea modes can be avoided using a constant pre-compensator designed according to Section 5.6.

The dynamic response following a 500 MW load disturbance (duration 1–2 s) at bus 4051 is simulated and the effect of dc link failure is investigated. The considered feedback signals are the relative machine speeds

$$\Delta\omega_i = \sum_{j=1}^{20} \mathcal{V}_{\Omega,ij}^\omega \omega_{ij}, \quad i \in \{1, 2\} \tag{5.14}$$

obtained by measuring generator speeds in both networks as shown in Figure 5.16. The notation $\mathcal{V}_{\Omega,i}^\omega$ indicates elements of $\mathcal{V}_{\Omega,i}$ corresponding to the vector of state variables $\boldsymbol{\omega}_i$; and $\mathcal{V}_{\Omega,ij}^\omega$ the elements of $\mathcal{V}_{\Omega,i}^\omega$ corresponding to the state variable ω_{ij}. For instance, if $\boldsymbol{x}_i$ are the states of network i, then $\Delta\omega_i = \mathcal{V}_{\Omega,i}^\omega \boldsymbol{x}_i$.

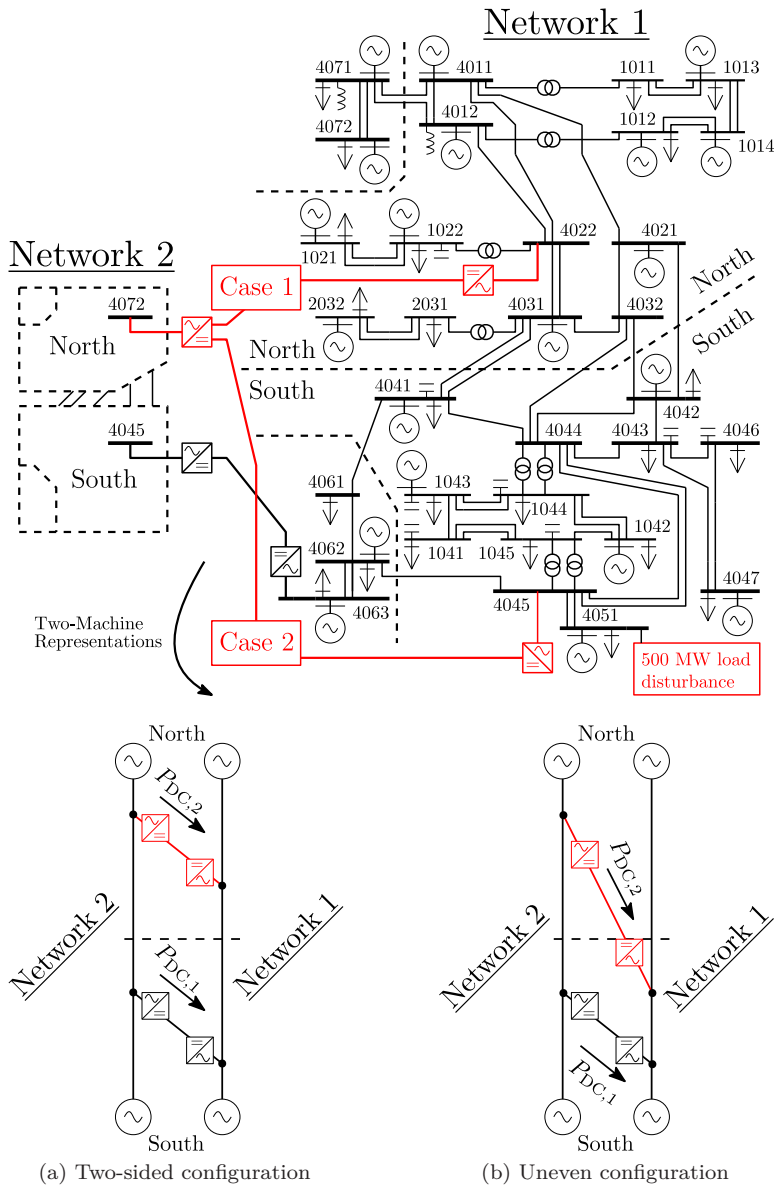

(a) Two-sided configuration (b) Uneven configuration

Figure 5.17: Two HVDC-interconnected N32 networks. The frequency of the interarea mode in Network 1 and Network 2 are 0.5 Hz and 0.6 Hz respectively.

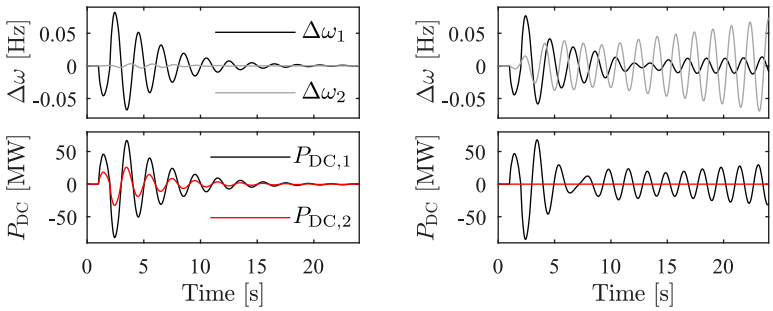

(a) Decoupling control (b) DC link 2 disconnected

Figure 5.18: Case 1: Two-sided HVDC-configuration, Figure 5.17a. Relative machine speeds and HVDC active power injections following a 500 MW load disturbance.

Case 1: Two-Sided HVDC-Configuration

The HVDC active power injection are given by

$$u = -k \begin{bmatrix} 1 & 0.5 \\ 0.4 & 1 \end{bmatrix} \begin{bmatrix} \Delta\omega_1 \\ \Delta\omega_2 \end{bmatrix}, \quad k = 1000\,\mathrm{MW/Hz}.$$

The dc terminals are placed on both side of the electrical mid point in each system as shown in Figure 5.17a. Similar to the one-sided configuration in Figure 5.2 this violates the $N-1$ stability criterion (5.9). Thus, disconnection of one HVDC link lead to instability as shown in Figure 5.18.

Case 2: Uneven HVDC-Configuration

The HVDC active power injection are given by

$$u = -k \begin{bmatrix} 1 & -0.6 \\ 0.4 & 1 \end{bmatrix} \begin{bmatrix} \Delta\omega_1 \\ \Delta\omega_2 \end{bmatrix}, \quad k = 1000\,\mathrm{MW/Hz}.$$

The dc terminals are placed unevenly in the two systems as shown in Figure 5.17b such that the $N-1$ stability criterion is fulfilled. Therefore, disconnection of one HVDC link does not cause instability. Additionally, the system is controllable from one HVDC link. Thus the HVDC control still stabilizes the system as seen in Figure 5.19.

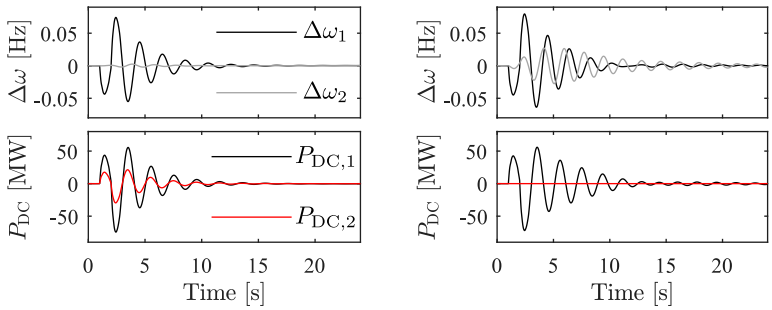

(a) Decoupling control (b) DC link 2 disconnected

Figure 5.19: Case 2: Uneven HVDC-configuration, Figure 5.17b. Relative machine speeds and HVDC active power injections following a 500 MW load disturbance.

5.9 Summary

Stability of oscillatory modes has become an increasing concern in the modern power system. In this chapter we have studied how HVDC active power modulation between two asynchronous ac networks can be used to improve POD. To achieve best performance, coordinated control of multiple controllable devices may be required. In this chapter we have analyzed the suitability of different coordinated HVDC control methods with respect to network topology. The focus has been on asynchronous power systems interconnected with two HVDC lines. For certain HVDC-configurations it was shown that a decoupling control method, avoiding excitation of selected troublesome interarea modes between the two networks, is a suitable option. For some configurations however, it was shown that decoupled control have an excessive input usage and might destabilize the system in the event of dc link failure. The decoupling control method was compared to decentralized, single-line, and centralized optimal control. It was found that the optimal $\mathcal{H}_2$ controller yielded the best combination of the previous methods for any HVDC-configuration.

Appendix

5.A Internal Stability

A system is internally stable if all the four closed-loop transfer functions in Figure 5.20,

$$\begin{aligned} u &= (I - KG)^{-1}d_u + K(I - GK)^{-1}d_y \\ y &= G(I - KG)^{-1}d_u + (I - GK)^{-1}d_y, \end{aligned} \tag{5.15}$$

from external input disturbances d_u and output disturbances d_y, are stable. Since G and K ((5.2) and (5.8) respectively) contains no open right half-plane (ORHP) poles it is sufficient to show that one of the transfer functions in (5.15) are stable [114]. If we assume failure of HVDC link 2, then internal stability can be assessed by picking the SISO internal sensitivity function from d_{u_1} to u_1

$$\frac{(s^2 + \Omega_1^2)(s^2 + \Omega_2^2)}{p(s)}.$$

Internal stability can then be assessed from the pole polynomial

$$p(s) \;=\; s^4 + s^3(b_1 + b_2) + s^2(\Omega_1^2 + \Omega_2^2) + s(b_1\Omega_2^2 + b_2\Omega_1^2) + \Omega_1^2\Omega_2^2. \tag{5.16}$$

where w_{11} and w_{12} are constant elements from the top row of the decoupling pre-compensator (5.7), and

$$b_1 := kb_{11}w_{11}, \quad b_2 := \operatorname{sgn}(b_{22})kb_{21}w_{12}. \tag{5.17}$$

Routh's algorithm provide a necessary and sufficient condition for stability of the system [135]. For the pole polynomial (5.16) to have negative-real-part roots its required that

$$1 > 0$$

$$b_1 + b_2 > 0 \tag{5.18}$$

$$\frac{b_1\Omega_1^2 + b_2\Omega_2^2}{b_1 + b_2} > 0 \tag{5.19}$$

$$\frac{b_1 b_2(\Omega_1^2 - \Omega_2^2)^2}{b_1\Omega_1^2 + b_2\Omega_2^2} > 0 \tag{5.20}$$

$$\Omega_1^2\Omega_2^2 > 0.$$

With (5.7) and (5.17) stability condition (5.18) becomes

$$b_1 + b_2 = kb_{11} - \operatorname{sgn}(b_{22})kb_{21}\frac{b_{12}}{b_{11}} > 0 \tag{5.21}$$

thus the condition simplifies to $b_{11}^2 > \operatorname{sgn}(b_{22})b_{21}b_{12}$. Similarly, condition (5.19) boils down to

$$b_{11}^2 > \operatorname{sgn}(b_{22})\frac{\Omega_2^2}{\Omega_1^2}b_{21}b_{12}. \tag{5.22}$$

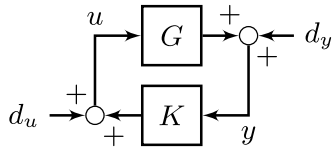

Figure 5.20: Closed-loop system used to study internal stability.

If (5.21), and thus (5.22) holds then the pole polynomial (5.16) have negative-real-part roots if (from (5.20))

$$b_1 b_2 = k^2 b_{11} \left(-\operatorname{sgn}(b_{22}) b_{21} \frac{b_{12}}{b_{11}} \right) > 0.$$

This gives the $N-1$ stability criterion

$$-\operatorname{sgn}(b_{22}) b_{21} b_{12} > 0, \quad \operatorname{sgn}(b_{11}), \quad \text{and} \quad \operatorname{sgn}(k) := 1. \tag{5.9}$$

If $\Omega_1 = \Omega_2$, b_{12}, or b_{21} the system is not controllable and thus cannot be stabilized nor destabilized by the remaining HVDC link.

5.B Closed-Loop System on Real Jordan Form

Consider the system (4.51) and (4.52) given on real Jordan form. Assume that the measurement

$$y_i = \begin{bmatrix} z_i \\ \bar{z}_i \end{bmatrix} = \begin{bmatrix} \operatorname{Re}(v_i^H) \\ \operatorname{Im}(v_i^H) \end{bmatrix} x$$

is available for feedback. The closed loop system then becomes

$$\dot{z} = Jz + \boldsymbol{V}^T B K \begin{bmatrix} z_i \\ \bar{z}_i \end{bmatrix} = \begin{bmatrix} \lambda_1 & 0 & & \vdots & & 0 \\ 0 & \ddots & & \vdots & & \vdots \\ \vdots & 0 & \begin{bmatrix} a_i & b_i \\ -b_i & a_i \end{bmatrix} & + \boldsymbol{V}^T B K & 0 \\ & & & & & \\ 0 & 0 & & \vdots & & \ddots \end{bmatrix} z$$

where K is some controller.

Complex eigenvalues are given by $\lambda_i = a_i \pm j b_i$. Since $b_i \neq 0$, λ_i (and its conjugate $\bar{\lambda}_i$) can be controlled with any of state variables in the pair $z_i, \bar{z}_i$ as long as either $\operatorname{Re}(v_i^H)B$ or $\operatorname{Im}(v_i^H)B \neq 0$.

Chapter 6

Transient Stability when Measuring Local Frequency

In this chapter, fundamental sensor feedback limitations for improving rotor angle stability using local frequency or phase angle measurement are derived. Using a two-machine power system model, it is shown that improved damping of interarea oscillations must come at the cost of reduced transient stability margins, regardless of the control design method. The control limitations stem from that the excitation of an interarea mode by external disturbances cannot be estimated with certainty using local frequency information. The results are validated on a modified Kundur four-machine two-area test system where the active power is modulated on an embedded high-voltage direct current (HVDC) link. Power oscillation damping (POD) control using local phase angle measurements, unavoidably leads to an increased rotor angle deviation following certain load disturbances. For a highly stressed system, it is shown that this may lead to transient instability. These findings may motivate the need for wide-area measurement systems (WAMS) in POD control.

In practice, POD is typically implemented as feedback control using locally available measurements. Shortcomings of these measurements, such as potentially poor observability of system-wide interarea modes, can be circumvented by collecting measurement also from distant geographical locations. With the increased number of installed phasor measurement units (PMUs), POD using WAMS has become popular. WAMS greatly improves system monitoring and control. This however, comes at the cost of an increased system complexity as well as potential reliability and security issues. Therefore, the use of WAMS should be well motivated.

Performance issues may be caused by the choice of measurements, but may also be a consequence of the control design. With optimization-based control design, good performance can often be achieved [58, 136]. However, tuning of the optimization criteria can be an endless task as evaluating the achieved closed-loop performance is often far from trivial. Fundamental design limitations helps us to understand if unsatisfactory closed-loop performance—be it with traditional or modern control

design methods—are due to a bad design or to inherent system limitations. The position of zeros relative to poorly damped poles are relevant since closed-loop poles tend to the position of nearby open-loop zeros with increasing feedback gain, as shown in Section 3.3. Because of this, it is desirable to select a combination of input and output signals that results in a large separation between poles and zeros [137, 138]. Although proven to be useful in practice, there is no straight-forward way to relate the notion of pole-zero separation, or the commonly used residue metric, to the fundamental limitations of the closed-loop performance. In this chapter, we use the Bode integral constraint to bridge the gap between small-signal analysis and control performance limitations.

The contribution of this chapter is in the analysis of fundamental limitations for improving the overall rotor angle stability of the power system using local frequency measurements. Transient rotor angle stability is considered in terms of the system's ability to maintain synchronism in the first swing following large load disturbances. The analysis is performed on a linearized two-machine power system representing a poorly damped interarea mode. It is shown that with ideal measurements, performance in terms of rotor angle stability is only limited by the available input power. Then it is shown, using Bode integral constraints on the filtering sensitivity, that the excitation of the interarea mode cannot be accurately estimated using local phase angle or frequency measurements. Last it is shown that the consequence of this filtering limitation is that any damping improvement based on local frequency measurements, must come at the cost of reduced transient stability margins, as implied by the findings of [17, 98]. The results are validated in nonlinear simulations using the well-known Kundur four-machine two-area test system, where the active power of an embedded HVDC link is modulated to improve damping of the dominant interarea mode. In the simulation study, we extend on the results by considering WAMS, local ac power flow measurement, and local bus voltage measurement.[1]

The remainder of this chapter is organized as follows. In Section 6.1 a linearized two-machine power system model is derived. Section 6.2 introduces results from the literature on sensor feedback limitations derived for general linear control and filtering problems. In Section 6.3 these results are applied to the two-machine power system model and explicit limitation are derived for two different sensor configurations. In Section 6.4 the results are validated on a nonlinear benchmark power system model. Section 6.5 summarizes the chapter.

6.1 Linearized Power System Model

In this section a linearized model of a two-machine power system is derived. A state-space representation is developed from physical equations based on simplifying assumptions (the same derivation is done in Chapter 4 but is repeated here for

[1] The four-machine test system and the control design examples are available at the GitHub repository: `https://github.com/joakimbjork/4-Machine`.

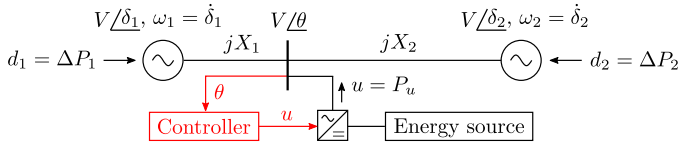

Figure 6.1: Two-machine power system with a controlled supplementary active power injection. The energy source could for instance be a wind power park, a controllable load, or an HVDC link connecting to an asynchronous system.

the sake of completeness). Then, transfer functions are derived, capturing the zero dynamics relevant for the control limitations studied in the chapter.

The derived model assumes active power control only at the bus where we measure the voltage phase angles. In Section 6.4 we assume modulation of active power in an HVDC link connecting two buses. Although input controllability is improved compared to a single point of injection, this does not affect the sensor feedback limitations.

6.1.1 State-Space Representation of a Two-Machine Power System

We consider a power system represented by two synchronous machines connected by an ac transmission line shown in Figure 6.1. Making simplifying assumptions in line with those of Chapter 4 this can be considered a simplistic representation of the dominant interarea mode in a more realistic multi-machine grid.

The electromechanical dynamics can be described using the swing equation

$$\begin{aligned} \dot{\delta}_i &= \omega_i \\ M_i\dot{\omega}_i &= -\frac{V^2}{X_i}\sin(\delta_i - \theta) - D_i\omega_i + \Delta P_i \end{aligned} \tag{6.1}$$

for $i \in \{1, 2\}$. Machines are modeled, using the classical machine model, as a stiff electromotive force behind a transient reactance [25]. Machine excitation and reactive power at the control bus are controlled so that all buses have constant voltages amplitudes V for the time frame of interest. The rotor phase angles δ_i and machine speed ω_i represents machine i's deviation from a synchronously rotating reference frame with frequency $2\pi f_{\text{nom}}$, where f_{nom} is usually 50 or 60 Hz. Constants M_i represents the frequency and pole-pair scaled inertia of each machine and D_i represent the equivalent damping of higher-order dynamics such as impact from machine damper windings, voltage regulators, system loads, and governors etc. The transmission is assumed lossless and the electrical distance between machine i and the control bus is represented by the reactance X_i, consisting of transient machine reactance, transformers, and transmission lines. The difference between the mechanical input power from the machines and the local loads is given by ΔP_i.

Voltage phase angle θ at the control bus is given by the active power balance

$$P_u + \sum_{i=1}^{2} \frac{V^2}{X_i} \sin(\delta_i - \theta) = 0 \tag{6.2}$$

where P_u is active power injected at the control bus.

Linearizing around a stationary operating point $\delta_i(t_0) = \delta_i^*$ and $\theta(t_0) = \theta^*$, we get $\frac{V^2}{X_i} \sin(\delta_i - \theta) \approx \frac{V^2}{X_i} \cos(\delta_i^* - \theta^*)(\delta_i - \theta) = X_i^{*-1}(\delta_i - \theta)$ in (6.1). From (6.2) then approximately

$$\theta = \frac{X_2^*}{X_\Sigma^*}\delta_1 + \frac{X_1^*}{X_\Sigma^*}\delta_2 + \frac{X_1^* X_2^*}{X_\Sigma^*} P_u \tag{6.3}$$

where $X_\Sigma^* = X_1^* + X_2^*$. Substituting (6.3) into (6.1) then gives us the linearized swing equation in state-space form

$$\begin{bmatrix} \dot{\boldsymbol{\delta}} \\ \mathcal{M}\dot{\boldsymbol{\omega}} \end{bmatrix} = \begin{bmatrix} 0 & I \\ -\mathcal{L}_\delta & -\mathcal{D} \end{bmatrix} \begin{bmatrix} \boldsymbol{\delta} \\ \boldsymbol{\omega} \end{bmatrix} + \begin{bmatrix} 0 & 0 \\ I & \mathcal{L}_\theta \end{bmatrix} \begin{bmatrix} \Delta P \\ P_u \end{bmatrix} \tag{6.4}$$

where inputs $\Delta P = [\Delta P_1, \Delta P_2]^T$, and state variables $\boldsymbol{\delta} = [\delta_1, \delta_2]^T$ and $\boldsymbol{\omega} = [\omega_1, \omega_2]^T$. Inertia and damping constants are given by $\mathcal{M} = \mathrm{diag}(M_1, M_2)$ and $\mathcal{D} = \mathrm{diag}(D_1, D_2)$, respectively, while 0 and I are appropriately sized zero and identity matrices, respectively. The linearized power flow are described by the network matrices

$$\mathcal{L}_\delta = \frac{1}{X_\Sigma^*} \begin{bmatrix} 1 & -1 \\ -1 & 1 \end{bmatrix}, \quad \text{and} \quad \mathcal{L}_\theta = \frac{1}{X_\Sigma^*} \begin{bmatrix} X_2^* \\ X_1^* \end{bmatrix}.$$

6.1.2 Transfer Function of a Two-Machine Power System

The sensor feedback limitations consider in this chapter are connected with the controllability and observability of the interarea mode. Commonly, the residue method [25] is used to characterize the input-output controllability and observability of modes in small-signal analysis studies and POD controller design. However, for the purpose of this analysis, residues provide insufficient information. Instead we use (6.4) to derive transfer functions capturing the poles and zero of relevant input-output combinations.

The electrical midpoint may differ from the *mass-weighted* electrical midpoint. However, to simplify notation we assume that the machines have identical inertia constants so that $M_1 = M_2 = M$. For convenience, we also assume that damping can be neglected so that $D_1 = D_2 = 0$ and that we consider the extreme case where load disturbances $d = [d_1, d_2]^T$ occur close to the machines so that $d_1 = \Delta P_1$ and $d_2 = \Delta P_2$. Consider $u = P_u$ in (6.4) to be a controlled active power injection somewhere between the two machines as shown in Figure 6.1. The transfer function of (6.4) mapping external inputs d and u to phase angles at machine and control

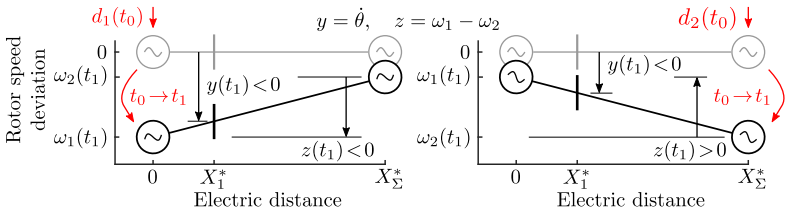

Figure 6.2: The system interpreted as two masses on a swing plank subject to an external force d_1 or d_2. At initial time t_0, $\omega_1(t_0) = \omega_2(t_0) = \dot{\theta}(t_0) = 0$.

buses $\delta = [\delta_1, \delta_2]^T$ and θ, respectively, are given by

$$\left[\begin{array}{c|c} G_{\delta d} & G_{\delta u} \\ \hline G_{\theta d} & G_{\theta u} \end{array}\right] = G_0 \left[\begin{array}{cc|c} s^2 + \Omega^2/2 & \Omega^2/2 & N_1 \\ \Omega^2/2 & s^2 + \Omega^2/2 & N_2 \\ \hline N_1 & N_2 & N_3 \end{array}\right], \tag{6.5}$$

where $\Omega = \sqrt{2/MX_\Sigma^*}$ is the undamped frequency of the interarea mode and

$$G_0 = \frac{1}{s^2 M \left(s^2 + \Omega^2\right)}. \tag{6.6}$$

In particular, for an unloaded system we have

$$N_1 = \frac{X_2^*}{X_\Sigma^*}\left(s^2 + \frac{1}{MX_2^*}\right), \quad N_2 = \frac{X_1^*}{X_\Sigma^*}\left(s^2 + \frac{1}{MX_1^*}\right), \tag{6.7}$$

and $N_3 = MX_\Sigma^* N_1 N_2$.

6.1.3 Mechanical Analogy

The machines in Figure 6.1 can be interpreted as masses on a swing plank with the electrical distance as physical distance. An external force applied to the system will initiate a relative swing between the two masses, if not applied directly at the center [93]. Now consider Figure 6.2. We want to design a sensor feedback controller using local frequency (or phase angle) measurement, $y = \dot{\theta}$, to attenuate the relative swing. At time t_0, a force d_1 or d_2 is applied to one of the machines. To dampen the swing, the sign of $z = \omega_1 - \omega_2$ need to be estimated. As seen in Figure 6.2, however, this information is not directly attained from the local frequency measurement. A damping controller may therefore cause transient stability issues by amplifying the first swing as observed in [17]. In this chapter, we study the fundamental limitations of this control problem.

6.2 Sensor Feedback Limitations

We review some results for general linear systems. In this chapter, the scope is limited to scalar systems. For more extended overview see [112–117]. In Section 6.3

the result will be used to show sensor feedback limitations for the two-machine power system derived in Section 6.1.

Let the scalar transfer function G_{yu} represent a plant with output y and input u. Consider a linear controller $u = -Ky$ where K is any proper rational transfer function.

Definition 6.1 (Sensitivity functions) The closed-loop sensitivity and complementary sensitivity functions are given by

$$\mathcal{S} = (1 + G_{yu}K)^{-1}, \quad \text{and} \quad \mathcal{T} = 1 - \mathcal{S},$$

respectively.

Lemma 6.1 (Interpolation constraints [112]) *For internal stability, no cancellation of open right half-plane (ORHP) poles or zeros*[2] *are allowed between the plant and the controller. Let p_i, $i = 1, \ldots, n_p$ and q_i, $i = 1, \ldots, n_q$ be the ORHP poles and zeros of the plant G_{yu}. Then for all p_i and q_i,*

$$\mathcal{S}(p_i) = 0, \quad \mathcal{T}(p_i) = 1, \quad \mathcal{S}(q_i) = 1, \quad \textit{and} \quad \mathcal{T}(q_i) = 0.$$

Since $\mathcal{S}$ and $\mathcal{T}$ represent closed-loop amplification of load disturbances and measurement noise, respectively. The interpolation constraints limits the achievable performance.

Lemma 6.2 (Bode integral [112]) *Suppose that the loop-gain $G_{yu}K$ is a proper rational function. Then, if $\mathcal{S}(\infty) \neq 0$*

$$\int_0^\infty \ln \left| \frac{\mathcal{S}(j\omega)}{\mathcal{S}(\infty)} \right| d\omega = \frac{\pi}{2} \lim_{s \to \infty} \frac{s\big(\mathcal{S}(s) - \mathcal{S}(\infty)\big)}{\mathcal{S}(\infty)} + \pi \sum_{i=1}^{n_p} p_i, \tag{6.8}$$

where $j = \sqrt{-1}$.

If the loop-gain is strictly proper, then $\mathcal{S}(\infty) = 1$. Typically, both G_{yu} and K are strictly proper. The limit in (6.8) then goes to 0. The reduction of the sensitivity at some angular frequencies then has to be compensated by an (at least) equally large amplification in other frequencies. This resembles the displacement of water in a water-bed. The Bode integral constraint is therefore also known as the water-bed effect.

In general the measured output y may differ from the performance variable z that we want to control. For an open-loop plant in the general control configuration

[2] ORHP poles and zeros are also referred to as non-minimum phase (NMP) poles and zeros.

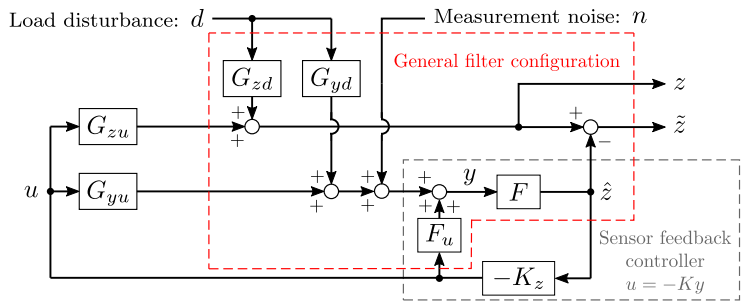

Figure 6.3: General control configuration as a control and filtering problem. The filter F_u decouples the control input u from the estimation error $\tilde{z}$.

shown in Figure 6.3, the goal is to design a sensor feedback controller K that reduces the amplitude of the closed-loop system from d to z, given by

$$\mathcal{T}_{zd} = G_{zd} - G_{zu}K(1 + G_{yu}K)^{-1}G_{yd}. \tag{6.9}$$

In the general control configuration, ORHP poles and zeros in G_{yd}, G_{zd}, and G_{zu} may put further restrictions on achievable performance [116]. The general control problem can be separated into a control and an estimation problem as shown in Figure 6.3. This chapter focuses on the latter by studying limitations in the linear filtering problem.

Assume that the system is detectable from y, i.e., all unobservable states are stable, and that $\hat{z} = Fy$ is an unbiased, bounded error estimate of z. An observer is a bounded error estimator if for all finite initial states, the estimation error $\tilde{z} = z - \hat{z}$ is bounded for all bounded inputs. A bounded error estimator is unbiased if u is decoupled from $\tilde{z}$ [112].

Definition 6.2 (Filtering sensitivity functions [112]) If G_{yd} is detectable, F is a stable filter, and G_{zd} is right invertible[3], the filtering sensitivity functions are given by

$$\mathcal{P} = (G_{zd} - FG_{yd})G_{zd}^{-1}, \quad \text{and} \quad \mathcal{M} = FG_{yd}G_{zd}^{-1},$$

with $\mathcal{P}(s) + \mathcal{M}(s) = 1$ at any $s \in \mathbb{C}$ that is not a pole of $\mathcal{P}$ or $\mathcal{M}$.

The filtering sensitivity function $\mathcal{P}$ represents the relative effect of disturbance d on the estimation error $\tilde{z}$, while the complementary filter sensitivity $\mathcal{M}$ represents the relative effect of d on the estimate $\hat{z}$.

[3]For G_{zd} to be right invertible there need to be at least as many inputs as signals to be estimated. Note that G_{zd}^{-1} is not necessarily proper.

Lemma 6.3 (Interpolation constraints for $\mathcal{P}$ and $\mathcal{M}$ [112]) *Let ρ_i, $i = 1, \ldots, n_\rho$ be the ORHP poles of G_{zd} and let ξ_i, $i = 1, \ldots, n_\xi$ be the ORHP zeros of G_{yd} that are not also zeros of G_{zd}. Assume that F is a bounded error estimator. Then*

$$\mathcal{P}(\rho_i) = 0, \quad \mathcal{M}(\rho_i) = 1, \quad \mathcal{P}(\xi_i) = 1, \quad \textit{and} \quad \mathcal{M}(\xi_i) = 0.$$

Lemma 6.4 (Bode integral for $\mathcal{P}$ [112]) *Suppose that $\mathcal{P}$ is proper and that F is a bounded error estimate. Let the ORHP zeros of $\mathcal{P}$ be ϱ_i, $i = 1, \ldots, n_\varrho$ and let ς_i, $i = 1, \ldots, n_\varsigma$ be the ORHP zeros of G_{zd} such that $F(\varsigma_i)G_{yd}(\varsigma_i) \neq 0$. Then if $\mathcal{P}(\infty) \neq 0$*

$$\int_0^\infty \ln \left| \frac{\mathcal{P}(j\omega)}{\mathcal{P}(\infty)} \right| d\omega = \frac{\pi}{2} \lim_{s\to\infty} \frac{s\big(\mathcal{P}(s) - \mathcal{P}(\infty)\big)}{\mathcal{P}(\infty)} + \pi \sum_{i=1}^{n_\varrho} \varrho_i - \pi \sum_{i=1}^{n_\varsigma} \varsigma_i.$$

Similar to Lemmas 6.1 and 6.2, this tells us that the estimation error cannot be made arbitrarily small over all angular frequencies.

6.3 Power System Sensor Feedback Limitations

The results from Section 6.2 will here be used to identify fundamental sensor feedback limitations for improving rotor angle stability in a two-machine power system. First we show that with ideal wide-area measurements, without communication delay, performance in terms of rotor angle stability is only limited by the available input power. Second we show that, using local phase angle measurements, it is impossible to perfectly estimate the excitation of the interarea mode. Water-bed constraints on the filtering sensitivity dictates that accurate estimation of the interarea mode has to be compensated by inaccuracy outside a certain angular frequency window. Finally, the main result of the chapter is presented. We show that the filtering limitation results in feedback limitation for the closed-loop system using local measurements. Consequently, amplification of certain disturbances are unavoidable.

6.3.1 Ideal Feedback Measurement $y = \omega_1 - \omega_2$

interarea oscillations are an electromechanical phenomena where groups of machines in one end of the system swing against machines in the other end of the system [25]. Consider the two-machine system shown in Figure 6.1. Here, the interarea mode is accurately observed from the modal speed [137] which for the two-machine system is given by the relative machine speed

$$z = \dot{\delta}_1 - \dot{\delta}_2 = \omega_1 - \omega_2. \tag{6.10}$$

If available, this is the ideal feedback signal [137]. With input-output mappings given by the transfer function matrix in (6.5) the system to stabilize with feedback control becomes

$$G_{zu} = \frac{X_1^* - X_2^*}{MX_\Sigma^*} \frac{s}{s^2 + \Omega^2}. \tag{6.11}$$

Proposition 6.5 *Suppose that $y = z$, G_{zu} has no ORHP zeros, and that $|G_{zd}|$ rolls off at higher angular frequencies. Then for every positive ϵ there exist a controller K such that*

$$|\mathcal{T}_{zd}(j\omega)| < \epsilon, \, \forall\omega. \tag{6.12}$$

Proof: First we note that $u = -K_z z$. Thus the closed-loop system (6.9) reduces to $\mathcal{T}_{zd} = \mathcal{S}G_{zd}$. Since $|\mathcal{T}_{zd}| \leq |\mathcal{S}||G_{zd}|$, the objective (6.12) is fulfilled if

$$|\mathcal{S}(j\omega)| < \epsilon/|G_{zd}(j\omega)|, \, \forall\omega.$$

If there are no ORHP zeros in G_{zu} then, by Lemma 6.1, $\mathcal{S}$ is not constrained at any specific angular frequencies.

■

Example 6.1 Suppose that we choose proportional control $u = -kz$ then with G_{zu} given by (6.11)

$$\mathcal{S} = \frac{s^2 + \Omega^2}{s^2 + sk\frac{X_1^* - X_2^*}{MX_\Sigma^*} + \Omega^2}.$$

According to Lemma 6.2 we then have

$$\int_0^\infty \ln|\mathcal{S}(j\omega)| \, d\omega = \frac{\pi}{2} \lim_{s\to\infty} s\big(\mathcal{S}(s) - 1\big) = -k\frac{\pi}{2}\frac{X_1^* - X_2^*}{MX_\Sigma^*}$$

which, for $k\,(X_1^* - X_2^*) > 0$, is always negative.

This implies that the excitation of the interarea mode, by load disturbances, can be made arbitrarily small for all angular frequencies. In terms of rotor angle stability, both POD and transient stability are then only limited by the available input power and the achievable actuator bandwidth.

6.3.2 Filtering Limitations — Local Measurement $y = \theta$

Typically the industry is restrained from using external communication for crucial system functions such as POD. Thus, using relative machine speed for feedback is normally not an option. The controller instead need to rely on local measurements.

Here we will show the limitations of estimating the relative machine speed (6.10) using local measurements.

Consider the two machine system shown in Figure 6.1 using local phase angle measurement, $y = \theta$. With transfer function

$$\begin{bmatrix} G_{zd_1} & G_{zd_2} \\ G_{yd_1} & G_{yd_2} \end{bmatrix} = G_0 \begin{bmatrix} s^3 & -s^3 \\ \frac{X_2^*}{X_\Sigma^*}\left(s^2 + \frac{1}{MX_2^*}\right) & \frac{X_1^*}{X_\Sigma^*}\left(s^2 + \frac{1}{MX_1^*}\right) \end{bmatrix} \tag{6.13}$$

given by (6.5) to (6.7). Assume that $0 \leq X_1^* < X_2^* \leq X_\Sigma^*$, i.e., machine 1 is closest to the measurement bus. Then the corresponding complex conjugated zero pairs $q_1 = \pm j\sqrt{1/MX_2^*}$ and $q_2 = \pm j\sqrt{1/MX_1^*}$ fulfill

$$\Omega/\sqrt{2} \leq |q_1| < |q_2| \leq \infty.$$

Partition the general control problem (6.9) into a control and an estimation problem as shown in Figure 6.3.

Proposition 6.6 *Suppose that $y = \theta$ and let $\mathcal{P}_1$ and $\mathcal{P}_2$ be the filtering sensitivity functions associated with d_1 and d_2 respectively. Then an estimator $\hat{z} = Fy$, such that*

$$|\mathcal{P}_i(j\omega)| < 1, \quad i \in \{1, 2\}$$

is only possible in a frequency interval $\left(\underline{\omega}, \bar{\omega}\right) \subset \left(|q_1|, |q_2|\right)$.

Proof: A minimum requirement for $|\mathcal{P}_i| < 1$ is that the estimate $\hat{z}$ has the same sign as z, i.e., that $\mathcal{M}_i > 0$. From (6.13), the complementary filtering sensitivities to consider becomes

$$\begin{aligned} \mathcal{M}_1(s) &= F(s)G_{yd_1}(s)G_{zd_1}^{-1}(s) = F(s)\frac{X_2^*}{X_\Sigma^*}\frac{s^2 + |q_1|^2}{s^3}, \\ \mathcal{M}_2(s) &= F(s)G_{yd_2}(s)G_{zd_2}^{-1}(s) = -F(s)\frac{X_1^*}{X_\Sigma^*}\frac{s^2 + |q_2|^2}{s^3}. \end{aligned} \tag{6.14}$$

Clearly, $\mathcal{M}_1(j\omega), \mathcal{M}_2(j\omega) > 0$ are then only possible if

$$\operatorname{sgn}\left(|q_1|^2 - \omega^2\right) = -\operatorname{sgn}\left(|q_2|^2 - \omega^2\right) = -1.$$

■

Proposition 6.7 *Suppose that $y = \theta$ and that a estimator $\hat{z} = Fy$ achieves*

$$\int_{\underline{\omega}}^{\bar{\omega}} \ln|\mathcal{P}_i(j\omega)|d\omega < 0, \quad i \in \{1, 2\}$$

in a frequency interval $\big(\underline{\omega},\bar{\omega}\big) \subset \big(|q_1|,|q_2|\big)$. *Then amplification of the disturbance on the relative estimation error,*

$$\sup_{\omega} \max\left(|\mathcal{P}_1(j\omega)|,|\mathcal{P}_2(j\omega)|\right) > 1,$$

is unavoidable in the frequency intervals $\omega < \underline{\omega}$ *and* $\omega > \bar{\omega}$.

Proof: Since $G_{yd_1}G_{zd_1}^{-1}$ and $G_{yd_2}G_{zd_2}^{-1}$ in (6.14) are strictly proper, $\mathcal{P}_i(\infty) = 1$. According to Lemma 6.4 we then have

$$\int_0^\infty \ln|\mathcal{P}_i(j\omega)|\,d\omega = \frac{\pi}{2}\lim_{s\to\infty} s\big(\mathcal{P}_i(s)-1\big) + C_i$$

where C_i is a non-negative constant resulting from any ORHP zeros in $\mathcal{P}_i$. From Definition 6.2, $\mathcal{P}_i - 1 = -\mathcal{M}_i$. With the complementary filtering sensitivities given by (6.14), then

$$\int_0^\infty \ln|\mathcal{P}_1(j\omega)|\,d\omega = -\frac{\pi}{2}F(\infty)\frac{X_2^*}{X_\Sigma^*} + C_1,$$
$$\int_0^\infty \ln|\mathcal{P}_2(j\omega)|\,d\omega = \frac{\pi}{2}F(\infty)\frac{X_1^*}{X_\Sigma^*} + C_2.$$

If the filter is strictly proper, then any region with $|\mathcal{P}_i(j\omega)| < 1$ need to be compensated with an (at least) equally large region with $|\mathcal{P}_i(j\omega)| > 1$. If the filter is proper, this holds true with respect to at least one of the disturbances d_1 or d_2.

■

Example 6.2 Consider the two-machine power system shown in Figure 6.1 with linear dynamics (6.13) derived in Section 6.1. Let the line reactance $X_\Sigma^* = 1\,\text{p.u.}$ and scale the machine inertia M so that the interarea modal frequency $\Omega = \sqrt{2/MX_\Sigma^*} = 1\,\text{rad/s}$. In addition, add a $0.05\,\text{p.u.}/(\text{rad/s})$ damping constant at each machine so that the interarea mode has small but positive damping. Figure 6.4 shows the Bode diagram of $G_{yd_i}G_{zd_i}^{-1}$, $i = 1, 2$, with $X_1^* = 0.1\,\text{p.u.}$ and $X_2^* = 0.9\,\text{p.u.}$, i.e., the control bus is located closer to machine 1.

Consider the case where the mode is estimated using a simple derivative filter. Following the numbers listed in Figure 6.4:

① The derivative filter adds 90° phase to $G_{yd_i}G_{zd_i}^{-1}$ and thus $\mathcal{M}_1(j\omega) > 0$ for $\omega > |q_2|$. However, disturbances d_2 coming from the other end of the system will result in an initial estimate with a 180° phase shift, i.e., $\mathcal{M}_2(j\omega) < 0$.

② At $\omega < |q_1|$ we will have the opposite problem.

The mechanical analogy in Section 6.1.3 thus appears as a sensor feedback limitation both around the high frequency zero q_2 and the low frequency zero q_1.

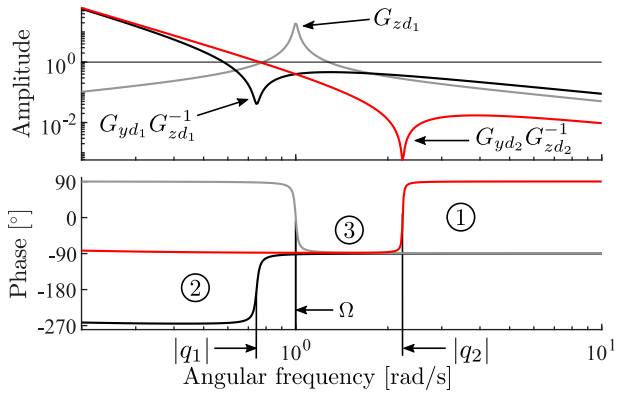

Figure 6.4: Bode diagram visualizing the filtering limitation when using local phase angle measurement, $y = \theta$, in Example 6.2.

③ In a frequency interval $(\underline{\omega}, \bar{\omega}) \subset (|q_1|, |q_2|)$ both transfer functions have the same phase. Thus $\mathcal{M}_1, \mathcal{M}_2 > 0$ can be guaranteed no matter the origin of the disturbance.

Remark 6.1 (Observability Analogy) If the control bus are at the electrical midpoint, then the relative frequency z is unobservable using local frequency measurement [93]. At the electrical midpoint, we also have $|q_1| = |q_2| = \Omega$ and thus the frequency interval in which the sign of z can be accurately estimated shrinks to zero. If the control bus are adjacent to a machine, then we have best achievable observability of z [93]. Similarly we have the maximum interval, $(\underline{\omega}, \bar{\omega}) \subset (\Omega/\sqrt{2}, \infty)$. Note that there is still a lower limit, so the considered filtering limitations applies. Ultimately, however, consequences for closed-loop performance are more relevant when the excitation of the mode is large. As seen in Figure 6.4, for $\omega \leq \Omega$, $|G_{zd}(j\omega)|$ decreases as $\omega \to 0$. Filtering limitations therefore becomes less significant when measuring closer to a machine.

Example 6.3 Consider again the two-machine system introduced in Example 6.2. An estimate of the mode is here obtained by the filter F_0, tuned to minimize the $\mathcal{H}_2$-norm from external inputs d and n to the weighted output e as shown in Figure 6.5.

Note that the $\mathcal{H}_2$ design does not allow for pure integrators in the plant. The pole of the output integral weight is therefore shifted slightly into the left half-plane (LHP). Additionally, the integrator in G_{yd} is canceled with a wash-out filter.

In the tuning process, external inputs are modeled as white noise with amplitudes $|d_1|, |d_2| = 0.2\,\text{p.u.}$ and $|n| = 0.05\,\text{rad}$. With the output weight fixed, the ratio $|d|/|n|$

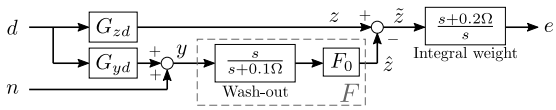

Figure 6.5: Block diagram for filter design in Example 6.3. The integral weight on the output reduces the steady-state estimation error.

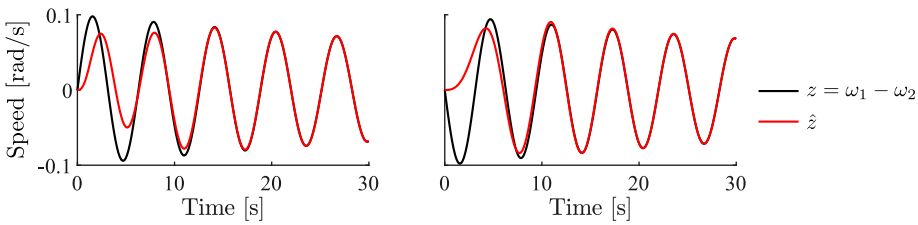

Figure 6.6: Relative machine speed z and estimate $\hat{z}$ using local phase angle measurement following a 0.2 p.u. load step d_1 (left) and d_2 (right) in Example 6.3.

determines the filter performance. As seen in Figure 6.6 the initial sign of z cannot accurately be estimated for both disturbances. By choosing $|d_1| \neq |d_2|$ in the tuning process, we can choose which disturbance to be favored by the filter. The corresponding filtering sensitivities $\mathcal{P}_1$ and $\mathcal{P}_2$ are shown in Figure 6.7.

6.3.3 Feedback Limitations — Local Measurement $y = \theta$

If there are no ORHP zeros or time-delays in G_{yu}, then the sensitivity can be made arbitrarily small, e.g., using an inverse based controller. However, making $\mathcal{S}$ small is not necessarily the same as making the closed-loop system (6.9) small if $y \neq z$. Here it will be shown that the filtering limitation in Propositions 6.6 and 6.7 result in closed-loop performance limitations in terms of achievable disturbance attenuation.

The aim of a feedback controller is to reduce the amplitude of the closed-loop system (6.9) compared to the open-loop system, i.e., to make $|\mathcal{T}_{zd}| < |G_{zd}|$. Multiplying with G_{zd}^{-1} this can be expressed using the disturbance response ratio

$$|\mathcal{R}_{zd}| = \left|1 - G_{zu}K(1 + G_{yu}K)^{-1}G_{yd}G_{zd}^{-1}\right| < 1. \tag{6.15}$$

Proposition 6.8 *Suppose $y = \theta$ and let $\mathcal{R}_{zd_1}$ and $\mathcal{R}_{zd_2}$ be the disturbance response ratios associated with d_1 and d_2 respectively. Then a sensor feedback controller $u = -Ky$, such that*

$$|\mathcal{R}_{zd_i}(j\omega)| < 1, \quad i \in \{1, 2\}$$

is only possible in a frequency interval $(\underline{\omega}, \bar{\omega}) \subset (|q_1|, |q_2|)$.

Proof: In Figure 6.3, decoupling of control input u from the estimation error is achieved by selecting F_u such that

$$G_{zu} = F(G_{yu} + F_u).$$

Substituting G_{yu} with $G_{yu} + F_u$ and K with $K_z F$ then (6.15) can be written as

$$|\mathcal{R}_{zd_i}| = |1 - (1 + G_{zu}K_z)^{-1} G_{zu} K_z \mathcal{M}_i| < 1. \tag{6.16}$$

The proof then follows from Proposition 6.6.

■

Proposition 6.9 *Suppose that $y = \theta$ and that a sensor feedback controller $u = -Ky$ achieves disturbance attenuation with*

$$\int_{\underline{\omega}}^{\bar{\omega}} \ln |\mathcal{R}_{zd_i}(j\omega)| d\omega < 0, \quad i \in \{1, 2\}$$

in a frequency interval $\left(\underline{\omega}, \bar{\omega}\right) \subset \left(|q_1|, |q_2|\right)$. Then disturbance amplification

$$\sup_{\omega} \max \left(|\mathcal{R}_{zd_1}(j\omega)|, |\mathcal{R}_{zd_2}(j\omega)|\right) > 1, \tag{6.17}$$

is unavoidable in the frequency intervals $\omega < \underline{\omega}$ and $\omega > \bar{\omega}$.

Proof: Bode integral constraints similar to Lemma 6.4 can be derived also for $\mathcal{R}_{zd}$. Suppose that the closed-loop two-machine system is stable and that the performance variable $z = \omega_1 - \omega_2$. Since both G_{zu} and $\mathcal{M}_i$ are strictly proper, $\mathcal{R}_{zd_i} - 1$ have a relative degree ≥ 2.[4] Thus,

$$\int_0^{\infty} \ln |\mathcal{R}_{zd_i}(j\omega)| \, d\omega = \pi \sum_{r=1}^{n_\gamma} \gamma_r \geq 0$$

where γ_r are ORHP zeros of $\mathcal{R}_{zd_i}$ [116]. It then follows that disturbance amplification (6.17) is unavoidable in the frequency intervals $\omega < \underline{\omega}$ and $\omega > \bar{\omega}$ due to the water-bed effect.

■

Remark 6.2 ORHP zeros of $\mathcal{P}_i$ are not necessarily shared with $\mathcal{R}_{zd_i}$. But if $K_z \to \infty$ in (6.16) then $\mathcal{R}_{zd_i} \to \mathcal{P}_i$.

[4] If we instead choose the performance variable as $z = \delta_1 - \delta_2$, then G_{zu} have a relative degree of 2 in itself.

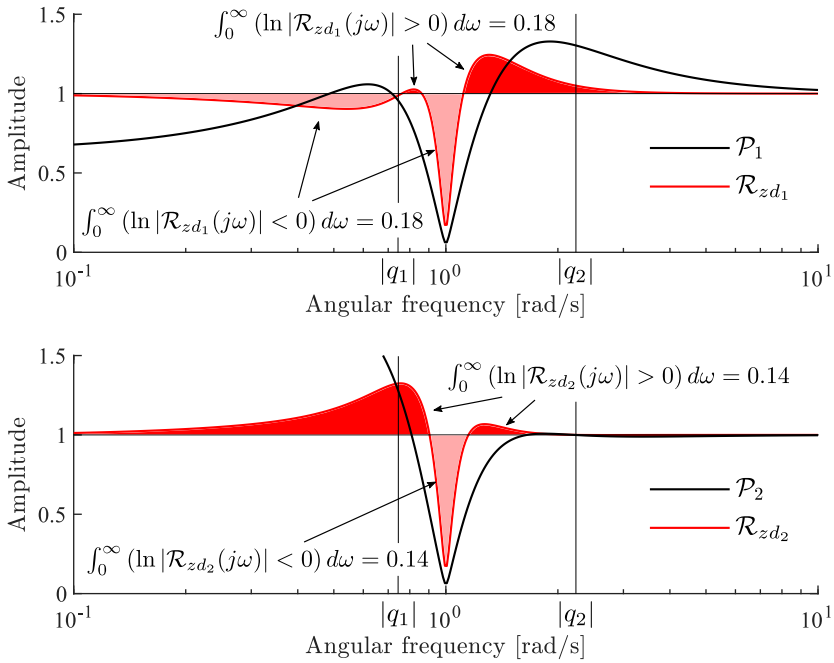

Figure 6.7: Filtering sensitivity and disturbance response ratio with respect to d_1 (top) and d_2 (bottom) in Examples 6.3 and 6.4. Due to the water-bed effect, disturbance amplification is unavoidable around the zero frequencies $|q_1|$ and $|q_2|$.

Example 6.4 Consider again the two-machine system with the filter F designed in Example 6.3. Since the filter gives an estimate of the mode, damping of the mode can be improved by closing the loop with a controller $K_z = 0.5\,\text{p.u.}/(\text{rad/s})$ as shown in Figure 6.3. In accordance with Propositions 6.8 and 6.9 this result in an unavoidable disturbance amplification outside the frequency interval $(\omega, \bar{\omega}) \subset (|q_1|, |q_2|)$ for either $\mathcal{R}_{zd_1}$ or $\mathcal{R}_{zd_2}$ as seen in Figure 6.7.

6.4 Simulation Study

In this section we study filtering limitations in a Simulink implementation [26] of the Kundur four-machine two-area test system [25] shown in Figure 6.8. For illustrative purposes, the system has been modified by reducing the POD. We assume the controllable devise is an embedded HVDC link where the dc power can be controlled in a linear region with sufficiently high bandwidth. Without further loss of generality, the dc dynamics are then neglected, as motivated in [30]. We begin this section

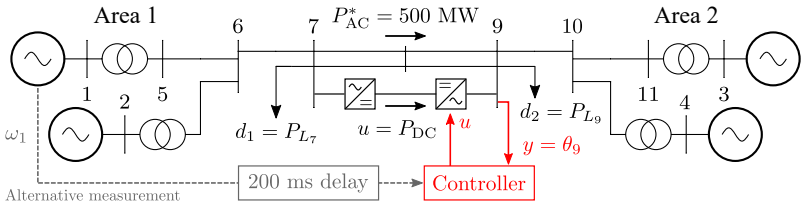

Figure 6.8: Four-machine two-area system [25, 26]. Modifications: embedded HVDC link, inertia reduced to 75%, interarea ac power flow increased to 500 MW, and PSSs tuned down for a marginally damped interarea mode.

by showing the filtering limitations associated with local phase angle or frequency measurement. Then we show the consequences this have on rotor angle stability. Finally, it is shown how alternative measurement signals can be useful to limit rotor angle stability issues associated with phase angle measurements in the considered four-machine test system.

To facilitate the analysis and controller design, we need a linear representation of the system. Using the Simulink linear analysis toolbox we obtain the 90^{th} order state-space realization

$$\begin{aligned} \dot{x} &= Ax + B_d d + B_u u \\ y &= C_y x + D_{yd} d + D_{yu} u \\ z &= C_z x \end{aligned} \tag{6.18}$$

where x is the state vector representing rotor speeds, rotor angles, generator voltages, controller states, etc.; d is a vector of external inputs, such as the active power load at buses 7 and 9; u is the controllable dc power in the HVDC link; y is some measured output such as the phase angle θ_9; and z is a performance variable chosen to represent the interarea mode.

6.4.1 Filtering Limitations — Local Measurement $y = \theta_9$

Let us illustrate how to extend the analysis in Section 6.3.2 to study the filtering limitations associated with local phase angle measurement in the four-machine system. To do this, it is convenient to represent (6.18) on its modal form.

Let λ_i, $i = 1, \ldots, 90$ be the eigenvalues of A so that $\det(A - \lambda_i I) = 0$. Let $\mathcal{V} = \begin{bmatrix} v_1, \ldots, v_{90} \end{bmatrix} \in \mathbb{C}^{90\times 90}$ and $\mathcal{U} = \begin{bmatrix} u_1, \ldots, u_{90} \end{bmatrix} \in \mathbb{C}^{90\times 90}$ be matrices of left and right eigenvectors so that $v_i^H A = v_i^H \lambda_i$, $Au_i = \lambda_i u_i$, and $\mathcal{V}^H = \mathcal{U}^{-1}$, where v_i^H is the complex conjugate transpose of v_i.

Transforming the state-space coordinates x into the modal coordinates $\zeta = \mathcal{V}^H x$ we can rewrite (6.18) as

$$\begin{aligned} \dot{\zeta} &= \mathcal{V}^H A \mathcal{U} \zeta + \mathcal{V}^H B_d d + \mathcal{V}^H B_u u \\ y &= C_y \mathcal{U} \zeta + D_{yd} d + D_{yu} u \\ z &= C_z \mathcal{U} \zeta \end{aligned} \tag{6.19}$$

where $\mathcal{V}^H A \mathcal{U} = \text{diag}(\lambda_1, \ldots, \lambda_{90}) \in \mathbb{C}^{90\times 90}$.

Oscillatory modes, λ_i, are characterized by two complex conjugated modal states. For instance let the oscillatory interarea mode be represented by the pair ζ_1 and $\zeta_2 = \bar{\zeta}_1$. Ideally, to stabilize the mode, we would like a good estimate of either ζ_1 or ζ_2. The problem is that most available numerical methods do not allow for a complex valued state-space representation. This can be amended by instead representing (6.19) on real Jordan form [126]. Let $\boldsymbol{V} = \begin{bmatrix}\boldsymbol{v}_1, \ldots, \boldsymbol{v}_{90}\end{bmatrix} \in \mathbb{R}^{90\times 90}$ be a transformation matrix with

- $\begin{bmatrix}\boldsymbol{v}_i, \boldsymbol{v}_{i+1}\end{bmatrix} = \begin{bmatrix}\text{Re}(v_i), \text{Im}(v_i)\end{bmatrix}$ if $\lambda_i = \bar{\lambda}_{i+1}$, and
- $\boldsymbol{v}_i = v_i$ if λ_i is real.

With the coordinate transform $\boldsymbol{\zeta} = \boldsymbol{V}^T x$, we rewrite the system (6.19) on real Jordan form

$$\begin{aligned}\dot{\boldsymbol{\zeta}} &= \boldsymbol{V}^T A \boldsymbol{U} \boldsymbol{\zeta} + \boldsymbol{V}^T B_d d + \boldsymbol{V}^T B_u u \\ y &= C_y \boldsymbol{U} \boldsymbol{\zeta} + D_{yd} d + D_{yu} u \\ z &= C_z \boldsymbol{U} \boldsymbol{\zeta}\end{aligned} \tag{6.20}$$

where $\boldsymbol{U}^{-1} = \boldsymbol{V}^T$ and $\boldsymbol{V}^T A \boldsymbol{U} \in \mathbb{R}^{90\times 90}$ is block-diagonal, as shown in Appendix 4.C.

The state-space realization (6.20) can be used to study the filtering limitations associated with local phase angle measurements. But first, to facilitate the subsequent controller design, let us rotate the eigenvectors so that $\boldsymbol{\zeta}_1$ and $\boldsymbol{\zeta}_2$ are suitable to represent the damping and synchronizing torque of the interarea mode.

For the undamped symmetrical two-machine system (6.5), suitable states to represent damping and synchronizing torque would be $\boldsymbol{\zeta}_1 = \omega_1 - \omega_2$ and $\boldsymbol{\zeta}_2 = \delta_1 - \delta_2$ respectively. Suitable states to represent damping and synchronizing torque in the detailed four-machine model (6.18) are not as obvious. However, if we assume that the interarea oscillations are still dominated by the mechanical dynamics of the synchronous machines we can rotate the corresponding eigenvectors, e.g., v_1 and $v_2 = \bar{v}_1$, so that the elements corresponding to machine speeds are aligned with the real axis, as shown in Figure 6.9. This makes

$$\boldsymbol{\zeta}_1 = \text{Re}\left(v_1^H\right) x = \boldsymbol{v}_1^T x \quad \text{and} \quad \boldsymbol{\zeta}_2 = \text{Im}\left(v_1^H\right) = \boldsymbol{v}_2^T x$$

state variables suitable for analyzing damping and synchronizing torque in the four-machine system even though governors, voltage dynamics, higher-order generator dynamics, etc., have been introduced. To target damping of the interarea mode, let the performance variable

$$z = \boldsymbol{\zeta}_1 = C_z x = \boldsymbol{v}_1^T x \tag{6.21}$$

where v_1 is the left eigenvector associated with the interarea mode, aligned with the real axis as shown in Figure 6.9.

Assume now that we use local measurement $y = \theta_9$ to improve POD in the four-machine system shown in Figure 6.8. The sensor feedback limitations considering active power disturbances d_1 and d_2 at buses 7 and 9, respectively, are shown in

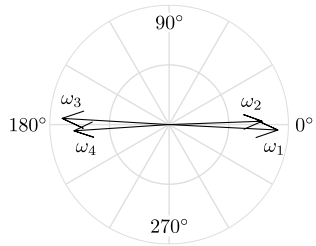

Figure 6.9: Mode shape of the interarea mode in the four-machine system.

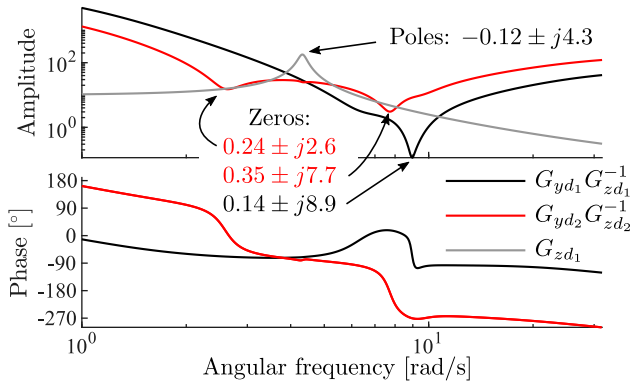

Figure 6.10: Bode diagram visualizing the filtering limitation with local phase angle measurement, $y = \theta_9$, and load disturbances d_1 and d_2 at buses 7 and 9 respectively, as shown in Figure 6.8.

Figure 6.10. The Bode diagram bares close resemblance to the simplified model in Figure 6.4. The main difference is that $G_{yd_2}G_{zd_2}^{-1}$ shows a prominent zero pair also at higher angular frequencies. This is because the disturbance d_2 occur at the measurement bus. As shown in (6.5), the transfer function G_{yd_2} therefore has a low frequency and a high frequency zero pair. Proposition 6.7 implies that it will be impossible to accurately determine the source of the load disturbance. According to Proposition 6.9, POD using local frequency measurements will therefore unavoidably amplify disturbances around the low frequency and high frequency zero pairs. In the following subsection, we show the consequence of this for transient rotor angle stability.

It is also worth noting that the electromechanical zero pairs are in the ORHP. This is often the case in power systems due to the destabilizing effect of generator excitation controllers, as shown in Chapter 3. Since we have ORHP zeros, interpolation constraints on the sensitivity further limits the achievable closed-loop performance, according to Lemma 6.1. Ultimately, this will have consequences for robustness. It is important to keep this in mind when designing the feedback controller [115].

6.4.2 Feedback Limitations — Local Measurement $y = \theta_9$

To show the consequences of the filtering limitations on rotor angle stability, we first need to design a feedback controller. In this section, we will compare two types of controllers. A conventional phase compensating controller, typically used for power system stabilizer (PSS) implementations, and a $\mathcal{H}_2$ optimal controller tuned to attenuate the performance variable (6.21).

PSS-Style Controller

Let $P_{\mathrm{DC}} = -K_{\mathrm{PSS}}\theta_9$

$$K_{\mathrm{PSS}} = s\,k_{\mathrm{PSS}} \underbrace{\frac{sT_1+1}{sT_2+1}}_{\text{Phase compensation}} \underbrace{\left(\frac{5\Omega_1}{s+5\Omega_1}\right)^2}_{\text{Low-pass}} \underbrace{\frac{s}{s+0.2\Omega_1}}_{\text{Wash-out}} \tag{6.22}$$

where $\Omega_1 = |\lambda_1| \approx 4.4\,\mathrm{rad/s}$ is the frequency of the poorly damped interarea mode. The eigenvalue sensitivity to small changes in K_{PSS} is given by the residue $R(\lambda_1) = -C_y u_1 v_1^H B_u$ [45]. We tune the phase compensation in (6.22) so that $\arg\big(R(\lambda_1)K(\lambda_1)\big) = -\pi$. Thus, feedback moves the eigenvalue, λ_1, associated with the interarea mode in the negative real direction as shown in Figure 6.11. Choosing $k_{\mathrm{PSS}} = 1.05$, the damping of the interarea mode improves from 2.7 % to 10 %. The low-pass filters in (6.22) are selected to avoid amplification of high frequency measurement noise. The wash-out filter is tuned to avoid amplification at low angular frequencies. The required phase compensation, $-5°$, is achieved with $T_1 = 0.21$ and $T_2 = 0.25$ in (6.22).

In Figure 6.12, the system response to a 1 s long 350 MW disturbance is shown. The worst case disturbances are those that increase the rotor phase angle difference. Therefore we consider a load loss at bus 5 and a generation loss at bus 11 (simulated as active power loads). This could for example represent the commutation failure of an exporting or importing HVDC link.

The trajectory of λ_1 in Figure 6.11 indicates that the implemented controller improves damping torque. It also marginally improves synchronizing torque. This could lead us to believe that both POD and transient stability have been improved. Indeed, as seen in Figure 6.12, both the damping and transient response are improved for disturbances occurring close to the measurement bus at bus 11. However, for disturbances occurring in the other end of the system, this is not the case. In accordance with Proposition 6.9, an erroneous control input and thus a disturbance amplification is unavoidable. This increases the initial angle, $\delta_1 - \delta_4$, leading to a system separation in the first swing.

$\mathcal{H}_2$ Optimal Controller

Let $P_{\mathrm{DC}} = -K_{\mathcal{H}_2}\theta_9$, where $K_{\mathcal{H}_2}$ is the controller that minimizes the $\mathcal{H}_2$-norm from white noise inputs d and n to weighted outputs in the extended system shown in Figure 6.13. Let power and phase be given in MW and degrees, respectively, and

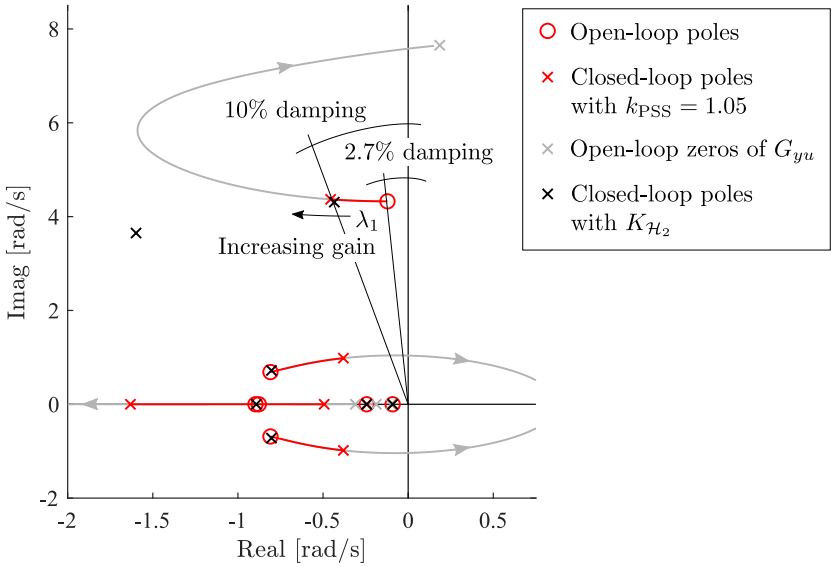

Figure 6.11: Root locus used for selecting controller gain k_{PSS}.

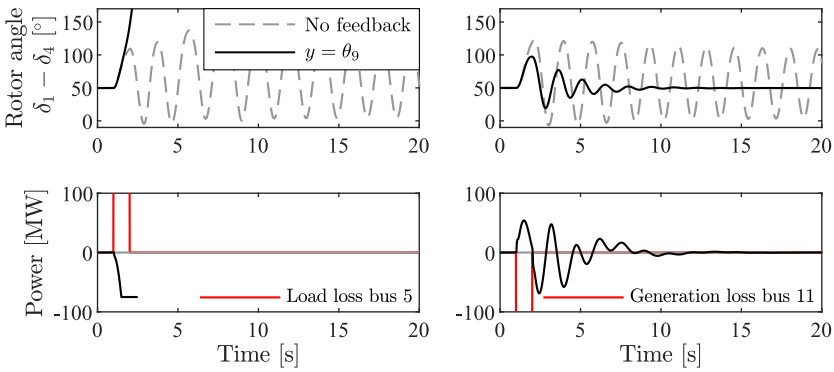

Figure 6.12: Rotor angle differences and control input following a 350 MW disturbance with $P_{\text{DC}} = -K_{\text{PSS}}\theta_9$.

- let load disturbances $|d| = 1$ and measurement noise $|n| = 1$, and let the input weights $W_d/W_n = 100$;
- let $W_u = 1$; and
- let $|C_z| = 1$ in (6.21) and $W_z = 40 \cdot 360$.

The tuned controller then achieves 10 % damping of the interarea mode. Closing the feedback loop, eigenvalues of the interarea mode are shifted into the LHP

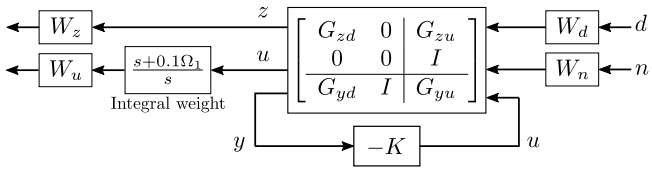

Figure 6.13: Extended system for optimal control design.

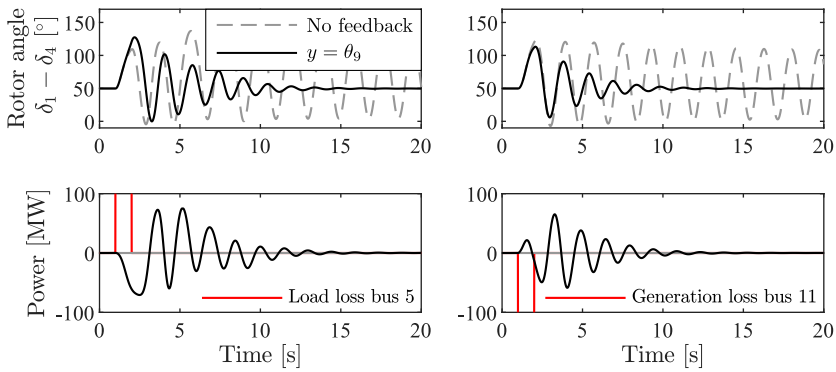

Figure 6.14: Rotor angle differences and control input following a 350 MW disturbance with $P_{\text{DC}} = -K_{\mathcal{H}_2}\theta_9$.

whereas the remaining open-loop poles are unaffected, as shown in Figure 6.11. The optimal controller has the same order as the extended system. Here however, it could be reduced to 4^{th} order without significantly changing the dynamic closed-loop performance. The implemented controller is

$$K_{\mathcal{H}_2} = \frac{0.042s(172-s)(s+12.6)(s+0.59)}{(s^2+3.9s+19.4)(s^2+3.4s+51.1)}. \tag{6.23}$$

Remark 6.3 Note that the reduced controller (6.23) has an ORHP at $s = 172$. However, since $\Omega_1 \ll 172$, this is insignificant for the closed-loop performance.

In Figure 6.14, the system response to a 1 s long 350 MW disturbance is shown. Just as in Figure 6.12 we see good damping as well as improved transient performance when disturbances occur close to the measurement bus. Unlike the PSS-style controller, we see that the $\mathcal{H}_2$ optimal controller survive the first swing, also for disturbances occurring at bus 5. This implies that transient stability issues may be avoided with proper controller tuning. However, also the well tuned $\mathcal{H}_2$ optimal controller amplifies the first swing as seen in Figure 6.14. In accordance with Proposition 6.9, this is unavoidable.

For the simulations, the controllable dc power variation has been saturated at ±75 MW from the steady-state set point. One way to reduce the erroneous excitation

of the interarea mode, is to reduce this saturation limit. This would improve the transient stability margin for disturbances occurring in the other end of the system. It is also worth noting that both the PSS-style controller and the $\mathcal{H}_2$ controller improve POD as well as first swing stability in the case where load disturbances occur in the same area. In a more distributed setting where POD is provided by decentralized controllers in each end of the system, then the negative effect on the first swing will be counterbalanced by controllers in the other end of the system.

Remark 6.4 (Weight Selection) There are many ways of choosing the input and performance weights. For instance, the inputs weights can be chosen to reflect the size and dynamics of expected load disturbances and to account for PMU measurement noise. Similarly, the performance weights can reflect the allowed signal sizes and input usage. This is particularly useful in $\mathcal{H}_\infty$ control design since then performance specifications can be considered together with the small-gain theorem, guaranteeing robust performance by ensuring that the $\mathcal{H}_\infty$-norm of the closed-loop is less than one. A convenient design procedure is often to first design the controller by optimizing the $\mathcal{H}_2$-norm, and then to assess robustness using the $\mathcal{H}_\infty$-norm [115].

6.4.3 Feedback Limitations — Alternative Measurements

In this section we will consider $\mathcal{H}_2$ optimal feedback control with alternative measurements. It will be shown that by using WAMS or by substituting local phase angle measurement with local power flow or voltage measurements, the transient stability issues associated with local phase angle measurements can be avoided. Conclusions from the analysis in Section 6.3 can, to some extent, be extrapolated to power flow and voltage measurements.

WAMS

System awareness can be improved by using WAMS. Complementary measurements should be selected at buses with good observability, and ideally in the other end of the system, to provide as much information as possible. To complement local phase angle measurement, one suitable candidate is therefore the rotor speed ω_1. Assume a 200 ms communication delay. Using the $\mathcal{H}_2$ optimal control design method in Section 6.4.2 the controller is tuned to achieve 10 % damping of the interarea mode. As shown in, Figure 6.15, the use of WAMS improves the transient performance by reducing the amplification of the first swing.

AC Power Flow $y = P_{\mathrm{AC}}$

Let the feedback controller be an $\mathcal{H}_2$ optimal controller tuned to improve the damping to 10 % using measurement of ac power flow in one of the lines between buses 8 and 9.

Since the power flow over the line depends on the angle difference, $\theta_9 - \theta_7$, it is useful for determining the source of the disturbance. This can be confirmed by

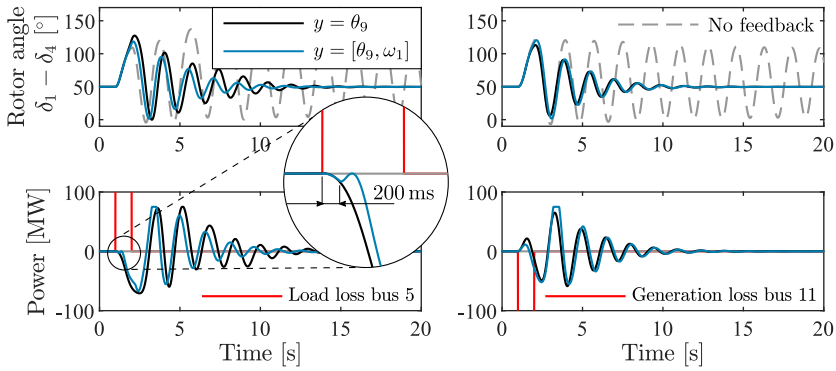

Figure 6.15: Rotor angle differences and control input following a 350 MW disturbance. Transient rotor angle stability is improved using WAMS.

studying the complementary filtering sensitivity in Figure 6.16. Therefore, as seen in Figure 6.17, power flow does not exhibit the same issues with transient stability as local phase angle measurements. For this reason, ac power flow would here be a better measurement choice compared to phase angle measurements. For a more complex system, however, this may not necessary be the case as observability will depend on the topology of the particular system. For instance, the initial surge of power will always be in the direction of the load disturbance. If measuring in a shunt, e.g. the electric power of a synchronous machine, then we may experience similar filtering limitations as with phase angle measurements. Power flow also shows more sensitivity to process noise. In Figure 6.17, although the attenuation of the rotor angle looks smooth, there is quite a bit of fluctuation in the input signal due to interaction with the local modes. To extend the analysis, it will be interesting to consider a more detailed network model.

Bus Voltage $y = V_9$

Let the feedback controller be an $\mathcal{H}_2$ optimal controller tuned to improve the damping to 10 % using measurement of local bus voltage V_9. As seen in Figure 6.17, using local voltage measurement, the feedback controller efficiently attenuates disturbances originating in either end of the system.

Typically, voltage measurement are best used in combination with reactive power control [93, 137, 138]. But it could also be used when controlling active power. Best observability of the interarea mode is achieved when measuring the voltage close to the electrical midpoint. As seen in Figure 6.17, POD control implemented using voltage measurement is less sensitive to the location of active power load disturbances. The reason for this is that the average speed mode is not observable in the voltage. But there could be other dynamical phenomena, for instance involving reactive power disturbances and short circuits faults that could exhibit similar first

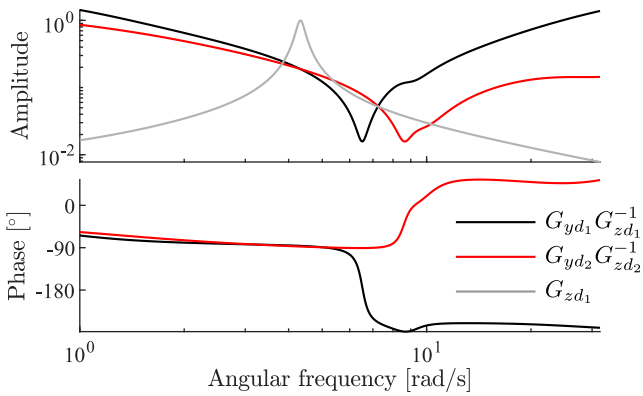

Figure 6.16: Bode diagram visualizing the complementary filtering sensitivity with local power flow measurement, $y = P_{\text{AC}}$, and load disturbances d_1 and d_2 at buses 7 and 9 respectively, as shown in Figure 6.8. Compared to Figure 6.10 we see that measurement of ac power flow does not show the same filtering limitations associated with local phase angle measurement.

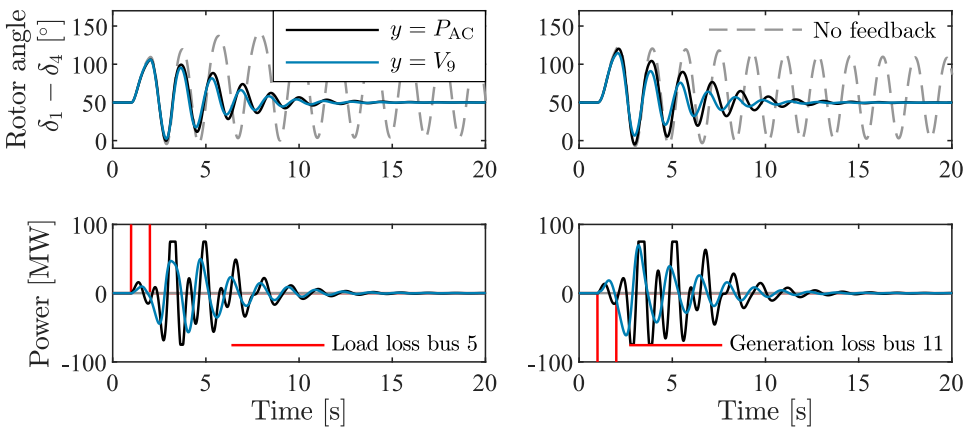

Figure 6.17: Rotor angle differences and control input following a 350 MW disturbance. For the considered two-area system, feedback control using ac power flow or local voltage measurement does not show the same issues with transient rotor angle stability as feedback from local phase angle measurement.

swing stability issues. The classical machine model (6.4) used for the analysis does not capture voltage dynamics. To properly extend the analysis, a more detailed machine modeling is needed.

It is also worth noting that the use of voltage measurement can have other drawbacks, not captured in this study. For instance, when using voltage measurement in combination with reactive power control, the residue angle is sensitive to load

dynamics [139]. This can have consequences for the robustness of the control design.

6.5 Summary

Sensor feedback limitations for improving rotor angle stability using feedback from local phase angle measurements has been studied. For a linearized two-machine power system model it was shown that, although arbitrarily good damping can be achieved, sensor feedback limitation dictates that damping improvement must come at the cost of decreased transient performance. Using a detailed power system model, it was shown that this decrease in transient performance may result in transient instability.

Part II

Frequency Stability

Chapter 7

Coordination of Dynamic Frequency Reserves

To ensure frequency stability in future low inertia power grids, fast ancillary services such as fast frequency reserves (FFR) have been proposed. In this chapter, the coordination of conventional (slow) frequency containment reserves (FCR) with FFR is treated as a decentralized model matching problem. The design results in a dynamic virtual power plant (DVPP) whose aggregated output fulfills the system operator requirements at all time scales, while accounting for the capacity and bandwidth limitation of participating devices. The results are illustrated in a 5-machine representation of the Nordic synchronous grid, where hydro-FCR is coordinated with FFR from wind.

Deregulation of the market and the transition towards renewable energy, is diversifying the mechanics behind electricity production. At the same time, the frequency stability of grids are becoming more sensitive to load imbalances due to the growing share of converter-interfaced generation [32]. A number of relatively recent blackouts are related to large frequency disturbances. These incidences are expected to become more common in the future; in fact they have doubled from the early 2000s [34]. With growing shares of renewables, system operators are therefore increasingly demanding renewable generation and other small-scale producers to participate in FCR [38].

Virtual power plants (VPPs), aggregating together groups of small-scale producers and consumers, are proposed to allow smaller producers with more variable production to enter into the market with the functionality of a larger conventional power plant [140, 141]. The main objectives are to coordinate dispatch, maximize the revenue, and to reduce financial risk of variable generation, in the day-ahead and intra-day markets [142, 143]. But also other services, such as voltage regulation [144] and allocation of FCR resources [145–147] have been proposed.

In this chapter, we design controllers that coordinate FCR over all time scales, beyond mere set-point tracking, forming a DVPP offering dynamic ancillary services

[148]. While none of the individual devices may be able to provide FCR consistently across all power and energy levels or over all time scales, a sufficiently heterogeneous ensemble will be able to do so. Examples of heterogeneous devices complementing each other while providing FFR include hybrid storage pairing batteries with supercapacitors providing regulation on different time scales [149, 150], demand response [151], or wind turbines (WTs) [73, 78] that can provide a quick response but subject to rebound effects that have to be compensated by other sources later on, if not operated below the maximum power point (MPP) [152].

The contribution of this chapter is the design of a decentralized dynamic ancillary service, distributing FCR between a heterogeneous ensemble of devices, to form a DVPP. The controllers rely on dynamic participation factors (DPFs) and are designed so that all devices collectively match the Bode diagram of a design target, specified by the system operator requirements. Stability is ensured by selecting a suitable design target and by ensuring that the DPFs account for the capacity and speed limitations of participating devices. To test the design, we consider a model of the Nordic synchronous grid. In the Nordic grid, FCR is almost exclusively provided by hydro power. The controllability and storage capability of hydropower makes it ideal for this purpose. In recent years however, the inertia reduction due to the renewable energy transition has made the bandwidth limitations associated with non-minimum phase (NMP) waterway dynamics a problem. Since the bandwidth of hydro-FCR cannot be increased without reducing the closed-loop stability margins [40], the Nordic system operator's have launched a project to complement hydro-FCR with FFR from other power sources [41]. In this chapter wind and hydro resources in the Nordic grid are coordinated as a DVPP. Numerical simulations indicate that the latest regulations can be fulfilled without the need for curtailment or battery installations.

The remainder of the chapter is structured as follows. Section 7.1 presents the control problem, introducing the test system and models of controllable energy sources. Section 7.2, formally introduces the DVPP control design. In Section 7.3 a local DVPP is designed and in Section 7.4 we close the frequency loop and coordinate FCR and FFR in the whole grid. Section 7.5 concludes the chapter with a discussion of the results.

7.1 Problem Formulation

In this chapter, we are interested in the frequency containment and post fault dynamics of the center of inertia (COI). That is, we do not directly address short term synchronization and interarea oscillations in the control design. In the end, stability is verified in simulations by applying the control to a detailed power system model designed for large signal analysis.

Power balance between production and consumption is ensured by controlling the COI frequency [25]. For a network with n_{gen} synchronous machines, the COI

frequency is

$$\omega_{\mathrm{COI}} = \frac{\sum_{i=1}^{n_{\mathrm{gen}}} M_i \omega_i}{M}, \quad M = \sum\nolimits_{i=1}^{n_{\mathrm{gen}}} M_i,$$

where ω_i is the speed and M_i the inertia of machine i. Assuming that the grid stays connected, the motion of the COI frequency is determined by the power balance

$$sM\omega_{\mathrm{COI}} = P_{\mathrm{COI}} = \sum\nolimits_{i=1}^{n} P_{\mathrm{in},i} - P_{\mathrm{out},i}$$

of the n inputs and outputs distributed all over the system.

For the analysis, we assume that physical frequency-dependent or frequency-controlled power sources can be linearized, e.g., neglecting effects of saturation. The power balance P_{COI} is divided into frequency-dependent power sources $F_i(s)\omega_{\mathrm{COI}}$ and external power sources u_i, so that

$$P_{\mathrm{COI}} = \sum\nolimits_{i=1}^{n} F_i(s)\omega_{\mathrm{COI}} + u_i = F(s)\omega_{\mathrm{COI}} + u.$$

We can then express the COI frequency disturbance response

$$\omega_{\mathrm{COI}} = \frac{1}{sM + F(s)} u. \tag{7.1}$$

Let $F_i(s)$ be broken up into $F_i(s) = D_i(s) + H_i(s)K_i(s)$, where $D_i(s)$ is some fixed frequency-dependent load or power source (typically assumed to be a constant), $H_i(s)$ represent the dynamics of some controllable power source, and $K_i(s)$ is a linear FCR controller taking a measurement of the local frequency as input. The goal is then to design $K_i(s)$, $i \in \{1, \ldots, n\}$, so that (7.1) fulfills the FCR requirements of the system operator. In this chapter we will study this problem using a case study of a 5-machine representation of the Nordic synchronous grid.

7.1.1 The Nordic 5-Machine Test System

Consider the Nordic 5-machine (N5) test system shown in Figure 8.2. The system is phenomenological but has dynamical properties similar to the Nordic synchronous grid. The model is adapted from the empirically validated 3-machine model presented in [153]. Loads, synchronous machines and WTs are lumped up into a single large unit at each bus. The model is developed in Simulink Simscape Electrical [51]. Hydro and thermal units are modeled as 16^{th} order salient-pole and round rotor machines, respectively. Assuming that inverters are operated within allowed limits and are fast enough so that their dynamics have only a marginal effect on (7.1), we model all inverter sources as grid-following controllable power loads.[1]

The amount of synchronous generation connected to the grid varies with the load demand and dispatch. Therefore the amount of system kinetic energy varies

[1] The full model, and test cases presented in this chapter, are available at the GitHub repository `https://github.com/joakimbjork/Nordic5`.

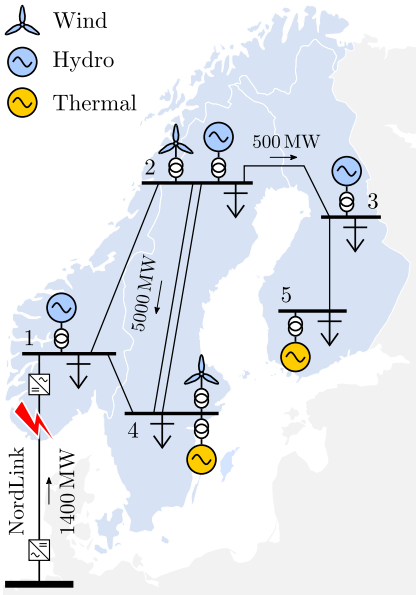

(a) One-line diagram.

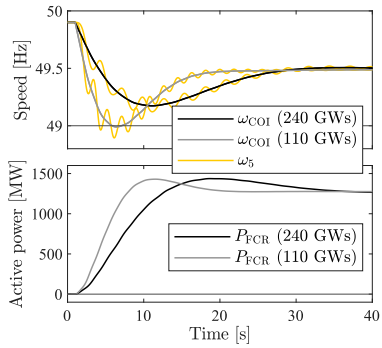

(b) Ideal FCR response.

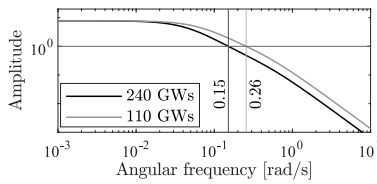

(c) Bode diagram of the FCR open-loop.

Figure 7.1: The N5 test system.

Table 7.1: Machine parameters for the 240 GWs and 110 GWs test cases.

Bus	W_{kin} [GWs]	P_e [MW]	W_{kin} [GWs]	P_e [MW]
1	67.5	18 000	34	9000
2	45	12 000	22.5	6000
3	7.5	2000	7.5	2000
4	73.3	11 000	33	5000
5	46.7	7000	13	2000
Σ	240		110	

greatly over the year [41]. Here, we will consider a high-inertia scenario, adapted from [153], with $W_{\text{kin}} = 240\,\text{GWs}$ and a low-inertia scenario with $W_{\text{kin}} = 110\,\text{GWs}$ distributed according to Table 7.1. Loads are modeled as constant power loads with a combined proportional frequency dependency $D(s) = D = 400\,\text{MW/Hz}$.

To specify a desired "ideal" FCR response, we use the FCR for disturbance (FCR-D) specifications in the Nordic synchronous grid. The FCR-D is used to contain the frequency outside normal operation. Following a rapid frequency fall from 49.9 to 49.5 Hz, the reserves should be 50 % activated within 5 s and fully activated in 30 s. Following larger disturbances the maximum instantaneous frequency deviation (the nadir) should be limited to 49.0 Hz [39]. Hence, we let the FCR-D design target

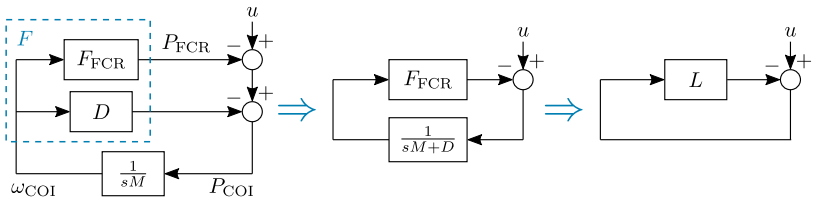

Figure 7.2: Block diagram of the FCR control loop.

take the form

$$F_{\text{FCR}}(s) = R_{\text{FCR}} \frac{6.5s + 1}{(2s + 1)(17s + 1)}. \tag{7.2}$$

Consider the dimensioning fault to be the instant disconnection of the NordLink high-voltage direct current (HVDC) cable [42] importing 1400 MW from Germany into Norway as shown in Figure 8.2. Choosing $R_{\text{FCR}} = 3100\,\text{MW/Hz}$, the post-fault system stabilizes at 49.5 Hz, as seen in Figure 7.1b. The second-order filter in (7.2) is tuned so that the FCR-D requirements are fulfilled for both scenarios, while also avoiding an overshoot and a second frequency dip when the frequency is restored.

In Figures 7.1b and 7.1c, we consider ideal actuation $H_i(s) = 1$. Thus, (7.2) is realized with ideal controllable power sources distributed at buses 1, 2, and 3 so that the total controlled input $P_{\text{FCR}} = F_{\text{FCR}}(s)(\omega_{\text{ref}} - \hat{\omega})$, where ω_{ref} is the frequency reference and $\hat{\omega} \approx \omega_{\text{COI}}$ is the locally measured frequency. As shown in Figure 7.1b, this approximation has no big impact on the result, assuming that the post fault system remains stable. With reduced inertia, the speed of the system increases. This also increases the cross-over frequency of the FCR open-loop

$$L(s) = F_{\text{FCR}}(s) \frac{1}{sM + D},$$

obtained by breaking the loop at the input/output of $F_{\text{FCR}}(s)$, as shown in Figure 7.2. Since real actuators will have bandwidth limitations, the low-inertia scenario therefore poses a greater control challenge.

When deviating from the above ideal actuation scenario, as we will see, the NMP characteristics of hydro units will make it impossible to match the design target (7.2). The target can be modified, by increasing the cross-over frequency, so that the FCR-D requirements are fulfilled even if FCR are delivered by hydro governors. However, due to bandwidth limitations imposed by the NMP zeros, see next section for details, this is not a good solution since this reduces the closed-loop stability margins [40]. Because of this, the Nordic system operators have developed a new market for FFR [41]. FFR can be provided by, e.g., battery sources or wind farms bidding on such a market.

In this chapter, we consider the control problem of coordinating multiple heterogeneous plants with different time constants and limitations. We will consider hydro units, batteries, and WTs.

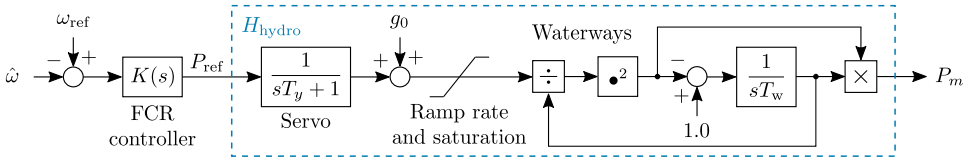

Figure 7.3: Block diagram of the hydro turbine and governor model.

7.1.2 Hydro Governor Model

The hydro governor model implemented in this chapter is an adaption of the hydro governor model available in the Simulink Simscape Electrical library [51]; modified to allow a general linear FCR controller, $K(s)$, instead of the predefined PID/droop control structure as shown in Figure 7.3. The nonlinear second-order model is useful for large-signal time-domain simulations. For the linear design, the turbine is modeled as

$$H_{\text{hydro}}(s) = 2\frac{z-s}{s+2z}\frac{1}{sT_y+1}, \quad z = \frac{1}{g_0 T_{\text{w}}}, \tag{7.3}$$

where T_y is the servo time constant, g_0 the initial gate opening, and T_{w} the water time constant [25]. Following a gate opening, the pressure over the turbine falls before the water accelerates, due to the inertia in the water column. Because of this, the initial power surge will be in the opposite direction of the gate opening change. This behavior results in a bandwidth limitation which in the linearized model (7.3) is characterized by the RHP zero [25].

7.1.3 Battery Storage Model

In the time frame of interest for frequency control, the dynamics of battery storage units are dominated by the dynamics of the inverter and its controls [145, 146]. Assuming that the inverter dynamics have no significant impact on (7.1), see for instance Example 2.3 or Remark 7.1 later on, we therefore model batteries as ideal controllable power sources, with

$$H_{\text{battery}}(s) = 1.$$

For the simulation case study we also keep track of the energy level, to indicate the required battery size. Depending on the size of the energy storage, batteries can be used as both FCR and FFR. In this chapter, we consider that the storage is limited so that batteries are used only for FFR.

7.1.4 Wind Power Model

We consider a 8^{th} order WT model shown in Figure 7.3. The model is based on the National Renewable Energy Laboratory (NREL) 5 MW baseline WT model [154]. The control system has been modified by adding a stabilizing feedback controller,

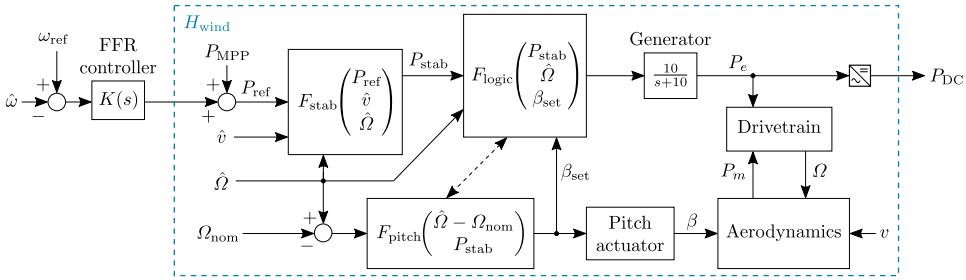

Figure 7.4: Block diagram of a variable-speed controlled WT WIND.

F_{stab}, to allow the turbine to participate in FFR. For a full description and analysis of the modified turbine, the reader is referred to Chapter 8. Here we give a brief overview of the WT model and its linearization.

The pitch controller, F_{pitch}, ensures that the rotor speed Ω does not exceed the rated speed Ω_{nom}, by adjusting the pitch angle β. The control logic, F_{logic} allows the turbine to operate in various operating modes by adjusting the generator set-point and choosing when to activate the pitch controller.

Assume uncurtailed operation at the MPP below rated wind speed, then $\beta = 0$ and $P_e = P_{\text{MPP}}$. Assuming that the inverter dynamics have no significant impact on (7.1), we let $P_{\text{in}} = P_{\text{DC}} = P_e$. The mechanical power P_m is a function of rotor speed Ω and the wind speed v. Any deviation from the optimal speed Ω_{MPP} will result in a reduced sustainable power output. However, if operated below rated speed, the electric power can be temporarily increased, allowing the WT to participate in FFR. This however will decelerate the rotor and reduce the sustainable steady-power, as shown by the power/speed characteristics in Figure 7.10b later on. To ensure stability, a variable speed feedback controller, F_{stab}, is implemented. The controller uses measurements $\hat{v}$ and $\hat{\Omega}$ of the wind and rotor speed, to modify the power reference P_{ref} to P_{stab}. As shown later in Chapter 8, the dynamics most relevant for FFR are

$$P_e \approx \frac{s - z}{s + k_{\text{stab}} - z} P_{\text{ref}},$$

where the RHP zero z is a function of the drivetrain and aerodynamics, and k_{stab} is the effective stabilizing feedback gain from F_{stab} at the current wind speed. As the turbine decelerates, z increases. Keeping the turbine above the minimum allowed speed, then $z \leq \bar{z}$. Let $k_{\text{stab}} = 2\bar{z}$, then

$$H_{\text{wind}}(s) = \frac{s - \bar{z}}{s + \bar{z}}$$

is a linear representation useful for analysis and control design. For the modified NREL turbine, $\bar{z} = 5.8v \cdot 10^{-3}$.

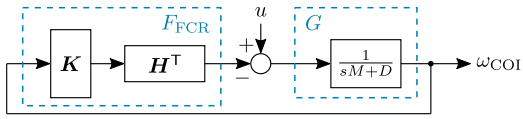

Figure 7.5: Block diagram of the FCR design problem.

7.2 Decentralized Control Design

Using FFR from wind to assist FCR from slower conventional generation has been proposed in the literature [73, 78, 152]. Here, we take this one step further. We develop a linear control design method that coordinates the dynamic response of a heterogeneous ensemble of plants, so that the combined Bode plot of all participating plants matches a target function over all frequency ranges. Using the target function (7.2) result is a DVPP that meet the system operator's FCR-D requirements. The method is general and allows us to take into account energy capacity, power, and bandwidth limitations. From a control design perspective, limitations imposed by NMP zeros will be the hardest to address, since they also affect stability margins. Therefore, this chapter focuses on combining hydro and wind.

This section presents a coordinated FCR and FFR control design method. It can be applied globally, or locally in a DVPP. Our design is based on the COI model and assumes asymptotic synchronization on the average mode. In the end, stability is verified by applying the control and simulating the power system model.

7.2.1 Coordinated FCR and FFR Using Model Matching

Let $D(s) = D$ represent the uncontrolled, proportional, frequency dependent loads in the system and let $\boldsymbol{H}(s) = [H_1(s), \dots, H_n(s)]^T$, and $\boldsymbol{K}(s) = [K_1(s), \dots, K_n(s)]^T$.

Breaking the loop at the input of $\boldsymbol{K}(s)$ in Figure 7.5 the *global* open-loop gain of the FCR control scheme becomes

$$L(s) = \sum_{i=1}^{n} L_i(s), \quad L_i(s) = G(s)H_i(s)K_i(s) \tag{7.4}$$

where $G(s) = 1/(sM + D)$.

We pose the DVPP design as a decentralized model matching problem. Let $L_{\text{des}}(s) = G(s)F_{\text{FCR}}(s)$ be the desired, stable and MP, loop-gain that fulfill the FCR-D specifications. The loop-gain of each plant is then given by

$$L_i(s) = c_i(s)L_{\text{des}}(s) = c_i(s)G(s)F_{\text{FCR}}(s) \tag{7.5}$$

where $c_i(s)$, are DPFs to be designed. DPFs are frequency-dependent version of static participation factors [25], which allow us to take the dynamic characteristics of each device into account. The controller for subsystem i is then given by

$$K_i(s) = c_i(s)F_{\text{FCR}}(s)/H_i(s).$$

We say that perfect model matching is achieved if

$$\sum_{i=1}^{n} c_i(s) = 1, \quad \forall s \in \mathbb{C} \tag{7.6}$$

in which case $L_1(s) + \cdots + L_n(s) = c_1(s)L_{\text{des}}(s) + \cdots + c_n(s)L_{\text{des}}(s) = L_{\text{des}}(s)$. However, taking into account dynamical constraint of the actuators $H_i(s)$, such as NMP zeros, we may have to relax (7.6) to ensure that $K_i(s)$ is proper and that the resulting closed-loop system is internally stable. We relax (7.6) by allowing a mismatch in the equality. Typically, we want a good match at steady-state up to some frequency ω_B, e.g., we want $\sum_{i=1}^{n} c_i(j\omega) = 1$ for $\omega \in [0, \omega_B]$.

Remark 7.1 A rule of thumb is that, for the resulting closed-loop system to be close to nominal, we want a good match up until at least ten times the cross-over frequency [115]. For model matching in the low-inertia N5 test case in Figure 7.1c this indicates that $\omega_B \approx 2.6\,\text{rad/s}$. This also justifies neglecting stable dynamics of batteries and power electronics in the FCR and FFR control design since these typically are $\gg 2.6\,\text{rad/s}$ [145, 146] (see Example 2.3).

7.2.2 Internal Stability

In addition to shaping the COI frequency disturbance response, we have to ensure internal stability with respect to the interfaces between the plant $G(s)$, the FCR controllers $K_i(s)$, and the controllable power sources $H_i(s)$ in Figure 7.5.

Theorem 7.1 *The system is internally stable if and only if the sensitivity*

$$\mathcal{S}(s) = \frac{1}{1 + L(s)} \tag{7.7}$$

is stable and no unstable pole-zero cancellation occur between plants and controllers $G(s)$, $H_i(s)$, and $K_i(s)$, $i \in \{1, \ldots, n\}$.

Proof: See Appendix 7.A. ∎

Corollary 7.2 *In case of RHP poles $p_j \in \mathbb{C}_+$ in $H_i(s)$ or $G(s)$ we need that*

$$L_i^{-1}(p_j) = 0.$$

Since we are not allowed to cancel RHP poles, any RHP poles must therefore remain in the global open-loop $L(s)$. However, if p_j belongs to $H_i(s)$, we may pre-stabilize $H_i(s)$ by first designing a local feedback controller [155].

Corollary 7.3 *In the case of NMP zeros $z_j \in \mathbb{C}_+$ in $H_i(s)$ or $G(s)$ we need that*

$$L_i(z_j) = 0.$$

Zeros cannot be moved by series compensation or feedback. So unlike unstable poles these must remain in the system. However, since zeros are moved by parallel connections, as in Figures 7.5 and 7.6, it is not necessary for the NMP zeros of $H_i(s)$ to remain in the global loop-gain $L(s)$.

For the remainder, we assume that $G(s)$ is stable and MP, and that any unstable poles in $H_i(s)$ have been pre-stabilized. The problem that remains is then how to deal with NMP zeros. Ideally, we want the global open-loop to be MP so that perfect matching (7.6) can be achieved.

7.2.3 Choosing Dynamic Participation Factors (DPFs)

There are many ways of choosing the DPFs $c_i(s)$, $i \in \{1, \dots, n\}$. Ideally, the factors are distributed between VPP units to play on their dynamic strengths, compensate for their weaknesses, and align with economic considerations. To illustrate how this can be achieved, we here propose a method where the frequency control is divided up into slower FCR and faster FFR.

Let $c_i(s)$, $i \in \{1, \dots, m\}$ and $c_i(s)$, $i \in \{m+1, \dots, n\}$ be the DPFs for FCR and FFR, respectively. Let each producer specify a variable k_i indicating their willingness or marginal cost for supplying FCR and FFR. Normalize the constants so that $\sum_{i=1}^{m} k_i = 1$ and $\sum_{i=m+1}^{n} k_i = 1$.

Starting with FCR, let

$$c_i(s) = k_i \mathcal{B}_i(s)/\mathcal{B}_i(0), \quad i \in \{1, \dots, m\}$$

where, as necessary according to Corollary 7.3,

$$\mathcal{B}_i(s) = \prod_{j=1}^{n_z} \frac{z_j - s}{s + p_j} \tag{7.8}$$

contains all the n_z NMP zeros of the plant $H_i(s)$. The poles p_j are design parameters, e.g., to adjust the cross-over frequency of $L_i(s)$. A good starting point however, is to let $p_j = z_j$ so that the DPFs are all-pass.

Next, we design the FFR participation factors. Let

$$c_i(s) = k_i \frac{\mathcal{B}_i(s)}{\mathcal{B}_i(\infty)} \left(1 - \sum\nolimits_{l=1}^{m} c_l(s)\right), \quad i \in \{m+1, \dots, n\}$$

where $\mathcal{B}_i(s)$ are first-order filters (7.8). Note that $\mathcal{B}_i(\infty)$ is a negative real number if n_z is odd.

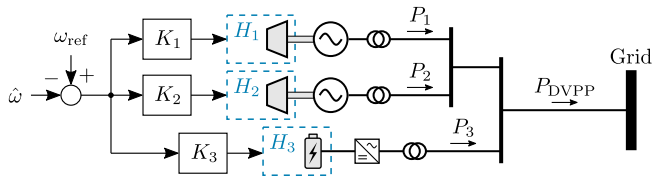

Figure 7.6: One-line diagram of a battery-hydro DVPP.

At this point, we have FCR and FFR controllers that achieves perfect matching $\sum_{i=1}^{n} c_i(s) = 1$ for $s = 0$ and $s \to \infty$. Since no NMP zeros are canceled, internal stability is achieved if the sensitivity (7.7) is stable. However, if any of the FFR plants $H_i(s)$ are NMP, we do not have perfect model matching, due to the required modifier $\mathcal{B}_i(s)/\mathcal{B}_i(\infty)$. If the total sum is MP however, this can be amended by adding a final normalization step $c_i'(s) = c_i(s)/\sum_{i=1}^{n} c_i(s)$.

7.3 Illustrative Examples

In this section we will show how a set of heterogeneous plants can be controlled so that they together form a DVPP with favorable MP characteristics. We do this, using DPFs as described in Section 7.2. For simplicity, we consider open-loop control of a subsystem connected to the grid. Therefore, it is not yet possible to state any requirement on the loop gains (7.4) and (7.5). Instead, the design is specified in terms of the ideal FCR response (7.2). The insight gained from this will later be used for the Nordic case study.

7.3.1 FCR Provided by two Hydro Units

Consider a subsystem with two 50 MVA hydro units exporting power to the grid as shown in Figure 7.6. Assume water time constants $T_{\text{w},1} = 1.25\,\text{s}$ and $T_{\text{w},2} = 2.5\,\text{s}$, respectively, and an initial gate opening $g_0 = 0.8$ and servo time constant $T_y = 0.2\,\text{s}$ for both turbines, then

$$H_1(s) = 2\frac{-s+1}{s+2}\frac{1}{0.2s+1},\quad H_2(s) = 2\frac{-s+0.5}{s+1}\frac{1}{0.2s+1}.$$

Goal

Design FCR controllers $K_1(s)$ and $K_2(s)$ for the two-hydro subsystem so that: both units increase their steady-power output by 10 MW following a 1 Hz frequency reference step, and so that $H_1(s)K_1(s) + H_2(s)K_2(s)$ comes close to the ideal FCR response (7.2) with $R_{\text{FCR}} = 20\,\text{MW/Hz}$.

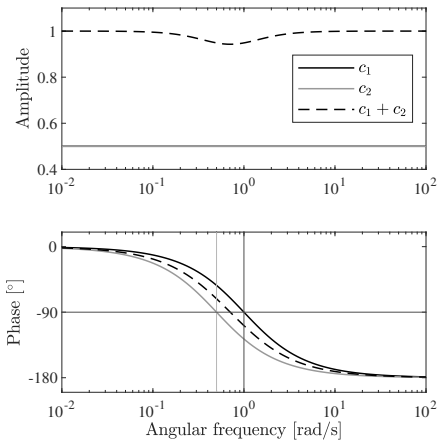

(a) Participation factors.

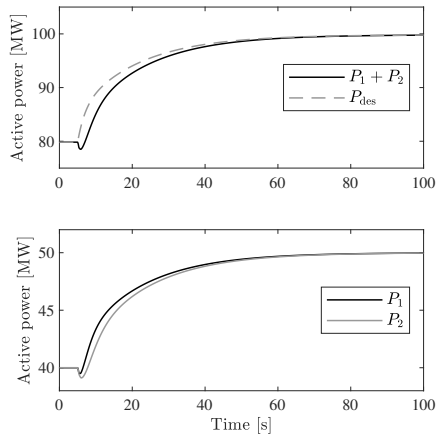

(b) Power injections.

Figure 7.7: Power output and bode diagram of the two hydro units.

Solution

From Proposition 7.4 in Appendix 7.B, we know that the two-hydro subsystem will have a RHP zero $z \in [0.5, 1]$. Thus, perfect matching is not realizable. The design criteria requires that $c_1(0) = c_2(0) = 0.5$, and for internal stability, RHP zeros need to be included. Let $K_i(s) = c_i(s)F_{\text{FCR}}(s)/H_i(s)$, $i \in \{1, 2\}$ with

$$c_1(s) = 0.5\frac{-s+1}{s+1} \quad \text{and} \quad c_2(s) = 0.5\frac{-s+0.5}{s+0.5}. \tag{7.9}$$

Result

The resulting sum equals

$$c_1(s) + c_2(s) = \frac{(-s+1/\sqrt{2})(s+1/\sqrt{2})}{(s+1)(s+0.5)}.$$

As shown in Figure 7.7a the model matching is fulfilled at steady-state with $c_1(0) + c_2(0) = 1$. However, the consequence of the RHP zero is that the DPF $c_1(s) + c_2(s)$ have a $-180°$ phase shift at higher frequencies. The 1 Hz reference step response in Figure 7.7b shows the characteristic NMP initial drop. This is an unavoidable physical property of the hydro governors that make it impossible to fulfill the design target (7.2).

Although perfect matching is impossible, the performance can be improved by modifying the participation factors, e.g., by selecting faster poles in (7.9), or by selecting a design target (7.2) with a higher cross-over frequency. However, in low-inertia power systems, this may result in dangerously low closed-loop stability

margins or even instability [40]. A more robust solution is to complement hydropower with FFR.

7.3.2 Battery Storage FFR Support

As shown in 7.3.1, it is impossible to achieve a MP FCR response using only hydro units. To improve the transient response, one solution is to assist the hydro units with FFR from a battery storage, forming a DVPP as shown in Figure 7.6.

Goal

Consider the battery storage as an ideal controllable power source, with $H_3(s) = 1$. Design $K_3(s)$ so that the DVPP, with $K_i(s) = c_i(s)F_{\text{FCR}}(s)/H_i(s)$, fulfills

$$\sum\nolimits_{i=1}^{3} K_i(s)H_i(s) = F_{\text{FCR}}(s), \tag{7.10}$$

that is, design the DPFs as in (7.6).

Solution

From Proposition 7.5 in Appendix 7.B, we know that since $\text{Re}\left(c_1(j\omega)+c_2(j\omega)\right) \leq 0$, $\forall\omega$, the complementary DPF

$$c_3(s) = 1 - \big(c_1(s) + c_2(s)\big) = 2s\frac{(s+0.75)}{(s+1)(s+0.5)}$$

is guaranteed to be stable and MP. With the battery dynamics, $H_3(s)$, being stable and MP, perfect matching is achieved with $K_3(s) = c_3(s)F_{\text{FCR}}(s)/H_3(s)$.

Result

As seen in Figure 7.8a, the battery compensates for the phase lag of the hydro units so that $\sum_{i=1}^{n} c_i(s) = 1$. As a result, the DVPP output in Figure 7.9a matches the ideal response $P_{\text{des}} = F_{\text{FCR}}(s)(\omega_{\text{ref}} - \hat{\omega})$. With a more detailed battery plus converter model, perfect matching can only be expected up to a certain frequency. Arguably however, the very high frequency dynamics will not be relevant for FFR and the COI response. From the "rule of thumb" argument in Remark 7.1, fast stable dynamics $\gg 10 \cdot 0.26\,\text{rad/s}$ can be neglected when we connect the DVPP to the low inertia N5 grid.

Having a stable MP controllable power source is ideal for providing FFR in a DVPP. With a battery storage, bounds on achievable performance are determined by the power rating and the storage capacity. As shown in Figure 7.9b, for assisting the 100 MVA hydro park, we need at least 5.5 MW and 17 kWh. An obvious drawback is that the battery needs to be recharged before it can provide any additional FFR. Taking into account the recharging needs, the long-term dynamics cannot be neglected.

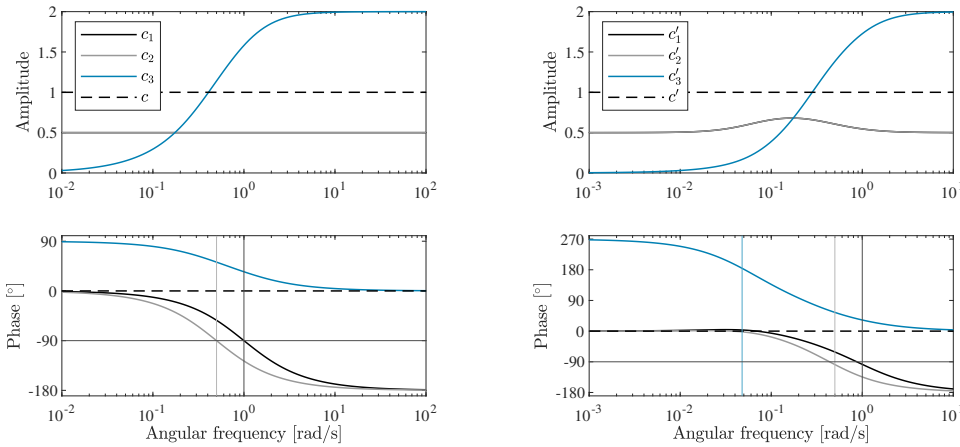

(a) Battery-hydro DVPP. (b) Wind-hydro DVPP.

Figure 7.8: Bode diagram of participation factors, where $c(s) = \sum_{i=1}^{n} c_i(s)$.

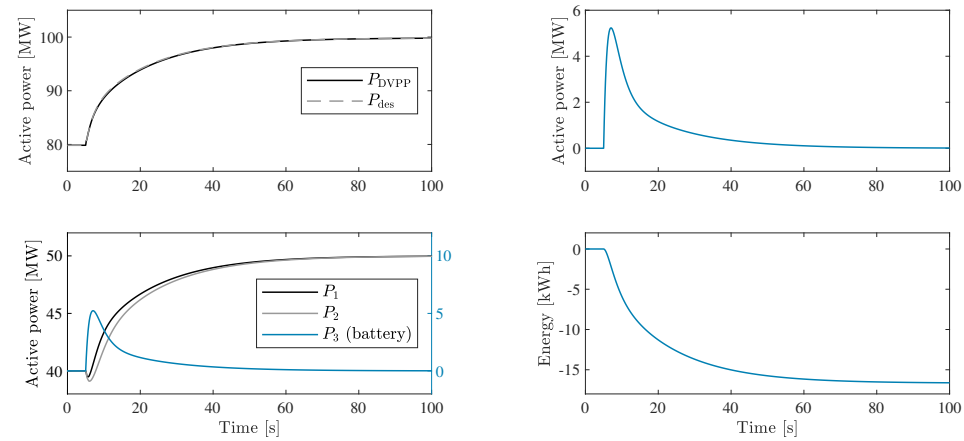

(a) Power injections. (b) Battery storage.

Figure 7.9: Power output of the battery-hydro DVPP.

7.3.3 Wind Power FFR Support

An alternative to providing FFR with battery storage, is to assist with FFR from wind power. Compared to the battery solution however, for the WT, its dynamics cannot be neglected. Here, we consider WTs operated at the MPP, but below rated wind speed so that the power output can, at least temporarily, be increased. When commanded by the FFR controller to exert power above the MPP, the rotor decelerates, and thus the sustainable steady-power output decreases, as shown by

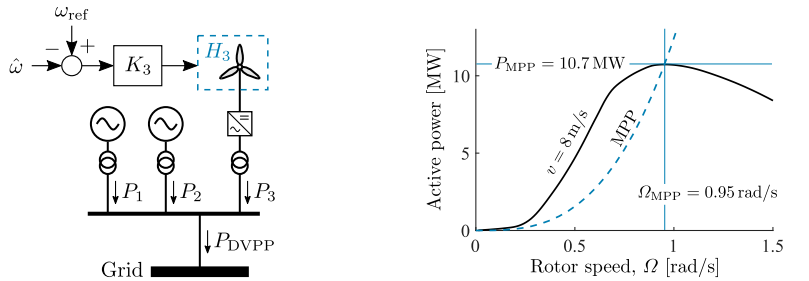

(a) One-line diagram of the DVPP. (b) Wind farm power/speed characteristic.

Figure 7.10: Wind-hydro DVPP with a 30 MW wind farm.

the power/speed characteristics in Figure 7.10b. The decline in sustainable power manifests in a NMP behavior.

Goal

Consider a 30 MW wind park connected to the subsystem as shown in Figure 7.10. Assume initially that $P_3 = P_{\text{MPP}}$. Let the wind speed be $v = 8\,\text{m/s}$. Then the all-pass filter

$$H_3(s) = \frac{s - 0.048}{s + 0.048} \tag{7.11}$$

is a suitable linear representation of the WT dynamics. Design $K_3(s)$ so that the DVPP fulfills (7.10).

Solution

Using the three-step approach in Section 7.2.3, let $c_1(s)$ and $c_2(s)$, as in (7.9), and $c_3(s) = \big(1 - c_1(s) - c_2(s)\big)H_3(s)$. The normalized DPFs $c_i'(s) = c_i(s)/\sum_{i=1}^3 c_i(s)$ then gives perfect model matching with $\sum_{i=1}^3 c_i'(s) = 1$.

Result

As seen in the Bode diagram Figure 7.8b, the wind farm compensates for the phase lag of the hydro units at higher frequencies. From Proposition 7.6 in Appendix 7.B, we know that that perfect matching can always be achieved, provided that we allow for interaction between the FCR and FFR controllers. For example, in order to achieve $\sum_{i=1}^3 c_i'(j\omega) = 1$ for low frequencies where $\text{Re}\,\big(c_3'(j\omega)\big) < 0$, then we need the hydro units to compensate with excessive FCR, i.e., $\text{Re}\,\big(c_1'(j\omega) + c_2'(j\omega)\big) > 1$. This is seen in Figure 7.8b, where the normalization step increases the gain of the hydro units at $\omega \approx 0.1\,\text{rad/s}$. A larger separation between the zeros, gives less interaction between the competing NMP dynamics.

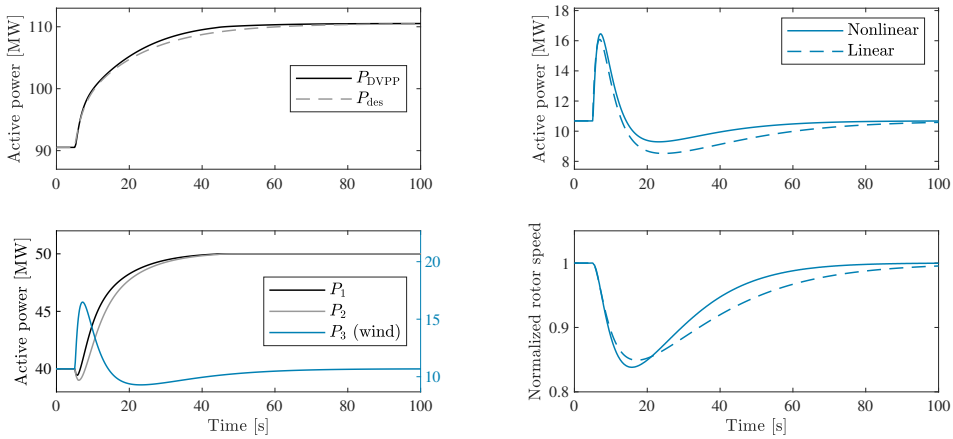

(a) Power injections. (b) WT response.

Figure 7.11: Power output of the wind-hydro DVPP.

The coordinated response to a 1 Hz reference step is shown in Figure 7.11a. The small discrepancy between the actual DVPP response and the ideal response comes from the fact that the linear model (7.11) underestimates the power output of the nonlinear WT dynamics as seen in Figure 7.11b.

7.3.4 Local A Priory Stability Guarantees

One benefit of the DVPP design is that it allows us to ensure stable interconnection to the system, e.g., using the scalable Nyquist stability criterion derived later in Chapter 9. Since both the WTs and hydro units present slow NMP dynamics, it will be hard to guarantee stability when connecting these individually to the grid, using only local information. One way to guarantee stable interconnection is to group units into DVPPs. If perfect matching is achieved, then the aggregated actuator of the DVPP matches the positive real plant (7.2). If all plants or DVPPs connected to the grid are positive real, then global stability is guaranteed.

7.4 Simulation Study

In this section, we study FCR and FFR control design in the N5 test system introduced in Section 7.1.1. First we show that, providing FCR solemnly from hydro power, the MP design target (7.2) cannot be achieved. Then we show that the desired MP design can be achieved by combining hydro and wind.

Table 7.2: Hydro parameters for the 110 GWs test case.

Bus	FCR [%]	T_y	T_w	g_0
1	60	0.2	0.7	0.8
2	30	0.2	1.4	0.8
3	10	0.2	1.4	0.8

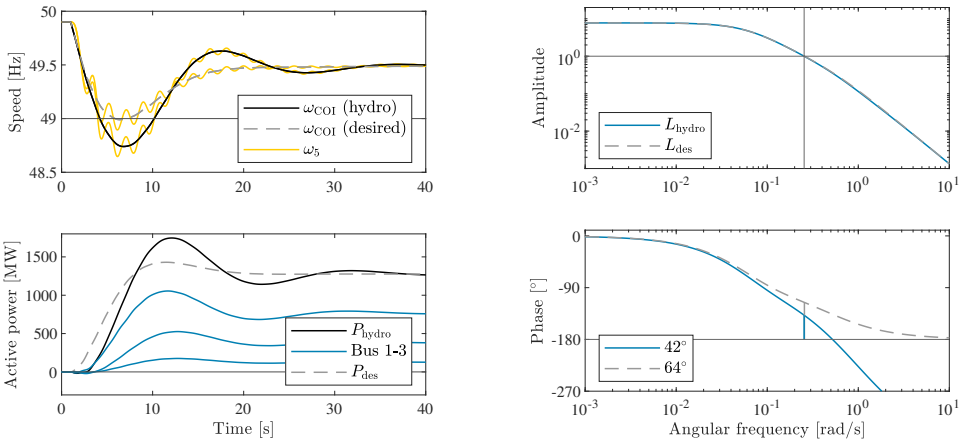

(a) FCR response to a 1400 MW fault.

(b) Bode diagram.

Figure 7.12: N5 test system with hydro FCR.

7.4.1 Hydropower FCR in the N5 Test System

Consider the N5 110 GWs test case studied in Section 7.1.1, but now assume that the FCR is provided by hydro units. Based on the test case in [153], let parameters and FCR resources be distributed according to Table 7.2. The FCR controllers for the three hydro units are designed following the same procedure as in Section 7.3.1. By design, the target (7.2) just barely fulfills the FCR-D requirements with ideal actuation and control $P_{\text{des}} = F_{\text{FCR}}(s)(\omega_{\text{ref}} - \hat{\omega})$. Since the hydro-FCR is NMP, the FCR-D requirements are no longer fulfilled since the combined output at buses 1, 2, and 3, $P_{\text{hydro}} \neq P_{\text{des}}$, as seen in Figure 7.12a. The reason for this is the negative phase shift, in the aggregated hydro open-loop $L_{\text{hydro}}(s)$ resulting from the NMP zero, shown in Figure 7.12b.

7.4.2 Coordinated Wind and Hydropower in the N5 Test System

Consider again the N5 110 GWs test case, but now let the hydro resources be complemented with FFR from wind power at buses 2 and 4, as shown in Figure 8.2. Assume that the WTs participating in FFR have a total nominal power rating of 2000 MW distributed according to Table 7.3. Using the same design procedure

Table 7.3: WT parameters for the 110 GWs test case.

Bus	P_{nom} [MW]	v [m/s]	P_{MPP} [MW]	FFR [%]
2	500	10	348	33
4	1500	8	534	67

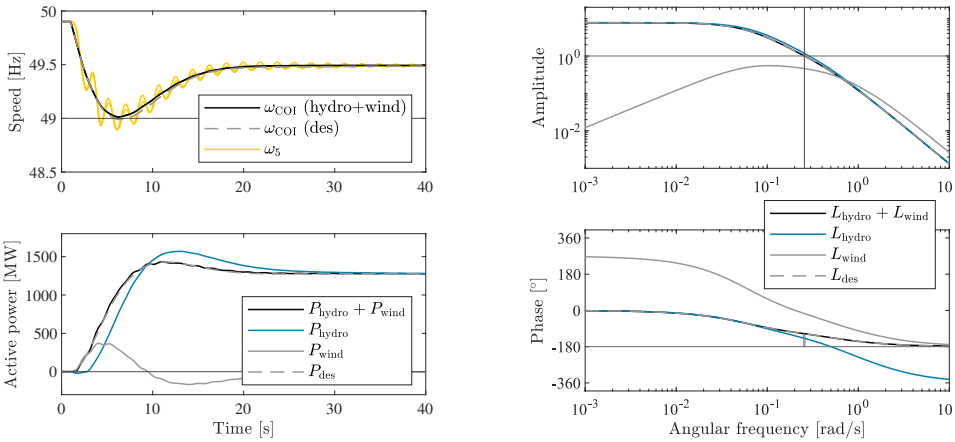

(a) Response to a 1400 MW fault. (b) Bode diagram.

Figure 7.13: N5 test system with coordinated FCR and FFR.

described in Section 7.3.3 we leverage the FFR capability of the WTs to achieve perfect matching. With a total output P_{wind}, the combined wind-hydro response closely matches the ideal response P_{des}, as seen in Figure 7.13a. As shown in Figure 7.13b, with the aggregate WT open-loop L_{wind}, the FCR-D requirements are now fulfilled with no significant change to the cross-over frequency of L_{hydro}.

The proposed DVPP design method is aligned with the FFR market solution developed to cope with future low-inertia scenarios in the Nordic grid [41]. To address limitations caused by the NMP characteristics of hydro and wind, the proposed DVPP solution targets the whole angular frequency range, so that the interactions between slow and fast dynamics can be addressed when distributing frequency reserves.

7.5 Summary

A method for distributing ancillary FCR services between a heterogeneous ensemble of controllable plants, by forming a DVPP, has been derived. The method matches the aggregated loop-gain of all participating devices to the Bode diagram of a target function, specified by the system operator's requirements. Treating the design as a decentralized model matching problem, the final controller can be implemented with

local frequency measurements. The proposed DVPP design was implemented in a model of the Nordic synchronous grid. By compensating for the NMP dynamics of hydro, the FCR-D requirements where fulfilled with quite moderate wind resources, without the need for curtailment or battery installations.

Appendix

7.A Proof of Theorem 7.1

The proof of Theorem 7.1 can be found in [114]. We write it here for completeness.

Proof: (Theorem 7.1) To ensure internal stability we need to consider the closed-loop system with respect to all control interfaces in Figure 7.5. This implies that we have to compute the multiple-input multiple-output (MIMO) "internal" sensitivity function $\mathcal{S}_I = (I + \boldsymbol{K}G\boldsymbol{H}^{\mathsf{T}})^{-1}$. However, using the push-through rule [115],

$$\underbrace{\left(I + \boldsymbol{K}G\boldsymbol{H}^{\mathsf{T}}\right)^{-1}}_{\mathcal{S}_I} \boldsymbol{K}G\boldsymbol{H}^{\mathsf{T}} = \boldsymbol{K}\underbrace{\left(1 + G\boldsymbol{H}^{\mathsf{T}}\boldsymbol{K}\right)^{-1}}_{\mathcal{S}} G\boldsymbol{H}^{\mathsf{T}},$$

we only have to consider the scalar sensitivity $\mathcal{S}$. If the sensitivity $\mathcal{S}$ is stable, then so is the complementary sensitivity $\mathcal{T} = 1 - \mathcal{S} = \mathcal{S}L$, and vice versa. Stability of $\boldsymbol{K}\mathcal{S}G\boldsymbol{H}^{\mathsf{T}}$ therefore entails stability of $\mathcal{S}_I$. It is therefore sufficient to check stability of $\mathcal{S}$, $\mathcal{S}G$, $S\boldsymbol{H}^{\mathsf{T}}\boldsymbol{K}$, $\mathcal{S}\boldsymbol{H}^{\mathsf{T}}$, $\mathcal{S}G\boldsymbol{H}^{\mathsf{T}}$, $\boldsymbol{K}\mathcal{S}$, $\boldsymbol{K}\mathcal{S}G$, and $\boldsymbol{K}\mathcal{S}G\boldsymbol{H}^{\mathsf{T}}$.

If no unstable pole-zero cancellations occur between plants and controllers in $G\boldsymbol{H}^{\mathsf{T}}\boldsymbol{K}$, then $\mathcal{S}$ has a zero polynomial containing all unstable poles of L, with multiplicity. A necessary and sufficient condition for internal stability is therefore that $\mathcal{S}$ is stable and that no unstable pole-zero cancellations occur in $G\boldsymbol{H}^{\mathsf{T}}\boldsymbol{K}$.

■

7.B Conditions for Perfect Model Matching with NMP Plants

Proposition 7.4 *Consider two stable plants $c_i(s)$, $i \in \{1, 2\}$ with one real NMP zero each at $z_i > 0$. Assume positive signed dc gain, i.e., let $c_i(0) > 0$. Then $c(s) = c_1(s) + c_2(s)$ must have at least one real NMP zero $z \in [z_1, z_2]$.*

Proof: Let $c_i(s) = a_i(s)(z_i - s)/b_i(s)$, where $b_i(s)$ and $a_i(s)$ are polynomials with no RHP roots. Without loss of generality, assume that plants have been normalized so that $b_1(s) = b_2(s) = b(s)$. Then $c(s) = c_1(s) + c_2(s)$ is

$$c(s) = \Big(z_1 a_1(s) + z_2 a_2(s) - s\big(a_1(s) + a_2(s)\big)\Big)\Big/ b(s),$$

and has zeros on the positive real axis where

$$\frac{z_1 a_1(\sigma) + z_2 a_2(\sigma)}{a_1(\sigma) + a_2(\sigma)} - \sigma = 0, \quad \sigma \geq 0. \tag{7.12}$$

With $c_i(0) > 0$, and with no zeros in the RHP, $a_i(\sigma) > 0$, $\forall \sigma \geq 0$. The first term in (7.12) is therefore a convex combination

$$\frac{z_1 a_1(\sigma) + z_2 a_2(\sigma)}{a_1(\sigma) + a_2(\sigma)} \in [z_1, z_2], \quad \forall \sigma \geq 0.$$

Since $0 < \min(z_1, z_2) \leq \max(z_1, z_2) < \infty$, (7.12) must have at least one real NMP zero where $\sigma = z \in [z_1, z_2]$.

■

Proposition 7.5 *Consider a stable and proper plant $c_1(s)$. If $\mathrm{Re}\left(c_1(j\omega)\right) \leq 1$, $\forall \omega$, then perfect matching is achieved with the stable and MP plant $c_2(s) = 1 - c_1(s)$.*

Proof: If $c_1(s)$ is stable and proper, then so is $c_2(s) = 1 - c_1(s)$. If $\mathrm{Re}\left(c_1(j\omega)\right) \leq 1$, $\forall \omega$, then $\mathrm{Re}\left(c_2(j\omega)\right) \geq 0$, $\forall \omega$. Since $c_2(s)$ is stable and positive real, it is also MP [156].

■

Proposition 7.6 *Consider a stable first-order plant*

$$c_1(s) = (1 + \varepsilon)\frac{z_1 - s}{s + z_1},$$

with RHP zero $z_1 > 0$ and $\varepsilon > 0$ so that $c_1(0) > 1$. Then under perfect matching, the assisting first-order plant $c_2(s) = 1 - c_1(s)$ is stable, has a RHP zero in $z_2 = z_1\varepsilon/(2 + \varepsilon)$, and has a negative steady-gain $c_2(0) = -\varepsilon < 0$.

Proof: The assisting plant $c_2(s)$ is

$$1 - c_1(s) = \frac{s(2 + \varepsilon) - z_1\varepsilon}{s + z_1} = \frac{2 + \varepsilon}{s + z_1}\left(s - \frac{z_1\varepsilon}{2 + \varepsilon}\right).$$

■

Chapter 8

Uncurtailed Wind Power for Fast Frequency Reserves

In this chapter, we design a wind turbine (WT) model useful for fast frequency reserves (FFR) control design. It is shown that the dynamical shortcomings of the WT, in providing steady-power or slow frequency support, is suitably described by a linear first-order transfer function with a slow non-minimum phase (NMP) zero. The new WT model is tested in a 5-machine representation of the Nordic synchronous grid. It is shown that the linearized NMP model is useful for designing a controller that coordinates FFR from wind with slow frequency containment reserves (FCR) from hydro turbines. Using the design procedure developed in Chapter 7, the WT model is then used to design a dynamic virtual power plant (DVPP) that coordinates FCR and FFR over all time scales.

Synthetic inertia allow to temporally increase the output power of a WT in exchange of reducing the rotor speed. If the turbine operates at its maximum power point (MPP), this implies the appearance of a recovery period after the initial power increase in which output power is less than the starting point, until the rotor speeds up again [73–78, 152]. This means that WTs are unable to provide FCR for a sustained period of time. However, the speed at which the converter-interfaced WTs are able to react makes them suitable for FFR, to complement conventional synchronous generation limited by the dynamic constraints of mechanical valves, servo systems, etc. [41].

The contributions of this chapter are, firstly, the design of a variable-speed feedback controller, allowing a WT to provide FFR without curtailment. The design is similar to the control implemented in [73], but here, the emphasis is on making the WT behave in a similar manner for different wind speed conditions so that a useful linearization can be obtained. When extracting power above the MPP, the turbine decelerates, thereby reducing its steady-state output. Consequently, the FFR control action puts the WT in an unstable mode of operation. To amend this, a model-based stabilizing controller is implemented, using wind speed measurement and feedback

Table 8.1: Parameters of the NREL 5 MW WT model.

Rated electric power	P_{nom}:	5 MW
Torque rate limit	$\frac{d}{dt}\tau_{\text{set}}$:	± 15 kNm/s
Electric efficiency	η:	94.4 %
Rated speed	Ω_{nom}:	12.1 rpm
Gearbox ratio	N:	97
Inertia, high speed shaft	J_e:	534.116 kg m^2
Inertia, low speed shaft	J_m:	35 444 067 kg m^2
Air density	ρ:	1.225 kg/m^3
Rotor radius	r:	63 m
Optimal tip speed ratio	λ_{opt}:	7.5

of the normalized rotor speed. The controller is designed so that the WT exhibits similar dynamic properties for various wind speed conditions. Secondly, a first-order linear approximation is derived. The linearized model is design to be a "worst-case" model, capturing the dynamic shortcomings relevant for safe coordination of FCR and FFR. Lastly, the linearized WT model is used for coordinating FCR and FFR from wind and hydro, using the model matching approach developed in Chapter 7. The modified WT and the coordinated controller are tested both in a local DVPP and in a model of the Nordic synchronous grid.

The remainder of the chapter is structured as follows: Section 8.1 presents the problem formulation. In Section 8.2, a benchmark 5 MW WT model is adapted in order to capture relevant dynamics related to FFR. In Section 8.3, it is shown how the modified WT model can be used to coordinate wind power with other resources. Lastly, Section 8.4 concludes the chapter with a discussion of the results.

8.1 Background and Problem Formulation

This section introduces the original National Renewable Energy Laboratory (NREL) 5 MW WT model. We also give a brief presentation of the Nordic 5-machine (N5) test system, previously introduced in Chapter 7.

8.1.1 The NREL 5 MW Baseline WT Model

The NREL WT model was developed to be representative of a typical utility-scale land- and sea-based WT [154], but did not envision the latest developments on the field, e.g., synthetic inertia. To overcome this, we modified its control system so that the turbine can participate in FFR even when operated at the MPP. Here we give a brief overview the simplified model depicted in Figure 8.1, which we used for the analysis and control design.

The drivetrain and turbine properties are presented in Table 8.1. For the analysis, the stable drivetrain dynamics are ignored. Therefore, we do not differentiate between

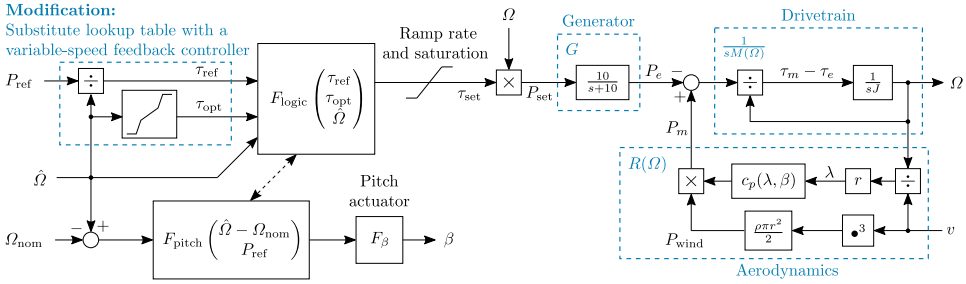

(a) Simplified block diagram.

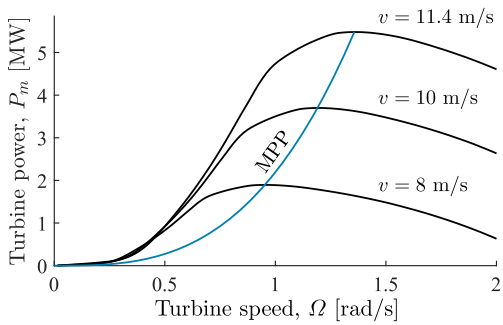

(b) Power/speed characteristic with $\beta = 0$.

Figure 8.1: The NREL 5 MW baseline WT model.

rotor speed and generator speed. Then, the total inertia with respect to the low speed shaft is $J = J_m + N^2 J_e = 40\,470\,000\,\mathrm{kg\,m^2}$. The acceleration of the rotor is determined by the electric power output P_e of the generator and the mechanical power input P_m from the turbine. The main component of the control system is the logic operator shown as F_{logic} in Figure 8.1. It controls P_e by adjusting the electric torque set-point τ_{set} to $\min(\tau_{\mathrm{ref}}, \tau_{\mathrm{opt}})$, where the reference torque τ_{ref} is given by the external power reference P_{ref} and τ_{opt} is the optimal torque read from the MPP lookup table. If the measured rotor speed $\hat{\Omega}$ exceeds the rated speed Ω_{nom}, then F_{logic} activates the pitch controller F_{pitch} as to stabilize the speed at $\Omega = \Omega_{\mathrm{nom}}$. This is done by increasing the pitch β, thereby reducing the aerodynamic power coefficient c_p and thus the power P_m extracted from the wind. Assuming operation below rated speed, then $\beta = 0$. Thus, the power coefficient is only a function of the tip speed ratio λ. If $\tau_{\mathrm{ref}} \geq \tau_{\mathrm{opt}}$, the turbine operates at the MPP curve shown in Figure 8.1b.

The control structure of the original NREL model does not allow the WT to participate in FFR without curtailment. To amend this, the lookup table in Figure 8.1a is replaced with a variable-speed feedback controller.

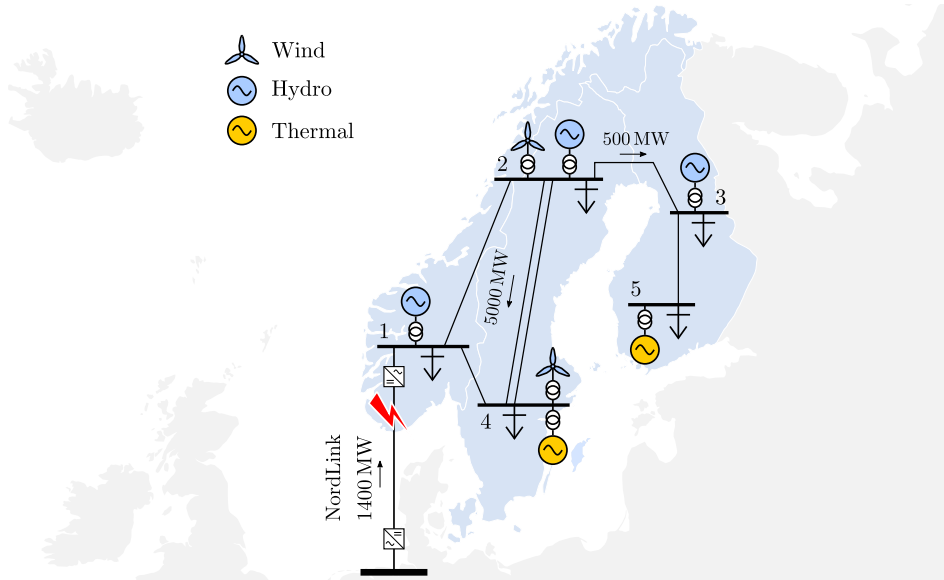

Figure 8.2: One-line diagram of the N5 test system.

8.1.2 Nordic 5-Machine (N5) Test System

Consider the N5 test system shown in Figure 8.2; introduced earlier in Chapter 7. The N5 test system is adapted from the empirically validated 3-machine model presented in [153]. The system is fictitious but has dynamic properties similar to those of the Nordic synchronous grid. The test system is implemented in Simulink Simscape Electrical [51]. Loads, synchronous machines, and WTs are lumped up into a single large unit at each bus. The hydro and thermal units are modeled as 16^{th} order salient-pole and round rotor machines, respectively. Assuming that inverters are operated within allowed limits, and have high enough bandwidth so that they have no significant impact on the studied frequency dynamics, we assume that all inverters can be modeled as controllable power loads. The WTs, modified to participate in FFR, are of 8^{th} order.[1]

The system's kinetic energy varies greatly over the year, as the amount of synchronous generation connected to the grid depends on the demand [41]. For the purpose of this analysis, we consider a low inertia scenario with $W_{\text{kin}} = 110\,\text{GWs}$ distributed according to Table 8.2. Loads are modeled as constant power loads with a combined frequency dependency of 400 MW/Hz.

[1] The full model, and test cases presented in this chapter, are available at the GitHub repository `https://github.com/joakimbjork/Nordic5`.

Table 8.2: Machine parameters for the 110 GWs test case. Time constants and distribution of FCR are based on the case study in [153].

Bus	W_{kin} [GWs]	P_{gen} [MW]	FCR [%]	T_y	T_{w}	g_0
1	34	9000	60	0.2	0.7	0.8
2	22.5	6000	30	0.2	1.4	0.8
3	7.5	2000	10	0.2	1.4	0.8
4	33	5000	–	–	–	–
5	13	2000	–	–	–	–

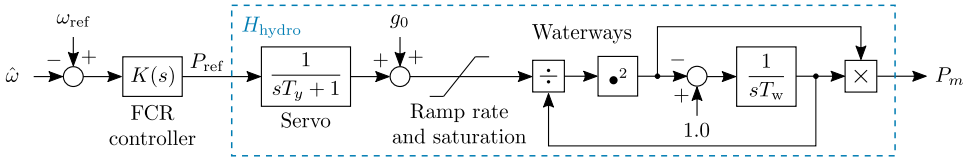

Figure 8.3: Block diagram of the hydro turbine and governor model.

The FCR control is designed to ensure that the center of inertia (COI) frequency

$$\omega_{\text{COI}} = \frac{\sum_{i=1}^{5} W_{\text{kin},i}\omega_i}{\sum_{i=1}^{5} W_{\text{kin},i}}$$

is kept within allowed dynamic bounds. Here, ω_i notates the synchronous rotor speed and $W_{\text{kin},i}$ the total kinetic energy of machines in area i. In the Nordic synchronous grid, FCR is primarily provided by hydro. The hydro governor implemented in this chapter is an adaption of the model available in the Simulink Simscape Electrical library [51]. It has been modified to allow a general linear FCR controller, $K(s)$, instead of the fixed PID/droop control structure, as shown in Figure 8.3. The servo rate limit is set to the default ± 0.1 p.u./s. The nonlinear second-order model is useful for large-signal time-domain simulations. For the linear analysis, the turbine is modeled as

$$H_{\text{hydro}}(s) = 2\frac{z-s}{s+2z}\frac{1}{sT_y+1}, \quad z = \frac{1}{g_0 T_{\text{w}}} \tag{8.1}$$

where T_y is the servo time constant, g_0 the initial gate opening, T_{w} the water time constant, $\hat{\omega}$ the locally measured frequency, and ω_{ref} the frequency reference.

8.1.3 The FCR and FFR Control Problem

In this chapter, we will coordinate FFR from wind with FCR from hydro, to fulfill an FCR design goal that cannot be achieved individually by the two resources. To do this in a methodical manner, we derive a linear model, similar to the well known hydro model (8.1), that captures the shortcomings of wind-FFR.

To specify a desired FCR response, we use the FCR for disturbance (FCR-D) specifications in the Nordic synchronous grid. As described in Section 7.1.1, the

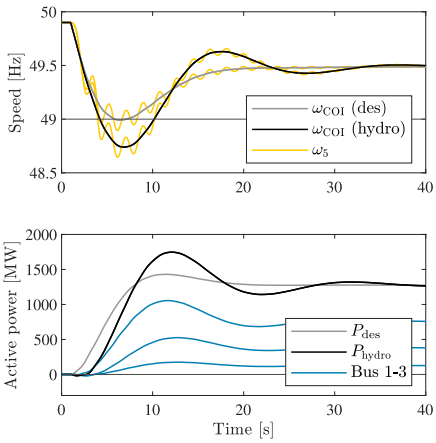

(a) FCR response.

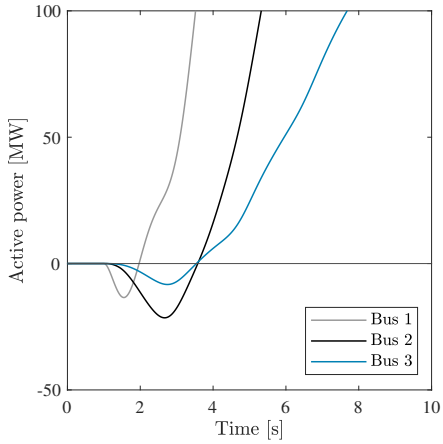

(b) Zoom in on hydro FCR response.

Figure 8.4: System response to a 1400 MW fault with hydro FCR.

FCR-D is used to contain the frequency outside normal operation in the frequency range 49.9 to 49.5 Hz. Following larger disturbances the maximum instantaneous frequency deviation (the nadir) should be limited to 49.0 Hz [39]. As in Section 7.1.1, we let the FCR-D design target take the form

$$F_{\text{FCR}}(s) = R_{\text{FCR}} \frac{6.5s + 1}{(2s + 1)(17s + 1)}. \tag{8.2}$$

Choosing $R_{\text{FCR}} = 3100\,\text{MW/Hz}$, the post-fault system stabilizes at 49.5 Hz, following the dimensioning fault. The dimensioning fault is here considered to be the instant disconnection of the NordLink high-voltage direct current (HVDC) cable [42] importing 1400 MW from Germany into Norway as shown in Figure 8.2.

The system response following the dimensioning fault is shown in Figure 8.4a. If we consider ideal controllable power sources, the FCR control action $P_{\text{des}} = F_{\text{FCR}}(\omega_{\text{ref}} - \hat{\omega})$. In this case, we see that the FCR-D requirement are fulfilled.

Now consider a more realistic scenario, where the total FCR, P_{hydro}, is delivered by the hydro units at buses 1, 2, and 3. With hydro-FCR, the FCR-D requirements are no longer fulfilled using the design target (8.2). This is because the initial surge of power from the hydro turbines are in the opposite direction of the gate opening change, as seen in Figure 8.4b. As the gate opens, the pressure over the turbine falls before the water, due to the inertia in the water column, has time to accelerate to a new steady-value [25]. This behavior is characterized by the NMP zero in (8.1). The implemented hydro model also captures nonlinear ramp rate and saturation constraints. However, with hydro-FCR resources distributed according to Table 8.2, absolute capacity and rate limiters are not a problem. The dynamic limitations due to NMP zeros will be more relevant.

The design target (8.2) can be modified so that the FCR-D requirements are fulfilled even if FCR are delivered by hydro governors. However, due to the bandwidth limitations imposed by the NMP zeros, this is not a good solution since this reduces the closed-loop stability margins [40]. Because of this, the Nordic system operators have developed a new market for FFR [41].

8.2 Design of a New Variable-Speed Wind Turbine Model

In this section, we design a new model-based variable-speed feedback control, allowing WTs to participate in FFR without curtailment. The control scheme is similar to [73], but is designed so that the turbine can be conveniently linearized, thereby allowing the WT to be easily coordinated with other power sources. The result is a first-order linear model, similar to the commonly accepted hydro governor model (8.1). The model is compared to the detailed nonlinear model in a simulation study, validating that the linearized model captures dynamics relevant for FFR control design.

The dynamic properties of the WT varies greatly with the wind speed. Because of this, it is convenient to express the dynamics in terms of the normalized speed ratio

$$x := \Omega/\Omega_{\mathrm{MPP}} = \lambda/\lambda_{\mathrm{opt}}, \tag{8.3}$$

where Ω_{MPP} is the MPP turbine speed.

8.2.1 Open-Loop Stable and Unstable Operating Modes

The open-loop characteristic of the WT are described by the nonlinear differential equation

$$\frac{d}{dt}\Omega = \frac{\Omega R(\Omega) - P_e}{M(\Omega)}.$$

Linearizing around the operating point $\Omega = \Omega_0$, $P_e = P_0$, and $x = x_0 = \Omega_0/\Omega_{\mathrm{MPP}}$, with some abuse of notation, we get the transfer function

$$\Omega = \frac{-1}{sM(\Omega_0) - R(\Omega_0)} P_e, \tag{8.4}$$

where the inertia

$$M(\Omega_0) = J\Omega_{\mathrm{MPP}} x_0$$

and the power coefficient derivative

$$R(\Omega_0) = \frac{\partial}{\partial\Omega} P_m \bigg|_{\Omega=\Omega_0} = \frac{P_{\mathrm{wind}}}{\Omega_{\mathrm{MPP}}} \frac{\partial}{\partial x} c_p \bigg|_{x=x_0}. \tag{8.5}$$

Due to the nonlinear power–speed characteristics in Figure 8.5, the WT presents both stable and unstable operating modes.

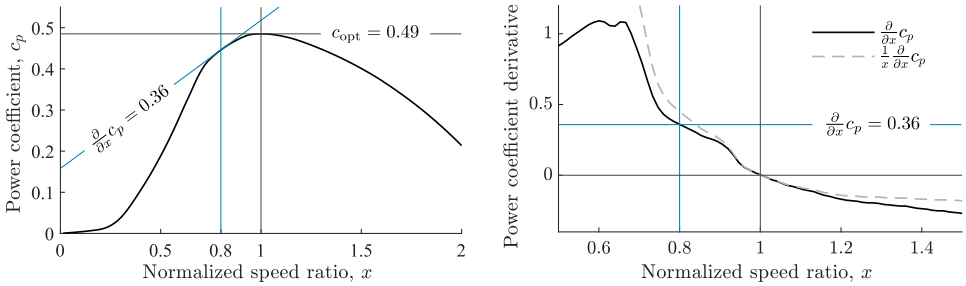

(a) Power coefficient. (b) Derivative of power coefficient.

Figure 8.5: Power efficiency coefficient of the NREL 5 MW turbine with $\beta = 0$.

Stable Operating Mode

Forcing the turbine to accelerate above optimal speed reduces the mechanical output power, which automatically reduces the acceleration. This, intuitively results in a stable mode of operation which can be verified by (8.5). As seen in Figure 8.5b, $\frac{\partial}{\partial x} c_p < 0$ for operation above optimal speed. Thus, the open-loop system (8.4) has a single pole in the left-half complex plane

$$s = R(\Omega_0)/M(\Omega_0) < 0, \quad \text{for} \quad x_0 > 1$$

and is therefore stable.

Unstable Operating Mode

Forcing the turbine to decelerate below optimal speed reduces the mechanical output power, which is automatically enhanced as it continues to reduce the mechanical power. This results in an unstable operating mode. Again, from (8.4) we see that the open-loop system will have an unstable pole at

$$s = R(\Omega_0)/M(\Omega_0) > 0, \quad \text{for} \quad x_0 < 1. \tag{8.6}$$

If we assume that the turbine is controlled, such that the normalized speed ratio is bounded from below by $\underline{x} > 0$, then $M(\Omega_0) > J\Omega_{\text{MPP}}\,\underline{x}$. Moreover, as seen in Figure 8.5b, $\frac{\partial}{\partial x} c_p > 0$. Consequently, the unstable open-loop pole (8.6) is bounded from above by

$$s = \frac{P_{\text{wind}}}{J\Omega_{\text{MPP}}^2} \frac{1}{x_0} \left.\frac{\partial}{\partial x} c_p\right|_{x=x_0} < \frac{P_{\text{wind}}}{J\Omega_{\text{MPP}}^2} \frac{1}{\underline{x}} \left.\frac{\partial}{\partial x} c_p\right|_{x=\underline{x}}. \tag{8.7}$$

Remark 8.1 (Scalability) Note that

$$\frac{P_{\text{wind}}}{J} \frac{1}{\Omega_{\text{MPP}}^2} = \frac{\rho \pi r^2 v^3}{2J} \frac{r^2}{\lambda_{\text{opt}}^2 v^2} = \frac{\rho \pi r^2}{2J} \frac{r^2}{\lambda_{\text{opt}}^2} v.$$

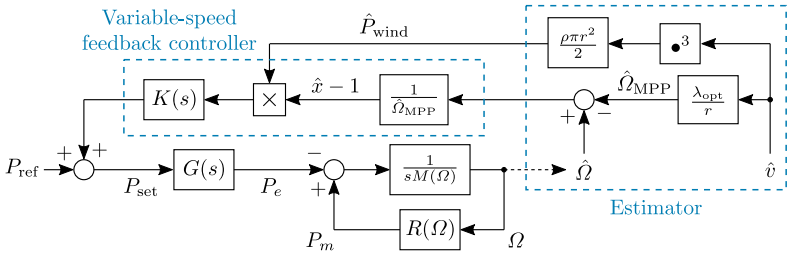

Figure 8.6: Block diagram of WT with variable-speed feedback control.

Thus, the open-loop pole (8.7)

$$s = \underbrace{\frac{\pi r^2}{J}}_{\substack{\text{size/inertia}\\ \text{constant}}} \frac{\rho}{2} \underbrace{\frac{r^2}{\lambda_{\text{opt}}^2}}_{\substack{\text{aerodynamic}\\ \text{constant}}} v \frac{1}{x_0} \frac{\partial}{\partial x} c_p \bigg|_{x=x_0} = Cv \frac{1}{x_0} \frac{\partial}{\partial x} c_p \bigg|_{x=x_0} \tag{8.8}$$

varies linearly with the wind speed v. The constant C should be fairly consistent for all WT models. Thus, the location of the unstable pole should be similar for WTs of various ratings.

8.2.2 Variable-Speed Feedback Controller

To operate the WT in the unstable region, we implement a stabilizing variable-speed feedback controller. The closed-loop system in Figure 8.6 from reference to output is

$$P_e = G(s) \frac{sM(\Omega_0) - R(\Omega_0)}{sM(\Omega_0) + G(s)\hat{K}(s) - R(\Omega_0)} P_{\text{ref}}$$

where the generator dynamics $|G(j\omega)| \approx 1$ in the frequency range of interest. Note that the closed-loop system has a NMP zero at the location of the unstable open-loop pole that is unaffected by the generator dynamics and the controller design.

Let $K(s)$ be a linear controller and let

$$\hat{K}(s) = K(s)\hat{P}_{\text{wind}}/\hat{\Omega}_{\text{MPP}} \tag{8.9}$$

where the notation $\hat{P}_{\text{wind}}$ and $\hat{\Omega}_{\text{MPP}}$ indicate estimates of P_{wind} and Ω_{MPP} respectively, e.g., from wind speed measurements as shown in Figure 8.6. The purpose of $\hat{K}(s)$ is to stabilize the WT. For this, a proportional feedback controller $\hat{K}(s) = k\hat{P}_{\text{wind}}/\hat{\Omega}_{\text{MPP}}$ is sufficient. Neglecting generator and measurement dynamics, the WT is described by the transfer functions

$$P_e = \frac{s-z}{s+p} P_{\text{ref}} \quad \text{and} \quad \Omega = \frac{-1}{J\Omega_{\text{MPP}}(s+p)} P_{\text{ref}}. \tag{8.10}$$

8.2.3 Linearization Capturing Undesirable NMP Characteristics

To be useful for FFR control design, we let the model be a "worst case" realization of (8.10) with fastest possible zero and slowest possible pole. This will result in a model that underestimates the WT's power output.

Assuming operation at a normalized speed $\underline{x} < x < 1$, $\underline{x} = 0.8$. The unstable open-loop pole (8.7), and consequently the NMP closed-loop zero

$$z = Cv\frac{1}{x_0}\left.\frac{\partial}{\partial x}c_p\right|_{x=x_0} \leq \bar{z} = Cv\frac{1}{\underline{x}}\left.\frac{\partial}{\partial x}c_p\right|_{x=\underline{x}}. \tag{8.11}$$

With a proportional feedback controller

$$p = k\frac{\hat{P}_{\text{wind}}}{\hat{\Omega}_{\text{MPP}}}\frac{1}{J\Omega_{\text{MPP}}x_0} - z \approx Cv\frac{1}{x_0}\left(k - \left.\frac{\partial}{\partial x}c_p\right|_{x=x_0}\right) \tag{8.12}$$

with equality if $\hat{P}_{\text{wind}} = P_{\text{wind}}$ and $\hat{\Omega}_{\text{MPP}} = \Omega_{\text{MPP}}$. Note that since the zero is bounded from above, the stabilized pole (8.12) is bounded from below by

$$p \geq \underline{p} = Cv\frac{1}{\underline{x}}\left(k - \left.\frac{\partial}{\partial x}c_p\right|_{x=\underline{x}}\right). \tag{8.13}$$

For the analysis, (8.10) is linearized by setting z and p to their bounds $\bar{z}$ and $\underline{p}$, respectively. A good starting point is to select k so that the unstable pole (8.7) is reflected into the LHP, in which case $\underline{p} = \bar{z}$. Inserting values from the NREL 5 MW WT into (8.8), then

$$C = 0.013, \quad \left.\frac{\partial}{\partial x}c_p\right|_{x=0.8} = 0.36, \quad k = 2 \cdot 0.36,$$

and the transfer function from P_{ref} to P_e

$$H_{\text{wind}}(s) = \frac{s - \bar{z}}{s + \bar{z}}, \quad \bar{z} = 5.8v \cdot 10^{-3}. \tag{8.14}$$

We will show that that (8.14) is a worst case representation of the WT, useful for designing a coordinated FCR and FFR controller.

8.2.4 Validating the Properties of the Linearized WT Model

The purpose of the linearized model (8.14) is to capture the dynamics most relevant for FFR. Because of this, it is designed to underestimate the electric power output of the WT. In addition, the model also need to capture the dynamics that are relevant for safe operation, with minimal conservatism. Since the most important property in this context is the normalized speed ratio (8.3), the linear model is designed to overestimate the decline in turbine speed. To ensure stability of the WT, regardless

Table 8.3: Model properties for the step response simulations.

k	v [m/s]	P_{MPP} [MW]	Ω_{MPP} [rad/s]	$\bar{z}$ [rad/s]	$\underline{p}$ [rad/s]
0.72	8	1.8	0.95	0.048	0.048
0.72	10	3.5	1.19	0.060	0.060
1.08	8	1.8	0.95	0.048	0.096

of the power reference input, we also implement a low speed protection mechanism. To show that the linearized model (8.14) possess the desired properties, we here compare it with the nonlinear modified NREL WT model. Model properties such as pole and zero bounds for various wind speeds and controller gains are shown in Table 8.3.

Varying Wind Speeds

Let $k = 0.72$ so that the WT is stable for operation with a normalized speed ratio above $\underline{x} = 0.8$. Consider operation at wind speeds 8 and 10 m/s.

As shown in Figure 8.7, after a +20 % reference step, the active electric power output is initially increased above the MPP. Consequently, the rotor speed decreases, which reduces the aerodynamic efficiency of the WT according to Figure 8.1b. Therefore, the increased power output cannot be sustained for long and eventually falls below the initial MPP output.

The location of the open-loop pole (8.8) and consequently the closed-loop zero (8.11) varies linearly with the wind speed. However, since the variable-speed controller (8.9) uses feed forward of the estimated wind energy $\hat{P}_{\mathrm{wind}}$, it will be equally efficient for different wind speeds, as seen in Figure 8.7b.

Note that the linear model (8.14) is conservative in the sense that it overestimates the size of the nonlinear NMP zero (8.11) which varies with the power coefficient derivative Figure 8.5b. Thus the linear model overestimates the decline in power from the turbine. Similarly it overestimates the decline in turbine speed since the pole (8.13) is underestimated.

Varying Feedback Gain

The choice of feedback gain affects the size of of the stabilized pole $\underline{p}$ as shown in Table 8.3. In Figure 8.8a we see that increasing the feedback gain makes the output decline faster. Consequently the rotor speed and output power stabilizes at a higher level.

Low Speed Protection

For stability, it is important that the normalized speed ratio does not decline below $x = 0.8$, since for $x < 0.8$, the power efficient derivative changes rapidly as shown in Figure 8.5b. With the stabilizing gain $k = 0.72$ we have designed the turbine to safely

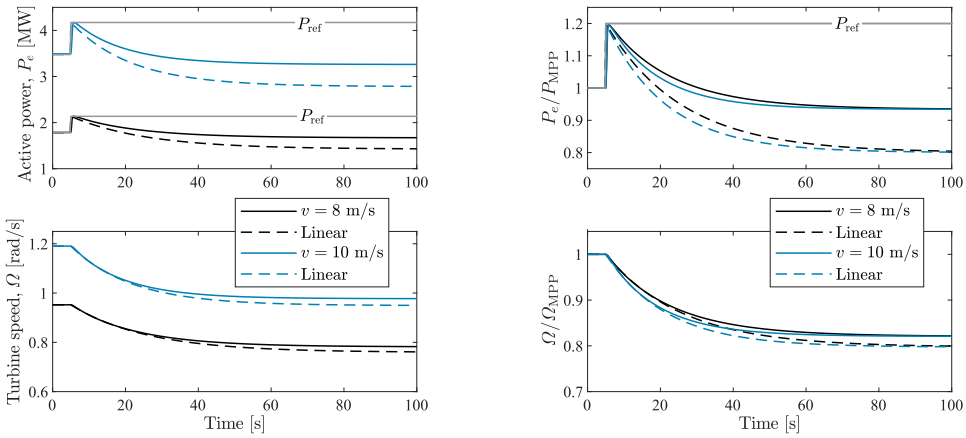

(a) SI-units. (b) Normalized.

Figure 8.7: Power output and rotor speed with feedback gain $k = 0.72$.

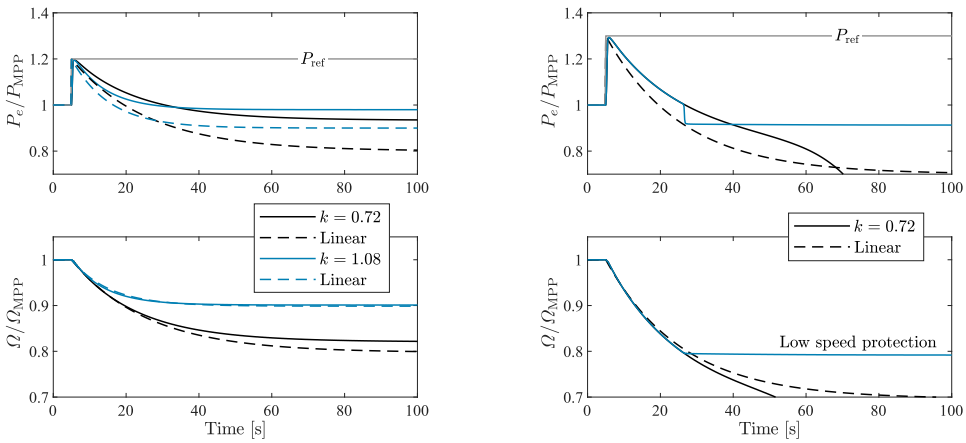

(a) Varying feedback gain. (b) Low speed protection.

Figure 8.8: Power output and rotor speed at 8 m/s wind speed.

operate at normalized speeds $x > 0.8$. As shown in Figure 8.8a, a +20 % reference step almost reaches the speed limit. Increasing the step size to +30 % makes the turbine decelerate to much so that it becomes unstable, as seen in Figure 8.8b.

Stability can be ensured by increasing the feedback gain. However, when controlling the WT to provide FFR, the focus is on the output power, P_e, not on the internal operation of the WT. Stable poles can then very well be canceled by a FFR controller, as we will see in Section 8.3.1. The location of the stable WT pole is therefore not critical in closed-loop FFR control, as long as stability is

ensured. To hinder accidental destabilization of the WT, a low speed safety measure is implemented, that disables the FFR controller and halt the deceleration when the normalized speed fall below $x = 0.8$. Let

$$P_{\text{set}} = \begin{cases} P'_{\text{set}} = P_{\text{ref}} + \hat{P}_{\text{wind}} k(\hat{x} - 1), & \hat{x} > 0.8 \\ \min\left(P_{0.8}\left(1 - 100(\hat{x} - 0.8)^2\right),\ P'_{\text{set}}\right), & \hat{x} < 0.8 \end{cases}$$

where $P_{0.8} = P_m(x = 0.8)$. As shown in Figures 8.8b and 8.12b this stabilizes the WT, bringing the turbine speed back to $x \approx 0.8$.

8.3 Simulation Study

In this section, we show how the linearized WT model (8.14) can be used for designing FFR. In particular, we will show how the NMP characteristics captured by (8.14) are useful for coordinating FFR from wind with slow FCR from hydro, so that a common design goal is achieved.

We do this in two steps. First, we will show how to coordinate wind-hydro resources in a open-loop FCR and FFR setting, creating a DVPP that fulfills design objectives that cannot be fulfilled with wind or hydro individually. Finally, we show the implementation of closed-loop FCR and FFR controller using feedback from local frequency measurement. We show how FFR from wind resources can be used to fulfill the FCR-D requirements in the hydro dominated N5 test system.

8.3.1 Open-Loop FCR and FFR in a Wind-Hydro DVPP

Consider a region with wind and hydro turbines exporting power to the grid as shown in Figure 8.9. For simplicity, assume that all hydro units are lumped into a single 100 MVA unit, that the 20 MW wind power park is lumped into a single (scaled) NREL WT, and that the two lumped models are connected to the same bus.

Assuming an initial gate opening $g_0 = 0.8$, servo time constant $T_y = 0.2\,\text{s}$, and water time constant $T_{\text{w}} = 2\,\text{s}$, then the linearized hydro model

$$H_1(s) = 100\frac{1}{0.2s + 1}2\frac{-s + 0.625}{s + 1.25}.$$

Let $v = 8\,\text{m/s}$, then the linearized WT model

$$H_2(s) = 4 \cdot 1.8\frac{s - 0.048}{s + 0.048}.$$

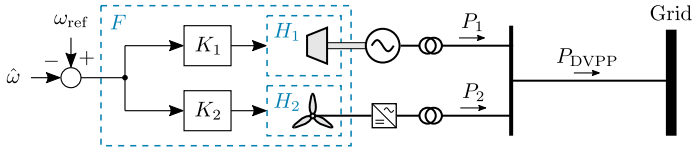

Figure 8.9: One-line diagram of a wind-hydro DVPP.

Goal

Design controllers K_1 and K_2 so that the hydro unit and wind park behaves like an DVPP fulfilling the FCR requirement,

$$H_1K_1 + H_2K_2 = F := 20\frac{6.5s+1}{(2s+1)(17s+1)}.$$

Solution

Using the model matching procedure described in Chapter 7, design dynamic participation factors $c_1(s) + c_2(s) = 1$ so that $H_1K_1 + H_2K_2 = F$ is fulfilled for all $s \in \mathbb{C}$ using the controllers

$$K_i(s) = c_i(s)F(s)/H_i(s), \quad i = 1, 2. \tag{8.15}$$

For internal stability, cancellation of NMP zeros is not allowed. Thus, NMP zeros need to be present in c_1 and c_2.

1. Starting with the hydro unit, including the NMP zero, let
$$c_1' = \frac{-s+0.625}{s+0.625}$$
where we have included a stable pole to make c_1' proper. The location of the pole is a design parameter, but a good starting point is to make c_1' all-pass.

2. With c_1' defined, the naive approach is to let $c_2' = 1 - c_1'$. But since H_2 is NMP, this is not possible. Instead, let
$$c_2' = \left(1 - c_1'\right)\frac{s-0.048}{s+0.048}. \tag{8.16}$$

3. The sum
$$c_1' + c_2' = \frac{s^2+0.48s+0.03}{s^2+0.67s+0.03} \approx 1 + j0$$
so we could stop here. However, since $c_1' + c_2'$ is stable and MP, model matching with $c_1(s) + c_2(s) = 1$ is achievable using
$$c_1 = \frac{c_1'}{c_1' + c_2'}, \quad \text{and} \quad c_2 = \frac{c_2'}{c_1' + c_2'}. \tag{8.17}$$
Controllers K_1 and K_2 are then obtained by substituting (8.17) into (8.15).

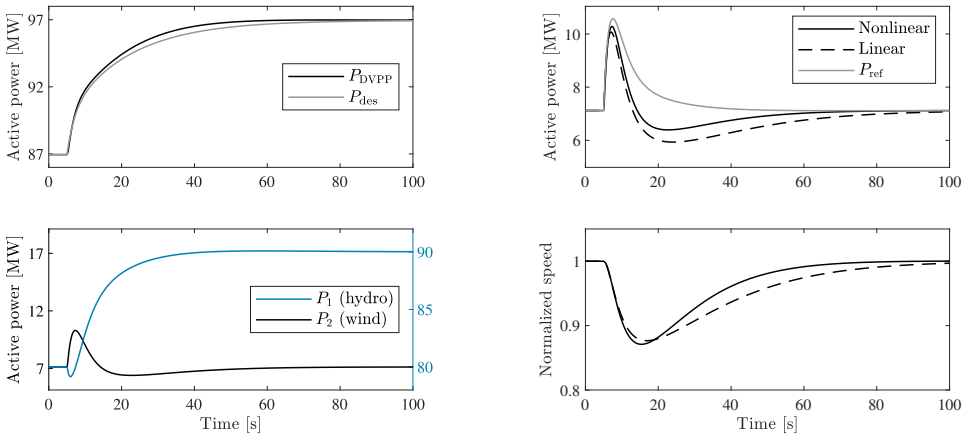

(a) Power injections. (b) WT response.

Figure 8.10: Power output of the wind-hydro DVPP.

Table 8.4: WT parameters for the 110 GWs test case.

Bus	P_{nom} [MW]	v [m/s]	P_{MPP} [MW]	FFR [%]
2	500	10	348	33
4	1500	8	534	67

Result

The coordinated response to a 0.5 Hz reference step is shown in Figure 8.10. As shown in Figure 8.10a the DVPP closely matches the desired output $P_{\text{des}} = F(s)(\omega_{\text{ref}} - \hat{\omega})$. The discrepancy between the actual response and the desired response comes from the underestimation of wind power output seen in Figure 8.10b.

In (8.16) we leverage the fact that we can allow the WT to draw power as $|s| \to 0$. To avoid dynamic interaction we want the NMP zero of the hydro unit to be much faster than the NMP zero of the WT. Note that the WT zero varies significantly with the turbine speed, but that it is bounded from above (8.11). Thus, the control design, using the derived linearized WT model (8.14), assumes worst case interaction.

8.3.2 Closed-Loop FCR and FFR in the N5 Test System

Consider the N5 test system introduced in Section 8.1.2. Assume that the hydro-FCR is complemented with FFR from wind power at buses 2 and 4 as shown in Figure 8.2. Assume that the WTs participating in FFR have a total nominal power rating of 2000 MW distributed according to Table 8.4.

Goal

Design coordinated FCR and FFR controllers fulfilling the FCR-D requirements in Section 8.1.3, with feedback from local frequency measurements. That is, design controllers K_i, $i \in \{1, \ldots, 5\}$ so that (8.2) is fulfilled, with

$$\sum_{i=1}^{5} H_i(s)K_i(s) = F_{\mathrm{FCR}}(s) = R_{\mathrm{FCR}} \frac{6.5s+1}{(2s+1)(17s+1)}.$$

Solution

Using the three-step model matching approach in Section 8.3.1, dynamic participation factors $c_i(s)$ are designed so that $\sum_{i=1}^{5} c_i(s) = 1$, $\forall s \in \mathbb{C}$. Let the shares of FCR and FFR be distributed according to Table 8.2 and Table 8.4, respectively. The resulting controllers $K_i(s) = c_i(s)F_{\mathrm{FCR}}(s)/H_i(s)$ will be fourth order.

Result

The system response following the dimensioning fault, i.e., the disconnection of the 1400 MW NordLink HVDC cable, is shown in Figure 8.11. Comparing Figure 8.4a with Figure 8.11a we see that the transient frequency response is improved when the hydro-FCR, P_{hydro}, is supported by, P_{wind}, from WTs at buses 2 and 4. The combination $P_{\mathrm{hydro+wind}} = P_{\mathrm{hydro}} + P_{\mathrm{wind}}$ matches the desired response $P_{\mathrm{des}} = F_{\mathrm{FCR}}(s)(\omega_{\mathrm{ref}} - \hat{\omega})$. With the nadir kept above 49.0 Hz, the FCR-D requirement are now fulfilled. By utilizing the WTs for FFR, this is achieved without increasing the bandwidth of the hydro units. Thus, the frequency response is improved without reducing the closed-loop stability margin [40].

In Figure 8.11b we see that the WTs participating in FFR decelerate to around 90 % of optimal speed following the fault. Since the WT based on the NREL model allows for a deceleration to around 80 % of optimal speed, there is more room for FFR improvement. Note however that the 500 MW WT at bus 2 almost reaches rated power. If the limit is reached, the WT will saturate. However, the WT at bus 4 have plenty of margin left. This shows how only a limited wind resource is enough to compensate for the FCR bandwidth limitation of hydro power in this power system. In fact, the FCR-D requirements can be fulfilled with significantly less wind resources.

Sensitivity Study with 50 % Wind Resources

Consider the same scenario shown in Figure 8.11 but now let $P_{\mathrm{nom}} = 250$ MW at bus 2 and $P_{\mathrm{nom}} = 750$ MW at bus 4. As shown in Figure 8.12b, the WT at bus 2 now reaches its saturation limit. This has a small effect on the nadir in Figure 8.12a, but not enough to violate the FCR-D requirement. With less wind resources, the FFR response gives a larger deceleration of the participating WTs. As seen in

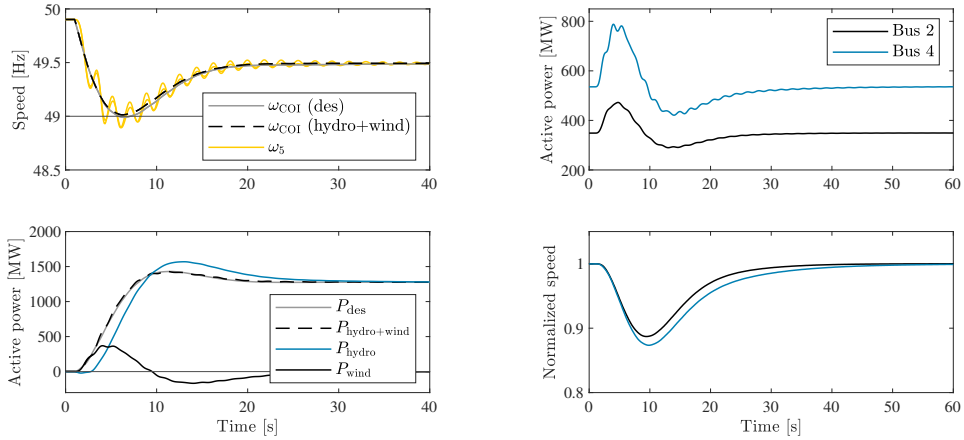

(a) FCR and FFR response. (b) WT output and speed.

Figure 8.11: System response to a 1400 MW fault with coordinated FCR and FFR.

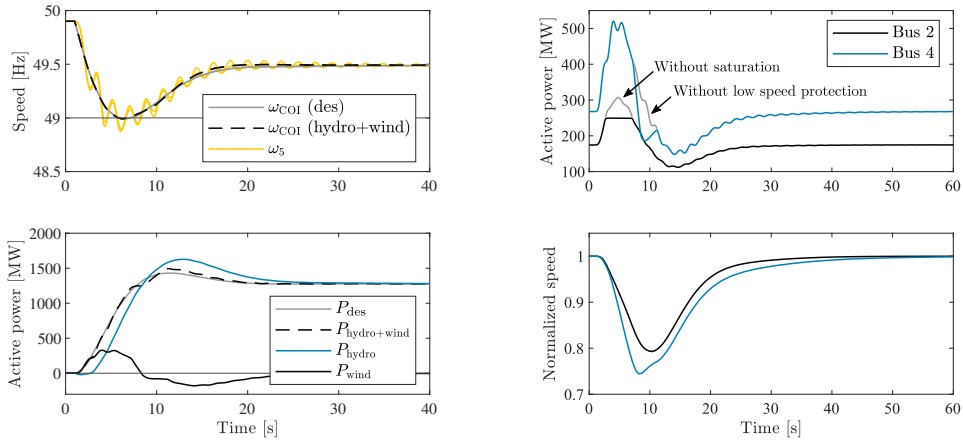

(a) FCR and FFR response. (b) WT output and speed.

Figure 8.12: Sensitivity study with 50 % of the wind resources in Figure 8.11.

Figure 8.12b, the low speed protection is activated for the WTs at bus 4, ensuring stability of the WTs.

8.4 Summary

A variable-speed controlled WT model based on the NREL 5 MW baseline WT model has been presented. The new model-based variable-speed feedback controller allows the WT to provide temporary FFR when operated at the MPP, without the need

for curtailment. The controller has been designed to give the WT similar dynamic properties for various wind speeds. This facilitated a meaningful linearization of the WT, resulting in a first-order linearized model, capturing the relevant dynamic properties for FFR control design at various wind speeds. The linear WT model is useful for coordinating wind-FFR with slow hydro-FCR, fulfilling dynamic design objectives not achievable by wind or hydro individually. This was shown in a local DVPP and in a 5-machine representation of the Nordic synchronous grid. During FFR, WTs take the lead (via synthetic inertia) in order to limit the frequency nadir and compensate for the initial under production of hydro units, as depicted in Figure 8.4b. After this initial transitory, hydro units take over during FCR recovery, compensating not only for the initial down frequency event, but also for the kickback effect caused by the WT-based FFR. In the linearized WT model, the kickback effect is characterized by a NMP zero. Including this NMP characteristic in the coordinated FCR and FFR control design, results in an excellent frequency recovery as depicted in Figures 8.11a and 8.12a, compared to hydro-only FCR in Figure 8.4a.

Chapter 9

A Scalable Nyquist Stability Criterion

In this chapter, we develop a theoretical framework to bridge the gap between small-signal rotor angle stability and frequency stability. We combine tools from linear algebra, graph theory, and complex analysis to formulate a scalable Nyquist stability criterion. This allows us to provide a priori stability guarantees for connecting new devices to the network. The method is applied to a power system, where the most dominating dynamic feature is the synchronous machines. In the model, these are modeled as integrators. The new stability criterion requires only locally available information and is shown to be less conservative than existing methods.

In a synchronous grid, balancing between load and production is achieved by controlling the center of inertia (COI) frequency. Higher-order dynamics can often be ignored, given sufficient time-scale separation [157]. In frequency control, stability of interarea modes are therefore typically ignored and treated as a separate problem. However, with an increasing share of converter-interfaced generation, the inertia is decreasing. Consequently, faster frequency control is required. Because of this, the assumption that interarea modes can be ignored is becoming harder to motivate. With renewable and small-scale generation connecting to the grid, the number of possible system configurations increases drastically. This makes it difficult to apply conventional control design methods, since one cannot determine a priori the model to use, or which set of network configurations or operating points to consider. Methods addressing global stability has to be scalable and computationally effective, since the computational effort grows with the system size [158].

Local requirements that ensures global stability are essential. If we do not have any information about the network, we need to make some conservative assumptions in order to guarantee stability. Homogeneity, i.e., assuming identical or proportional subsystems, is one such conservative assumption. In [159], a Nyquist-like criterion is derived for checking the stability of a network of homogeneous single-input single-output (SISO) agents, connected over a static network. In [160], these results are generalized to include networks of homogeneous multiple-input multiple-output (MIMO) agents interconnected over a dynamics network. Other methods, allowing

for heterogeneous plants, guarantee stability using passivity assumptions or by using the small gain theorem [161]. Consensus protocols for networks with directed information flow and switching topology has also received attention in the study of self-organizing networked systems [162, 163]. For power system applications, however, we are concerned with fixed networks. In [155], a robust scale-free syntheses method is developed, guaranteeing stability by identifying a separating hyperplane in the Nyquist diagram. The method provide a priori stability guarantees for connecting new devices to the grid, with limited knowledge of the network. In this chapter, we will present a generalization of the results in [155, 159], using the generalized Nyquist criterion in combination with the field of values.

The main contribution of this chapter is a scalable Nyquist stability criterion allowing for a network of heterogeneous agents coupled over a connected (possibly lossy) network. We distinguish between exponential stability and asymptotic synchronization on the average network mode. For a system to be exponentially stable we require asymptotic synchronization, but also that the average mode is stable [163]. In power systems, we are concerned about the average frequency mode. Typically, the average frequency mode is approximated as the COI frequency mode. One problem is that the COI mode contains information about higher-order network modes, making it hard to derive closed form expressions for heterogeneous networks. In this chapter, we instead focus on the average frequency dynamics, which can be expressed from the network equations also for heterogeneous networks. If the system achieves asymptotic synchronization on the average mode, then the COI frequency mode converges to the average frequency mode.

The remainder of this chapter is organized as follows. Section 9.1 introduces the Nyquist theorem and field of values. Section 9.2 presents the addressed problem. In Section 9.3, the average frequency dynamics are derived from a modal decomposition of the network equations. Section 9.4 presents the main result: a scalable Nyquist stability criterion guaranteeing asymptotic synchronization on the average mode using only local information. Section 9.5 evaluates the proposed method on a power system example. Section 9.6 concludes the chapter.

9.1 Preliminaries

We review some results for MIMO linear time-invariant (LTI) systems [114, 115, 164–166].

Let $L(s)$ denote a square, proper, and rational transfer matrix with no internal right half-plane (RHP) pole-zero cancellations. Assume that the feedback system with return ratio $-L(s)$ is well posed. Let $\det\big(I + L(s)\big) = \frac{\phi_{cl}(s)}{\phi_{ol}(s)}$, where $\phi_{ol}(s)$ and $\phi_{cl}(s)$ are the open- and closed-loop characteristic polynomials, respectively. The closed-loop system is stable if and only if $\phi_{cl}(s)$ have no roots in the RHP. Define the Nyquist $\mathcal{D}$-contour as a contour in the complex plane that includes the entire $j\omega$-axis and an infinite semi-circle into the RHP, making small indentations into the RHP to avoid any open-loop poles of $L(j\omega)$ (roots of $\phi_{ol}(s)$) directly on the $j\omega$-axis.

Lemma 9.1 (Generalized Nyquist theorem [164, Theorem 2.9]) *If $L(s)$ has P_{ol} unstable (Smith-McMillan) poles, then the closed-loop system with return ratio $-L(s)$ is stable if and only if the eigenloci of $L(s)$, taken together, encircle the point -1 P_{ol} times anticlockwise, as s goes clockwise around the Nyquist $\mathcal{D}$-contour.*

The spectrum of a matrix A is the set $\lambda(A) = \{\lambda_1(A), \ldots, \lambda_n(A)\}$ of eigenvalues $\lambda_i(A)$, $i \in \{1, \ldots, n\}$. The spectrum lies inside the field of values

$$\mathrm{F}(A) := \left\{ v^H A v : v \in \mathbb{C}^n, v^H v = 1 \right\}$$

see [167]. Consider matrices $A \in \mathbb{C}^{n\times n}$ and $B \in \mathbb{R}^{n\times n}$. Assume that B is positive semi-definite with the eigenvalue decomposition $B = \mathcal{V}\Lambda\mathcal{V}^T$, where $\Lambda = \operatorname{diag}\left(\lambda_1(B), \ldots, \lambda_n(B)\right)$ and $\mathcal{V}^T\mathcal{V} = I$. It follows that $\lambda\big(A\mathcal{V}\Lambda\mathcal{V}^T\big) = \lambda\big(\mathcal{V}^T A\mathcal{V}\Lambda\big)$ and $\mathrm{F}(A) = \mathrm{F}(\mathcal{V}^T A\mathcal{V})$. Assume that the eigenvalues are ordered such that $0 \leq \lambda_1(B) \cdots \leq \lambda_n(B)$. Then the ij^{th} element of the matrix product AB

$$\lambda_1(B)(A_{ij}) \leq (AB)_{ij} \leq \lambda_n(B)(A_{ij}).$$

Consequently,

$$\lambda\big(AB\big) \subset \mathrm{F}\left(AB\right) = \left\{ v^H A v : v \in \mathbb{C}^n, v^H v \in [\lambda_1(B), \lambda_n(B)] \right\}$$

where

$$\mathrm{F}\left(AB\right) = \alpha\, \mathrm{F}\left(A\right) = \left\{ v^H A v : v \in \mathbb{C}^n, v^H v = \alpha, \alpha \in [\lambda_1(B), \lambda_n(B)] \right\}. \tag{9.1}$$

9.2 Problem Formulation

In this section we present the network stability problem. We consider rotor angle stability in a power system with n buses. The dynamics at bus $i \in \{1, \ldots, n\}$ is described by the transfer function

$$g_i(s) := \frac{1}{s^2 M_i + s F_i(s) + R_i(s)}, \tag{9.2}$$

for instance, representing the dynamics of a synchronous machine with or without governor, a load, or a power electronics device. The scalar transfer functions $R_i(s)$ and $F_i(s)$ represent local phase angle and frequency dependent actuators, respectively, whereas the constant $M_i \geq 0$ represents the inertia. If $M_i > 0$, then the agent represents a synchronous machine. The closed-loop network dynamics can be described by the feedback interconnection

$$\begin{aligned} \boldsymbol{\delta} &= \mathcal{G}(s)(\boldsymbol{d} - \boldsymbol{u}) \\ \boldsymbol{u} &= \mathcal{L}\boldsymbol{\delta}, \end{aligned} \tag{9.3}$$

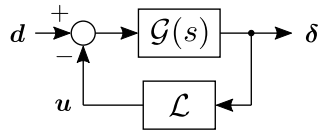

Figure 9.1: Network of n agents coupled through the network $\mathcal{L}$.

where outputs $\boldsymbol{\delta} = [\delta_1, \ldots, \delta_n]^T$ are the voltage phase angles, $\boldsymbol{u} = [u_1, \ldots, u_n]^T$ are the inputs, and $\boldsymbol{d} = [d_1, \ldots, d_n]^T$ are some external disturbances. The agent dynamics $\mathcal{G}(s) = \operatorname{diag}\big(g_1(s), \ldots, g_n(s)\big)$ is coupled through a lossless network described by the Laplacian matrix $\mathcal{L}$.

We make the standard assumptions that bus voltage magnitudes are constant for the time frame of interest, transmission is lossless, and reactive power does not affect bus voltage phase angles and frequency [25]. Then the elements of $\mathcal{L}$ is given by

$$\mathcal{L}_{ij} = -\frac{\partial}{\partial \delta_j} \sum\nolimits_{l=1}^{n} V_i^* V_l^* b_{il} \sin(\delta_i - \delta_l)\Big|_{\boldsymbol{\delta}=\boldsymbol{\delta}^*}, \tag{9.4}$$

where $\boldsymbol{V}^* = [V_1^*, \ldots, V_n^*]^T \in \mathbb{R}^n$ and $\boldsymbol{\delta}^* = [\delta_1^*, \ldots, \delta_n^*]^T \in \mathbb{R}^n$ represent the voltage magnitude and phase angles, respectively, at the steady-state linearization point, and $b_{il} \geq 0$ is the susceptance of the transmission line connecting buses i and l. If $b_{il} = 0$, then buses are not directly connected [155].

Equivalently, (9.3) can be written as

$$sE \begin{bmatrix} \boldsymbol{\delta} \\ \boldsymbol{\omega} \end{bmatrix} = A(s) \begin{bmatrix} \boldsymbol{\delta} \\ \boldsymbol{\omega} \end{bmatrix} + B\boldsymbol{d}, \quad E = \operatorname{diag}(I, \mathcal{M}), \tag{9.5}$$

where

$$A(s) = \begin{bmatrix} 0 & I \\ -\mathcal{L} - \mathcal{R}(s) & -\mathcal{F}(s) \end{bmatrix}, \quad B = \begin{bmatrix} 0 \\ I \end{bmatrix}, \tag{9.6}$$

and the transfer matrices $\mathcal{R}(s) = \operatorname{diag}[R_1(s), \ldots, R_n(s)]$ and $\mathcal{F}(s) = \operatorname{diag}[F_1(s), \ldots, F_n(s)]$, and the constant matrix $\mathcal{M} = \operatorname{diag}(M_1, \ldots, M_n)$. The vector $\boldsymbol{\omega} = [\omega_1, \ldots, \omega_n]^T = s\boldsymbol{\delta}$ represent the voltage frequency at each node. We assume that there are no algebraic network nodes, i.e., there are no node i such that $M_i = F_i(s) = R_i(s) = 0$. This is not a restriction since we can always formulate a reduced network model without algebraic nodes by taking the Schur complement of $\mathcal{L}$ with respect to the algebraic nodes. This reduction of an electric network is known as Kron reduction [132].

Let eigenvalue decomposition of $\mathcal{L}$ be

$$\operatorname{diag}\big(\lambda_1(\mathcal{L}), \ldots, \lambda_n(\mathcal{L})\big) = \operatorname{diag}(\lambda_1, \ldots, \lambda_n) = \mathcal{V}^T \mathcal{L} \mathcal{V}$$

where $\mathcal{V} \in \mathbb{R}^{n \times n}$ is a unitary matrix of eigenvectors $\mathcal{V} = \big[v_1, \ldots, v_n\big]$ so that $\mathcal{V}^T\mathcal{V} = I$. Let the eigenvalues be arranged in ascending order so that $0 = \lambda_1 < \lambda_2 \leq \cdots \leq \lambda_n$. Since $\mathcal{L}$ is a Laplacian matrix, $\lambda_1 = 0$ and the corresponding eigenvector $v_1 = \frac{1}{\sqrt{n}}\mathbf{1}$,

where $\mathbf{1}$ is a vector of ones. The mode $\Lambda_1 = v_1^T \boldsymbol{\delta}$ describes the average phase angle, whereas $\Omega_1 = v_1^T \boldsymbol{\omega}$ describes the average frequency of the network.

In this chapter we want to identify a criterion that guarantees stability of the feedback interconnection (9.3) using only locally available information. We differentiate between exponential stability, and asymptotic synchronization on the average mode.

9.3 Classification of Network Stability

In this section we present the classification of network stability used in this chapter. A common way to characterize stability of a power system is by diagonalizing the system equations [25]. The system stability is then expressed in terms of the stability of network modes, e.g., the average mode plus interarea modes.

Consider the coordinate change to modal states

$$\left[\Lambda_1, \Omega_1, \ldots, \Lambda_n, \Omega_n\right]^T := W^T \begin{bmatrix} \boldsymbol{\delta} \\ \boldsymbol{\omega} \end{bmatrix} \tag{9.7}$$

using the transformation matrix

$$W := \begin{bmatrix} v_1 & 0 & \cdots & v_n & 0 \\ 0 & v_1 & \cdots & 0 & v_n \end{bmatrix} \in \mathbb{R}^{2n \times 2n},$$

made up of the eigenvectors v_i, $i \in \{1, \ldots, n\}$ of $\mathcal{L}$. Since $W^T = W^{-1}$, the coordinate transform (9.7) applied to (9.5),

$$sW^T E W W^T \begin{bmatrix} \boldsymbol{\delta} \\ \boldsymbol{\omega} \end{bmatrix} = W^T A(s) W W^T \begin{bmatrix} \boldsymbol{\delta} \\ \boldsymbol{\omega} \end{bmatrix} + W^T B W W^T \boldsymbol{d},$$

is a similarity transformation. It gives a block-diagonal realization of (9.5), with the 2×2 blocks

$$s \begin{bmatrix} \Lambda_i \\ M_{\lambda_i} \Omega_i \end{bmatrix} = \begin{bmatrix} 0 & 1 \\ -\lambda_i - R_{\lambda_i}(s) & -F_{\lambda_i}(s) \end{bmatrix} \begin{bmatrix} \Lambda_i \\ \Omega_i \end{bmatrix} + \begin{bmatrix} 0 \\ 1 \end{bmatrix} v_i^T \boldsymbol{d},$$

characterizing the dynamics of network mode i, where $M_{\lambda_i} = v_i^T \mathcal{M} v$, $F_{\lambda_i}(s) = v_i^T \mathcal{F}(s) v$, and $R_{\lambda_i} = v_i^T \mathcal{R}(s) v$.

The transfer function from $v_i^T \boldsymbol{d}$ to Λ_i is

$$\frac{1}{s^2 M_{\lambda_i} + s F_{\lambda_i}(s) + R_{\lambda_i}(s) + \lambda_i} = \frac{h_i(s)}{1 + \lambda_i h_i(s)}, \tag{9.8}$$

where

$$h_i(s) := \frac{1}{s^2 M_{\lambda_i} + s F_{\lambda_i}(s) + R_{\lambda_i}(s)}.$$

Since the similarity transform preserves stability, the network (9.5) is stable if (9.8) is stable for all $i \in \{1, \ldots, n\}$. At this point, we could apply the Nyquist criterion

on the SISO return ratio $-\lambda_i h_i(s)$. The crux, however, is that it is impossible to say anything with certainty about $h_i(s)$ without complete information of $\mathcal{L}$ and $\mathcal{G}(s)$. What we do instead is to characterize the agent's contribution to the average mode $\{\Lambda_1, \Omega_1\}$ since the eigenvector $v_1 = \frac{1}{\sqrt{n}}\mathbf{1}$ is known.

Introduce COI frequency

$$\omega_{\text{COI}} := \frac{\sum_{i=1}^n M_i \omega_i}{M}, \quad M = \sum\nolimits_{i=1}^n M_i. \tag{9.9}$$

If the actuator parameters are proportional to inertia, then the COI frequency corresponds to the average frequency mode of the network [168].

The transfer function (9.8) of the average frequency mode is

$$\Omega_1 = s\Lambda_1 = \frac{s\sqrt{n}}{s^2 M + sF(s) + R(s)} \sum_{i=1}^n d_i, \tag{9.10}$$

where $F(s) = \sum_{i=1}^n F_i(s)$ and $R(s) = \sum_{i=1}^n R_i(s)$. Scaling (9.10) with $1/\sqrt{n}$, the average frequency disturbance response

$$\omega_{\text{avg}} := \Omega_1/\sqrt{n} = \frac{s}{s^2 M + sF(s) + R(s)} \sum\nolimits_{i=1}^n d_i.$$

Note that we can incorporate network losses and phase angle dependent actuators in $\mathcal{R}(s)$ into $\mathcal{F}(s)$ by substituting $\mathcal{F}(s)$ with $\mathcal{F}(s) + \frac{1}{s}\mathcal{R}(s)$ in (9.6). Thus, with the first-order network model, the average frequency disturbance response is given by

$$\omega_{\text{avg}} = \frac{1}{sM + F(s)} \sum\nolimits_{i=1}^n d_i. \tag{9.11}$$

Remark 9.1 If we have homogeneous or proportional agents, then $\omega_{\text{avg}} = \omega_{\text{COI}}$. With heterogeneous agents, the exact representation of the COI mode cannot easily be obtained [168]. The problem is that the COI mode contains information about the higher-order network modes, the interarea modes $\{\Lambda_i, \Omega_i\}$, $i \in \{2, \ldots, n\}$. This makes the transient response of (9.9) different from (9.11) (this is shown later in Section 9.5.3). However, if the system achieves asymptotic synchronization on the average mode then ω_{COI} and ω_{avg} converge.

We classify stability of (9.3) using the following terminology. If

- (9.8) is stable for all $i \in \{1, \ldots, n\}$ then the system is exponentially stable;
- (9.8) is stable for all $i \in \{2, \ldots, n\}$ then the system achieves asymptotic synchronization on the average mode (the system has stable interarea modes). Exponential stability therefore implies asymptotic synchronization;
- $h_1(s)$ is stable, then the average mode is stable; and if
- (9.11) is stable, then the average frequency mode is stable.

We say that the feedback interconnection (9.8) has stable frequency dynamics if it has stable interarea modes and a stable average frequency mode.

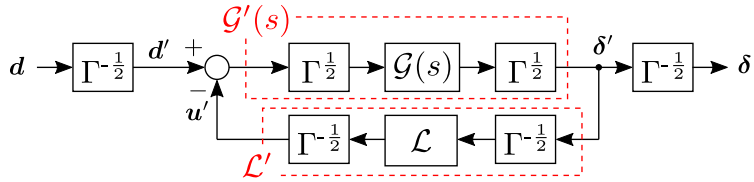

Figure 9.2: Feedback interconnection of n agents coupled through the output over a lossless network $\mathcal{L}$. Normalized using (9.12).

9.4 Asymptotic Synchronization Criterion

Let

$$\mathcal{G}'(s) := \Gamma^{\frac{1}{2}}\mathcal{G}(s)\Gamma^{\frac{1}{2}}, \quad \text{and} \quad \mathcal{L}' := \Gamma^{-\frac{1}{2}}\mathcal{L}\,\Gamma^{-\frac{1}{2}}, \tag{9.12}$$

where Γ is the diagonal matrix

$$\Gamma := \operatorname{diag}(\gamma_1, \ldots, \gamma_n) = 2 \cdot \operatorname{diag}(\mathcal{L}_{11}, \ldots, \mathcal{L}_{nn})$$

with $\mathcal{L}_{ii}$, being the diagonal entries of the network matrix (9.4). The eigenvalues of $\mathcal{L}'$ are then $0 = \mu_1 < \mu_2 \leq \cdots \leq \mu_n \leq 1$. The constant μ_2 is refereed to as the algebraic connectivity of the network $\mathcal{L}'$ [163]. Stability of the interconnection of $\mathcal{G}(s)$ over $\mathcal{L}$ is equivalent to stability of the normalized interconnection of $\mathcal{G}'(s)$ over $\mathcal{L}'$, as shown in Figure 9.2 [155]. The first eigenvector u_1, $\mathcal{L}'u_1 = 0$, is typically not parallel to $\mathbf{1}$.

Theorem 9.2 *Assume that $\mathcal{G}'(s)$ has P_{ol} unstable poles. Then the closed-loop system with return ratio $-\mathcal{L}'\mathcal{G}'(s)$ achieves asymptotic synchronization on the average mode if and only if the eigenloci $\{\lambda_2(\mathcal{L}'\mathcal{G}'(s)), \ldots, \lambda_n(\mathcal{L}'\mathcal{G}'(s))\}$ taken together, encircle the point -1 P_{ol} times anticlockwise, as s goes clockwise around the Nyquist $\mathcal{D}$-contour.*

Proof sketch: The closed-loop system is exponentially stable if the transfer functions

$$\begin{aligned} &\mathcal{G}'(s)\mathcal{L}'\big(I + \mathcal{G}'(s)\mathcal{L}'\big)^{-1}, \quad \big(I + \mathcal{G}'(s)\mathcal{L}'\big)^{-1} \\ &\mathcal{G}'(s)\big(I + \mathcal{G}'(s)\mathcal{L}'\big)^{-1}, \quad \mathcal{L}'\big(I + \mathcal{G}'(s)\mathcal{L}'\big)^{-1} \end{aligned} \tag{9.13}$$

are all stable. Consider first the special case where we assume that the network is lossy[1], e.g., substitute the matrix $\mathcal{L}'$ with $\mathcal{L}' + \epsilon I$ in (9.13), where $\epsilon > 0$. Since $\mathcal{L}'$ is constant and has full rank, it is sufficient to check one of the four transfer functions

[1] As noted in Section 9.3, this can represent a system (9.6) where one or more of the frequency dependent actuators $F_i(s)$ has integral action.

in (9.13). Factorize $\mathcal{L}' = \mathcal{W}Y\mathcal{W}^T$, where the diagonal matrix $Y > 0$, and $\mathcal{W}^T\mathcal{W} = I$. We have that

$$\mathcal{L}'(I + \mathcal{G}'(s)\mathcal{L}')^{-1} = \mathcal{W}Y\mathcal{W}^T(I + \mathcal{G}'(s)\mathcal{W}Y\mathcal{W}^T)^{-1} = \mathcal{W}Y(I + \mathcal{W}^T\mathcal{G}'(s)\mathcal{W}Y)^{-1}\mathcal{W}^T$$

Clearly, this is stable if the sensitivity function

$$\big(I + P(s)\big)^{-1} := \big(I + \mathcal{W}^T\mathcal{G}'(s)\mathcal{W}Y\big)^{-1} \tag{9.14}$$

is stable. Since the feedback system with return ratio $-P(s)$ is well posed, we can assess stability using Lemma 9.1. Let P_{ol} be the number of unstable poles in $\mathcal{G}'(s)$. The closed-loop (9.14) is then stable if and only if the image of

$$\det\big(I + P(s)\big) = \prod_{i=1}^{n} \lambda_i\big(I + P(s)\big) = \prod_{i=1}^{n} \Big(1 + \lambda_i\big(P(s)\big)\Big)$$

makes P_{ol} anticlockwise encirclements of the origin as s goes clockwise around the Nyquist $\mathcal{D}$-contour. Note that the image of $1 + \lambda_i\big(P(s)\big)$ encircles the origin if $\lambda_i\big(P(s)\big)$ encircles the point -1; and that the argument of a product is the same as the sum of the arguments. The closed-loop system (9.14) is therefore stable if and only if the eigenloci of $P(s)$, taken together, encircle the point -1 P_{ol} times.

Returning to the closed-loop system with a lossless network matrix $\mathcal{L}$. Here, the feedback system is ill-posed and we can therefore not use Lemma 9.1 to assess stability of the the four transfer functions (9.13). To continue, we instead make some observations that connect the case with a lossless network ($\lambda_1(\mathcal{L}') = 0$) to the case with a lossy network ($\lambda_1(\mathcal{L}') > 0$) studied above.

Factorizing $\mathcal{L}' = \mathcal{U}X\mathcal{U}^T = \hat{\mathcal{U}}\hat{X}\hat{\mathcal{U}}^T$ allows us to separate the average mode from the interarea modes. Normalized using (9.12), then

$$0 \le X \le I \in \mathbb{R}^{n\times n}, \quad \mathcal{U} = [u_1, \ldots, u_n] \in \mathbb{R}^{n\times n},$$

while

$$\mu_2 I \le \hat{X} \le I \in \mathbb{R}^{n-1\times n-1}, \quad \hat{\mathcal{U}} = [u_2, \ldots, u_n] \in \mathbb{R}^{n\times n-1}.$$

Note that

$$\mathcal{U}\mathcal{U}^T = u_1u_1^T + \hat{\mathcal{U}}\hat{\mathcal{U}}^T = I \in \mathbb{R}^{n\times n}.$$

The transfer function from $\boldsymbol{d}'$ to $\boldsymbol{\delta}'$ is therefore equivalent for the closed-loop systems shown in Figure 9.2 and Figure 9.3.

The transfer function

$$\mathcal{L}'\big(I + \mathcal{G}'(s)\mathcal{L}'\big)^{-1} = \hat{\mathcal{U}}\hat{X}\hat{\mathcal{U}}^T(I + \mathcal{G}'(s)\hat{\mathcal{U}}\hat{X}\hat{\mathcal{U}}^T)^{-1} = \hat{\mathcal{U}}\hat{X}(I + \hat{\mathcal{U}}^T\mathcal{G}'(s)\hat{\mathcal{U}}\hat{X})^{-1}\hat{\mathcal{U}}^T$$

is stable if the $(n-1)\times(n-1)$ sensitivity function

$$\big(I + L(s)\big)^{-1} := \big(I + \hat{\mathcal{U}}^T\mathcal{G}'(s)\hat{\mathcal{U}}\hat{X}\big)^{-1} \tag{9.15}$$

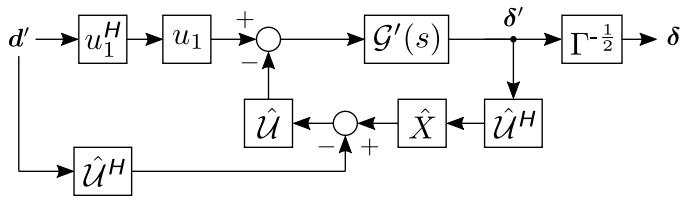

Figure 9.3: The normalized feedback interconnection shown in Figure 9.2 with interarea modes isolated from the average mode.

is stable. Since the feedback system with return ratio $-L(s)$ is well posed, we can assess stability using Lemma 9.1. The sensitivity (9.15) is stable if

$$\det\big(I + L(s)\big) = \prod_{i=1}^{n-1} \lambda_i\big(I + L(s)\big) = \prod_{i=1}^{n-1} \Big(1 + \lambda_i\big(L(s)\big)\Big) \tag{9.16}$$

makes P_{ol} anticlockwise encirclements of the origin as s goes clockwise around the Nyquist $\mathcal{D}$-contour. That is, if the eigenloci of $L(s)$, taken together, encircle the point -1 P_{ol} times.

Stability of (9.13) is equivalent to stability of the n transfer functions

$$\frac{h_i(s)}{1 + \lambda_i h_i(s)} \tag{9.17}$$

in (9.8). This can only be the case if

$$\lambda_i h_i(s) = \lambda_i\big(\mathcal{G}(s)\mathcal{L}\big) = \lambda_i\big(\mathcal{G}'(s)\mathcal{L}'\big).$$

If $\lambda_1 = 0$, then (9.17) is exponentially stable if and only if $h_1(s)$ is stable, and if (9.15) is stable (i.e., the interarea modes are stable). If the interarea modes are stable, and if $sh_1(s)$ is stable, then the system has stable frequencies dynamics.

If we assume that $P_{ol} = 0$, then we can formulate a conservative stability criterion using (9.1).

Corollary 9.3 (Scalable Nyquist Stability Criterion) *Let $\mu_2 = \lambda_2(\mathcal{L}')$ denote the algebraic connectivity of the network $\mathcal{L}'$. Assuming that $\mathcal{G}'(s)$ has no unstable poles, then asymptotic synchronization on the average mode is guaranteed if the field of values*

$$\alpha\,\mathrm{F}\big(\mathcal{G}'(s)\big), \quad \alpha \in [\mu_2, 1] \tag{9.18}$$

does not encircle the point -1 as s goes around the Nyquist $\mathcal{D}$-contour.

Proof sketch: We have that

$$\lambda_i\big(\mathcal{L}'\mathcal{G}'(s)\big) \in \lambda\big(\hat{\mathcal{U}}^T\mathcal{G}'(s)\hat{\mathcal{U}}\hat{X}\big), \quad \forall i \in \{2,\dots,n\},$$

where $\hat{X} = \operatorname{diag}(\mu_2,\dots,\mu_n)$ and $0 < \mu_2 \leq \cdots \leq \mu_n = 1$. Consequently, (9.1) gives

$$\lambda\big(\hat{\mathcal{U}}^T\mathcal{G}'(s)\hat{\mathcal{U}}\hat{X}\big) \subset \alpha\,\mathrm{F}\left(\hat{\mathcal{U}}^T\mathcal{G}'(s)\hat{\mathcal{U}}\right) = \alpha\,\mathrm{F}\left(\mathcal{G}'(s)\right), \quad \alpha \in [\mu_2, 1].$$

Stability of the interarea modes can then be assessed using (9.15) and (9.16), noting that if the field of values does not include or encircle the point -1, then the eigenloci can not encircle -1.

The proposed method is similar to the robust scale-free criterion [155, Theorem 1] briefly summarized below:

Assume that the system (9.3) has been normalized using (9.12) so that $\mathcal{L}' = \hat{\mathcal{U}}\hat{X}\hat{\mathcal{U}}^H$, $\epsilon I \leq \hat{X} \leq I \in \mathbb{C}^{n-1\times n-1}$, $\epsilon > 0$; and that for all $i \in \{1,\dots,n\}$,

(i) $sg_i(s)$ is a stable transfer function;

(ii) $\lim_{s\to 0} sg_i(s) \neq 0$; and

(iii) $h(s)\big(1+\gamma_i g_i(s)\big)$ is extended strictly positive real, where the multiplier function $h(s)$ is a positive real transfer function that is continuous on the extended imaginary axis.

Then (9.3) has stable frequency dynamics.

Since (i) assumes that there are no unstable poles, the robust scale-free criterion can be compared to Corollary 9.3. Condition (ii) implies that actuators $F_i(s)$ in (9.2) are not allowed to have integral action. Graphically, (iii) can be interpreted as the existence of a separating hyperplane between the vertices $\gamma_i g_i(j\omega)$, $\omega > 0$, and the point -1 [155]. If this is the case, then there also is a separating hyperplane between the point -1 and the field of values (9.18). Thus the separating hyperplane method fulfills the asymptotic synchronization criterion in Corollary 9.3. Note that the robust scale-free criterion makes no assumption on the algebraic connectivity of the network μ_2, other than that $\mu_2 > 0$. However, since this cannot be viewed as locally available information, this does not obstruct the ability to assess stability using locally available information.

As argued above, a system that fulfills the separating hyperplane theorem will also fulfill Corollary 9.3. However, the reverse is not true. In the following section we will present a example to further discuss the distinction between the two criteria.

9.5 Power System Application

The scalable Nyquist stability criterion (Corollary 9.3) gives us a graphical interpretation to the stability problem, similar to the separating hyperplane theorem. In this section we will present an example, highlighting the difference between Corollary 9.3 and the separating hyperplane method.

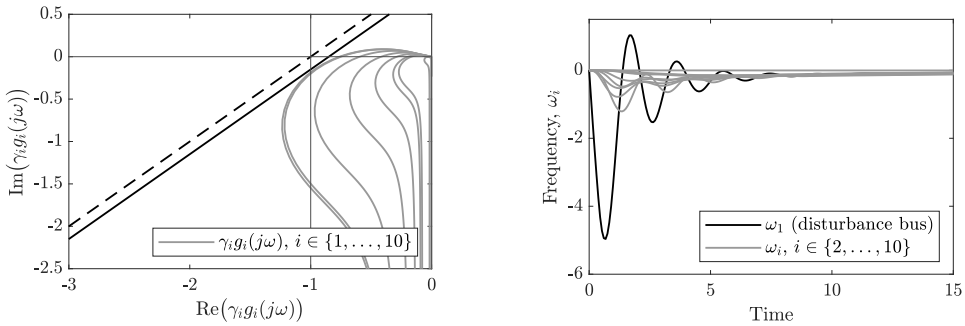

(a) Nyquist diagram of vertices.

(b) Step disturbance, d_1, at bus 1.

Figure 9.4: Agents fulfill (9.19) to (9.21).

9.5.1 Synchronization Criterion Based on a Separating Hyperplane

Consider a power systems with n agents connected over a lossless network. We assume that each agent is participating in the frequency containment reserves (FCR) using a proportional droop, and that this droop is subject to a time delay. In order to get simpler criteria, governor and turbine dynamics are neglected. Let the agents be represented by

$$g_i(s) = \frac{1}{s} \frac{1}{sM_i + D_i + K_i e^{-s\tau_i}}, \tag{9.19}$$

where $M_i \geq 0$ and $D_i \geq 0$. Assume that D_i is unknown and close to zero. Then it can be shown that if

$$\sqrt{\gamma_i M_i / 2} \leq K_i, \tag{9.20}$$

for all i, stability is guaranteed if the delays, τ_i, satisfy

$$0 \leq \tau_i \leq \pi M_i / 4K_i. \tag{9.21}$$

For a system that fulfill (9.19) to (9.21), a separating hyperplane like the one shown in Figure 9.4a, are guaranteed to exist [155]. The system frequency is therefore stable, as shown in Figure 9.4b.

If one of the agents does not participate in FCR, e.g., if $K_2 = 0$, then it is impossible to find a separating hyperplane (Figure 9.5a), even though the system is clearly stable (Figure 9.5b). This is a problem for the separating hyperplane method since many of the devices connected to a power grid only provide steady set-point power, without participating in FCR. It is also a problem if any of the agents are unable to increase their steady-output, i.e., if $F_i(0) = 0$. This rules out agents that cannot increase their output for an unforeseeable time horizon, such as a limited battery storage.

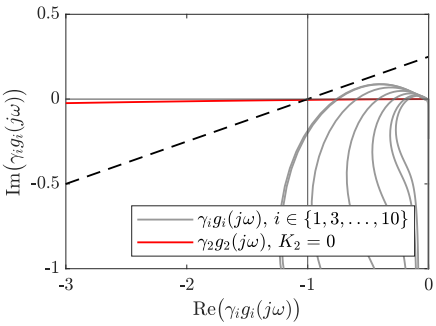

(a) Nyquist diagram of vertices.

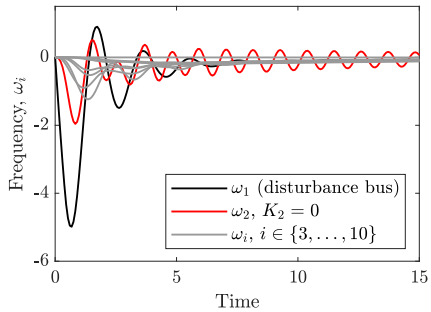

(b) Step disturbance, d_1, at bus 1.

Figure 9.5: The agent shown in blue does not participate in FCR.

9.5.2 Synchronization Criterion Based on the Field of Values

Consider again the example in Section 9.5.1, with agents (9.19) coupled through the output over a lossless network. If we assume worst-case unknown damping constant $D_i = 0$, then $\gamma_i g_i(j\omega)$ crosses over the real axis at $\omega = \pi/2\tau_i$. This means that for $\omega > \pi/2\tau_i$, $\gamma_i g_i(j\omega)$ can attract vertices of the eigenloci up into the top left quadrant, thereby possibly encircling the critical point -1.

A sufficient condition for asymptotic synchronization is that agents (9.19) either fulfill (9.20) and (9.21), or that

$$|\gamma_i g_i(j\omega)| = \left|\gamma_i/\omega^2 M_i\right| \leq 1, \quad \text{for} \quad \omega \geq \pi/2\bar{\tau},$$

where $\bar{\tau} = \max_i \tau_i$, $i \in \{1, \ldots, n\}$. That is, we need that

$$M_i \geq \gamma_i 4\bar{\tau}^2/\pi^2.$$

As an example, consider a two-machine network, with agents

$$g_1(s) = \frac{1}{s}\frac{1}{sM_1 + K_1 e^{-s\bar{\tau}}}, \quad \text{and} \quad g_2(s) = \frac{1}{s}\frac{1}{sM_2}. \tag{9.22}$$

Let $M_1 = 1$, $K_1 = 1/\sqrt{2}$, and $\bar{\tau} = \pi\sqrt{2}/4$; and assume that the network is normalized so that

$$\mathcal{L} = 0.5\begin{bmatrix} 1 & -1 \\ -1 & 1 \end{bmatrix}, \quad \lambda(\mathcal{L}) = \{0, 1\}, \quad \text{and} \quad \gamma_1 = \gamma_2 = 1.$$

As seen in Figure 9.6a, if $M_2 = 1.2\gamma_2 4\bar{\tau}^2/\pi^2$, then the eigenlocus passes to the right of -1. Asymptotic synchronization is therefore achieved. If instead $M_2 = 0.8\gamma_2 4\bar{\tau}^2/\pi^2$, as in Figure 9.6b, then the eigenlocus encircles -1, making the system unstable.

Note that for a two-node network, the eigenlocus of interest is only one single vertex $\lambda_2\big(\mathcal{L}\mathcal{G}(j\omega)\big)$. In Figure 9.6, the field of values wherein $\lambda_2\big(\mathcal{L}\mathcal{G}(j\omega)\big)$ must be

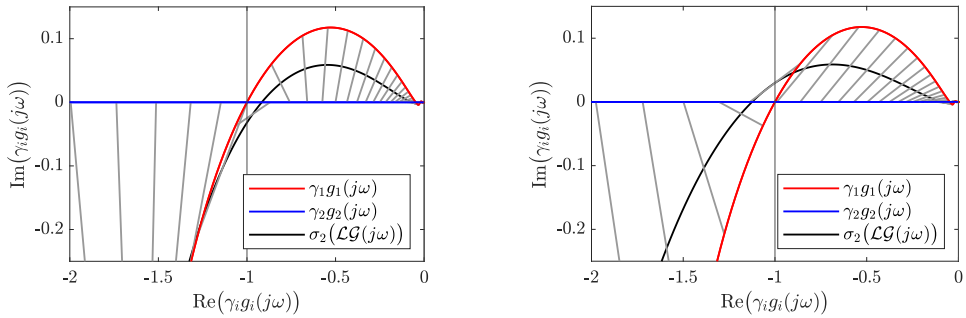

(a) Stable, $M_2 > \gamma_2 4\bar{\tau}^2/\pi^2$. (b) Unstable, $M_2 < \gamma_2 4\bar{\tau}^2/\pi^2$.

Figure 9.6: Nyquist diagram of two-machine system with $K_2 = 0$.

contained, is shown as a gray lined area between $\gamma_1 g_1(j\omega)$ and $\gamma_2 g_2(j\omega)$ for some evenly spaced values of ω. In general, $\lambda_2\big(\mathcal{LG}(j\omega)\big)$, can be anywhere inside the field of values. But for a two-node network, it will be exactly in the center.

9.5.3 Stability of the Average Frequency Mode

The average frequency (9.11) for agents (9.19) is

$$\omega_{\text{avg}} = \frac{1}{sM + D + \sum_{i=1}^{n} K_i e^{-s\tau_i}} \sum_{i=1}^{n} d_i, \tag{9.23}$$

where $M = \sum_{i=1}^{n} M_i$ and $D = \sum_{i=1}^{n} D_i$. Using Lemma 9.1, stability is ensured if the open-loop

$$L(s) = \frac{1}{sM}\left(D + \sum_{i=1}^{n} K_i e^{-s\tau_i}\right) \tag{9.24}$$

does not encircle -1, as s goes around the Nyquist $\mathcal{D}$-contour.

If $\tau_i = 0$, $i \in \{1, \dots, n\}$, then stability is guaranteed if $D + \sum_{i=1}^{n} K_i > 0$. With $\tau_i > 0$, however, there is a possibility for (9.23) to become unstable. Assuming worst-case time delay in all plants, $\tau_i = \bar{\tau}$, and worst-case unknown damping constant $D = 0$, then (9.24) simplifies to

$$L(s) = \frac{1}{sM} K e^{-s\bar{\tau}}, \quad K = \sum_{i=1}^{n} K_i.$$

Instability occur if $|L(j\omega)| \geq 1$ at the point where $\arg\left(e^{-j\omega\bar{\tau}}\right) = -\omega\bar{\tau} = -\pi/2$. A sufficient stability criterion is therefore that $|\frac{2\bar{\tau}}{\pi}\frac{K}{M}| < 1$. Since

$$\arg\left(\frac{1}{j\omega M}\left(D + Ke^{-j\omega\bar{\tau}}\right)\right) \geq \arg\left(\frac{1}{j\omega M} K e^{-j\omega\bar{\tau}}\right),$$

this is a worst case criterion.

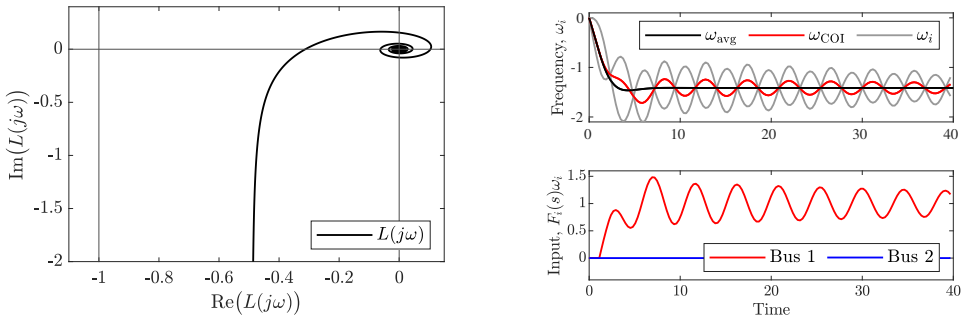

(a) Nyquist diagram of the average frequency mode.

(b) Step disturbance, d_1, at bus 1.

Figure 9.7: Frequency dynamics of the stable system in Figure 9.6a.

Consider again the two-machine network with agents (9.22), where

$$L(s) = \frac{1}{s(M_1 + M_2)} K_1 e^{-s\bar{\tau}}. \tag{9.25}$$

As seen in Figure 9.7a, with the considered parameters, the average frequency mode is clearly stable. If the system also achieves asymptotic synchronization, then the frequency dynamics are stable, as illustrated in Figure 9.7b. Note that ω_{COI} oscillate around ω_{avg}. As noted in Remark 9.1, this is to be expected since the COI contains information about the oscillatory interarea mode.

9.6 Summary

A scalable, decentralized, stability criterion has been derived. By applying the generalized Nyquist criterion on the filed of values spanned by the agents, the method allowed us to analyze the system, without making prior assumption on network losses or agent dynamics. Using the proposed method, a local stability criterion was derived for a network with time delayed droop control, as well as agents with no actuation control.

Part III

Conclusions

Chapter 10

Conclusions and Future Work

In this chapter we conclude the thesis. In Section 10.1 we summarize and discuss the presented results, and in Section 10.2 outline some possible extensions and future work.

10.1 Conclusions

In this thesis, we have considered fundamental control performance limitations for improving the damping of interarea modes and frequency stability. Broadly, these have been partitioned into limitations associated with the dynamics of the controlled power source, and limitations associated with the measurements.

10.1.1 Interarea Oscillation Damping

Zero Dynamics Coupled to High-Speed Excitation Control

In Chapter 3, we studied the connection between high-speed excitation control from automatic voltage regulators (AVRs) and the presence of non-minimum phase (NMP) zeros in transfer functions with frequency (or phase angle) measurements as the output. NMP, or open right half-plane (ORHP), zeros are of particular interest since they impose interpolation constraints on the sensitivity function and therefore limit the achievable closed-loop performance.

It is well known that zeros cannot be moved by feedback. However, AVR uses feedback from voltage measurements. With respect to frequency measurements, this can be viewed as parallel compensation. Therefore, the AVR does have some effect on the zeros associated with frequency measurements. In Chapter 3, we showed that the destabilizing effect of AVR on the electromechanical mode also meant that zero pairs, observed in the frequency measurement, moved into the ORHP. Even though these control loops show NMP zeros, frequency measurement is still suitable for power oscillation damping (POD). Since feedback does not move the locations of zeros, this means that NMP zeros will remain in the ORHP, even though their

corresponding electromechanical poles have been stabilized and moved into the left half-plane (LHP).

Interactions Between HVDC Interconnected Power Systems

Active power modulation of high-voltage direct current (HVDC) transmission is useful for improving the POD of interarea modes. In Chapters 4 and 5, we have studied the control of point-to-point HVDC lines that interconnect asynchronous power grids. When controlling the active power between asynchronous grids, the interarea modes are affected in both grids. This system interaction limits the achievable POD improvement.

In Chapter 4, we studied the case where two asynchronous power systems were interconnected with a single HVDC line. For the analysis, the troublesome interarea mode was represented abstractly as a two-machine network. It was shown that active power modulation is suitable for improving POD. If the dynamics of the power source can be neglected, then performance is essentially only limited by the available power. However, since active power (unlike reactive power if voltage source converters are used) cannot be controlled independently at the two dc terminals, interactions between the two systems are unavoidable.

By studying the controllability Gramian, a fundamental measure, independent of the control structure, was obtained for how hard it is to control the interarea oscillations. When considering damping improvement of both networks simultaneously, the ratio between modal frequencies was shown to set a fundamental limitation to achievable performance. With moderate feedback gains, differences in open-loop modal frequencies between the interconnected systems could be used to increase system performance in terms of POD. With a too aggressive control, the interarea oscillations of the two systems will essentially be synchronized. High feedback would allow the networks to share inertial response following disturbances. However, if POD is desired, then feedback gains are limited by the modal interaction. This is because the disturbance propagates and excites the interarea mode in the neighboring system. The findings were validated on a detailed power system of two HVDC-interconnected 32-bus networks.

In Chapter 5, we considered the case with additional HVDC links. It is well known that for a system to be functionally controllable it is required that there are at least as many inputs as outputs. In other words, if we want to freely control the two outputs (i.e. the interarea mode in each network) then we need an additional controllable input. Adding control to an additional HVDC link could solve this problem. Assuming that the condition number of the resulting multiple-input multiple-output (MIMO) system is sufficiently small, individual control of the two interarea modes is achievable. It was shown that if we want to improve damping of the dominant interarea mode in each of the HVDC-interconnected networks, using two HVDC links and linear control, there are three main control structures: single-line, decentralized, and decoupled. The latter of these avoid interaction between the

two modes altogether. This could be desirable if system operators in the different networks are concerned by the excitation of poorly damped modes.

Centralized optimal control was also investigated. By targeting input usage and the desired modes (given by corresponding left eigenvectors), an $\mathcal{H}_2$ optimal design proved convenient for obtaining the most suitable trade-off between the three, previously mentioned, control methods. For certain configurations of the HVDC links, decoupling control risks destabilizing the system in the event of communication or actuator failure. However, decoupling control would here require excessive input usage and is thus not $\mathcal{H}_2$ optimal. If the condition number is sufficiently small, the $\mathcal{H}_2$ design would instead opt for a controller resembling the decentralized controller.

In the study, we have considered that external measurements are available from the machines involved in the interarea oscillations, giving us a nearly perfect estimation of the interarea mode to be used as a feedback signal. However, the results also extend to local measurements since an observer can be used to estimate the mode. Using the proposed $\mathcal{H}_2$ method, this is achieved without much adjustments since the designer only has to specify the available measurements in the tuning process. Additional control criteria, such as damping of additional modes can also easily be included by adding these to the performance criteria, as was done in Section 5.4.3. However, with only local measurements, the information available for the controller is limited. This may impose additional control limitations.

Limitations Using Local Measurements

Local frequency feedback is a popular design choice for modulating active power injections since it yields a damping controller with good linear robustness properties while avoiding the need for external communication systems. As studied in Chapter 3, the usefulness of frequency measurements may be limited by the presence of NMP zeros. But these limitations may be mitigated by choosing to implement the control at a suitable network bus with good controllability and observability of the considered interarea mode. It has been observed however, that proportional control implemented using local frequency measurement may have a negative effect on transient (first swing) stability following contingencies involving a generator or load trip. In Chapter 6, we addressed this problem by studying the Bode integral constraints of the filtering sensitivity. We showed that improved POD must come at the cost of reduced transient stability margins, regardless of the control design method. It was found that the issue can be characterized by the zero dynamics of the general control configuration. The control limitations stem from that the excitation of an interarea mode by external disturbances cannot be estimated with certainty using local frequency information. The studied sensor feedback limitations are relevant in the bandwidth window between interarea oscillation damping and fast acting primary reserves, or fast frequency reserves (FFR). They are therefore important to account for when designing FFR control schemes in low-inertia power systems.

10.1.2 Frequency Stability

Coordinated Dynamic Frequency Reserves from Hydro and Wind

In Chapter 7, we considered coordination of frequency containment reserves (FCR). Of particular interest was to develop a method that takes into account the fast dynamic constraints of the participating devices. Because of this, the focus was on the fast spectra of FCR, i.e., the coordination of FCR and FFR. The control problem was treated as a decentralized model matching problem. The controllers of each device were designed so that their combined control effort matched the Bode diagram of a design target, specified by the system operator requirements. Even if power capacity is available, there are still dynamic constraints that may limit the bandwidth of participating devices. These include ramp rate limits and dynamic stability limits. In Chapter 7, we payed extra attention to the dynamic stability limitations imposed by NMP zeros.

A case study was performed on a 5-machine test system, representing the Nordic synchronous grid. The Nordic power system is a relatively small grid with FCR almost exclusively provided by hydropower. Under low-inertia conditions, hydropower may not be able to act fast enough to fulfill the FCR requirements, in part due to the NMP zeros of the waterways. With the proposed method we were able to identify an upper limit on the open-loop cross-over frequency, imposed by the NMP zeros of all participating hydro units. If all units that supply FCR are NMP, then the aggregated response will also be NMP. The NMP zero of the aggregated response will be located in a bandwidth window spanned by the NMP zeros of all participating devices. It was shown that this issue could be solved by complementing the hydro-FCR with FFR from minimum phase (MP) power sources such as fast acting thermal units or battery storage. This however, may be an unnecessarily costly solution. We therefore investigated how to achieve the FCR requirements by supplementing hydro-FCR with FFR from wind.

With respect to FCR, wind power has the opposite problem compared to hydro. If operated below rated power, then the wind turbine (WT) can almost immediately increase its electric power output. However, if the turbine is operating at the maximum power point (MPP) the output will eventually fall below the initial steady-output. In Chapter 8, we showed that this behavior manifests in a NMP behavior. WTs operating at the MPP have a slow NMP zero (around 0.05 rad/s) that imposes a lower bandwidth limit on the FFR response. That is, the WT can only sustain an increased electric power output for a limited time. This makes it ideal to combine with hydropower, whose response has an upper bandwidth limit due to the comparatively faster NMP zeros (around 1–2 rad/s) of the waterways. To achieve this, we designed a new variable-speed WT controller, enabling the WT to participate in FFR without the need for curtailment. What sets the design apart from existing methods [73] is that the controller is designed with the end goal of facilitating a useful linearization for coordinating wind-FFR with hydro-FCR, using the method developed in Chapter 7.

Stability in Large Heterogeneous Networks

In Part I, we studied rotor angle stability of interarea oscillations, ignoring the center of inertia (COI) frequency; whereas in Chapters 7 and 8 we studied the COI frequency stability problem, ignoring the dynamics of interarea modes. This is a fairly common approach in power system analysis. However, with an increasing penetration of renewable energy and power electronic devices, the grid inertia is decreasing. This increases the need for FFR. Because of this, the separation between frequency stability and rotor angle stability is becoming harder to motivate.

In Chapter 9, we developed a theoretical framework to bridge the gap between small-signal rotor angle stability and frequency stability. Combining tools from linear algebra, graph theory, and complex analysis we formulated a scalable Nyquist stability criterion. The power system is expressed as a set of agents, coupled through the output over a network. The method allowed us to study the effect of different machines and actuators on the stability of network modes (average/COI frequency mode and oscillatory interarea modes) in closed form, albeit with some conservative assumptions. The method tells us if any of the agents may have a destabilizing effect on the network modes. If we assume that all agents have stable dynamics, we can also use the method to formulate a decentralized stability criterion.

A scalable Nyquist stability criterion was derived, providing a priori stability guarantees for connecting new devices to the network, using only locally available information. The developed method was shown to be a practically useful improvement over other similar methods by allowing for a more general set of agents. Unfortunately, since the method requires all agents to be stable, this rules out FFR from wind. Agents that model uncurtailed wind turbines are unstable since their corresponding transfer functions will have the NMP actuator dynamics in the denominator. In Chapter 7, we showed how this issue can be circumvented by controlling the WTs in a subsystem with other power sources, forming a dynamic virtual power plant (DVPP) whose combined output can be shaped to fulfill the scalable Nyquist stability criterion.

10.2 Future Work

We conclude this thesis by providing some interesting future research directions.

10.2.1 Fundamental Control Limitations in Multi-Machine Networks

In Part I, we considered fundamental control limitations for improving POD. An interesting extension would be to extend the results by including more complex models directly in the analysis. A way to obtain insightful results also for higher-order systems is to opt for a conservative approach using the methodology developed in Chapter 9. Possible extension could involve heterogeneous multi-machine networks with more detailed governor dynamics as well as second-order network modeling to include voltage dynamics and reactive power.

10.2.2 Economical Allocation of Control Reserves

In Chapter 7, we considered the allocation of FCR and FFR over different frequency ranges to match the Bode diagram of a design target. We classified reserves into two groups: slow and fast. An extension to this is to generalize the allocation process by developing optimization methods to dispatch reserves over continuous or discrete frequency ranges. The method can be designed, not only to fulfill the system operator requirements, but also to optimize some frequency dependent economic cost function. Another interesting issue would be to develop economic methods to deal with NMP plants. The challenge is that these act as producers in some frequency ranges, but as consumers in other ranges.

10.2.3 Practical Implementation of Coordinated Frequency Reserves

In Chapter 7, we studied the coordination of devices participating in FCR by forming a DVPP. In particular, we were concerned with coordinating FCR from hydro with FFR from wind using the WT model developed in Chapter 8. It would be interesting to test the proposed control method in a real-world experiment by controlling a subsystem, for instance consisting of hydro units and WTs, as a DVPP. It would be interesting to test the proposed WT control for different turbine models, and to see how the hydro-FCR controller could be retrofitted into an existing hydro governor control system. In addition, it would be interesting to see how the hydro-FCR control, proposed in Chapter 7, could address concerns with the slow 60 s period oscillations experienced in the Nordic system [153].

10.2.4 Experimental Study of HVDC POD Control

In Chapters 4 and 5, we considered POD control limitations when controlling HVDC links between asynchronous power systems. It would be interesting to test the obtained results in practice. One challenge for such a study is that asynchronous grids often have different transmission system operators. Proposing experiments that may introduce disturbances from another system may therefore be met with skepticism. For this, the coordinated control methods proposed in Chapter 5 could be easier to justify since they can reduce the interactions between the systems. It would also be interesting to see how relevant the considered control limitations are when connecting grids of vastly different sizes, such as the Nordic grid to the Continental European grid.

Bibliography

[1] H. Ritchie and M. Roser, "Renewable energy," *Our World in Data*, 2020, Accessed on: Apr. 16, 2021. [Online]. Available: https://ourworldindata.org/renewable-energy/

[2] BP, "Statistical review of world energy," 2020, Accessed on: Apr. 16, 2021. [Online]. Available: https://www.bp.com/en/global/corporate/energy-economics/statistical-review-of-world-energy.html

[3] Ember, "EU ETS data," 2021, Accessed on: Apr. 16, 2021. [Online]. Available: https://ember-climate.org/data/

[4] M. Ilić, F. Galiana, and L. Fink, *Power Systems Restructuring: Engineering and Economics*. New York: Springer Science+Business Media, 1998.

[5] M. Ilić, "From hierarchical to open access electric power systems," *Proceedings of the IEEE*, vol. 95, no. 5, pp. 1060–1084, May 2007.

[6] A. Nyman, K. Jaaskelainen, M. Vaitomaa, B. Jansson, and K. G. Danielsson, "The Fenno-Skan HVDC link commissioning," *IEEE Transactions on Power Delivery*, vol. 9, no. 1, pp. 1–9, Jan. 1994.

[7] K. Uhlen, L. Vanfretti, M. M. de Oliveira, A. B. Leirbukt, V. H. Aarstrand, and J. O. Gjerde, "Wide-area power oscillation damper implementation and testing in the Norwegian transmission network," in *2012 IEEE Power and Energy Society General Meeting*, San Diego, CA, Jul. 2012.

[8] P. Kundur, J. Paserba, V. Ajjarapu, G. Andersson, A. Bose, C. Canizares, N. Hatziargyriou, D. Hill, A. Stankovic, C. Taylor, T. Van Cutsem, and V. Vittal, "Definition and classification of power system stability IEEE/CIGRE joint task force on stability terms and definitions," *IEEE Transactions on Power Systems*, vol. 19, no. 3, pp. 1387–1401, May 2004.

[9] M. A. Elizondo, R. Fan, H. Kirkham, M. Ghosal, F. Wilches-Bernal, D. A. Schoenwald, and J. Lian, "Interarea oscillation damping control using high voltage dc transmission: A survey," *IEEE Transactions on Power Systems*, vol. 33, no. 6, pp. 6915–6923, Nov. 2018.

[10] A. Mešanović, U. Münz, and C. Heyde, "Comparison of H∞, H2, and pole optimization for power system oscillation damping with remote renewable generation," *IFAC-PapersOnLine*, vol. 49, no. 27, pp. 103–108, Oct. 2016.

[11] Y. Pipelzadeh, B. Chaudhuri, and T. C. Green, "Control coordination within a VSC HVDC link for power oscillation damping: A robust decentralized approach using homotopy," *IEEE Transactions on Control Systems Technology*, vol. 21, no. 4, pp. 1270–1279, Jul. 2013.

[12] R. Preece, J. V. Milanović, A. M. Almutairi, and O. Marjanovic, "Damping of inter-area oscillations in mixed AC/DC networks using WAMS based supplementary controller," *IEEE Transactions on Power Systems*, vol. 28, no. 2, pp. 1160–1169, May 2013.

[13] F. Dörfler, M. R. Jovanović, M. Chertkov, and F. Bullo, "Sparsity-promoting optimal wide-area control of power networks," *IEEE Transactions on Power Systems*, vol. 29, no. 5, pp. 2281–2291, Sep. 2014.

[14] S. P. Azad, J. A. Taylor, and R. Iravani, "Decentralized supplementary control of multiple LCC-HVDC links," *IEEE Transactions on Power Systems*, vol. 31, no. 1, pp. 572–580, Jan. 2016.

[15] R. L. Cresap and W. A. Mittelstadt, "Small-signal modulation of the Pacific HVDC intertie," *IEEE Transactions on Power Apparatus and Systems*, vol. 95, no. 2, pp. 536–541, Mar. 1976.

[16] R. L. Cresap, W. A. Mittelstadt, D. N. Scott, and C. W. Taylor, "Operating experience with modulation of the Pacific HVDC Intertie," *IEEE Transactions on Power Apparatus and Systems*, vol. PAS-97, no. 4, pp. 1053–1059, Jul. 1978.

[17] D. Trudnowski, D. Kosterev, and J. Undrill, "PDCI damping control analysis for the western North American power system," in *Proc. IEEE/PES General Meeting*, Vancouver, Canada, Jul. 2013.

[18] P. Pourbeik, P. S. Kundur, and C. W. Taylor, "The anatomy of a power grid blackout - Root causes and dynamics of recent major blackouts," *IEEE Power and Energy Magazine*, vol. 4, no. 5, pp. 22–29, Sep. 2006.

[19] D. N. Kosterev, C. W. Taylor, and W. A. Mittelstadt, "Model validation for the August 10, 1996 WSCC system outage," *IEEE Transactions on Power Systems*, vol. 14, no. 3, pp. 967–979, Aug. 1999.

[20] J. L. Domínguez-García, F. D. Bianchi, and O. Gomis-Bellmunt, "Control signal selection for damping oscillations with wind power plants based on fundamental limitations," *IEEE Transactions on Power Systems*, vol. 28, no. 4, pp. 4274–4281, Nov. 2013.

[21] L. Harnefors, N. Johansson, L. Zhang, and B. Berggren, "Interarea oscillation damping using active-power modulation of multiterminal HVDC transmissions," *IEEE Transactions on Power Systems*, vol. 29, no. 5, pp. 2529–2538, Sep. 2014.

[22] M. Ndreko, A. van der Meer, M. Gibescu, B. G. Rawn, and M. A. M. M. van der Meijden, "Damping power system oscillations by VSC-based HVDC networks: A North Sea grid case study," in *12th Wind Integration Workshop*, London, UK, 2013.

[23] E. Tegling, "Fundamental limitations of distributed feedback control in large-scale networks," Ph.D. dissertation, KTH Royal Institute of Technology, Stockholm, Sweden, 2018.

[24] B. J. Pierre, F. Wilches-Bernal, D. A. Schoenwald, R. T. Elliott, D. J. Trudnowski, R. H. Byrne, and J. C. Neely, "Design of the Pacific DC Intertie wide area damping controller," *IEEE Transactions on Power Systems*, vol. 34, no. 5, pp. 3594–3604, Sep. 2019.

[25] P. Kundur, *Power System Stability and Control*. New York: McGraw-Hill, 1994.

[26] I. Kamwa, "Performance of three PSS for interarea oscillations," *Mathworks*, Accessed on: Sep. 24, 2019. [Online]. Available: https://mathworks.com/help/physmod/sps/ug/performance-of-three-pss-for-interarea-oscillations.html

[27] CIGRÉ Working Group B4-57, "Guide for the development of models for HVDC converters in a HVDC grid," CIGRÉ, Tech. Rep., Dec. 2014.

[28] R. Preece, "A probabilistic approach to improving the stability of meshed power networks with embedded HVDC lines," Ph.D. dissertation, University of Manchester, Manchester, UK, 2013.

[29] E. Björk, "Load characteristic influence on power oscillation damping: Case study on HVDC-interconnected AC-grids," Master Thesis, KTH Royal Institute of Technology, Stockholm, Sweden, 2018.

[30] L. Harnefors, N. Johansson, and L. Zhang, "Impact on interarea modes of fast HVDC primary frequency control," *IEEE Transactions on Power Systems*, vol. 32, no. 2, pp. 1350–1358, Mar. 2017.

[31] B. J. Kirby, "Frequency regulation basics and trends," Oak Ridge National Lab., Oak Ridge, TN, Tech. Rep., 2005.

[32] F. Milano, F. Dörfler, G. Hug, D. J. Hill, and G. Verbič, "Foundations and Challenges of Low-Inertia Systems (Invited Paper)," in *Power Systems Computation Conference*, Dublin, Ireland, Jun. 2018.

[33] W. Winter, K. Elkington, G. Bareux, and J. Kostevc, "Pushing the limits: Europe's new grid: Innovative tools to combat transmission bottlenecks and reduced inertia," *IEEE Power and Energy Magazine*, vol. 13, no. 1, pp. 60–74, Jan. 2015.

[34] K. M. J. Rahman, M. M. Munnee, and S. Khan, "Largest blackouts around the world: Trends and data analyses," in *IEEE International WIE Conference on Electrical and Computer Engineering*, Pune, India, Dec. 2016, pp. 155–159.

[35] UCTE Investigation Committee, "Final report of the investigation committee on the 28 September 2003 blackout in Italy," UCTE, Tech. Rep., 2004.

[36] AEMO, "Black system S-Australia 28 September 2016," Tech. Rep., 2017.

[37] G. Beck, D. Povh, D. Retzmann, and E. Teltsch, "Global blackouts - lessons learned," in *POWER-GEN Europe*, Milan, Italy, Jun. 2005.

[38] R. Bründlinger, "Review and assessment of latest grid code developments in Europe and selected international markets with respect to high penetration PV," in *6th Solar Integration Workshop*, Vienna, Austria, Nov. 2016.

[39] ENTSO-E, "Nordic synchronous area proposal for the frequency quality defining parameters and the frequency quality target parameter in accordance with Article 127 of the Commission Regulation (EU) 2017/1485 of 2 August 2017 establishing a guideline on electricity transmission system operation," 2017.

[40] E. Agneholm, S. A. Meybodi, M. Kuivaniemi, P. Ruokolainen, J. N. Ødegård, N. Modig, and R. Eriksson, "FCR-D design of requirements – phase 2," ENTSOE-E, Tech. Rep., 2019.

[41] ENTSO-E, "Fast frequency reserve – solution to the Nordic inertia challenge," Tech. Rep., 2019.

[42] Statnett, "NordLink," Accessed on: Feb. 13, 2021. [Online]. Available: https://www.statnett.no/en/our-projects/interconnectors/nordlink/

[43] CIGRÉ Task Force 38-08-08, "Long term dynamics phase II final report," CIGRÉ, Tech. Rep., Mar. 1995.

[44] J. R. Winkelman, J. H. Chow, B. C. Bowler, B. Avramovic, and P. V. Kokotovic, "An analysis of interarea dynamics of multi-machine systems," *IEEE Transactions on Power Apparatus and Systems*, vol. PAS-100, no. 2, pp. 754–763, Feb. 1981.

[45] F. L. Pagola, I. J. Perez-Arriaga, and G. C. Verghese, "On sensitivities, residues and participations: Applications to oscillatory stability analysis and control," *IEEE Transactions on Power Systems*, vol. 4, no. 1, pp. 278–285, Feb. 1989.

[46] J. L. Domínguez-García, C. E. Ugalde-Loo, F. Bianchi, and O. Gomis-Bellmunt, "Input–output signal selection for damping of power system oscillations using wind power plants," *International Journal of Electrical Power & Energy Systems*, vol. 58, pp. 75–84, Jun. 2014.

[47] J. Björk and K. H. Johansson, "Control limitations due to zero dynamics in a single-machine infinite bus network," in *IFAC World Congress*, Berlin, Germany, Jul. 2020.

[48] J. Björk, K. H. Johansson, and L. Harnefors, "Fundamental performance limitations in utilizing HVDC to damp interarea modes," *IEEE Transactions on Power Systems*, vol. 34, no. 2, pp. 1095–1104, Mar. 2019.

[49] J. Björk, K. H. Johansson, L. Harnefors, and R. Eriksson, "Analysis of coordinated HVDC control for power oscillation damping," in *IEEE eGrid*, Charleston, SC, Nov. 2018.

[50] J. Björk, "Performance quantification of interarea oscillation damping using HVDC," Licentiate Thesis, KTH Royal Institute of Technology, Stockholm, Sweden, 2019.

[51] Hydro-Québec and The MathWorks, "Simscape Electrical Reference (Specialized Power Systems)," Natick, MA, Tech. Rep., 2020.

[52] P. W. Sauer and M. A. Pai, *Power System Dynamics and Stability*. Upper Saddle River, NJ: Prentice hall, 1998.

[53] K. Morison, L. Wang, and P. Kundur, "Power system security assessment," *IEEE Power and Energy Magazine*, vol. 2, no. 5, pp. 30–39, Sep. 2004.

[54] T. Van Cutsem and C. Vournas, *Voltage Stability of Electric Power System*. Boston, MA: Springer US, 1998.

[55] ENTSO-E, "Supporting document for the network code on electricity balancing," Tech. Rep., 2014.

[56] ——, "Frequency stability evaluation criteria for the synchronous zone of continental europe," Tech. Rep., 2016.

[57] M. Pavella, D. Ernst, and D. Ruiz-Vega, *Transient Stability of Power Systems: A Unified Approach to Assessment and Control*. New York: Kluwer Academic Publishers, 2000.

[58] D. Mondal, A. Chakrabarti, and A. Sengupta, *Power System Small Signal Stability Analysis and Control*. Boston, MA: Academic Press, 2014.

[59] K. Uhlen, L. Warland, J. O. Gjerde, O. Breidablik, M. Uusitalo, A. B. Leirbukt, and P. Korba, "Monitoring amplitude, frequency and damping of power system oscillations with PMU measurements," in *IEEE Power and Energy Society General Meeting - Conversion and Delivery of Electrical Energy in the 21st Century*, Pittsburgh, PA, Jul. 2008.

[60] A. T. Gullberg, D. Ohlhorst, and M. Schreurs, "Towards a low carbon energy future – Renewable energy cooperation between Germany and Norway," *Renewable Energy*, vol. 68, pp. 216–222, Aug. 2014.

[61] ENTSO-E, "Analysis of CE inter-area oscillations of 1st December 2016," SG SPD Report, Jul. 2017.

[62] ——, "Oscillation event 03.12.2017: System protection and dynamics WG," Tech. Rep., Mar. 2018.

[63] A. B. Attya, J. L. Domínguez-García, and O. Anaya-Lara, "A review on frequency support provision by wind power plants: Current and future challenges," *Renewable and Sustainable Energy Reviews*, vol. 81, pp. 2071–2087, Jan. 2018.

[64] D. Obradović, "Coordinated frequency control between interconnected ac/dc systems," Licentiate Thesis, KTH Royal Institute of Technology, Stockholm, Sweden, 2020.

[65] M. Andreasson, R. Wiget, D. V. Dimarogonas, K. H. Johansson, and G. Andersson, "Distributed frequency control through MTDC transmission systems," *IEEE Transactions on Power Systems*, vol. 32, no. 1, pp. 250–260, Jan. 2017.

[66] S. P. Teeuwsen, G. Love, and R. Sherry, "1400 MW New Zealand HVDC upgrade: Introducing power modulation controls and round power mode," in *IEEE Power Energy Society General Meeting*, Vancouver, Canada, Jul. 2013.

[67] C. W. Taylor and S. Lefebvre, "HVDC controls for system dynamic performance," *IEEE Transactions on Power Systems*, vol. 6, no. 2, pp. 743–752, May 1991.

[68] M. Guan, J. Cheng, C. Wang, Q. Hao, W. Pan, J. Zhang, and X. Zheng, "The frequency regulation scheme of interconnected grids with VSC-HVDC links," *IEEE Transactions on Power Systems*, vol. 32, no. 2, pp. 864–872, Mar. 2017.

[69] M. A. Elizondo, N. Mohan, J. O'Brien, Q. Huang, D. Orser, W. Hess, H. Brown, W. Zhu, D. Chandrashekhara, Y. V. Makarov, D. Osborn, J. Feltes, H. Kirkham, D. Duebner, and Z. Huang, "HVDC macrogrid modeling for power-flow and transient stability studies in north american continental-level interconnections," *CSEE Journal of Power and Energy Systems*, vol. 3, no. 4, pp. 390–398, Dec. 2017.

[70] ENTSO-E, "Transmission system map," Accessed on: Apr. 16, 2021. [Online]. Available: https://www.entsoe.eu/data/map/

[71] Statnett, Fingrid, Energinet.dk, and S. Kraftnät, "Challenges and opportunities for the Nordic power system," Tech. Rep., 2016.

[72] I. Graabak, S. Jaehnert, M. Korpås, and B. Mo, "Norway as a battery for the future european power system—Impacts on the hydropower system," *Energies*, vol. 10, no. 12: 2054, Dec. 2017.

[73] J. Morren, S. W. H. de Haan, W. L. Kling, and J. A. Ferreira, "Wind turbines emulating inertia and supporting primary frequency control," *IEEE Transactions on Power Systems*, vol. 21, no. 1, pp. 433–434, Feb. 2006.

[74] N. R. Ullah, T. Thiringer, and D. Karlsson, "Temporary primary frequency control support by variable speed wind turbines—potential and applications," *IEEE Transactions on Power Systems*, vol. 23, no. 2, pp. 601–612, May 2008.

[75] J. Lee, E. Muljadi, P. Srensen, and Y. C. Kang, "Releasable kinetic energy-based inertial control of a DFIG wind power plant," *IEEE Transactions on Sustainable Energy*, vol. 7, no. 1, pp. 279–288, Jan. 2016.

[76] Y. Li, Z. Xu, J. Østergaard, and D. J. Hill, "Coordinated control strategies for offshore wind farm integration via VSC-HVDC for system frequency support," *IEEE Transactions on Energy Conversion*, vol. 32, no. 3, pp. 843–856, Sep. 2017.

[77] D. Ochoa and S. Martinez, "Fast-frequency response provided by DFIG-wind turbines and its impact on the grid," *IEEE Transactions on Power Systems*, vol. 32, no. 5, pp. 4002–4011, Sep. 2017.

[78] X. Zhao, Y. Xue, and X.-P. Zhang, "Fast frequency support from wind turbine systems by arresting frequency nadir close to settling frequency," *IEEE Open Access Journal of Power and Energy*, vol. 7, pp. 191–202, 2020.

[79] J. Arrillaga, *High Voltage Direct Current Transmission*, 2nd ed. London, UK: The Institution of Engineering and Technology, 2008.

[80] Å. Ekström, *High Power Eelectronic HVDC and SVC*. Stockholm, Sweden: KTH Royal Institute of Technology, Jun. 1990.

[81] L. Zhang, L. Harnefors, and H. P. Nee, "Interconnection of two very weak ac systems by VSC-HVDC links using power-synchronization control," *IEEE Transactions on Power Systems*, vol. 26, no. 1, pp. 344–355, Feb. 2011.

[82] K. Sharifabadi, L. Harnefors, H.-P. Nee, S. Norrga, and R. Teodorescu, *Design, Control and Application of Modular Multilevel Converters for HVDC Transmission Systems*. Chichester, UK: John Wiley & Sons, Ltd, Oct. 2016.

[83] R. Eriksson, "A new control structure for multiterminal dc grids to damp interarea oscillations," *IEEE Transactions on Power Delivery*, vol. 31, no. 3, pp. 990–998, Jun. 2016.

[84] W. Du, Q. Fu, and H. Wang, "Strong dynamic interactions between multi-terminal dc network and ac power systems caused by open-loop modal coupling," *IET Generation, Transmission & Distribution*, vol. 11, no. 9, pp. 2362–2374, Jun. 2017.

[85] R. Shah, R. Preece, and M. Barnes, "Impact of MTDC grid reconfiguration and control on the dynamics of the GB system," in *15th IET International Conference on AC and DC Power Transmission*. Coventry, UK: IET Digital Library, Jan. 2019.

[86] J. A. Ansari, C. Liu, and S. A. Khan, "MMC based MTDC grids: A detailed review on issues and challenges for operation, control and protection schemes," *IEEE Access*, vol. 8, pp. 168 154–168 165, 2020.

[87] G. Buigues, V. Valverde, A. Etxegarai, P. Eguía, and E. Torres, "Present and future multiterminal HVDC systems: Current status and forthcoming," *Renewable Energy and Power Quality Journal*, vol. 1, pp. 83–88, Apr. 2017.

[88] H. Rao, "Architecture of Nan'ao multi-terminal VSC-HVDC system and its multi-functional control," *CSEE Journal of Power and Energy Systems*, vol. 1, no. 1, pp. 9–18, Mar. 2015.

[89] G. Tang, Z. He, H. Pang, X. Huang, and X. p Zhang, "Basic topology and key devices of the five-terminal dc grid," *CSEE Journal of Power and Energy Systems*, vol. 1, no. 2, pp. 22–35, Jun. 2015.

[90] M. Callavik, M. Larsson, and S. Stoeter, "Powering the world," *ABB review special report: 60 years of HVDC*, pp. 6–11, Aug. 2014.

[91] M. Barnes, D. Van Hertem, S. P. Teeuwsen, and M. Callavik, "HVDC systems in smart grids," *Proceedings of the IEEE*, vol. 105, no. 11, pp. 2082–2098, Nov. 2017.

[92] "IEEE guide for control architecture for high power electronics (1 MW and greater) used in electric power transmission and distribution systems," *IEEE Std 1676-2010*, pp. 1–47, Feb. 2011.

[93] T. Smed and G. Andersson, "Utilizing HVDC to damp power oscillations," *IEEE Transactions on Power Delivery*, vol. 8, no. 2, pp. 620–627, Apr. 1993.

[94] Y. Cao, W. Wang, Y. Li, Y. Tan, C. Chen, L. He, U. Häger, and C. Rehtanz, "A virtual synchronous generator control strategy for VSC-MTDC system," *IEEE Transactions on Energy Conversion*, vol. 33, no. 2, pp. 750–761, 2017.

[95] C. E. Grund, R. V. Pohl, and J. Reeve, "Control design of an active and reactive power HVDC modulation system with Kalman filtering," *IEEE Power Engineering Review*, vol. PER-2, no. 10, pp. 61–61, Oct. 1982.

[96] S. G. Johansson, G. Asplund, E. Jansson, and R. Rudervall, "Power system stability benefits with VSC dc transmission systems," in *CIGRE Session*, Paris, France, Aug. 2004.

[97] W. Li, "PMU-based state estimation for hybrid ac and dc grids," Ph.D. dissertation, KTH Royal Institute of Technology, Stockholm, Sweden, 2018.

[98] I. Kamwa, J. Beland, G. Trudel, R. Grondin, C. Lafond, and D. McNabb, "Wide-area monitoring and control at Hydro-Québec: Past, present and future," in *Proc. IEEE/PES General Meeting*, Montréal, Canada, Jun. 2006.

[99] A. Almutairi, "Enhancement of power system stability using wide area measurement system based damping controller," Ph.D. dissertation, University of Manchester, Manchester, UK, 2010.

[100] M. Hadjikypris, O. Marjanovic, and V. Terzija, "Damping of inter-area power oscillations in hybrid AC-DC power systems based on supervisory control scheme utilizing FACTS and HVDC," in *Power Systems Computation Conference*. Genoa, Italy: IEEE, Jun. 2016.

[101] W. Juanjuan, F. Chuang, and Z. Yao, "Design of WAMS-based multiple HVDC damping control system," *IEEE Transactions on Smart Grid*, vol. 2, no. 2, pp. 363–374, Jun. 2011.

[102] X. Wu and M. R. Jovanović, "Sparsity-promoting optimal control of consensus and synchronization networks," in *IEEE American Control Conference*, Portland, OR, Jun. 2014, pp. 2936–2941.

[103] S. Zhang and V. Vittal, "Design of wide-area power system damping controllers resilient to communication failures," *IEEE Transactions on Power Systems*, vol. 28, no. 4, pp. 4292–4300, Nov. 2013.

[104] A. Teixeira, "Toward cyber-secure and resilient networked control systems," Ph.D. dissertation, KTH Royal Institute of Technology, Stockholm, Sweden, 2014.

[105] W. Wang and Z. Lu, "Cyber security in the Smart Grid: Survey and challenges," *Computer Networks*, vol. 57, no. 5, pp. 1344–1371, Apr. 2013.

[106] U. Adhikari, T. Morris, and S. Pan, "WAMS cyber-physical test bed for power system, cybersecurity study, and data mining," *IEEE Transactions on Smart Grid*, vol. 8, no. 6, pp. 2744–2753, Nov. 2017.

[107] A. Jevtić and M. Ilić, "A dynamic strategy for cyber-attack detection in large-scale power systems via output clustering," in *2020 American Control Conference*, Jul. 2020, pp. 4231–4236.

[108] A. Fuchs and M. Morari, "Placement of HVDC links for power grid stabilization during transients," in *IEEE PowerTech*, Grenoble, France, 2013.

[109] W. Wang, Y. Li, Y. Cao, U. Häger, and C. Rehtanz, "Adaptive droop control of VSC-MTDC system for frequency support and power sharing," *IEEE Transactions on Power Systems*, vol. 33, no. 2, pp. 1264–1274, Mar. 2018.

[110] D. Van Hertem, R. Eriksson, L. Söder, and M. Ghandhari, "Coordination of multiple power flow controlling devices in transmission systems," in *9th IET International Conference on AC and DC Power Transmission*, London, UK, Oct. 2010.

[111] H. W. Bode, *Network Analysis and Feedback Amplifier Design*. New York: Van Nostrand, 1945.

[112] M. M. Seron, J. H. Braslavsky, and G. C. Goodwin, *Fundamental Limitations in Filtering and Control*. London, UK: Springer, 1997.

[113] J. S. Freudenberg and D. P. Looze, *Frequency Domain Properties of Scalar and Multivariable Feedback Systems*. Berlin, Germany: Springer-Verlag, 1988.

[114] K. Zhou, *Robust and Optimal Control*. Englewood Cliffs, NJ: Prentice Hall, 1996.

[115] S. Skogestad and I. Postlethwaite, *Multivariable Feedback Control: Analysis and Design*, 2nd ed. New York: Wiley, 2007.

[116] J. S. Freudenberg, C. V. Hollot, R. H. Middleton, and V. Toochinda, "Fundamental design limitations of the general control configuration," *IEEE Transactions on Automatic Control*, vol. 48, no. 8, pp. 1355–1370, Aug. 2003.

[117] S. Fang, J. Chen, and H. Ishii, *Towards Integrating Control and Information Theories*, ser. Lecture Notes in Control and Information Sciences. Cham, Switzerland: Springer International Publishing, 2017, vol. 465.

[118] L. E. Jones, "On zero dynamics and robust control of large AC and DC power systems," Ph.D. dissertation, KTH Royal Institute of Technology, Stockholm, Sweden, 1999.

[119] N. Martins, H. J. C. P. Pinto, and L. T. G. Lima, "Efficient methods for finding transfer function zeros of power systems," *IEEE Transactions on Power Systems*, vol. 7, no. 3, pp. 1350–1361, Aug. 1992.

[120] A. C. Antoulas, *Approximation of Large-Scale Dynamical Systems*. Society for Industrial and Applied Mathematics, Jan. 2005.

[121] W. J. Rugh, *Linear System Theory*, 2nd ed. Upper Saddle River, NJ: Pearson, 1995.

[122] C.-T. Chen, *Linear System Theory and Design*, 3rd ed., ser. Oxford Series in Electrical and Computer Engineering. New York: Oxford University Press, 1999.

[123] J. H. Chow, Ed., *Time-Scale Modeling of Dynamic Networks with Applications to Power Systems.* New York: Springer, 1982, vol. Vol. 46.

[124] C. Nordling, *Physics Handbook for Science and Engineering*, 7th ed. Lund, Sweden: Studentlitteratur, 2004.

[125] A. Monticelli, *Power System Oscillations.* Boston, MA: Kluwer Academic Publishers, 1999.

[126] R. A. Horn and C. R. Johnsson, *Matrix Analysis.* Cambridge, UK: Cambridge University Press, 1985.

[127] V. Klema and A. Laub, "The singular value decomposition: Its computation and some applications," *IEEE Transactions on Automatic Control*, vol. 25, no. 2, pp. 164–176, Apr. 1980.

[128] D. Xue and Y. Chen, *Solving Applied Mathematical Problems with MATLAB.* Boca Raton, FL: CRC Press, 2009.

[129] N. R. Chaudhuri, A. Domahidi, R. Majumder, B. Chaudhuri, P. Korba, S. Ray, and K. Uhlen, "Wide-area power oscillation damping control in Nordic equivalent system," *IET Generation, Transmission & Distribution*, vol. 4, no. 10, pp. 1139–1150, 2010.

[130] D. Ruiz-Vega and M. Pavella, "A comprehensive approach to transient stability control. I-II," *IEEE Transactions on Power Systems*, vol. 18, no. 4, pp. 1446–1460, Nov. 2003.

[131] C. V. Loan, "Computing integrals involving the matrix exponential," *IEEE Transactions on Automatic Control*, vol. 23, no. 3, pp. 395–404, Jun. 1978.

[132] F. Dörfler and F. Bullo, "Kron reduction of graphs with applications to electrical networks," *IEEE Transactions on Circuits and Systems I: Regular Papers*, vol. 60, no. 1, pp. 150–163, Jan. 2013.

[133] F. Milano and Á. Ortega, "Frequency divider," *IEEE Transactions on Power Systems*, vol. 32, no. 2, pp. 1493–1501, Mar. 2017.

[134] J. Zhang, C. Y. Chung, and Y. Han, "A novel modal decomposition control and its application to PSS design for damping interarea oscillations in power systems," *IEEE Transactions on Power Systems*, vol. 27, no. 4, pp. 2015–2025, Nov. 2012.

[135] T. Glad and L. Ljung, *Reglerteknik: Grundläggande Teori*, 4th ed. Lund, Sweden: Studentlitteratur, 2006.

[136] M. A. Abido, "Optimal design of power-system stabilizers using particle swarm optimization," *IEEE Transactions on Energy Conversion*, vol. 17, no. 3, pp. 406–413, Sep. 2002.

[137] E. V. Larsen, J. J. Sanchez-Gasca, and J. H. Chow, "Concepts for design of FACTS controllers to damp power swings," *IEEE Transactions on Power Systems*, vol. 10, no. 2, pp. 948–956, May 1995.

[138] U. P. Mhaskar and A. M. Kulkarni, "Power oscillation damping using FACTS devices: Modal controllability, observability in local signals, and location of transfer function zeros," *IEEE Transactions on Power Systems*, vol. 21, no. 1, pp. 285–294, Feb. 2006.

[139] E. V. Larsen and J. H. Chow, "SVC control design concepts for system dynamic performance," *IEEE special symposium on application of static VAR systems for system dynamic performance*, pp. 36–53, 1987.

[140] H. Saboori, M. Mohammadi, and R. Taghe, "Virtual power plant (VPP), definition, concept, components and types," in *Asia-Pacific Power and Energy Engineering Conference*, Wuhan, China, Mar. 2011.

[141] S. Ghavidel, L. Li, J. Aghaei, T. Yu, and J. Zhu, "A review on the virtual power plant: Components and operation systems," in *IEEE International Conference on Power System Technology*, Wollongong, Australia, Sep. 2016.

[142] M. Vasirani, R. Kota, R. L. G. Cavalcante, S. Ossowski, and N. R. Jennings, "An agent-based approach to virtual power plants of wind power generators and electric vehicles," *IEEE Transactions on Smart Grid*, vol. 4, no. 3, pp. 1314–1322, Sep. 2013.

[143] M. Alvarez, S. K. Rönnberg, J. Bermúdez, J. Zhong, and M. H. J. Bollen, "A generic storage model based on a future cost piecewise-linear approximation," *IEEE Transactions on Smart Grid*, vol. 10, no. 1, pp. 878–888, Jan. 2019.

[144] P. Moutis, P. S. Georgilakis, and N. D. Hatziargyriou, "Voltage regulation support along a distribution line by a virtual power plant based on a center of mass load modeling," *IEEE Transactions on Smart Grid*, vol. 9, no. 4, pp. 3029–3038, Jul. 2018.

[145] H. H. Alhelou, P. Siano, M. Tipaldi, R. Iervolino, and F. Mahfoud, "Primary frequency response improvement in interconnected power systems using electric vehicle virtual power plants," *World Electric Vehicle Journal*, vol. 11, no. 2, p. 40, May 2020.

[146] J. Schiffer, D. Goldin, J. Raisch, and T. Sezi, "Synchronization of droop-controlled microgrids with distributed rotational and electronic generation," in *52nd IEEE Conference on Decision and Control*, Firenze, Italy, Dec. 2013, pp. 2334–2339.

[147] W. Zhong, J. Chen, M. Liu, M. A. A. Murad, and F. Milano, "Coordinated control of virtual power plants to improve power system short-term dynamics," *Energies*, vol. 14, no. 4, p. 1182, Feb. 2021.

[148] POSYTYF, "Concept & objectives," Accessed on: Feb. 16, 2021. [Online]. Available: https://posytyf-h2020.eu/project-overview/work-plan/

[149] W. Li and G. Joos, "A power electronic interface for a battery supercapacitor hybrid energy storage system for wind applications," in *IEEE Power Electronics Specialists Conference*, Rhodes, Greece, Jun. 2008, pp. 1762–1768.

[150] M. E. Glavin, P. K. W. Chan, S. Armstrong, and W. G. Hurley, "A standalone photovoltaic supercapacitor battery hybrid energy storage system," in *13th International Power Electronics and Motion Control Conference*, Poznan, Poland, Sep. 2008, pp. 1688–1695.

[151] F. L. Müller and B. Jansen, "Large-scale demonstration of precise demand response provided by residential heat pumps," *Applied Energy*, vol. 239, pp. 836–845, Apr. 2019.

[152] F. Wilches-Bernal, J. H. Chow, and J. J. Sanchez-Gasca, "A fundamental study of applying wind turbines for power system frequency control," *IEEE Transactions on Power Systems*, vol. 31, no. 2, pp. 1496–1505, Mar. 2016.

[153] L. Saarinen, P. Norrlund, U. Lundin, E. Agneholm, and A. Westberg, "Full-scale test and modelling of the frequency control dynamics of the Nordic power system," in *IEEE Power and Energy Society General Meeting*, Boston, MA, Jul. 2016.

[154] J. Jonkman, S. Butterfield, W. Musial, and G. Scott, "Definition of a 5-MW reference wind turbine for offshore system development," NREL, USA, Tech. Rep., 2009.

[155] R. Pates and E. Mallada, "Robust scale-free synthesis for frequency control in power systems," *IEEE Transactions on Control of Network Systems*, vol. 6, no. 3, pp. 1174–1184, Sep. 2019.

[156] P. Ioannou and G. Tao, "Frequency domain conditions for strictly positive real functions," *IEEE Transactions on Automatic Control*, vol. 32, no. 1, pp. 53–54, Jan. 1987.

[157] P. V. Kokotovic, J. J. Allemong, J. R. Winkelman, and J. H. Chow, "Singular perturbation and iterative separation of time scales," *Automatica*, vol. 16, no. 1, pp. 23–33, Jan. 1980.

[158] M. Arcak, C. Meissen, and A. Packard, *Networks of Dissipative Systems*, ser. SpringerBriefs in Electrical and Computer Engineering. Cham, Switzerland: Springer International Publishing, 2016.

[159] J. A. Fax and R. M. Murray, "Information flow and cooperative control of vehicle formations," *IEEE Transactions on Automatic Control*, vol. 49, no. 9, pp. 1465–1476, Sep. 2004.

[160] A. Gattami and R. Murray, "A frequency domain condition for stability of interconnected MIMO systems," in *Proceedings of the 2004 American Control Conference*, vol. 4, Boston, MA, Jun. 2004, pp. 3723–3728.

[161] L. Huang, H. Xin, and F. Dörfler, "H∞-Control of grid-connected converters: Design, objectives and decentralized stability certificates," *IEEE Transactions on Smart Grid*, vol. 11, no. 5, pp. 3805–3816, Sep. 2020.

[162] R. Olfati-Saber, J. A. Fax, and R. M. Murray, "Consensus and cooperation in networked multi-agent systems," *Proceedings of the IEEE*, vol. 95, no. 1, pp. 215–233, Jan. 2007.

[163] F. Bullo, *Lectures on Network Systems*. Kindle Direct Publishing, 2020.

[164] J. M. Maciejowski, *Multivariable Feedback Design*, ser. Electronic Systems Engineering Series. Wokingham, England: Addison-Wesley, 1989.

[165] I. Postlethwaite and A. G. J. MacFarlane, *A Complex Variable Approach to the Analysis of Linear Multivariable Feedback Systems*. Berlin, Germany: Springer, 1979, no. 12.

[166] J. W. Brown and R. V. Churchill, *Complex Variables and Applications*, 7th ed. Boston, MA: McGraw-Hill Higher Education, 2004.

[167] R. A. Horn and C. R. Johnson, *Topics in Matrix Analysis*, 1st ed. Cambridge, UK: Cambridge University Press, 1991.

[168] F. Paganini and E. Mallada, "Global analysis of synchronization performance for power systems: Bridging the theory-practice gap," *IEEE Transactions on Automatic Control*, vol. 65, no. 7, pp. 3007–3022, Jul. 2020.